Magnetic order and excitations in perovskite iridates studied with resonant X-ray scattering techniques

Stefano Boseggia

A thesis presented for the degree of
Doctor of Philosophy

Department of Physics and Astronomy
University College London
United Kingdom
July 2014

I, Stefano Boseggia confirm that the work presented in this thesis is my own. Where information has been derived from other sources, I confirm that this has been indicated in the thesis.

to Maya and Massimiliano

Magnetic order and excitations in perovskite iridates studied with resonant X-ray scattering techniques

Stefano Boseggia

Abstract

Transition metal oxides containing a $5d$ element are increasingly attracting attention as an arena in which to search for novel electronic states. These are proposed to derive from the interplay between the strong spin-orbit interaction (SOI) in the $5d$s, the electronic correlations and crystal field effects. Iridium based compounds have featured predominantly in this quest, with considerable focus on the layered perovskites in which a novel "spin-orbit induced" Mott-like insulating state emerges. In this case, the SOI leads to the $j_{\text{eff}} = 1/2$ ground state for the Ir^{4+} ($5d^5$) ions observed in Sr_2IrO_4.

In this thesis I demonstrate that resonant X-ray scattering techniques at the Ir L edges are a valuable tool to investigate the electronic and magnetic properties of iridium oxides. In particular the evolution of the $j_{\text{eff}} = 1/2$ state as a function of structural distortions in the single layer iridates Sr_2IrO_4 and Ba_2IrO_4, and as a function of the dimensionality in the bilayer $\text{Sr}_3\text{Ir}_2\text{O}_7$ is investigated. My findings show that the magnetic and electronic structures in the single layered perovskites are remarkably robust to structural distortions. Conversely, adding an extra IrO_6 layer ($\text{Sr}_2\text{IrO}_4 \rightarrow \text{Sr}_3\text{Ir}_2\text{O}_7$) the ground and excited states change dramatically. Both these phenomena can be linked directly to the unique three-dimensional character of the $j_{\text{eff}} = 1/2$ state.

Furthermore, the X-ray resonant scattering cross-section of Ir^{4+} at the $L_{2,3}$ edges, calculated in a single-ion model, shows a non-trivial dependence on the direction of the magnetic moment, μ. These results provide important insights into the interpretation of X-ray data from the iridates, including that a $j_{\text{eff}} = 1/2$ ground state cannot be assigned on the basis of L_2/L_3 intensity ratio alone.

List of publications

1. M. Moretti Sala, M. Rossi, A. Al-Zein, **S. Boseggia**, R. S. Perry, D. Prabhakaran, A. T. Boothroyd, N. B. Brookes, D. F. McMorrow, G. Monaco and M. Krish. "*Crystal field splitting in* Sr_2IrO_4 *and* $Sr_3Ir_2O_7$ *probed by X-ray Raman spectroscopy*", accepted in Phys. Rev. B.

2. L. Moreschini, S. Moser, A. Ebrahimi, B. Dalla Piazza, K. S. Kim, **S. Boseggia**, D. McMorrow, H. Rønnow, J. Chang, D. Prabhakaran, A. T. Boothroyd, E. Rotenberg, A. Bostwick and M. Grioni. "*Giant bilayer splitting and wave functions symmetry in* $Sr_3Ir_2O_7$", Phys. Rev. B **89**, 201114(R) (2014) .

3. M. Moretti Sala, M. Rossi, **S. Boseggia**, J. Akimitsu, N. B. Brookes, M. Isobe, M. Minola, H. Okabe, H. M. Rønnow, L. Simonelli, D. F. McMorrow, G. Monaco. "*Orbital occupancies and the putative* $j_{\mathrm{eff}} = 1/2$ *ground state in* Ba_2IrO_4*: a combined oxygen K edge XAS and RIXS study*", Phys. Rev. B **89**, 121101(R) (2014).

4. M. Moretti Sala, **S. Boseggia**, D. F. McMorrow and G. Monaco. "*Resonant X-ray Scattering and the* $j_{\mathrm{eff}} = 1/2$ *Electronic Ground State in Iridate Perovskites*", Phys. Rev. Lett. **112**, 026403 (2014).

5. **S. Boseggia**, H. C. Walker, J. Vale, R. Springell, Z. Feng, R. S. Perry,M. Moretti Sala, H. M. Rønnow, S. P. Collins and D. F. Mc-

Morrow. “*Locking of iridium magnetic moments to the correlated rotation of oxygen octahedra in Sr_2IrO_4 revealed by X-ray resonant scattering*”, J. Phys.: Condens. Matter **25** 422202 (2013).

6. **S. Boseggia**, R. Springell, H. C. Walker, Ch. Rüegg, H. Okabe, M. Isobe, H. M. Rønnow, R. S. Perry, S. P. Collins and D. F. McMorrow.“*Robustness of Basal-Plane Antiferromagnetic Order and the* $J_{\text{eff}} = 1/2$ *State in Single-Layer Iridate Spin-Orbit Mott Insulators*”, Phys. Rev. Lett. **110**, 117207 (2013).

7. B. M. Wojek, M. H. Berntsen1, **S. Boseggia**, A. T. Boothroyd, D. Prabhakaran, D. F. McMorrow, H. M. Rnnow, J Chang and O Tjernberg. “*The* $J_{\text{eff}} = 1/2$ *insulator* $Sr_3Ir_2O_7$ *studied by means of angle-resolved photoemission spectroscopy*”, J. Phys.: Condens. Matter **24** 415602 (2013).

8. **S. Boseggia**, R. Springell, H. C. Walker, A. T. Boothroyd,D. Prabhakaran, S. P. Collins and D. F. McMorrow. “*On the magnetic structure of* $Sr_3Ir_2O_7$*: an X-ray resonant scattering study*”, J. Phys.: Condens. Matter **24** 312202 (2012).

9. **S. Boseggia**, R. Springell, H. C. Walker, A. T. Boothroyd,D. Prabhakaran, S. P. Collins and D. F. McMorrow. “*Antiferromagnetic order and domains in* $Sr_3Ir_2O_7$ *probed by X-ray resonant scattering*”, Phys. Rev. B **85**, 184432 (2012).

Contents

List of Figures

List of Tables

Introduction

Interest in strongly correlated electronic systems has recently been extended from $3d$ transition metal oxides (TMOs) to $5d$ oxides. $3d$ TMOs host a plethora of phenomena in solid state physics, from high temperature superconductivity in cuprates, to colossal magnetoresistance in perovskite manganites and, more recently, multiferroicity. These effects are mainly ascribed to the strong electronic correlations that distinguish $3d$ TMOs. $5d$ TMOs are generally expected to be weakly correlated. However, the interplay between the strong spin-orbit interaction (SOI) possessed by $5d$ systems and correlation effects pushes these materials towards the strongly correlated regime, favouring the emergence of new correlated ground states with the added ingredient of entangled spin and orbital moments. As a consequence, $5d$ TMOs show a rich phase diagram as a function of the electronic correlation U/t, and the SOI λ/t, in units of the hopping amplitude t (see Fig. 1). In the bottom-left corner of Fig. 1 reside simple metals or band insulators. In the top-left corner where the effect of electronic correlation dominates, lie Mott insulators. In the strong SOI regime (bottom-right corner) we find topological insulators. At the center of the phase diagram where electronic correlations and SOI cooperate, reside $5d$ TMOs.

To date most attention has been focused on iridates, as a consequence of the reported realization of a novel quantum "$j_{\mathrm{eff}} = 1/2$" ground state. This state emerges from the combined effects of cubic crystal field and

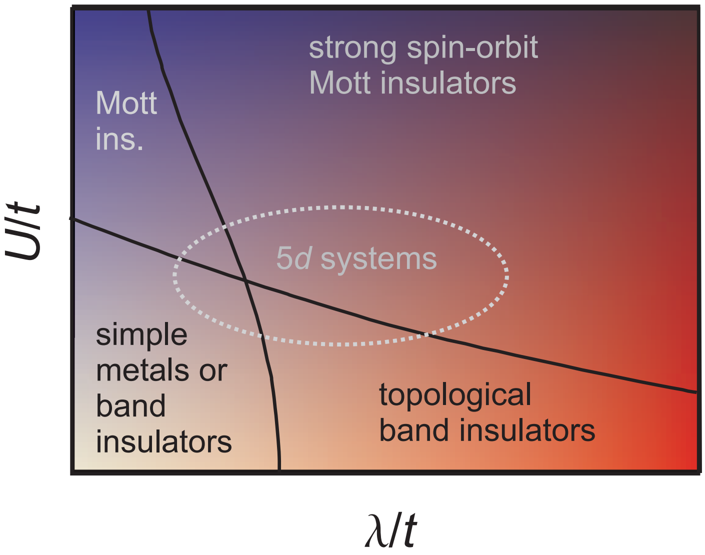

Figure 1: Schematic phase diagram for electronic material as a function of the electronic correlation U/t and the SOI λ/t, where t is the hopping amplitude. In the bottom-left corner reside simple metals or band insulators. In the top-left corner where the effect of electronic correlation dominates, lie Mott insulators. In the strong SOI regime (bottom-right corner) we find topological insulators. At the center of the phase diagram where electronic correlations and SOI cooperate, reside $5d$ TMOs like iridates. Adapted from Ref. [1]

the SOI which act jointly on the Ir ion. This novel ground state shows an unusual 3-dimensional shape which is a direct manifestation of the spin-orbit entanglement. Since the macroscopic physical properties always reflect the microscopic ones, a tool sensitive to the atomic wave functions is highly desirable to derive a fundamental understanding of the displayed phenomena. X-ray resonant scattering techniques have played a leading role in driving this field forward, due to the fact that the incident X-ray energy can be tuned to excite transitions between specific electronic wave functions.

The purpose of this thesis is therefore to fully exploit the power of resonant scattering techniques to investigate the magnetic order and the excited states in layered perovskite iridates.

In Chapter 1 I present the main ingredients that characterize $5d$ TMOs and distinguish them from the $3d$ counterpart. I introduce the “spin-orbit induced” $j_{\text{eff}} = 1/2$ state and discuss its dependence on the magnetic moment orientation and the tetragonal crystal field as obtained from a single-ion model. Finally, I present the superexchange Hamiltonian usually used to describe layer perovskite iridates.

In the first part of Chapter 2 the general formalism of resonant X-ray scattering is presented. The central part of the chapter is dedicated to the calculation of the resonant scattering cross-section in iridium oxides within a single ion model. As I will demonstrate, these calculations provide a valuable tool to interpret the resonant elastic (REXS) and inelastic (RIXS) X-ray scattering experiments performed at the Ir $L_{2,3}$ edges presented in Chapters 3–5.

In the last part of the Chapter 2, I briefly introduce two synchrotron beamlines which have been used in the present work. I16 at Diamond Light Source is a magnetic scattering beamline where the magnetic structure can be investigated by means of resonant or non-resonant magnetic scattering techniques. ID20 at the ESRF is a RIXS beamline dedicated to the study of momentum-resolved magnetic and electronic excitations.

Chapters 3–5 contain the main experimental results. In Chapter 3, I investigate the evolution of the $j_{\mathrm{eff}} = 1/2$ state as a function of structural distortions in the single layer iridates Sr_2IrO_4 and Ba_2IrO_4. The first part of the chapter is dedicated to the Sr based single layer iridate. Sr_2IrO_4 is a prototype of the class of "spin-orbit induced" Mott insulators believed to be described by a $j_{\mathrm{eff}} = 1/2$ ground state. In Sr_2IrO_4, the strong SOI is predicted to manifest itself in the locking of the magnetic moments to the correlated rotation of the oxygen octahedra that characterizes its twisted layered perovskite structure. Using X-ray resonant magnetic scattering (XRMS) at the Ir L_3 edge I unravel fine details of the basal-plane canted antiferromagnetic structure. Furthermore, I confirm that in Sr_2IrO_4 the magnetic moments rigidly follow the rotation of the oxygen octahedra, indicating that, even in the presence of significant non-cubic structural distortions, it is a close realization of the $j_{\mathrm{eff}} = 1/2$ state.

The second part of Chapter 3 deals with the magnetic and electronic properties of Ba_2IrO_4 and offers a comparative study with the Sr-based compound. In Ba_2IrO_4, the lack of octahedral rotation leads to a simple basal-plane antiferromagnetic structure which I report for the first time by means of Ir L_3 edge XRMS. A comparative study between the single layer iridates reveals that the dominant, long-range antiferromagnetic order is remarkably similar in the two compounds. The robustness of the magnetic properties to the considerable structural differences between the Ba and Sr analogues is discussed in terms of the enhanced role of the spin-orbit interaction in $5d$ transition metal oxides.

Chapters 4–5 explore the evolution of the $j_{\text{eff}} = 1/2$ state as a function of the dimensionality in the bilayer member of the Ruddlesden-Popper series $Sr_{n+1}Ir_nO_{3n+1}$, $Sr_3Ir_2O_7$. Chapter 4 is dedicated to the investigation of the ground state properties of $Sr_3Ir_2O_7$ by means of XRMS. Surprisingly, the addition of an extra IrO_6 layer greatly modifies the magnetic structure of the bilayer compound which, in contrast to the single layer iridates, shows a c-axis collinear antiferromagnetic state. However, the $j_{\text{eff}} = 1/2$ state is stable even for a system in proximity of a metal-to-insulator transition, as established by my investigation.

Chapter 5 finally presents a comprehensive RIXS study of the magnetic excitations in $Sr_3Ir_2O_7$. Ir L_3 edge RIXS is a technique that has emerged only very recently to study propagating magnetic excitations in iridium oxides and can be seen as a complement in the hard X-ray regime of the more established Cu L_3 RIXS. In the first part of Chapter 5, I present calculations of the RIXS cross-section for a single ion model which demonstrate the possibility to observe “spin-flip” processes at the Ir L_3 edge. In the second part I exploit L_3 edge RIXS to study the low-energy magnetic excitations in $Sr_3Ir_2O_7$. My study reveals the presence of two gapped magnetic modes that are assigned to transitions from a dimerised singlet ground state to two triplet excited states. My findings reveal the dominant role of the intrinsic strong anisotropies which distinguishes the bilayer $Sr_3Ir_2O_7$ from the single layer compounds.

Chapter 6 briefly summarizes the main conclusions of the present work and introduces future developments linked to this subject.

Chapter 1

Novel electronic states in perovskite iridates

Recently, Ir-based transition metal oxides (TMOs) have been identified as a fertile ground to search for novel correlated ground states and excitations. The salient interactions in these compounds (the electronic band width, on-site Coulomb repulsion, and spin-orbit coupling) are on a similar energy scale, opening the doors to exotic new states of matter. In this Chapter we will first introduce the main ingredients that characterize $5d$ TMOs and distinguish them from the $3d$ counterpart. Afterwards, we will introduce the "spin-orbit induced" $j_{\text{eff}} = 1/2$ state and we discuss its dependence on magnetic moment orientation and tetragonal crystal field as obtained from a single-ion model. Finally, we present the superexchange Hamiltonian currently used to describe layered perovskite iridates.

Contents

1.1 Strongly correlated electron systems

In the last few decades transition metal oxides (TMOs) have been the subject of intensive studies. This is due to the fact that these materials host a number of intriguing phenomena: from high temperature superconductivity in cuprates [2], to colossal magnetoresistance in perovskite manganites [3] and, more recently, multiferroicity [4]. This colourful range of physical properties is due to the interplay of charge, spin, and orbital degrees of freedom, which all play an active role in TMOs. Band structure calculations often fail to describe the behaviour of the non-fully itinerant electrons in these materials, mainly because they are treated as independent particles. Actually, different particles cannot be treated as independent and, in general

$$\langle AB \rangle \neq \langle A \rangle \langle B \rangle, \tag{1.1}$$

i.e. the expectation value of a product of quantities usually differs from the product of the expectation values of the single quantities. This effect is called *correlation* and it is particularly relevant when electrons are confined in space, as for example in the case of localized $3d$ bands (as it will be show in the Section 1.2.2).

Significant theoretical efforts have been made to produce a new framework to describe appropriately these systems. A model that has been successfully used to describe $3d$ electrons in solids is the single-band Hubbard model [5, 6]. This is an extension of the tight-binding model where an additional interaction term $\mathcal{H}_{\mathrm{I}}$ is added to the hopping term $\mathcal{H}_{\mathrm{H}}$. The total Hamiltonian is usually written as

$$\mathcal{H} = \mathcal{H}_{\mathrm{H}} + \mathcal{H}_{\mathrm{I}} = \sum_{i,j} \sum_{\sigma} t_{ij} \mathbf{c}^{\dagger}_{i\sigma} \mathbf{c}_{j\sigma} + h.c. + U \sum_{i} \mathbf{n}_{i\uparrow} \mathbf{n}_{i\downarrow} \tag{1.2}$$

where $\mathbf{c}^{\dagger}_{i\sigma}(\mathbf{c}_{i\sigma})$ are operators that create (annihilate) an electron of spin

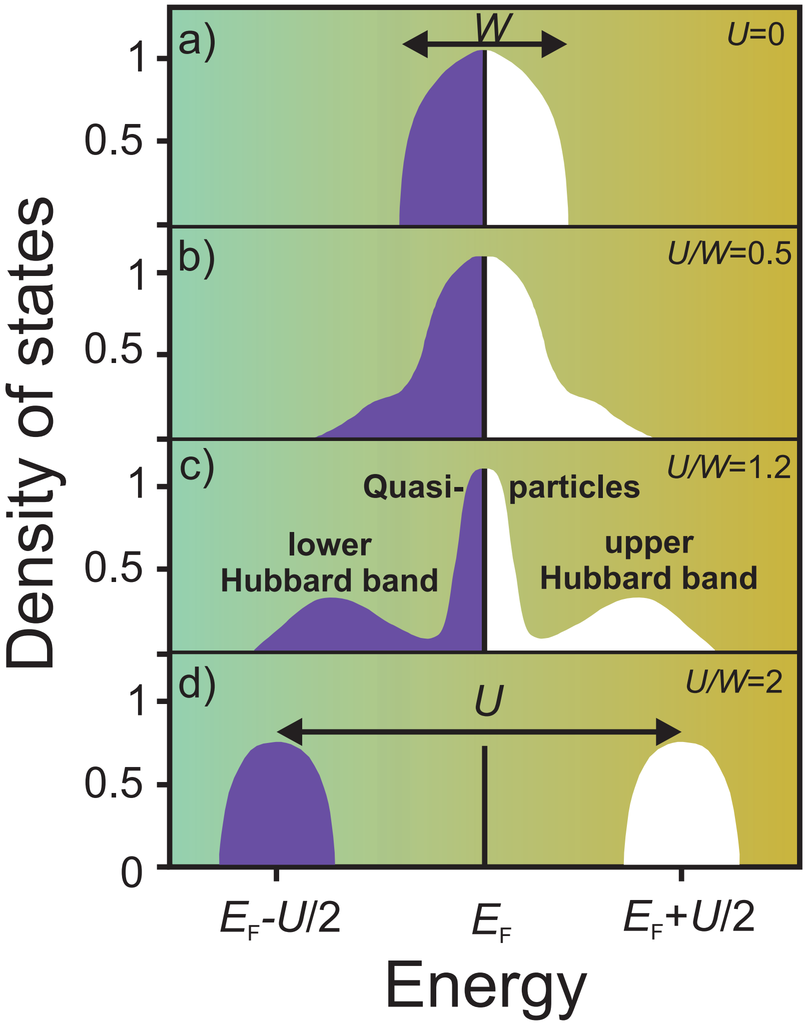

Figure 1.1: Evolution of the density of states (DOS) of electrons in the dynamical mean-field solution of the Hubbard model at half filling. U is the on-site electron correlation, W is the bandwidth of non-interacting electrons which is proportional to the effective hopping integral via the coordination number N. (a) For non interacting electrons ($U = 0$) the Fermi level is located at the middle of the band and the system is a classical metal. (b) In the weakly correlated regime ($U/W < 1$) electrons can be described as quasiparticle whose DOS resembles the one of free electrons. (c) Enhancing the level of correlation ($U/W > 1$) the spectrum shows 3 peaks typical of correlated metals: a quasi-particle feature at the Fermi level and a lower (for $E < E_F$) and an upper (for $E > E_F$) Hubbard band start to grow more apart. (d) In the strongly correlated regime ($U/W \gg 1$) a Mott-Hubbard transition into an insulating state takes place. Adapted from [7].

$\sigma =\uparrow, \downarrow$ at a site i, $t_{ij} = t_{ji}$ is the hopping integral between adjacent sites, and $\mathbf{n}_{i\sigma} = \mathbf{c}^{\dagger}_{i\sigma}\mathbf{c}_{i\sigma}$. Two electrons at the same lattice site i pay a greater energy cost U. This model describes in a very simple way the competition between the kinetic term $\mathcal{H}_{\mathrm{H}}$ that tries to delocalize the electrons making the system a conductor and the correlation term $\mathcal{H}_{\mathrm{I}}$ that forces the electrons to remain localized near a site. If we consider a single electron per site, i.e. a half filled band, in the limit $U/t \rightarrow 0$ the system is metallic, in agreement with band theory calculations. In the opposite limit, $U/t \rightarrow \infty$, a double occupation of the same site is energetically very unfavourable and thus strongly suppressed. In this case $\langle \mathbf{n}_{i\uparrow}\mathbf{n}_{i\downarrow} \rangle$ cannot be factorized since $\langle \mathbf{n}_{i\uparrow}\mathbf{n}_{i\downarrow} \rangle \neq \langle \mathbf{n}_{i\uparrow} \rangle \langle \mathbf{n}_{i\downarrow} \rangle$ and the electronic correlations localize electrons on a site driving the system into an insulating state. We will therefore expect a metal-to-insulator (MIT) transition to happen as a function of U/t, this is the so-called “Mott-Hubbard” transition. Fig. 1.1 shows the evolution of the density of states (DOS) of electrons calculated in a dynamical mean field approach for increasing values of U from a classical metal ($U = 0$) (a) to a Mott insulator ($U/W \gg 1$)(d), where the bandwidth W is proportional to the hopping term t via the coordination number N. Several $3d$ TMOs undergo a “Mott-Hubbard” MIT, for a comprehensive review see Ref. [8].

An interesting feature of the Hubbard model is that in the strong-coupling limit ($U/W \gg 1$), where electrons are mainly localized, it favours an antiferromagnetic coupling between nearest neighbours. This is in fact the only way electrons can hop to the nearest site respecting the Pauli exclusion principle. Therefore, in the strong coupling regime, the Hubbard model is converted into the antiferromagnetic Heisenberg model

$$\mathcal{H} = J \sum_{i,j} \mathbf{S}_i \cdot \mathbf{S}_j \tag{1.3}$$

where $J = 4t^2/U$ is the superexchange between nearest neighbors i, j. As will be shown in the next chapters, the Heisenberg term is often the dominant in the low energy physics of layered perovskite iridates.

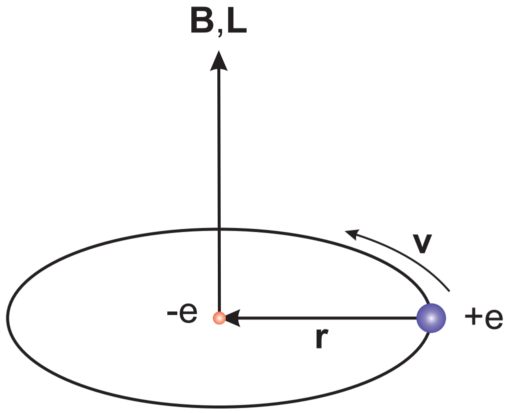

Figure 1.2: A hydrogen-like atom in the electron rest frame

1.2 From 3*d* to 5*d* TMOs

In the next sections we will show how the main ingredients that make the physics of $3d$ transition metal compounds so peculiar and fascinating are modified for the $5d$ counterpart. Moving down from the $3d$ transition metal row to the $5d$ transition metal row we are dealing with much heavier ions. This has two major consequences: a strong enhancement of the spin-orbit interaction and a greater spatial extension of the valence d-orbitals.

1.2.1 Spin-orbit coupling

In this section we derive in a semiclassical way the spin-orbit coupling term emphasizing its dependence on the atomic number Z. We consider a hydrogen-like system with an electron orbiting around a positively charged nucleus. This problem can be more conveniently reformulated in the electron rest frame, where a positively charged particle is orbiting around an electron at rest (See Fig.1.2). The positive charge produces a magnetic field $\mathbf{B}$ that tends to align the magnetic moment of the electron $\boldsymbol{\mu}$ along the direction of the field. The magnetic field experienced by the electron at the origin is given by

$$\mathbf{B} = -\frac{\mathbf{v} \times \mathbf{E}}{c^2} = -\frac{\mathbf{v} \times (-\nabla V(r))}{c^2} = \frac{1}{c^2}\mathbf{v} \times \mathbf{r}\frac{1}{r}\frac{dV(r)}{dr}, \qquad (1.4)$$

where $V(r)$ is the electrostatic potential due to the nucleus and $\mathbf{v}$ is the velocity of the electron (nucleus). Taking into account the definition of the orbital angular momentum, $\hbar\mathbf{L} = m_e\mathbf{v} \times \mathbf{r}$, Eq.1.4 can be rewritten as:

$$\mathbf{B} = \frac{\hbar}{m_e c^2}\mathbf{L}\frac{1}{r}\frac{dV(r)}{dr}. \tag{1.5}$$

The magnetic moment of the electron interacting with this magnetic field is given by

$$\boldsymbol{\mu} = -\frac{e}{2m_e}\hbar g\mathbf{S} = -\frac{e}{m_e}\hbar\mathbf{S}, \tag{1.6}$$

where $\mathbf{S}$ is the spin angular momentum and a spin g-factor g=2 has been assumed. The Hamiltonian representing the interaction between the magnetic field due to the orbiting nucleus and the electron magnetic moment can be written as:

$$\mathcal{H}_{\mathrm{SO}} = -\boldsymbol{\mu}\cdot\mathbf{B} = \frac{e\hbar^2}{m_e^2 c^2}\mathbf{S}\cdot\mathbf{L}\frac{1}{r}\frac{dV(r)}{dr}. \tag{1.7}$$

Substituting the electrostatic potential in a hydrogen-like system, $V(r) = Ze/4\pi\epsilon_0 r$, the Hamiltonian becomes

$$\mathcal{H}_{\mathrm{SO}} = \frac{Ze^2\hbar^2}{8\pi m_e^2 c^2\epsilon_0}\mathbf{S}\cdot\mathbf{L}\frac{1}{r^3}, \tag{1.8}$$

where a factor 1/2, known as Thomas precession [9], has been added in order to correct for the transformation from one inertial system to the other. We note that an elegant derivation of the spin-orbit interaction naturally comes out of the relativistic Dirac equation [10]. By recalling that for a $|n,l\rangle$ electronic state

$$\langle r^{-3}\rangle_{n,l} = \frac{Z^3}{a_0^3}\frac{2}{n^3 l(l+1)(2l+1)}, \tag{1.9}$$

where a_0 is the Bohr radius, the spin-orbit Hamiltonian finally reads as

$$\mathcal{H}_{\mathrm{SO}} = \frac{Z^4 e^2\hbar^2}{4\pi m_e^2 c^2\epsilon_0 a_0^3 n^3 l(l+1)(2l+1)}\mathbf{L}\cdot\mathbf{S} = \lambda\mathbf{L}\cdot\mathbf{S} \tag{1.10}$$

The term Z^4/n^3 explains the significant variation in the spin-orbit coupling (SOC) constant λ that takes place moving from $3d$ ions ($\lambda_{3d} \sim 20-40$ meV) [11] to $5d$ ions ($\lambda_{5d} \sim 200-500$ meV) [12].

1.2.2 More delocalized d states

The second difference between $3d$ and $5d$ transition metal ions is that the $5d$ orbitals are more delocalized than the corresponding $3d$ orbitals of lighter atoms. In Fig.1.3 we show the radial distribution function $r^2 R_{nd}(r)^2$ of cobalt and iridium, where $R_{nd}(r)$ is the radial wave function that reads

$$R_{3d}(r) = \frac{1}{9\sqrt{30}}\rho^2 \left(\frac{Z_{\text{eff}}}{a_0}\right)^{\frac{3}{2}} e^{-\rho/2}, \tag{1.11}$$

$$R_{5d}(r) = \frac{1}{150\sqrt{70}}\left(42 - 14\rho + \rho^2\right)\rho^2 \left(\frac{Z_{\text{eff}}}{a_0}\right)^{\frac{3}{2}} e^{-\rho/2} \tag{1.12}$$

in atomic units, for $n = 3, 5$ respectively. $\rho = \frac{2Z_{\text{eff}} r}{3a_0}$, where a_0 is the Bohr radius and Z_{eff} is the effective nuclear charge screened by the inner electrons. We have chosen $Z_{\text{eff}}(3d) = 11.86$ (for Co $3d^7$) and $Z_{\text{eff}}(5d) = 18.70$ (for Ir $5d^7$) [13]. We notice that for a $3d$-ion there is an increased probability to find a d-electron very close to the nucleus at $r \sim 0.4\,\text{Å}$, whereas for the corresponding $5d$-ion, the electron is more likely to be found at $r \sim 1\,\text{Å}$. This means that when the single ion is included in a crystal the strength of the interactions with the surrounding ligands can be rather different in the two cases.

A typical structure of transition metal oxides is a 6-fold coordinated octahedron where the d-metal occupies the center of the octahedron and the negatively charged ligands (usually oxygens) the vertexes (see for example Fig 1.3 and Fig A.1). In this structure, the orbitals that point toward the ligands experience a stronger Coulomb repulsion that the others. This is evident if we look at the bottom panel of Fig. 1.3, where we present a $3d$ and a $5d$ ion at the center of a octahedral cage of oxygens in the xy plane, for a typical d-ion-O distance of about 2 Å. In the xy plane the interactions with the oxygen atoms are mainly due to the metal xy and $x^2 - y^2$ orbitals. Owing to the more extended nature of $5d$ orbitals, the difference in the distance between the xy orbitals and the $x^2 - y^2$ orbital from the negatively charged oxygens $(r_2^{nd} - r_1^{nd})$ is greater for the bigger ion. As a consequence the difference in the electrostatic potential experienced by xy and $x^2 - y^2$ orbitals respectively will be greater in $5d$-

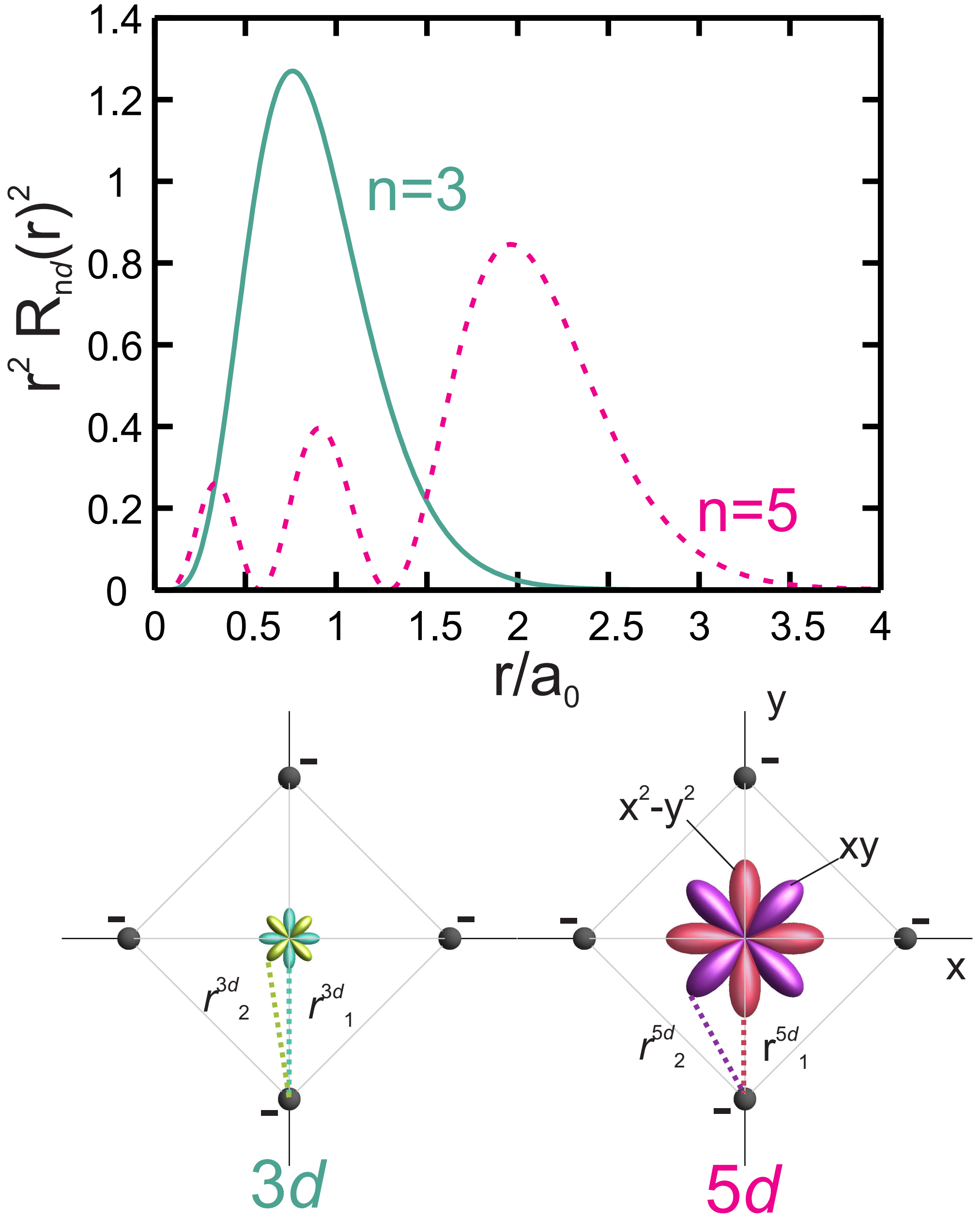

Figure 1.3: Top panel: Radial density probability $r^2 R_{nd}(r)^2$ for $3d$ orbitals of Co (light purple) and $5d$ orbitals of Ir in atomic units. Bottom panel: real space representation in the xy plane of an oxygen octhaedron of the $x^2 - y^2$ and xy orbital states for $3d$-system (left) and $5d$-system (right). Due to the more extended nature of the $5d$-orbitals the difference in the Coulomb repulsion experienced by $x^2 - y^2$ and xy orbitals is more significant than in the $3d$ counterpart.

systems. In general, the effect of the octahedral cage of oxygens will be to reduce the symmetry of the metal ions from spherical to cubic (O_h) and to split the atomic degenerate d-states into a lower triplet, the t_{2g} states and a upper doublet, the e_g states. The latter being the orbitals that point toward the ligand oxygens. A full derivation of the d-orbitals in a cubic ligand field is given in Appendix A. Here we report only the conclusions. The energy splitting between e_g and t_{2g} states is given by

$$E(e_g) - E(t_{2g}) = 10Dq = \frac{35Ze^2}{4a^5}\frac{2}{105}\langle r^4\rangle_{nd} \tag{1.13}$$

where $\langle r^4\rangle_{nd} = \int r^4 r^2 |R_{nd}(r)|^2 dr$ ands a is the distance between metal and ligand atoms. Applying Eq. 1.13 with $\langle r^4\rangle_{3d} = 1.28527\, a_0^4$ and $\langle r^4\rangle_{5d} = 20.2859\, a_0^4$ to the Co and Ir ions, one gets $10Dq(3d) \approx 151$ meV, and $10Dq(5d) \approx 2.34$ eV respectively. Even if this result is the outcome of a pure ionic model, where any covalency in the bonds has been neglected, it provides a good estimate of the change in the strength of the crystal field interaction when moving from $3d$ to $5d$ transition metal oxides. A direct effect of the enhanced crystal field interaction is that $5d$-ions are usually in a low-spin configuration because it is more convenient to minimize the strong crystal field energy rather than the Hund's exchange coupling. Experimental values of the crystal field splitting in $5d$-system are usually ~ 3 eV [14, 15, 16, 17].

Another consequence of the more delocalized nature of $5d$-orbitals is that the bandwidth is increased in $5d$ compounds. In order to illustrate this we refer to the tight-binding model. In this approximation the crystal Hamiltonian can be written as a sum of the atomic one plus a term that contains all the corrections to the atomic potential required to produce the full periodic potential of the crystal,

$$\mathcal{H} = \mathcal{H}_{at} + \Delta U(\mathbf{r}). \tag{1.14}$$

Diagonalizing the Hamiltonian in the basis of a linear combination of atomic orbitals gives the band dispersion $\epsilon(\mathbf{k})$ where the bandwidth W is proportional to the overlap integral

$$\gamma_{ij}(\mathbf{R}) = -\int \phi_i^*(\mathbf{r})\Delta U(\mathbf{r})\phi_j(\mathbf{r}-\mathbf{R}) \tag{1.15}$$

where $\phi_i(\mathbf{r})$, $\phi_j(\mathbf{r}-\mathbf{R})$ are the atomic wave function on different sites. More delocalized atomic d states lead to a greater value of the overlap integral γ_{ij} and corresponding higher bandwidth W. Experimental values of W range from 2 eV to 4 eV and 4 eV to 10 eV for $3d$ and $5d$ orbitals, respectively. The bandwidth W has also important effects on the mobility of the electrons. In fact writing the electron effective mass as

$$m^* = \frac{\hbar^2}{\partial^2\epsilon(\mathbf{k})/\partial\mathbf{k}^2} \sim \frac{\hbar^2}{W} \tag{1.16}$$

we notice that a narrow band results in an high effective mass. This means that in a narrow $3d$ band electrons are heavier and slower whereas in a wider $5d$ bands they are lighter and faster. The narrower a band, the longer an electron resides on an atom experiencing the presence of other electrons resulting in an enhancement of the electronic correlations U. This is the reason why $3d$ systems are usually considered "strongly-correlated electron systems" ($U \sim 5$–7 eV), while $5d$ systems are described as "weakly-correlated electron systems" ($U \leq 2$ eV).

1.3 Phase diagram of *5d* systems

In the previous section we have described how the most significant interactions are modified by the inclusion of heavy $5d$-atoms. The simple Hubbard model of Eq. 1.2 will thus be modified by the addition of the spin-orbit coupling term as:

$$\mathcal{H} = \sum_{i,j}\sum_{\sigma} t_{ij}^{\sigma}\mathbf{c}_{i\sigma}^{\dagger}\mathbf{c}_{j\sigma} + h.c. + U\sum_{i}\mathbf{n}_{i\uparrow}\mathbf{n}_{i\downarrow} + \lambda\sum_{i}\mathbf{L}_i\cdot\mathbf{S}_i \tag{1.17}$$

Witczak-Krempa et al. [1] and Pesin and Balents [18] have proposed a schematic phase diagram based on the solution of Eq. 1.17 in terms of the electronic correlation U/t and the SOC λ/t. The phase diagram (Fig. 1) is initially divided into four quadrants derived from the intersection of two lines separating the weak from the strong correlation regimes and the weak from the strong SOC regimes. The traditional $3d$ transition metals lie on the left hand side of the diagram and a metal-insulator transition (MIT) from a simple metal to a Mott insulator is expected when $U/t \sim 1$. By contrast upon increasing the SOC λ, a simple metal can be transformed into a topological insulator[1].

Considering the combined effect of electronic correlations and SOC, we realize that the two phenomena tend to cooperate rather than compete. Let consider first the effect of the SOC. This usually acts on the valence electrons by removing degeneracies thus forcing the narrowing of the valence bands. The narrower bands generated by SOC are then more susceptible to the Coulomb repulsion U, resulting in a downward shift of the horizontal boundary upon increasing λ. If we consider correlation effects first, U favours a localization of the electrons, as a consequence SOC that is usually insensitive to delocalization, is relatively enhanced. In fact, in the $U/t \gg 1$ regime, the low energy physics of the system is dictated by superexchange $J \sim t^2/U$ rather than the hopping process t. This means that the SOC regime is greatly enhanced with increasing correlations, since the effective bandwidth is J rather than t. A weak SOC system should in fact satisfy $\lambda \ll J \ll t$. As a consequence, for $U/t \gg 1$ the vertical boundary of the phase diagram shifts to the left.

There is an interesting intermediate region where the insulating behavior is obtained through the combined action of correlations and SOC. In this area reside $5d$-systems like iridium oxides and osmium oxides. The former have attracted significant attention after the first observation of a "spin-orbit induced" Mott-insulating state in Sr_2IrO_4 [19]. The majority of these oxides are weakly insulating materials containing iridium Ir^{4+} ions. Since the orbital moment is no longer quenched like in $3d$ metals due to the SOC effect, interactions are thought to depend strongly on the lattice geometry.

Most interesting crystal structures are a large family of $R_2Ir_2O_7$ ($R =$

---

[1] A topological insulator is a material with time reversal symmetry and non-trivial topological order, that behaves as an insulator in its interior but whose surface contains conducting states.

rare earth) pyrochlores, the honeycomb lattice $(Li/Na)_2IrO_3$ and the layered perovskites $(Ba/Sr)_{n+1}Ir_nO_{3n+1}$ (n =1, 2, ∞). The pyrochlore iridates host along the whole series from Ho to Nd a peculiar continuous MIT that in most of the cases is connected to a magnetic transition to an antiferromagnetic all-in all-out state [20]. For this class of material, exotic topological phases have been predicted based on theoretical investigations, ranging from topological insulators [1, 18], to spin liquid behaviour, Weyl semimetals [21], and axion insulators [22].

The honeycomb lattice iridates $(Li/Na)_2IrO_3$ have been the subject of several theoretical studies. They are in fact considered a promising platform for the realization of the Kitaev-Heisenberg model, a perfect solvable Hamiltonian relevant for quantum computing [23, 24]. Several experimental studies followed these predictions looking for the footprint of the realization of Kitaev Hamiltonian, e.g. the onset of a spin-liquid state [25, 26, 27].

The latter class of iridates is composed by the Ruddlesden-popper series $(Ba/Sr)_{n+1}Ir_nO_{3n+1}$ (n =1, 2, ∞). The interest in these compounds was first triggered by the observation of a “spin-orbit induced” insulating state in Sr_2IrO_4 [19, 14]. Further impetus was added by their structural and magnetic similarities to layered cuprates, and not least the prediction of superconducting states in the doped compounds [28, 29]. Layered perovskite iridates will be the main subject of this thesis.

1.4 The $j_{\text{eff}} = 1/2$ state

Irrespective of the crystal structure adopted by these systems, the starting point to describe iridium oxides is an Ir^{4+} ion in a $5d^5$ configuration at the center of a IrO_6 octahedron. As discussed in Section 1.2, the 5-fold degenerate d-orbital states, under the influence of a cubic crystal field (O_h symmetry), are split into a lower orbital triplet, the t_{2g} states, and an upper orbital doublet, the e_g states. Due to the strong crystal field splitting ($\sim$ 3 eV), the 5 d-electrons reside only in the t_{2g} manifold, the Ir ion adopts thus a low spin configuration and we can neglect as a good aproximation the contribution of the e_g orbitals. The system can be treated as a one-hole particle in the t_{2g} subspace. It is known that the projection of the orbital angular momentum operator onto the t_{2g} subspace is equivalent to an effective angular momentum $L_{\mathrm{eff}} = -1$ [30]. This can be seen by calculating the angular momentum matrices for one particle in the d-states, which read:

$$L_x = \left(\begin{array}{cc|ccc} 0 & 0 & 0 & 0 & -i \\ 0 & 0 & 0 & 0 & -i\sqrt{3} \\ \hline 0 & 0 & 0 & i & 0 \\ 0 & 0 & -i & 0 & 0 \\ i & i\sqrt{3} & 0 & 0 & 0 \end{array}\right), L_y = \left(\begin{array}{cc|ccc} 0 & 0 & 0 & -i & 0 \\ 0 & 0 & 0 & i\sqrt{3} & 0 \\ \hline 0 & 0 & 0 & 0 & -i \\ i & -i\sqrt{3} & 0 & 0 & 0 \\ 0 & 0 & i & 0 & 0 \end{array}\right) \tag{1.18}$$

$$\text{and} \quad L_z = \left(\begin{array}{cc|ccc} 0 & 0 & 2i & 0 & 0 \\ 0 & 0 & 0 & 0 & 0 \\ \hline -2i & 0 & 0 & 0 & 0 \\ 0 & 0 & 0 & 0 & i \\ 0 & 0 & 0 & -i & 0 \end{array}\right).$$

The matrices are given in the $\{|x^2-y^2\rangle, |3z^2-r^2\rangle, |xy\rangle, |xz\rangle, |yz\rangle\}$ basis. The calculation is straightforward by writing the d-states in the spherical harmonic basis $|Y_{l,m_l}\rangle$ and by using the relations:

$$L_z|Y_{l,m_l}\rangle = m_l\hbar|Y_{l,m_l}\rangle \quad \text{and} \quad L_\pm|Y_{l,m_l}\rangle = \hbar\sqrt{l\,(l+1) - m_l\,(m_l \pm 1)}|Y_{l,m_{l\pm 1}}\rangle \tag{1.19}$$

with $L\pm = L_x \pm iL_y$. By inspecting the matrices 1.18, we notice that in the e_g subspace block the matrix elements of $\mathbf{L}$ are zero. This means that the orbital angular momentum is completely quenched. Conversely, the matrix elements in the t_{2g} subspace are equivalent to that of an orbital angular momentum -1: $|L_z = 0\rangle \equiv |xy\rangle$ and $|L_z = \pm 1\rangle \equiv -\frac{1}{\sqrt{2}}\,(i|xz\rangle \pm |yz\rangle)$.

Adding the SOC to the $L_{\mathrm{eff}} = -1$ manifold, removes the degeneracies of the t_{2g} subspace via the formation of a total angular momentum quartet, the $j_{\mathrm{eff}} = 3/2$ state, lower in energy, and an upper $j_{\mathrm{eff}} = 1/2$ doublet (see Fig. 1.4). The former is fully occupied by 4 electrons, the latter is half filled. The multiplet structure is therefore reversed compared to the atomic orbital angular momentum $l = 1$. This is in agreement with

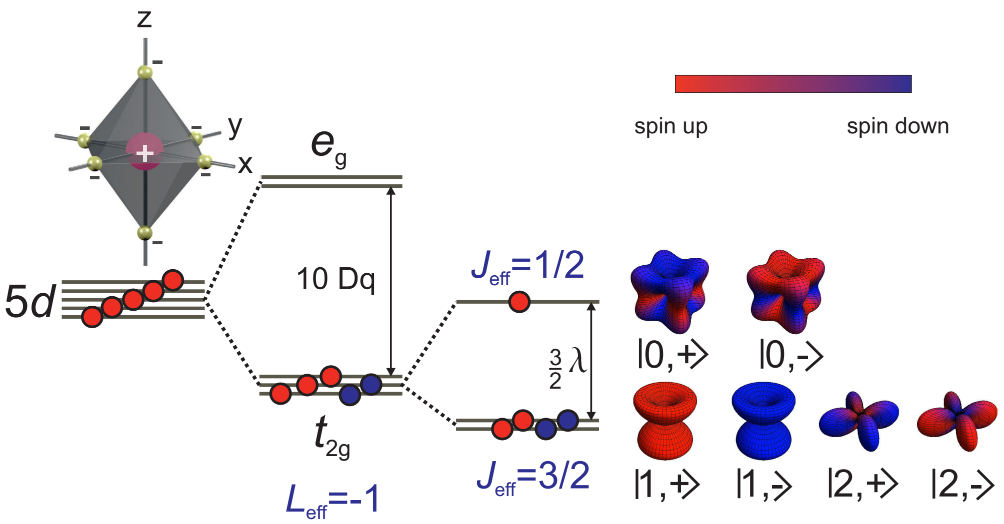

Figure 1.4: Schematic energy diagram for Ir $5d$ (t_{2g}^5) configuration. The energy levels of the Ir^{4+} ion are split first by a strong octahedral crystal field, secondly by the action of the SOC that produces a filled $j_{\text{eff}} = 3/2$ quartet, and a half filled $j_{\text{eff}} = 1/2$ doublet. The ground state of the system is therefore a hole in the $j_{\text{eff}} = 1/2$ state. A real space representation of the wave functions of the $j_{\text{eff}} = 3/2$ state ($|1, \pm\rangle$ and $|2, \pm\rangle$ doublets) and the $j_{\text{eff}} = 1/2$ state ($|0, \pm\rangle$ doublet) are given. The $|0, \pm\rangle$, $|1, \pm\rangle$, and $|2, \pm\rangle$ doublets are defined in Eqs. 1.34–1.36.

Hund's third rule if we consider first the effect of SOC and subsequently the octahedral crystal field. In this scenario the $j_{\text{eff}} = 1/2$ state is branched off from the atomic $j = 5/2$ through the effect of the cubic crystal field [19].

The strong SOC that characterizes $5d$-ions produces a very narrow $j_{\text{eff}} = 1/2$ band. The electronic correlations U, even if modest compared to $3d$-metals, act on an effective bandwidth that has been reduced by the SOC and the system is close to the Mott instability, $\frac{W_{\text{eff}}}{U} \sim 1$. The cooperation between U and SOC drives the system into an insulating state by splitting the $j_{\text{eff}} = 1/2$ band into a lower and upper Hubbard band separated by a small energy gap (~ 0.5 eV) [31]. The onset of this insulating state has been observed in several iridates: from the layered perovskites Sr_2IrO_4 [32], $Sr_3Ir_2O_7$ [33], Ba_2IrO_4 [34] to other crystal structures like $CaIrO_3$ [35], $(Na/Li)_2IrO_3$ [36] and the pyrochlores $R_2Ir_2O_7$ [20].

The "spin-orbit assisted" Mott insulating model was first proposed in the pioneering work of Kim et al. [19] in Sr_2IrO_4, based on optical conductivity, angle resolved photoemission (ARPES), X-ray absorption spectroscopy (XAS) measurements and first-principle band calculations. This novel ground state is a coherent superposition of the three t_{2g} orbitals with opposite spin polarization between xy and xz/yz states, and it is usually written as:

$$|j_{\text{eff}} = 1/2, \pm\rangle = \frac{\pm|xy, \pm\rangle + |yz, \mp\rangle \pm i|xz, \mp\rangle}{\sqrt{3}} \tag{1.20}$$

where ± indicates the spin polarization. A direct consequences of Eq. 1.20 is that in the $j_{\text{eff}} = 1/2$ state magnetic and electronic interactions are strongly directionally dependent. This is due to the admixture of orbitals of different symmetry by the SOC and is evident from the "3D shape" of the $j_{\text{eff}} = 1/2$ doublet. For a real space representation of the $j_{\text{eff}} = 1/2$ wavefuncion see Fig.1.4. We emphasize that the pure $j_{\text{eff}} = 1/2$ state is realized only in perfect cubic symmetry. The effect of tetragonal or trigonal distortions that typically affect the octahedral environment in iridium oxides can significantly alter and, for strong non-cubic field, even destroy the $j_{\text{eff}} = 1/2$ state.

Another important point to note in the expression of the $j_{\text{eff}} = 1/2$ state is that Eq. 1.20 is valid only for magnetic moments parallel to the quantization axis z in the octahedral reference frame. As we show in Section 1.4.1 when the magnetic moment lies in the basal-plane the $j_{\text{eff}} = 1/2$ wave function has a different form (see Eq.1.40). Although this does not have significant consequences on the physics at play, the resonant scattering cross-section is strongly dependent on the moment direction (see Section 2.3).

1.4.1 Single ion model: competition between SOC and tetragonal distortion

The work presented in this section has been published as "*Resonant X-ray Scattering and the* $j_{\text{eff}} = 1/2$ *Electronic Ground State in Iridate Perovskite*" by M. Moretti Sala, S. Boseggia, D. F. McMorrow and G. Monaco, Phys. Rev. Lett. **112**, 026403 (2014) [37].

In order to investigate how the competition between SOC λ and tetragonal crystal field Δ affects the $j_{\text{eff}} = 1/2$ state, we exploited a single-ion model, in the t_{2g} subspace, hole representation, where λ and Δ are treated on an equal footing. The Hamiltonian thus reads:

$$\mathcal{H} = \mathcal{H}_{SO} + \mathcal{H}_{CF} = \lambda \mathbf{L} \cdot \mathbf{S} - \Delta L_z^2, \tag{1.21}$$

The calculation of the SOC Hamiltonian is straightforward in the spherical harmonic basis and making use of Eq.1.18 together with

$$S_z|s, m_s\rangle = m_s\hbar|s, m_s\rangle,\, S_\pm|s, m_s\rangle = \hbar\sqrt{s\,(s+1) - m_s\,(m_s \pm 1)}|s, m_{s\pm1}\rangle \tag{1.22}$$

to calculate

$$\mathcal{H}_{SO} = \lambda \mathbf{L} \cdot \mathbf{S} = \lambda \left(L_z S_z + \frac{1}{2}\left(L^+ S^- + L^- S^+\right)\right). \tag{1.23}$$

In order to include the explicit dependence on the magnetic moment direction we have to bear in mind that spin-orbit coupling entangles spin and orbital moments. We therefore derive an expression for the spin along an arbitrary direction $\mathbf{r}$ and assume that the orbital moment points along the same direction. In spherical coordinates

$$\mathbf{r} = \sin\theta\cos\phi\mathbf{x} + \sin\theta\sin\phi\mathbf{y} + \cos\theta\mathbf{z}. \tag{1.24}$$

The spin angular momentum matrix for a generic spin direction will then be

$$\boldsymbol{\sigma}(\theta_s, \phi_s) = \boldsymbol{\sigma_x}\sin\theta_s\cos\phi_s + \boldsymbol{\sigma_y}\sin\theta_s\sin\phi_s + \boldsymbol{\sigma_z}\cos\theta_s, \tag{1.25}$$

where θ_s and ϕ_s are defined in Fig. 1.5 and $\boldsymbol{\sigma}_x$, $\boldsymbol{\sigma}_y$, $\boldsymbol{\sigma}_z$ are the Pauli matrices. Calculating the eigenspinors of

$$\boldsymbol{\sigma}|\pm\rangle = \pm 1|\pm\rangle \tag{1.26}$$

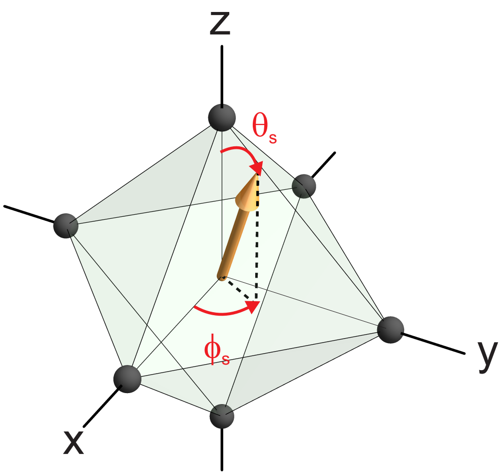

Figure 1.5: Orientation of the atomic spin moment in the octahedral reference system. The angle θ_s controls the projection of the moment along the z-axis, while the angle ϕ_s control the component of the moment in the xy plane respect to the x-axis.

one obtains

$$|+\rangle = \begin{pmatrix} \alpha_+ \\ \beta_+ \end{pmatrix} = \begin{pmatrix} \cos\left(\frac{\theta_s}{2}\right) \\ e^{i\phi_s} \sin\left(\frac{\theta_s}{2}\right) \end{pmatrix} \tag{1.27}$$

$$|-\rangle = \begin{pmatrix} \alpha_- \\ \beta_- \end{pmatrix} = \begin{pmatrix} \sin\left(\frac{\theta_s}{2}\right) \\ -e^{i\phi_s} \cos\left(\frac{\theta_s}{2}\right) \end{pmatrix} \tag{1.28}$$

where α and β give the weight to the spin up and spin down component along the quantization axis z. By making use of Eqs. 1.27–1.28 we can calculate a spin-dependent transformation matrix from the 5d spherical harmonic basis$\{|Y^+_{2,2}\rangle$, $|Y^-_{2,2}\rangle$,$|Y^+_{2,1}\rangle$, $|Y^-_{2,1}\rangle$, $|Y^+_{2,0}\rangle$, $|Y^-_{2,0}\rangle$, $|Y^+_{2,\bar{1}}\rangle$, $|Y^-_{2,\bar{1}}\rangle$, $|Y^+_{2,\bar{2}}\rangle$, $|Y^-_{2,\bar{2}}\rangle\}$ to the 5d real cubic basis $\{|x^2 - y^2, +\rangle$, $|x^2 - y^2, -\rangle$, $|3z^2 - r^2, +\rangle$, $|3z^2 - r^2, -\rangle$,

$|xy,+\rangle$, $|xy,-\rangle$, $|xz,+\rangle$, $|xz,-\rangle$, $|yz,+\rangle$, $|yz,-\rangle\}$ as:

$$T = \frac{1}{\sqrt{2}} \begin{pmatrix} \alpha_+ & \alpha_- & 0 & 0 & -i\alpha_+ & -i\alpha_- & 0 & 0 & 0 & 0 \\ \beta_+ & \beta_- & 0 & 0 & -i\beta_+ & -i\beta_- & 0 & 0 & 0 & 0 \\ 0 & 0 & 0 & 0 & 0 & 0 & -\alpha_+ & -\alpha_- & i\alpha_+ & i\alpha_- \\ 0 & 0 & 0 & 0 & 0 & 0 & -\beta_+ & -\beta_- & i\beta_+ & i\beta_- \\ 0 & 0 & \sqrt{2}\alpha_+ & \sqrt{2}\alpha_- & 0 & 0 & 0 & 0 & 0 & 0 \\ 0 & 0 & \sqrt{2}\beta_+ & \sqrt{2}\beta_- & 0 & 0 & 0 & 0 & 0 & 0 \\ 0 & 0 & 0 & 0 & 0 & 0 & \alpha_+ & \alpha_+ & i\alpha_+ & i\alpha_- \\ 0 & 0 & 0 & 0 & 0 & 0 & \beta_+ & \beta_+ & i\beta_+ & i\beta_- \\ \alpha_+ & \alpha_- & 0 & 0 & i\alpha_+ & i\alpha_- & 0 & 0 & 0 & 0 \\ \beta_+ & \beta_- & 0 & 0 & i\beta_+ & i\beta_- & 0 & 0 & 0 & 0 \end{pmatrix}. \tag{1.29}$$

This is a unitary transformation, so that $T^\dagger T = TT^\dagger = 1$. In this way every operator in the spherical harmonic basis $\mathcal{A}_{sph}$ can be transformed in the real cubic basis by

$$\mathcal{A}_{cub} = T^\dagger \mathcal{A}_{sph} T. \tag{1.30}$$

For moments pointing along the octahedral z axis, i.e. $\theta_s = 0$, $\alpha_{+(-)}$ is $1(0)$ and $\beta_{+(-)}$ is $0(1)$. Matrix 1.29 is therefore reduced to the classical way of writing d-states as a linear combination of spherical harmonics. By applying Eqs. 1.29–1.30 to the SOC operator of Eq. 1.23 one can write the spin-orbit Hamiltonian in the cubic harmonic basis as:

$$\mathcal{H}_{SO_c} = \frac{\lambda}{2} \begin{pmatrix} 0 & 0 & 0 & -i & 0 & 1 \\ 0 & 0 & -i & 0 & -1 & 0 \\ 0 & i & 0 & 0 & -i & 0 \\ i & 0 & 0 & 0 & 0 & i \\ 0 & -1 & i & 0 & 0 & 0 \\ 1 & 0 & 0 & -i & 0 & 0 \end{pmatrix}, \tag{1.31}$$

for magnetic moments pointing along the octahedral z-axis ($\boldsymbol{\mu} \parallel [0\ 0\ 1]$), and

$$\mathcal{H}_{SO_{ab}} = \frac{\lambda}{2\sqrt{2}} \begin{pmatrix} 0 & 0 & -i & 1 & i & 1 \\ 0 & 0 & -1 & i & -1 & -i \\ i & -1 & 0 & 0 & 0 & i\sqrt{2} \\ 1 & -i & 0 & 0 & i\sqrt{2} & 0 \\ -i & -1 & 0 & -i\sqrt{2} & 0 & 0 \\ 1 & i & -i\sqrt{2} & 0 & 0 & 0 \end{pmatrix}, \tag{1.32}$$

for magnetic moments pointing along the xy octahedral direction ($\boldsymbol{\mu} \parallel [1\ 1\ 0]$). Here we have considered a reduced basis of only t_{2g} states, $\{|xy,+\rangle$, $|xy,-\rangle$, $|xz,+\rangle$, $|xz,-\rangle$, $|yz,+\rangle$, $|yz,-\rangle\}$. As already mentioned, neglecting the contribution of the e_g orbitals to the ground state is a good approximation by virtue of the strong crystal field separating e_g and t_{2g} ($10Dq \sim 3$ eV). This value has been inferred from several experimental studies via different techniques such as XRMS [15, 16, 14], RIXS [38] and oxygen K edge XAS [17].

In the cubic t_{2g} basis the tetragonal crystal field matrix is diagonal and reads

$$\mathcal{H}_{CF} = \Delta \begin{pmatrix} 1 & 0 & 0 & 0 & 0 & 0 \\ 0 & 1 & 0 & 0 & 0 & 0 \\ 0 & 0 & 0 & 0 & 0 & 0 \\ 0 & 0 & 0 & 0 & 0 & 0 \\ 0 & 0 & 0 & 0 & 0 & 0 \\ 0 & 0 & 0 & 0 & 0 & 0 \end{pmatrix}. \tag{1.33}$$

Combining Eq. 1.33 with Eq. 1.31 we can easily diagonalize the general Hamiltonian $\mathcal{H}$(Eq. 1.21). The resulting eigenvectors for magnetic moments $\boldsymbol{\mu} \parallel [0\ 0\ 1]$ are the three doublets:

$$|0,\pm\rangle_c = \frac{\pm A|xy,\pm\rangle + |yz,\mp\rangle \pm i|xz,\mp\rangle}{\sqrt{2+A^2}} \tag{1.34}$$

$$|1,\pm\rangle_c = \frac{|yz,\pm\rangle \pm i|xz,\pm\rangle}{\sqrt{2}} \tag{1.35}$$

$$|2,\pm\rangle_c = \frac{\mp B|xy,\pm\rangle + |yz,\mp\rangle \pm i|xz,\mp\rangle}{\sqrt{2+B^2}} \tag{1.36}$$

of eigenvalues:

$$E_0 = \frac{\lambda}{4}\left(1+\delta+\sqrt{9+(\delta-2)\delta}\right) \tag{1.37}$$

$$E_1 = -\frac{\lambda}{2} \tag{1.38}$$

$$E_2 = \frac{\lambda}{4}\left(1+\delta-\sqrt{9+(\delta-2)\delta}\right). \tag{1.39}$$

If instead of Eq. 1.31 we make use of Eq. 1.32 we obtain the eigenvectors for magnetic moments $\boldsymbol{\mu} \parallel [1\ 1\ 0]$, as

$$|0,\pm\rangle_{ab} = \frac{A(\pm|xy,\pm\rangle \mp i|xy,\mp\rangle)/\sqrt{2} + |yz,\mp\rangle + i|xz,\pm\rangle}{\sqrt{2+A^2}} \tag{1.40}$$

$$|1,\pm\rangle_{ab} = \frac{|yz,\pm\rangle - i|xz,\mp\rangle}{\sqrt{2}} \tag{1.41}$$

$$|2,\pm\rangle_{ab} = \frac{B(\mp|xy,\pm\rangle \pm i|xy,\mp\rangle)\sqrt{2} + |yz,\mp\rangle + i|xz,\pm\rangle}{\sqrt{2+B^2}}. \tag{1.42}$$

The parameters $A = \frac{-1+\delta+\sqrt{9+(-2+\delta)\delta}}{2}$ and $B = \frac{1-\delta+\sqrt{9+(-2+\delta)\delta}}{2}$ control the effect of the tetragonal crystal field via $\delta = 2\Delta/\lambda$. We mainly consider $\boldsymbol{\mu} \parallel [0\ 0\ 1]$ and $\boldsymbol{\mu} \parallel [1\ 1\ 0]$ because this is the case for the layered perovskite iridates $Sr_3Ir_2O_7$ and $(Ba/Sr)_2IrO_4$, respectively. States $|n,+\rangle$,$|n,-\rangle$ $(n=0,1,2)$ are connected by a time-reversal symmetry, i.e. are the so-called Kramers doublet. An unequal occupation of these doublets produces magnetic order.

With five electrons occupying the three doublets, the system is left with one hole in the $|0,\pm\rangle$ doublets that is therefore the ground state in the hole representation. In the absence of any tetragonal crystal field, $\Delta=\delta=0$ $(A=1)$, the pure $j_{\text{eff}} = 1/2$ state is realized and Eqs. 1.34,1.40 become

$$|j_{\text{eff}} = 1/2,\pm\rangle_c = \frac{\pm|xy,\pm\rangle + |yz,\mp\rangle \pm i|xz,\mp\rangle}{\sqrt{3}}, \quad \text{and} \tag{1.43}$$

$$|j_{\text{eff}} = 1/2,\pm\rangle_{ab} = \frac{(\pm|xy,\pm\rangle \mp i|xy,\mp\rangle)/\sqrt{2} + |yz,\mp\rangle + i|xz,\pm\rangle}{\sqrt{3}} \tag{1.44}$$

respectively, whereas the eigenvalue E_0 become equal to λ (See Fig. 1.6(b)). This state is formed by even combination of the three t_{2g} state $|xy\rangle$, $|xz\rangle$,

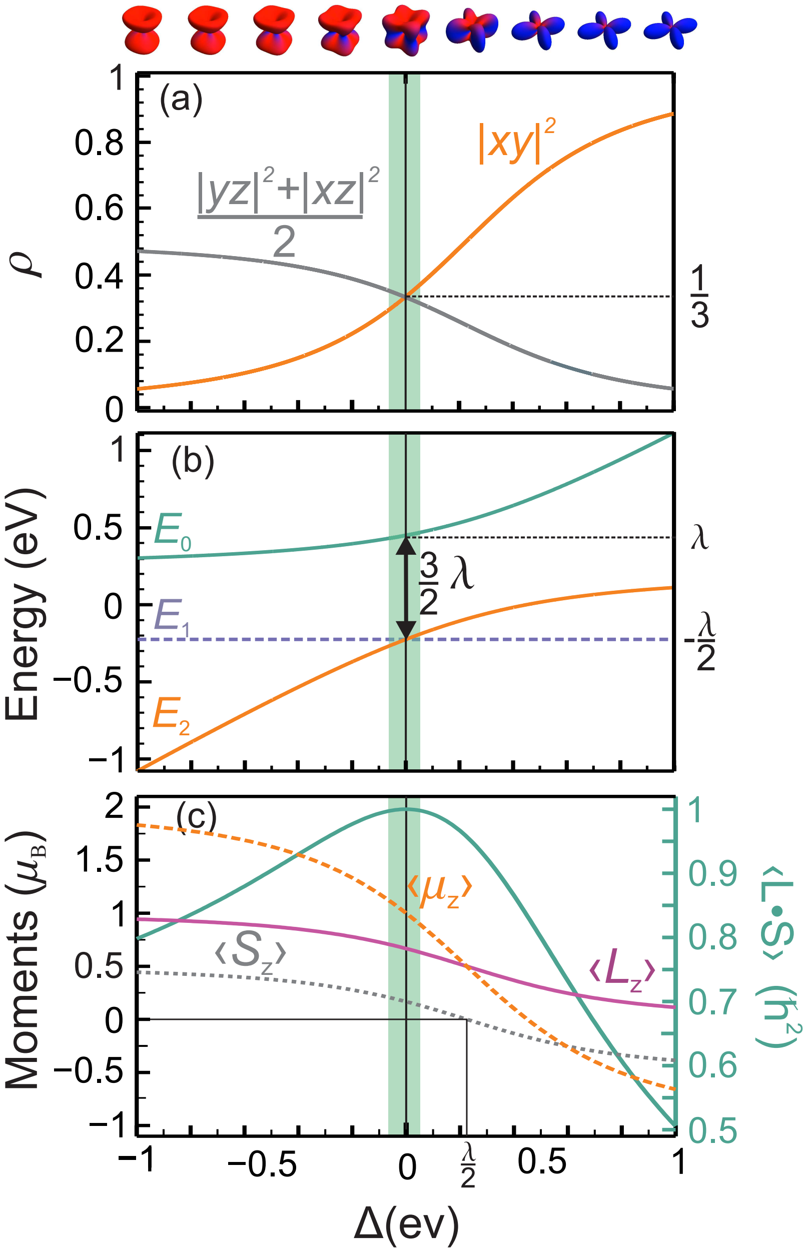

Figure 1.6: Effective tetragonal crystal field dependence Δ of (a) the ground state orbital occupancy of the $|xy,-\rangle$ (orange line) and $(|yz,+\rangle + |xz,+\rangle)/\sqrt{2}$ (grey line) states, respectively, (b) the eigenvalues of Eqs. 1.34–1.36: E_0 (green line), E_1 (dashed purple line), E_2 (orange line), and (c) the expectation values of the orbital ($\langle L_z\rangle$, purple), spin ($\langle S_z\rangle$, dotted grey), and total ($\langle \boldsymbol{\mu}_z\rangle$, dashed orange) magnetic moment components along z, and the angular part of the SOC operator $\langle \mathbf{L}\cdot\mathbf{S}\rangle$ (green). At the top a real space representation of the wave function of Eq. 1.34 ($|0,-\rangle$ state) is given for spin up (red) and spin down (blue) polarization. The shaded area in the panels represents the value of Δ inferred from our XRMS study on Sr_2IrO_4 [39].

$|yz\rangle$ with mixed spin polarization. A real space representation of the corresponding wave function as a function of the tetragonal crystal field Δ for a value of the SOC ($\lambda = 0.42$ eV), as extracted from experiments [16], is given in Fig. 1.6. For $\Delta = 0$ the well-know "cubic shape" is realized. This is due to the coherent superposition of all the t_{2g} orbitals of different symmetry.

For finite value of Δ the admixture of orbital contribution is changed and the ground state varies between a novel $j_{\text{eff}} = 1/2$ system and a classical $s = 1/2$ system with the ratio of SOC to tetragonal crystal field. For $\Delta \gg \lambda$ and $\Delta \ll -\lambda$ we recover the classical $s = 1/2$ limit and the ground state is $|xy, \pm\rangle$ and $\left(|yz, \mp\rangle \pm i|xz, \mp\rangle\right)/\sqrt{2}$, respectively. The ground state orbital occupancies (ρ) for the $|0, -\rangle$ ground state are presented in Fig. 1.6(a). At $\Delta = 0$ the occupancy is the same for the three orbitals: $\rho(|xy, -\rangle) \equiv \rho(|xz, +\rangle) \equiv \rho(|yz, +\rangle) = (1/\sqrt{3})^2 = 1/3$.

In the absence of the tetragonal crystal field the lower doublets $|1, \pm\rangle$ and $|2, \pm\rangle$ collapse into the $j_{\text{eff}} = 3/2$ quartet of energy $E_1 \equiv E_2 = -\lambda/2$. The separation between $j_{\text{eff}} = 1/2$ and $j_{\text{eff}} = 3/2$ states is therefore $3\lambda/2$ (See Fig. 1.6(b)). A real space representation of these state at $\Delta = 0$ can be found in Fig. 1.4. More generally, if some tetragonal splitting is included the $|1, \pm\rangle$ and $|2, \pm\rangle$ are no longer degenerate and $j_{\text{eff}} = 3/2$ and $j_{\text{eff}} = 1/2$ states are mixed together.

By close inspection of Fig.1.6(b) we can now discuss the insulating properties of iridium oxides. In the approximation of a pure ionic model it is evident that the tetragonal crystal field Δ has only a marginal effect on the transport properties, and an insulating state persists in these materials even far from perfect cubic symmetry, i.e. when the $j_{\text{eff}} = 1/2$ state is realized. In fact, the energy splitting between the $|0, \pm\rangle$ doublet and the $|1, \pm\rangle$ doublet is barely reduced from the maximum value $3/2\lambda$ at $\Delta = 0$ to λ for $\Delta \to -\infty$. Therefore, even in the scenario of a strong non-cubic distortion, a reasonably small on-site Coulomb repulsion U can split the valence band and drive the system into an insulating state. Strong SOC is ultimately the fundamental ingredient to explain transport properties in iridium oxides.

Having determined the ground state wave function, we can now calculate the orbital angular momentum and spin angular momentum matrices projected along z for $\boldsymbol{\mu} \parallel [0\ 0\ 1]$ in the $\{|0,+\rangle$, $|0,-\rangle$, $|1,+\rangle$, $|1,-\rangle$, $|2,+\rangle$, $|2,-\rangle\}$ basis as

$$L_z = \begin{pmatrix} -\frac{2}{2+A^2} & 0 & 0 & 0 & \frac{2}{\sqrt{(2+A^2)(2+B^2)}} & 0 \\ 0 & \frac{2}{2+A^2} & 0 & 0 & 0 & \frac{-2}{\sqrt{(2+A^2)(2+B^2)}} \\ 0 & 0 & -1 & 0 & 0 & 0 \\ 0 & 0 & 0 & 1 & 0 & 0 \\ \frac{2}{\sqrt{(2+A^2)(2+B^2)}} & 0 & 0 & 0 & -\frac{2}{2+B^2} & 0 \\ 0 & \frac{-2}{\sqrt{(2+A^2)(2+B^2)}} & 0 & 0 & 0 & \frac{2}{2+B^2} \end{pmatrix} \tag{1.45}$$

and

$$2S_z = \begin{pmatrix} \frac{A^2-2}{2+A^2} & 0 & 0 & 0 & \frac{2+AB}{\sqrt{(2+A^2)(2+B^2)}} & 0 \\ 0 & -\frac{A^2-2}{2+A^2} & 0 & 0 & 0 & -\frac{2+AB}{\sqrt{(2+A^2)(2+B^2)}} \\ 0 & 0 & 1 & 0 & 0 & 0 \\ 0 & 0 & 0 & -1 & 0 & 0 \\ \frac{2+AB}{\sqrt{(2+A^2)(2+B^2)}} & 0 & 0 & 0 & \frac{B^2-2}{2+B^2} & 0 \\ 0 & -\frac{2+AB}{\sqrt{(2+A^2)(2+B^2)}} & 0 & 0 & 0 & -\frac{B^2-2}{2+B^2} \end{pmatrix}, \tag{1.46}$$

respectively. The expectation values of the magnetic moments relative to the ground state are thus $\langle 0,-|L_z|0,-\rangle = 2/(2+A^2)$, $\langle 0,-|2S_z|0,-\rangle = (2-A^2)/(2+A^2)$, $\langle 0,-|\mu_z|0,-\rangle = \langle L_z + 2S_z\rangle = (4-A^2)/(2+A^2)$. The variation of $\langle L_z\rangle$, $\langle S_z\rangle$, $\langle \mu_z\rangle$ as a function of Δ for the $|0,-\rangle$ state is shown in Fig. 1.6(c). For $\Delta = 0$, this ionic model returns the values $\langle L_z\rangle = 2/3$, $\langle 2S_z\rangle = 1/3$, and $\langle \mu_z\rangle = 1$, all in units of μ_{B}. This is a proof of the unusual magnetic behaviour of the $j_{\mathrm{eff}} = 1/2$ state, already mentioned in the previous section. Whereas the atomic $j = 1/2$ state has a total magnetic moments $\langle L_z + 2S_z\rangle = \pm 1/3$ with opposite orbital and spin direction, the $j_{\mathrm{eff}} = 1/2$ state has $\langle L_z + 2S_z\rangle = \pm 1$, with parallel spin and orbital moments. The $j_{\mathrm{eff}} = 1/2$ $(|\mathbf{L_{eff}} - \mathbf{S}|)$ is in fact equivalent to the $j = 1/2(|\mathbf{L} - \mathbf{S}|)$, mapping $L_{\mathbf{eff},z} \to -L_z$. Observed experimental values of the magnetic moment in Sr_2IrO_4 and $Sr_3Ir_2O_7$ are actually reduced by approximately a factor two [40, 41, 42]. This could be understood by extending the ionic picture to include itinerancy effects and $5d$(Ir)-$2p$(O) hybridization. A recent dynamical mean field theory study has in fact reported that including such effects, the pure $j_{\text{eff}} = 1/2$ moment 1 μ_{B} becomes 0.55 and 0.58 μ_{B} in Sr_2IrO_4 and $\text{Sr}_3\text{Ir}_2\text{O}_7$ respectively [43].

It is interesting to note that for $\Delta = \lambda/2$ the spin moment vanishes (Fig. 1.6(c)). For this tetragonal distortion the superexchange Hamiltonian that will be introduced in Section 1.5 predicts a spin-flop transition from a basal-plane canted antiferromagnetic (AF) state to a c-axis collinear AF state. This behaviour could be reasonably captured in our single ion model: at $\Delta = \lambda/2$ the magnetic interactions have only orbital character and the octahedral elongation could potentially favour the alignment of the moment along the c-axis.

Conversely, for magnetic moment pointing along the $\boldsymbol{\mu} \parallel [1\,1\,0]$ one has: $\langle L_x\rangle = -\langle L_y\rangle = \sqrt{2}A/\,(2 + A^2)$, $\langle 2S_x\rangle = -\langle 2S_y\rangle = \sqrt{2}A^2/\,(4 + 2A^2)$, and $\langle \mu_x\rangle = -\langle \mu_y\rangle = \sqrt{2}A\,(2 + A)\,/\,(2 + A^2)$; in this case, $\langle L_x\rangle$, $\langle 2S_x\rangle$ and $\langle \mu_x\rangle$ reduce to $\sqrt{2}/3$, $\sqrt{2}/6$ and $1/\sqrt{2}$, respectively, for $\Delta = 0$.

Finally the expectation value of the angular part of the spin-orbit operator for both moment orientations, $\langle \mathbf{L}\cdot\mathbf{S}\rangle$ equals $(1 + 2A)\,/\,(2 + A^2)$, which reduces to 1 for $\Delta = 0$ (See Fig. 1.6(c)). It should be noted that the value of $\langle \mathbf{L}\cdot\mathbf{S}\rangle$ calculated in an ionic model is underestimated. As will be shown in Section 3.3.2, the experimental value inferred from X-ray absorption spectroscopy measurements is more than twice the ionic value. This is due to the admixture of the e_g orbitals in the absorption process. However, in the resonant scattering process, the approximation of limiting ourself to the t_{2g} subspace still holds.

Although the expression for the ground state doublet $|0,\pm\rangle$ (Eqs. 1.34, 1.40) and the excited state doublets $|1,\pm\rangle$ (Eqs. 1.35, 1.41) and $|2,\pm\rangle$ (Eqs. 1.36, 1.42) depends on the magnetic moment direction, the physics at play does not. However, the calculation of the resonant scattering cross-section shows a strong dependence on the moment orientation that significantly affects the interpretation of experimental results. This will be treated in detail in Section 2.3.

1.5 Hamiltonian for layered perovskite iridates

In the previous section we have derived the expression for the ground state of the Ir^{4+} ion in a strong cubic crystal field in the presence of competing SOC interaction and tetragonal distortion. In order to pass from the one-particle ionic Hamiltonian to the many-body Hamiltonian that describes the full system we need to consider the hopping of a $j_{\mathrm{eff}} = 1/2$ hole between adjacent Ir sites via ligand oxygens. Due to the peculiar 3D shape of the $j_{\mathrm{eff}} = 1/2$ state, multidirectional electronic and magnetic interactions are allowed, enhancing the importance of the local symmetry. Layered perovskite iridates belong to the so-called Ruddlesden-Popper series $A_{n+1}\mathrm{Ir}_n\mathrm{O}_{3n+1}$, where A are divalent alkaline elements. This structure includes in the unit cell two sets of n-IrO_2 planes (see Fig. 1.7(a-b)), which are connected via apical oxygens and separated by an intergrowth AO layer of rock salt structures. Varying n in the layered perovskite structure corresponds to dimensionality control from a quasi 2D ($n = 1$) single layer as, for instance in $\mathrm{Ba_2IrO_4}$ and $\mathrm{Sr_2IrO_4}$, to a 3D bilayer as in $\mathrm{Sr_3Ir_2O_7}$, and to the conventional cubic perovskite $A\mathrm{IrO_3}$ ($n = \infty$). The most famous examples of $n = 1$ compounds are $\mathrm{Ba_2IrO_4}$ and $\mathrm{Sr_2IrO_4}$. The former has a perfect straight Ir-O-Ir bond geometry, the latter undergoes a correlated alternated rotation about the c-axis of the $\mathrm{IrO_6}$ octahedra of about 12° (Fig. 1.7(a-b)). Adding an extra $\mathrm{IrO_6}$ layer of opposite octahedral rotation to $\mathrm{Sr_2IrO_4}$, results in the double layer perovskite $\mathrm{Sr_3Ir_2O_7}$.

A microscopic superexchange Hamiltonian for layered perovskite iridates was derived in the seminal work of Jackeli and Khaliullin [23]. The starting point is the $j_{\mathrm{eff}} = 1/2$ single-band Hubbard model in the hole representation. We therefore rewrite Eq.1.2 as

$$\mathcal{H} = \sum_{i,j} \sum_{\sigma} t^{\sigma}_{ij} \mathbf{d}^{\dagger}_{i\sigma} \mathbf{d}_{j\sigma} + h.c. + U \sum_{i} \mathbf{n}_{i,+} \mathbf{n}_{i,-} \tag{1.47}$$

where $\mathbf{d}^{\dagger}_{i\sigma}(\mathbf{d}_{j\sigma})$ creates (annihilates) a hole in the $|0, \pm\rangle$ Kramers doublets and $\mathbf{n}_{i,\sigma} = \mathbf{d}^{\dagger}_{i\sigma}\mathbf{d}_{j\sigma}$. Considering the staggered rotation of $\mathrm{IrO_6}$ octahedra typical of iridium layered perovskites the hopping integral between nearest neighbors t^{σ}_{ij} is spin dependent and the hopping probability amplitude has a complex part. The resulting Hamiltonian is usually written as

$$\mathcal{H}_{ij} = J\mathbf{S}_i \cdot \mathbf{S}_j + J_z S^z_i S^z_j + \mathbf{D} \cdot [\mathbf{S}_i \times \mathbf{S}_j] + \mathcal{H}'. \tag{1.48}$$

The terms on the righthand side are an isotropic Heisenberg superexchange, a pseudo-dipolar (PD) interaction, the antisymmetric Dzyaloshinsky-Moriya (DM) exchange, and finally an anisotropic contribution from the Hund's coupling. $\mathbf{S}_{i,j}$ is a pseudospin operator acting on the $j_{\text{eff}} = 1/2$ manifold. This Hamiltonian is controlled by two microscopic parameters: the tetragonal distortion Δ which mixes the different t_{2g} orbitals in the $|0, \pm\rangle$ ground state and the octahedral rotation ρ that, together with the Hund's coupling determines the strength of the anisotropic terms.

In the case of straight Ir-O-Ir bonds ($\rho = 0$) the second and third term vanishes and the system is described by a pure Heisenberg term that supports an antiferromagnetic ground state like in Ba_2IrO_4. In this case the small anisotropies are only due to Hund's coupling. However, even for $\rho \neq 0$, the anisotropies can be gauged away by proper site-dependent spin rotation. The twisted Hubbbard model can than be mapped onto a $SU(2)$-invariant pseudospin-1/2 system, like in the undistorted case (Ba_2IrO_4). Here, the straight Ir-O-Ir bonds preserve the inversion symmetry, as a consequence the DM interaction is no longer active and the system shows a simple basal plane antiferromagnetic structure. To obtain the magnetic structure of the twisted system, we have to transform the isotropic system back. As a result, the spins are canted exactly like the IrO_6 octahedra. This is the case of the single layered Sr_2IrO_4 where a basal-plane canted antiferromagnetic structure is observed. Here the spin canting angle ϕ is controlled by the D/J ratio and in the strong spin-orbit coupling limit (for $\Delta \to 0$) ϕ/α approaches unity.

The strong link between lattice and magnetic degrees of freedom is certainly a peculiarity of the orbital character of the $j_{\text{eff}} = 1/2$ ground state. The spin canting angle ϕ in units of the octahedral rotation ρ as a function of the tetragonal distortion θ is shown in Fig. 1.7(c). θ parameterizes the competition between SOC λ and effective tetragonal crystal field Δ as $\tan(2\theta) = 2\sqrt{2}\lambda/(\lambda - 2\Delta)$. It is interesting to note that the Hamiltonian 1.48 supports two magnetic structures: a basal-plane canted antiferromagnetic structure for $\theta \leq \pi/4$ and a collinear c-axis magnetic structure for $\theta > \pi/4$. Therefore, in principle, a significant tetragonal distortion could cause a drastic spin reorientation.

Including interlayer coupling terms, the Hamiltonian 1.48 can be extended to the bilayer compound $Sr_3Ir_2O_7$. Here, the anisotropic terms cannot be gauged away by site-dependent spin rotation because the octahedral rotation has opposite sign between the two IrO_6 layers. As a consequence PD interactions are greatly enhanced and the collinear c-axis magnetic structure is stable in a wider window of the θ parameter space. The enhanced effect of the anisotropies is relevant not only to the magnetic structure but also to the excitation spectrum. In fact, as we will show in Chapters 4-5 the addition of an extra IrO_6 layer modifies deeply the microscopic interactions.

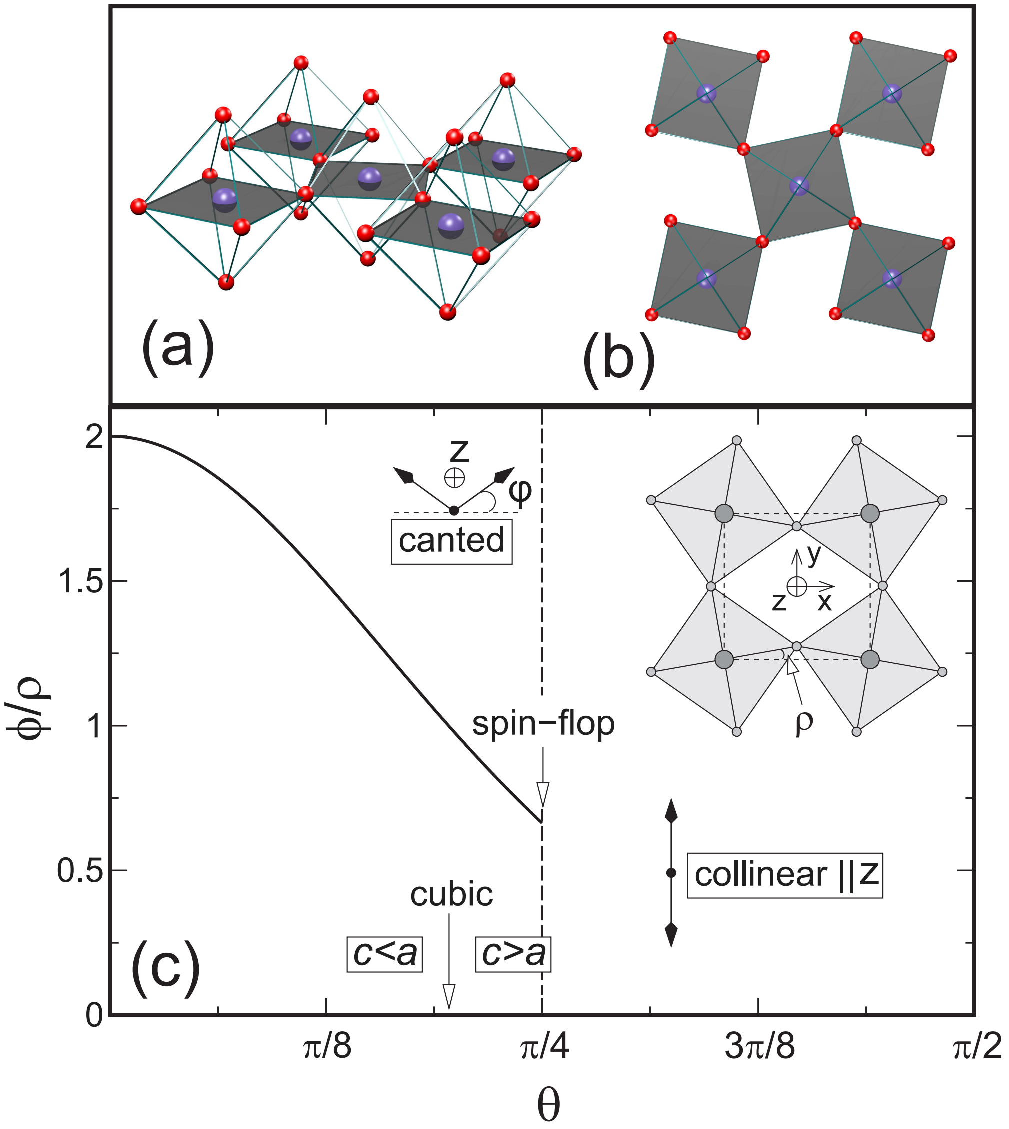

Figure 1.7: (a) A typical IrO_6 perovskite layer. Ir^{4+} ions (blue) are at the center of corner shared oxygen (red) octahedra which are rotated alternatively by an angle $\pm\rho$ about the z axis. (b) Layered perovskite structure in the basal-plane. (c) Spin canting angle ϕ (in units of ρ) as a function of the tetragonal distortion parameter θ. For perfect cubic symmetry ($\theta \simeq \pi/5$), $\phi \equiv \rho$. At $\theta = \pi/4$ this model supports a spin-flop transition from a basal-plane canted antiferromagnetic state to a collinear c-axis state. Panel adapted from Ref. [23].

Chapter 2

Resonant X-ray scattering: theory and practice

Here we present the general formalism of resonant X-ray scattering. These techniques have had a major impact in driving forward the field of iridium oxides by allowing the study of the ground and excited states in these compounds. The central part of the chapter is dedicated to the calculation of the resonant scattering cross section in iridium oxides within a single ion model as a function of tetragonal crystal field and magnetic moment direction. These calculations provide a valuable tool to interpret resonant elastic (REXS) and inelastic (RIXS) X-ray scattering experiments performed at the Ir $L_{2,3}$ edges. In particular, we find a non trivial dependence of the resonant scattering cross section on the magnetic moment direction which will be discussed in view of the experimental results of the next chapters.

In the last part of the chapter we will present two synchrotron beamlines which have been used in the present work. I16 at Diamond Light Source is a model magnetic scattering beamline where the magnetic structure can be investigated by means of resonant or non-resonant magnetic scattering techniques. ID20 at the ESRF is a RIXS beamline dedicated to the study of momentum-resolved magnetic and electronic excitations.

Contents

2.1 General remarks

X-ray scattering techniques have recently become valuable tools for the investigation of magnetic order and low energy excitations in solids, complementing neutron scattering in a field of research that was once its sole preserve. Neutrons have an intrinsic magnetic moment which interacts with the field produced by unpaired electrons in crystals. Notably, the strength of this interaction is the same order of magnitude of the one with the atomic nucleus [44]. Although neutron scattering has to be considered the first port of call for studying magnetic properties of crystals, it has several limitations. The low neutrons fluxes (2×10^{13} neutrons cm^{-2} s^{-1} for the average flux of a spallation source, 1.5×10^{15} neutrons cm^{-2} s^{-1} for a reactor source) implies that big samples (several mm^3) have to be used. Furthermore, the strong neutron absorption of some isotopes has to be taken into account, this is the case for example of iridium where the naturally occurring isotopes ^{191}Ir (954 barns) and ^{193}Ir (111 barns) are strong neutron absorbers. The availability of only small single crystals (in the order of few hundreds of microns) containing iridium and its strong absorption properties therefore makes neutron scattering a very challenging technique to apply to iridium oxides.

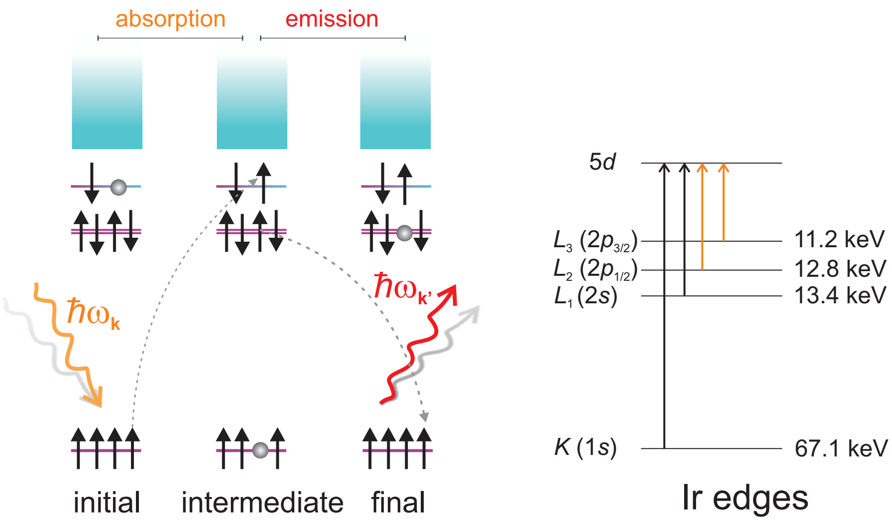

Figure 2.1: Left panel: Schematic representation of the RIXS(REXS) process. Right panel: main absorption edges of Ir ions. The orange arrows represent the dominant dipole transitions $2p_{\frac{1}{2}} \rightarrow 5d$ (L_2) and $2p_{\frac{3}{2}} \rightarrow 5d$ (L_3).

The scattering of X-rays with matter, and in particular with magnetic moments, is quite different. The interaction between the magnetic field of the electromagnetic wave and the magnetic moment of the electrons in solids is due to small relativistic effects and was first studied in the pioneering work by de Bergevin and Brunel [45, 46] using a common X-ray tube. Unfortunately, this scattering process is very weak (the intensity is approximately 6-8 orders of magnitude weaker than the normal charge scattering in an intermediate energy range (∼10 keV) [47]) and, in order to become a useful technique, X-ray scattering had to await the availability of very high-brilliance sources, the modern synchrotron radiation facilities. The discovery of a strong enhancement of the scattering signal when the energy of the incoming radiation is tuned to an absorption edge (resonance) of the material (Hannon et al. [48]) has however pushed X-ray scattering techniques to the front line in the study of magnetic phenomena.

X-ray resonant scattering is a second order process, its basic two-step mechanism is illustrated in Fig. 2.1 (left panel). In the first step, a photon of energy $\hbar\omega_{\mathbf{k}}$ impinges on the sample promoting an electron from a core-level to the valence band (*absorption*). This intermediate state is very unstable due to a hole in the core level. The system will therefore decay, within the lifetime of the intermediate state, emitting a photon of energy $\hbar\omega_{\mathbf{k}'}$ (*emission*). Considering energy and momentum conservation for the total system (photons + electrons) one has

$$\begin{aligned} \hbar\omega_{\mathbf{k}} - \hbar\omega_{\mathbf{k}'} &= \hbar\omega \\ \mathbf{k} - \mathbf{k}' &= \mathbf{K}. \end{aligned} \tag{2.1}$$

In general an excitation of energy $\hbar\omega$ and momentum $\mathbf{K}$ is created. The study of the momentum and energy dependence of excitations in solids is thus named Resonant inelastic X-ray scattering (RIXS). When $\hbar\omega_{\mathbf{k}} = \hbar\omega_{\mathbf{k}'}$ initial and final states coincide and the scattering mechanism is purely elastic. In this case only momentum is transferred to the system. We refer to this scattering mechanism as Resonant elastic X-ray scattering (REXS)[1]. REXS gives access to the ground state of the system and permits the study of ordering phenomena such as charge, orbital and magnetic ordering. REXS and RIXS share several important common features:

1. *Bulk sensitivity.* RIXS and REXS are photon in-photon out techniques. This means that in the hard X-ray regime (11–13 keV is commonly used in iridates) the penetration depth of photons is some tens of microns, making these scattering techniques a valuable probe for the bulk nature of samples.

2. *Element, oxidation, and orbital specificity.* The possibility of tuning the energy of the incoming photons to a specific absorption edge, makes REXS/RIXS sensitive to the chemical species. This has the important advantage that the effect of two different magnetic atomic species on the overall magnetism can be disentangled. In addition, absorption edges are usually sensitive to the ionic oxidation state via a shift of the inner core levels. The study of charge ordering is therefore greatly enhanced by the resonant process. Finally, since

---

[1] When this scattering mechanism was discovered, it was named X-ray resonant exchange scattering. Here we use the acronym REXS in analogy with the resonant inelastic resonant process (RIXS).

the microscopic mechanism involves specific orbitals, REXS/RIXS are valuable probes for investigating the orbital state. In iridium ions the $5d$ valence electrons are responsible of magnetic and electronic interactions. A strong dipole transition is thus available from the inner $2p_{\frac{1}{2}} \rightarrow 5d$ and $2p_{\frac{3}{2}} \rightarrow 5d$ levels. These edges are usually called L_2 and L_3 and reside at ∼11.2 keV and ∼12.8 keV, respectively. An energy diagram of the main absorption edges of Ir is shown in Fig. 2.1 (right panel).

3. *Small samples.* X-rays can easily be focused down to a few μm by means of refractive lenses or mirrors. This permits the study of very small samples which is not feasible with neutron techniques. Furthermore, since a significant spatial resolution is obtained, X-ray scattering techniques can be used as an imaging tool.

4. *Momentum resolution.* The momentum transferred to the system during the scattering process is

$$|\mathbf{K}| = \frac{4\pi}{\lambda} \sin\theta \tag{2.2}$$

where 2θ is the scattering angle and λ is the wavelength of the incoming radiation. For X-ray energies in the 11–13 kev range, λ measures approximately 1 Å. This means that several Brillouin zones of the reciprocal space can be investigated. Differentiating Eq. 2.2 we can deduce that for a highly collimated X-ray beam, the small angular divergence leads to a high momentum resolution, significantly better than the neutron counter part. That is one of the reasons why REXS is usually exploited to refine magnetic structures previously studied with neutrons. One should note that in RIXS instruments, in order to maximize the photon flux the angular acceptance of the spectrometer is significant ($\theta \sim 1$–2°). In view of this the momentum resolution is usually much lower that in REXS instruments.

Finally, the polarization of the photon can be manipulated and measured. Although the incident polarization is easily varied for both the techniques, the outgoing polarization is currently only measured in REXS experiments, as measuring the polarization strongly decreases the photon flux and significantly degrades the energy resolution in RIXS measurements.

A feature of fundamental importance in RIXS is the *energy resolution*. For a long time RIXS was limited to a resolution greater than 1 eV. This is due to the fact that photons of wavelength $\lambda \sim 1$ Å correspond to energies of several keV. A tremendous resolving power $E/\triangle E$ of the order of 10^5 is therefore needed in order to reach a resolution in the meV range. The scenario is different for inelastic neutron scattering (INS) where, for the same wavelength, neutrons have energies in the meV range. However, recent progress in RIXS instruments have dramatically improved the resolution down to 25 meV in the favourable case of Ir L_3 edge [49], making RIXS a serious competitor of INS in the study of low energy excitations and in particular magnons.

In order to take advantage of all the features of X-ray scattering techniques, high brilliance, polarized, energy tunable sources are needed. This implies the use of third generation synchrotrons.

2.2 REXS/RIXS cross section

In this section we derive the REXS and RIXS cross-section following Blume [50]. We consider an ensemble of electrons interacting with a quantized electromagnetic field described by a vector potential $A(\mathbf{r}, t)$. The total Hamiltonian of the system derived from quantum electrodynamic theory, in the non-relativistic limit, can be written as

$$\begin{aligned}\mathcal{H} = &\sum_j \frac{1}{2m}\left(\mathbf{p}_j - \frac{e}{c}\mathbf{A}(\mathbf{r}_j)\right)^2 + \sum_{ij} V(\mathbf{r}_{ij}) \\ &- \frac{e\hbar}{2mc}\sum_j \mathbf{s}_j \cdot \nabla \times \mathbf{A}(\mathbf{r}_j) - \frac{e\hbar}{2(mc)^2}\sum_j \mathbf{s}_j \cdot \mathbf{E}(\mathbf{r}_j) \times \left(\mathbf{p}_j - \frac{e}{c}\mathbf{A}(\mathbf{r}_j)\right) \\ &+ \sum_{\mathbf{k}\lambda} \hbar\omega_{\mathbf{k}}\left(c^\dagger_\lambda(\mathbf{k})c_\lambda(\mathbf{k}) + \frac{1}{2}\right).\end{aligned} \tag{2.3}$$

Here $\mathbf{E}(\mathbf{r})$ is the electric field of radiation, $c^\dagger_\lambda(\mathbf{k})$ ($c_\lambda(\mathbf{k})$), in the language of second quantization, are operators that create (annihilate) a photon with quantum numbers ($\mathbf{k}$,λ), $\mathbf{s}_j$ and $\mathbf{p}_j$ are the spin and momentum operator of the jth electron at the site $\mathbf{r}_j$. The first term of Hamiltonian 2.3 contains the kinetic energy of an electron modified by the magnetic field, the second represents its potential energy. The third and fourth terms describe the interaction between the electron spin and the radiation field. They are the Zeeman term and spin-orbit interaction, respectively. The last term corresponds to the radiation field. The vector potential can be expanded as a sum of plane-waves, characterized by a wavevector $\mathbf{k}$ and by one of the two polarization modes $\lambda = 1, 2$ as

$$\mathbf{A}(\mathbf{r}, t) = \sum_{\mathbf{k},\lambda} \left(\frac{2\pi\hbar c^2}{\Omega\omega_{\mathbf{k}}} \right)^{1/2} \left[\boldsymbol{\epsilon}_\lambda(\mathbf{k}) c_\lambda(\mathbf{k}) e^{i(\mathbf{k}\cdot\mathbf{r}-\omega_{\mathbf{k}}t)} + \boldsymbol{\epsilon}^*_\lambda(\mathbf{k}) c^\dagger_\lambda(\mathbf{k}) e^{-i(\mathbf{k}\cdot\mathbf{r}-\omega_{\mathbf{k}}t)} \right], \tag{2.4}$$

where Ω is a quantization volume which will not be considered in any physically meaningful quantity, $\omega_{\mathbf{k}}$ is $c|\mathbf{k}|$, $\boldsymbol{\epsilon}_\lambda$ is the unit polarization vector associated with the mode λ. Because of the transversality of electromagnetic waves,

$$\mathbf{k} \cdot \boldsymbol{\epsilon}_\lambda(\mathbf{k}) = 0. \tag{2.5}$$

In order to derive the X-ray scattering cross-section we need to separate the Hamiltonian $\mathcal{H}$ into a term that describes the photon-electron interaction $\mathcal{H}'$ and a term that corresponds to the unperturbed system $\mathcal{H}_0$ which will be the sum of the electronic Hamiltonian $\mathcal{H}_{el}$ and the Hamiltonian relative to the radiation $\mathcal{H}_R$. The scattering process can thus be described as a transition between the eigenstates of $\mathcal{H}_{el}$ and $\mathcal{H}_R$ induced by the perturbation $\mathcal{H}'$. Scattering cross sections are calculated assuming that the solid is in an initial state $|a\rangle$, which is an eigenstate of $\mathcal{H}_{el}$ with energy E_a and a single photon $|\mathbf{k}\lambda\rangle$ is present. The probability of the transition induced by $\mathcal{H}'$ to a state $|b\rangle$ plus a photon $|\mathbf{k}'\lambda'\rangle$ is given by Fermi's "golden rule" to second order

$$w = \frac{2\pi}{\hbar} \left| \langle f|\mathcal{H}'|i\rangle + \sum_n \frac{\langle f|\mathcal{H}'|n\rangle\langle n|\mathcal{H}'|i\rangle}{E_i - En} \right|^2 \delta(E_i - E_f), \tag{2.6}$$

where $|i\rangle \equiv |a; \mathbf{k}\lambda\rangle$, $|f\rangle \equiv |b; \mathbf{k}'\lambda'\rangle$ and n runs over the intermediate states $|n\rangle$, eigenstates of the unperturbed Hamiltonian $\mathcal{H}_0$ with energies E_n. $|i\rangle$

and $|f\rangle$ are eigenstates of $\mathcal{H}_0$ of energy $E_i = E_a + \hbar\omega_{\mathbf{k}}$ and $E_f = E_b + \hbar\omega_{\mathbf{k}'}$, respectively and

$$\mathcal{H}_{el}|a\rangle = E_a|a\rangle \tag{2.7}$$

$$\mathcal{H}_{el}|b\rangle = E_b|b\rangle. \tag{2.8}$$

In order to extract $\mathcal{H}'$ from the Hamiltonian 2.3 we rewrite the electric field vector as $\mathbf{E} = -\nabla\phi - \frac{1}{c}\frac{\partial \mathbf{A}}{\partial t}$. The Hamiltonian 2.3 is thus written as

$$\mathcal{H} = \mathcal{H}_{el} + \mathcal{H}_R + \mathcal{H}', \tag{2.9}$$

with

$$\mathcal{H}_{el} = \sum_j \frac{1}{2m}\mathbf{p}_j^2 + \sum_{ij} V(\mathbf{r}_{ij}) + \frac{e\hbar}{2(mc)^2}\sum_j \mathbf{s}_j \cdot (\nabla\phi_j \times \mathbf{p}_j) \tag{2.10}$$

$$\mathcal{H}_R = \sum_{\mathbf{k}\lambda} \hbar\omega_{\mathbf{k}} \left(c_\lambda^\dagger(\mathbf{k}) c_\lambda(\mathbf{k}) + \frac{1}{2} \right) \tag{2.11}$$

$$\begin{aligned}\mathcal{H}' &= \frac{e^2}{2mc^2}\sum_j \mathbf{A}^2(\mathbf{r}_j) - \frac{e}{mc}\sum_j \mathbf{A}(\mathbf{r}_j)\cdot\mathbf{p}_j \\ &- \frac{e\hbar}{mc}\sum_j \mathbf{s}_j \cdot (\nabla \times \mathbf{A}(\mathbf{r}_j)) - \frac{e\hbar}{2(mc)^2}\frac{e^2}{c^2}\sum_j \mathbf{s}_j \cdot \left(\frac{\partial \mathbf{A}(\mathbf{r}_j)}{\partial t} \times \mathbf{A}(\mathbf{r}_j) \right) \\ &\equiv \mathcal{H}_1' + \mathcal{H}_2' + \mathcal{H}_3' + \mathcal{H}_4'.\end{aligned} \tag{2.12}$$

$\mathcal{H}_1'$ and $\mathcal{H}_4'$ are quadratic in $\mathbf{A}$, while $\mathcal{H}_2'$ and $\mathcal{H}_3'$ are linear. Since the scattering process conserves the number of photons and the operator $\mathbf{A}$ is linear in the creation and annihilation operators, the $\mathcal{H}_1'$ and $\mathcal{H}_4'$ term will contribute only to first order perturbation, whilst $\mathcal{H}_2'$ and $\mathcal{H}_3'$ will contribute to second order. Eq. 2.6 will thus be modified as

$$\begin{aligned} w = \frac{2\pi}{\hbar} \Bigg| &\langle b; \mathbf{k}'\lambda' | \mathcal{H}_1' + \mathcal{H}_4' | a; \mathbf{k}\lambda \rangle \\ &+ \sum_n \frac{\langle b; \mathbf{k}'\lambda' | \mathcal{H}_2' + \mathcal{H}_3' | n \rangle \langle n | \mathcal{H}_2' + \mathcal{H}_3' | a; \mathbf{k}\lambda \rangle}{E_a + \hbar\omega_{\mathbf{k}} - E_n} \Bigg|^2 \delta(E_a - E_b + \hbar\omega_{\mathbf{k}} - \hbar\omega_{\mathbf{k}'}).\end{aligned} \tag{2.13}$$

Inserting Eq. 2.12 into Eq. 2.13, the total cross-section is derived by multiplying the transition probability w by the density of final states and dividing by the incident flux:

$$\frac{d^2\sigma}{d\Omega' dE'} = w\rho(E_f)/I_0, \tag{2.14}$$

with

$$\rho(E_f) = \frac{\Omega}{(2\pi)^3}\frac{\omega^2_{\mathbf{k}'}}{\hbar c^3}, \qquad I_0 = \frac{c}{\Omega}. \tag{2.15}$$

The scattering cross-section finally reads

$$\begin{aligned}\frac{d^2\sigma}{d\Omega' dE'} &= \left(\frac{e^2}{mc^2}\right)^2 \frac{\omega_{\mathbf{k}'}}{\omega_{\mathbf{k}}} \Bigg| \left\langle b \middle| \sum_j e^{i\mathbf{K}\cdot\mathbf{r}_j} \middle| a \right\rangle \boldsymbol{\epsilon}' \cdot \boldsymbol{\epsilon} \\ &- i\frac{\hbar(\omega_{\mathbf{k}} + \omega_{\mathbf{k}'})}{2mc^2} \left\langle b \middle| \sum_j e^{i\mathbf{K}\cdot\mathbf{r}_j}\mathbf{s}_j \middle| a \right\rangle \boldsymbol{\epsilon}' \times \boldsymbol{\epsilon} + \frac{1}{m}\sum_c \sum_{ij} \\ &\Bigg(\frac{\left\langle b \middle| (\boldsymbol{\epsilon}' \cdot \mathbf{p}_i - i\hbar\,(\mathbf{k}' \times \boldsymbol{\epsilon}') \cdot \mathbf{s}_i)\, e^{-i\mathbf{k}'\cdot\mathbf{r}_i} \middle| c \right\rangle \left\langle c \middle| (\boldsymbol{\epsilon} \cdot \mathbf{p}_j + i\hbar\,(\mathbf{k} \times \boldsymbol{\epsilon}) \cdot \mathbf{s}_j)\, e^{i\mathbf{k}\cdot\mathbf{r}_j} \middle| a \right\rangle}{E_a - E_c + \hbar\omega_{\mathbf{k}} - i\Gamma_c/2} \\ &+ \frac{\left\langle b \middle| (\boldsymbol{\epsilon} \cdot \mathbf{p}_i + i\hbar\,(\mathbf{k} \times \boldsymbol{\epsilon}) \cdot \mathbf{s}_i)\, e^{i\mathbf{k}\cdot\mathbf{r}_i} \middle| c \right\rangle \left\langle c \middle| (\boldsymbol{\epsilon}' \cdot \mathbf{p}_j - i\hbar\,(\mathbf{k}' \times \boldsymbol{\epsilon}') \cdot \mathbf{s}_j)\, e^{-i\mathbf{k}'\cdot\mathbf{r}_j} \middle| a \right\rangle}{E_a - E_c - \hbar\omega_{\mathbf{k}'}} \Bigg) \Bigg|^2 \\ &\delta(E_a - E_b + \hbar\omega_{\mathbf{k}} - \hbar\omega_{\mathbf{k}'}),\end{aligned} \tag{2.16}$$

where $\boldsymbol{\epsilon} \equiv \epsilon_\lambda(\mathbf{k})$, $\boldsymbol{\epsilon}' \equiv \epsilon^*_{\lambda'}(\mathbf{k}')$, and $\mathbf{K} = \mathbf{k} - \mathbf{k}'$ is the scattering vector. The first term of Eq. 2.16 represent the usual Thomson scattering for $|a\rangle = |b\rangle$ and $\omega_{\mathbf{k}} = \omega'_{\mathbf{k}}$. It contains the dependence on the Fourier transform of the electron density $\sum_j e^{i\mathbf{K}\cdot\mathbf{r}_j}$ and when the periodicity of the crystal is taken in account it originates Bragg scattering. This scattering mechanism dominates when the incident energy $\hbar\omega_{\mathbf{k}}$ is much higher than any resonance of the material. When $|a\rangle \neq |b\rangle$ and $\omega_{\mathbf{k}} \neq \omega'_{\mathbf{k}}$ this term give also rise to non-resonant inelastic X-ray scattering (IXS). The second term is a genuine magnetic scattering term which depends on the spin density Fourier transform $\sum_j e^{i\mathbf{K}\cdot\mathbf{r}_j}\mathbf{s}_j$ and it is reduced, compared to Thomson scattering, by a factor $\hbar\omega/mc^2$. For photons at the Ir $L_{2,3}$ edges (11-13 KeV) and given $mc^2 \sim 0.511$ MeV, $\hbar\omega/mc^2$ is about 0.02. The third and fourth terms derive from second order perturbation theory and contain dispersive corrections to the scattering amplitude via an energy dependent denominator. A $-i\Gamma_c/2$ term has been added to the third term in order to avoid any nonphysical divergence in the denominator and to take into account the finite lifetime the intermediate $|c\rangle$ states. These terms are both reduced by a factor $\hbar\omega/mc^2$ with respect to Thomson scattering, however the amplitude of the third term can be greatly enhanced when the incident energy is tuned to a resonance, $\hbar\omega_{\mathbf{k}} \sim E_c - E_a$. Hidden in the last two terms there is a non resonant contribution that must be separated and added to the second term. In order to do this we rewrite the denominators of Eq. 2.16 as

$$
\begin{aligned}
\frac{1}{E_a - E_c + \hbar\omega_{\mathbf{k}} - i\Gamma_c/2} &= \left[\frac{1}{E_a - E_c + \hbar\omega_{\mathbf{k}} - i\Gamma_c/2} - \frac{1}{\hbar\omega_{\mathbf{k}}}\right] + \frac{1}{\hbar\omega_{\mathbf{k}}} \\
&= \left[-\frac{E_a - E_c - i\Gamma_c/2}{\hbar\omega_{\mathbf{k}}}\frac{1}{E_a - E_c + \hbar\omega_{\mathbf{k}} - i\Gamma_c/2}\right] + \frac{1}{\hbar\omega_{\mathbf{k}}} \\
&= \begin{cases} \frac{1}{\hbar\omega_{\mathbf{k}}} & \text{for} \quad \hbar\omega_{\mathbf{k}} \gg E_c - E_a \\ -\frac{E_a - E_c}{\hbar\omega_{\mathbf{k}}}\frac{1}{E_a - E_c + \hbar\omega_{\mathbf{k}} - i\Gamma_c/2} & \text{for} \quad \hbar\omega_{\mathbf{k}} \approx E_c - E_a \end{cases}
\end{aligned}
\tag{2.17}
$$

and

$$
\begin{aligned}
\frac{1}{E_a - E_c - \hbar\omega_{\mathbf{k}}} &= \left[\frac{1}{E_a - E_c - \hbar\omega_{\mathbf{k}}} + \frac{1}{\hbar\omega_{\mathbf{k}}}\right] - \frac{1}{\hbar\omega_{\mathbf{k}}} \\
&= \left[\frac{E_a - E_c}{\hbar\omega_{\mathbf{k}}}\frac{1}{E_a - E_c - \hbar\omega_{\mathbf{k}}}\right] - \frac{1}{\hbar\omega_{\mathbf{k}}} \\
&= \begin{cases} -\frac{1}{\hbar\omega_{\mathbf{k}}} & \text{for} \quad \hbar\omega_{\mathbf{k}} \gg E_c - E_a \\ \frac{E_a - E_c}{\hbar\omega_{\mathbf{k}}}\frac{1}{E_a - E_c - \hbar\omega_{\mathbf{k}}} & \text{for} \quad \hbar\omega_{\mathbf{k}} \approx E_c - E_a. \end{cases}
\end{aligned}
\tag{2.18}
$$

We distinguish two regimes, one when the energy of the incoming radiation is far from any absorption edge and the denominators are well approximated by $\pm\hbar\omega_{\mathbf{k}}$. The corresponding term must be added to the second term of Eq. 2.16 to obtain the full non resonant scattering cross-section. By contrast,when the incoming energy is tuned to a resonance of the material, the $\frac{1}{E_a - E_c + \hbar\omega_{\mathbf{k}} - i\Gamma_c/2}$ denominator becomes dominant. After some algebras and applying the closure relation to the sum of the intermediate state we rewrite the scattering cross-section as

$$\frac{d^2\sigma}{d\Omega' dE'} = \left(\frac{e^2}{mc^2}\right)^2 \frac{\omega_{\mathbf{k}'}}{\omega_{\mathbf{k}}} \left|\mathcal{A}_0 + \mathcal{A}_{nonres} + \mathcal{A}_{res}\right|^2 \delta(E_a - E_b + \hbar\omega_{\mathbf{k}} - \hbar\omega_{\mathbf{k}'}). \tag{2.19}$$

where $\mathcal{A}_0$ is the first term of Eq. 2.16. $\mathcal{A}_{nonres}$ is the pure non-resonant magnetic scattering which reads

$$\begin{aligned} \mathcal{A}_{nonres} &= -i\frac{\hbar\omega_{\mathbf{k}}}{mc^2}\left\langle b \left| \sum_j e^{i\mathbf{K}\cdot\mathbf{r}_j}\left(i\frac{\mathbf{K}\times\mathbf{p}_j}{\hbar k^2}\cdot\mathbf{A}' + \mathbf{s}_j\cdot\mathbf{B}'\right)\right| a\right\rangle \\ &= -i\frac{\hbar\omega_{\mathbf{k}}}{mc^2}\left(\frac{1}{2}\mathbf{L}(\mathbf{Q})\cdot\mathbf{A}'' + \mathbf{S}(\mathbf{Q})\cdot\mathbf{B}'\right), \end{aligned} \tag{2.20}$$

where $\mathbf{A}'$, $\mathbf{A}''$, $\mathbf{B}'$ are beam dependent factors, $\mathbf{L}(\mathbf{Q})$ and $\mathbf{S}(\mathbf{Q})$ are the Fourier transform of the orbital and spin magnetization density. Since non-resonant magnetic scattering techniques have not been exploited in this thesis work we will not fully develop this term. However, it is important to mention the great advantage of this scattering mechanism: by a close inspection of Eq. 2.20, we see that orbital and spin magnetization densities are associated with different polarization vectors. This means that by analyzing the polarization of the scattered radiation is possible to disentangle the spin from the orbital contribution, a peculiarity not accessible with neutron scattering techniques.

Regarding the resonant term, for energies typical of core levels the dominant term has been estimated to be $\boldsymbol{\epsilon}\cdot\mathbf{p}$ [51, 52], therefore will be the only one considered in the following. The pure resonant scattering amplitude will then be

$$\begin{aligned} \mathcal{A}_{res} &\approx -\frac{1}{m}\sum_c\sum_{ij}\frac{E_a - E_c}{\hbar\omega_{\mathbf{k}}} \\ &\left(\frac{\left\langle b\left|(\boldsymbol{\epsilon}'\cdot\mathbf{p}_i - i\hbar\,(\mathbf{k}'\times\boldsymbol{\epsilon}')\cdot\mathbf{s}_i)\,e^{-i\mathbf{k}'\cdot\mathbf{r}_i}\right|c\right\rangle\left\langle c\left|\,(\boldsymbol{\epsilon}\cdot\mathbf{p}_j + i\hbar\,(\mathbf{k}\times\boldsymbol{\epsilon})\cdot\mathbf{s}_j)\,e^{i\mathbf{k}\cdot\mathbf{r}_j}\right|a\right\rangle}{E_a - E_c + \hbar\omega_{\mathbf{k}} - i\Gamma_c/2}\right) \\ &= -\frac{1}{m}\sum_c\sum_{ij}\frac{E_a - E_c}{\hbar\omega_{\mathbf{k}}}\left(\frac{\left\langle b\left|(\boldsymbol{\epsilon}'\cdot\mathbf{p}_i)\,e^{-i\mathbf{k}'\cdot\mathbf{r}_i}\right|c\right\rangle\left\langle c\left|\,(\boldsymbol{\epsilon}\cdot\mathbf{p}_j)\,e^{i\mathbf{k}\cdot\mathbf{r}_j}\right|a\right\rangle}{E_a - E_c + \hbar\omega_{\mathbf{k}} - i\Gamma_c/2}\right). \end{aligned} \tag{2.21}$$

Eq. 2.21 determine the amplitude of REXS when $|a\rangle \equiv |b\rangle$ ($\hbar\omega_{\mathbf{k}} = \hbar\omega_{\mathbf{k}'}$) and and RIXS when $|a\rangle \neq |b\rangle$ ($\hbar\omega_{\mathbf{k}} \neq \hbar\omega_{\mathbf{k}'}$) and it is usually referred as the Kramers-Heisenberg (KH) formula. By looking closely at Eq. 2.21, an explicit dependence on scattering from magnetic moments is not present. One may thus wonder where the sensitivity to magnetic degrees of freedom comes from. The latter is mainly due to the joint effect of two ingredients: the Pauli principle and the SOC. The Pauli principle enters due to the dependence of the scattering amplitude on the availability of intermediate states. Let's assume a magnetic polarization of the valence states of an atom. This would mean a predominance of unoccupied states with the polarization of the minority. As a consequence, since the spin is conserved in optical transitions, electrons with the same spin as the unoccupied states will be promoted from a core level to the valence band. In case of core levels with $l \neq 0$ the SOC acts polarizing the orbital state via the coupling of spin and orbital degrees of freedom—this is for instance the case of the L_2 and L_3 edge of Ir. Because of the selection rules to the intermediate state, this orbital polarization translates into an imbalance in the different matrix elements which lead to a non-vanishing magnetic scattering amplitude.

In iridium oxides the orbitals involved in chemical bonds, thus responsible for magnetic and electronic interaction, are the Ir $5d$ orbitals. In order to access these intermediate states, optical transitions from $2p_{\frac{1}{2}}$ (L_2) and $2p_{\frac{3}{2}}$ (L_3) levels to $5d$ state can be exploited. These states are said to be accessible by electric dipole transition. In this approximation we can stop at the first order in the expansion of the $e^{i\mathbf{k}\cdot\mathbf{r}} \sim 1 + \mathbf{k}\cdot\mathbf{r} + \ldots$ term of Eq. 2.21. In addition, by making use of the commutator

$$[\mathcal{H}_{el}, \mathbf{r}] = \frac{\hbar}{i}\frac{\mathbf{p}}{m} \tag{2.22}$$

we can write

$$\begin{aligned}\left\langle c \left| (\boldsymbol{\epsilon}\cdot\mathbf{p}_j)\, e^{i\mathbf{k}\cdot\mathbf{r}_j} \right| a \right\rangle &\approx \langle c\,|(\boldsymbol{\epsilon}\cdot\mathbf{p}_j)|\,a\rangle \\ &= i\frac{m}{\hbar}\,\langle c\,|(\boldsymbol{\epsilon}\cdot[\mathcal{H}_{el},\mathbf{r}_j])|\,a\rangle \\ &= -i\frac{m}{\hbar}\,(E_a-E_c)\,\langle c\,|(\boldsymbol{\epsilon}\cdot\mathbf{r}_j)|\,a\rangle \\ &= -i\frac{m}{\hbar}\,(E_a-E_c)\,\langle c\,|\mathcal{D}_{\boldsymbol{\epsilon}}|\,a\rangle\end{aligned} \tag{2.23}$$

where the expression of the operator $\mathcal{D}_{\boldsymbol{\epsilon}}$ justifies the name an electric dipole. In view of this, Eq. 2.21 becomes

$$\mathcal{A}_{res} \approx m\sum_c\sum_{ij}\frac{(E_a-E_c)^3}{\hbar^3\omega_{\mathbf{k}}}\left(\frac{\langle b\,|(\boldsymbol{\epsilon}'\cdot\mathbf{r}_i)|\,c\rangle\,\langle c\,|\,(\boldsymbol{\epsilon}\cdot\mathbf{r}_j)|\,a\rangle}{E_a-E_c+\hbar\omega_{\mathbf{k}}-i\Gamma_c/2}\right) \tag{2.24}$$

Since in iridium oxides the dipole channel dominates, it will be the only one considered in this thesis work.

2.2.1 X-ray resonant magnetic scattering (XRMS)

Here we focus only on the elastic part of the Kramers-Heisenberg equation 2.24, i.e. our interest regards only the study of the ground state of the system and in particular the investigation of the magnetic structure of a system. For interpreting the majority of XRMS experiments it is not necessary to evaluate Eq. 2.24, but it is sufficient to use an expression derived by Hannon et al. [48] where the explicit dependence of the XRMS cross-section on the polarization of the photons and the direction of the magnetic moments is extracted from Eq 2.24. Here we follow the notation of Hill and McMorrow [53].

By expanding the matrix element in the form of vector spherical harmonics an explicit dependence of the scattering amplitude on the polarization vector and the moment orientation can be obtained

$$\mathcal{A}^{\mathrm{REXS}}_{j\mathrm{E1}} = (\boldsymbol{\epsilon}'\cdot\boldsymbol{\epsilon})\,F^0 - i\,(\boldsymbol{\epsilon}'\times\boldsymbol{\epsilon})\cdot\widehat{\mathbf{z}}_j F^1 + (\boldsymbol{\epsilon}'\cdot\widehat{\mathbf{z}}_j)\,F^2 \tag{2.25}$$

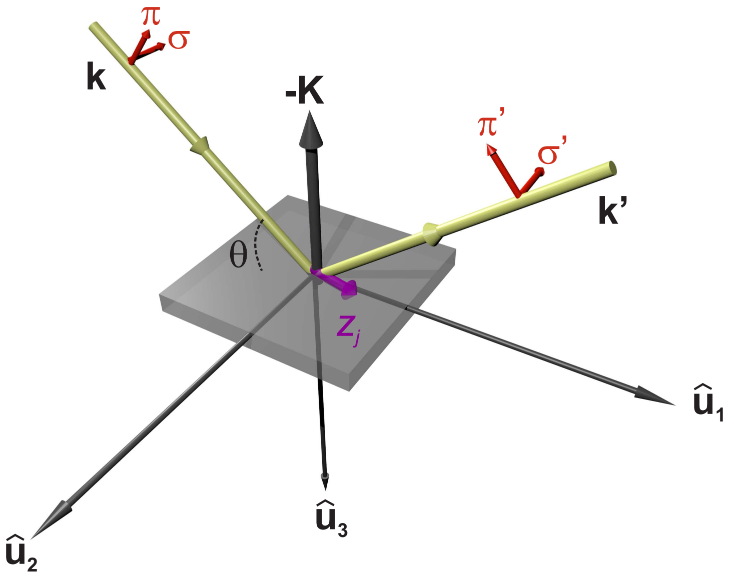

Figure 2.2: Coordinate system used in X-ray magnetic scattering.

with

$$F^0 = (3/4k)\,[F_{11} + F_{1\bar{1}}] \tag{2.26}$$

$$F^1 = (3/4k)\,[F_{11} - F_{1\bar{1}}] \tag{2.27}$$

$$F^2 = (3/4k)\,[2F_{10} - F_{11} - F_{1\bar{1}}] \tag{2.28}$$

where F_{LM} are factors that determine the strength of the resonance based on the atomic properties and $\widehat{\mathbf{z}}_j$ is a unit vector pointing in the direction of the magnetic moment of the jth ion. The first term of Eq 2.25 contains no dependence on the magnetic moment and it contributes to the Thomson scattering. The second therm is linear in the magnetic moment direction and produces first-harmonic magnetic satellites in antiferromagnets. The third term is quadratic in the magnetic moments direction and leads to second-harmonic magnetic satellites. Before proceeding further we defined the coordinate system used in magnetic scattering experiments. In order to describe the polarization of the incident (scattered) beam, the polarization vector is usually projected onto an orthogonal two vector basis either perpendicular (σ) or parallel (π) to the scattering plane. The dependence of the scattering amplitude on the photon polarization can therefore be expressed in terms of a 2×2 matrix in the (σ,π) basis as

$$(\boldsymbol{\epsilon}', \boldsymbol{\epsilon}) = \begin{pmatrix} (\boldsymbol{\epsilon}'_\sigma, \boldsymbol{\epsilon}_\sigma) & (\boldsymbol{\epsilon}'_\sigma, \boldsymbol{\epsilon}_\pi) \\ (\boldsymbol{\epsilon}'_\pi, \boldsymbol{\epsilon}_\sigma) & (\boldsymbol{\epsilon}'_\pi, \boldsymbol{\epsilon}_\pi) \end{pmatrix}. \tag{2.29}$$

Furthermore, we can define a coordinate system $\widehat{\mathbf{u}}_i$ with respect to the diffraction plane (see Fig. 2.2)

$$\begin{aligned} \widehat{\mathbf{u}}_1 &= \left(\widehat{\mathbf{k}} + \widehat{\mathbf{k}}'\right)/2\cos\theta \\ \widehat{\mathbf{u}}_2 &= \left(\widehat{\mathbf{k}} \times \widehat{\mathbf{k}}'\right)/\sin 2\theta\,. \\ \widehat{\mathbf{u}}_3 &= \left(\widehat{\mathbf{k}} - \widehat{\mathbf{k}}'\right)/2\sin\theta \end{aligned} \tag{2.30}$$

The polarization factor of the first term in Eq. 2.25 can thus be written as

$$\boldsymbol{\epsilon}' \cdot \boldsymbol{\epsilon} = \begin{pmatrix} 1 & 0 \\ 0 & \widehat{\mathbf{k}}' \cdot \widehat{\mathbf{k}} \end{pmatrix}. \tag{2.31}$$

It is therefore clear that this term connects states in the $(\sigma$-$\pi)$ basis for which the polarization is unchanged, characteristic of charge scattering. By contrast, the polarization dependence of the second term of Eq. 2.25, in its matrix representation, reads

$$(\boldsymbol{\epsilon}' \times \boldsymbol{\epsilon}) \cdot \widehat{\mathbf{z}}_j = \begin{pmatrix} 0 & \widehat{\mathbf{k}} \\ -\widehat{\mathbf{k}}' & \widehat{\mathbf{k}}' \times \widehat{\mathbf{k}} \end{pmatrix} \cdot \widehat{\mathbf{z}}_j. \tag{2.32}$$

In this case the mixing between different polarization channels is allowed but scattering in the σ-σ channel is forbidden. The matrix representation of the third term can be obtained along similar lines.

Finally, resolving each vector along the $\widehat{\mathbf{u}}_i$ coordinate system defined in Eq. 2.30 (Fig. 2.2) we write the dipole XRMS amplitude as

$$\begin{aligned} \mathcal{A}^{\mathrm{XRMS}}_{j\mathrm{E1}} &= -iF^1 \begin{pmatrix} 0 & \widehat{\mathbf{k}} \cdot \widehat{\mathbf{z}}_j \\ -\widehat{\mathbf{k}}' \cdot \widehat{\mathbf{z}}_j & (\widehat{\mathbf{k}}' \times \widehat{\mathbf{k}}) \cdot \widehat{\mathbf{z}}_j \end{pmatrix} \\ &= -iF^1 \begin{pmatrix} 0 & z_1\cos\theta + z_3\sin\theta \\ z_3\sin\theta - z_1\cos\theta & -z_2\sin 2\theta \end{pmatrix} \end{aligned} \tag{2.33}$$

where we have neglected the third term of Eq. 2.25 as second harmonic satellites are not observed in iridium oxides. θ is the Bragg angle and z_i are the components of the magnetic moments along the $\widehat{\mathbf{u}}_i$ axis. From Eq. 2.33 is possible to determine which component of the magnetic moment contributes to the resonant magnetic scattering for a given experimental geometry. This is, for instance, the principle exploited in the *azimuthal scans* to determine the magnetic moment direction in this work, that will be presented in the next chapters.

The cross-section derived up to now is valid for a single isolated ion. In order to extend the scattering amplitude to a periodic distribution of magnetic ions, one has to sum over the magnetic atoms that form the magnetic unit cell. The final expression for the scattering amplitude will then be

$$\mathcal{A}(\mathbf{K}) = \sum_j e^{i2\pi\mathbf{K}\cdot\mathbf{r}_j} \mathcal{A}_j^{\mathrm{XRMS}} \tag{2.34}$$

2.3 Cross-section for iridates

The work presented in this section has been published as "*Resonant X-ray Scattering and the $j_{\mathrm{eff}} = 1/2$ Electronic Ground State in Iridate Perovskite*" by M. Moretti Sala, S. Boseggia, D. F. McMorrow and G. Monaco, Phys. Rev. Lett. **112**, 026403 (2014) [37].

The first REXS/RIXS experiment conducted on iridium oxides was a XRMS study at the Ir $L_{2,3}$ edge in $\mathrm{Sr_2IrO_4}$ performed by Kim et al. [14]. Fig. 2.3 shows the resonant enhancement for the (1 0 22) magnetic reflection in the proximity of the Ir L edges. Whereas the magnetic signal is greatly enhanced at the Ir L_3 with a typical single Lorentzian shape resonance of dipolar origin, this behaviour is almost entirely missing at the Ir L_2. This anomalous observation was attributed to the realization of a pure $j_{\mathrm{eff}} = 1/2$ state in $\mathrm{Sr_2IrO_4}$. In fact, according to Kim et al. [14] interpretation the scattering amplitude at the L_2 edge vanishes completely in the strong SOC coupling regime, i.e. when the symmetry of the system is exactly cubic. In this scenario, an increasing tetragonal distortion would lead to a proportional increase of the magnetic signal at the L_2 edge and the XRMS intensity ratio I_{L_2}/I_{L_3} would give the robustness

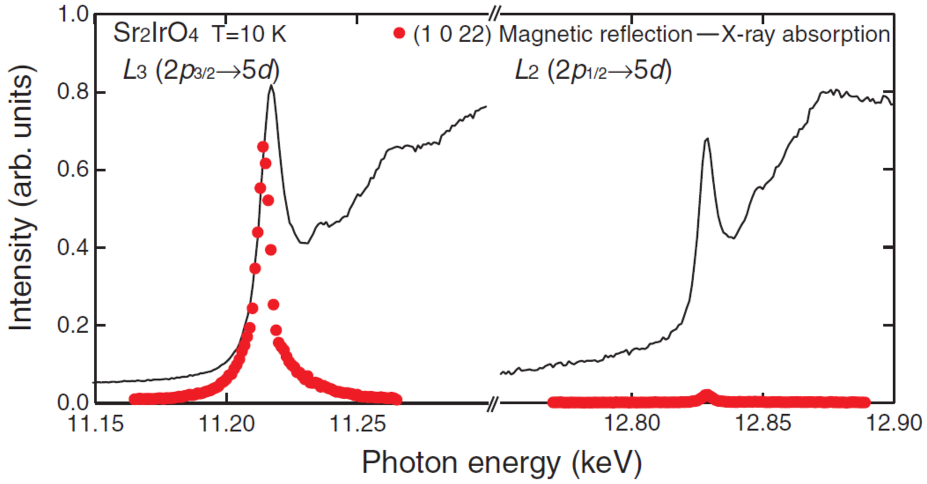

Figure 2.3: Resonant enhancement of the $(1\,0\,22)$ magnetic reflection at the Ir $L_{2,3}$ edges in Sr_2IrO_4. From Ref. [14].

of the $j_{\mathrm{eff}} = 1/2$ state. This enhanced sensitivity to the orbital state was proposed as a novel intriguing feature of X-ray scattering techniques in $5d$ iridates. However, some doubts have been raised concerning this interpretation [54, 55]. In order to understand the link between the novel $j_{\mathrm{eff}} = 1/2$ ground state and the intensity of the REXS/RIXS processes at the Ir L edges we have solved the KH equation (Eq. 2.24) that we rewrite as

$$\mathcal{A}^{\epsilon\epsilon'}_{|f,\pm\rangle} = \sum_n \frac{\langle f,\pm|\mathcal{D}^{\dagger}_{\epsilon'}|n\rangle\,\langle n\,|\mathcal{D}_{\epsilon}|\,0,-\rangle}{E_0 - E_n + \hbar\omega_{\mathbf{k}} - i\Gamma_n/2}. \tag{2.35}$$

In the hole representation, $|0,-\rangle$ is the ground state in iridium layered perovskites, and its expression is given in Eq. 1.34 for $\boldsymbol{\mu}||[0\,0\,1]$ and in Eq. 1.40 for $\boldsymbol{\mu}||[1\,1\,0]$. $|f,\pm\rangle$ is the final state, $\mathcal{D}_{\epsilon}(\mathcal{D}^{\dagger}_{\epsilon'})$ is the absorption (emission) dipole operator. The emission operator is obtained from the Hermitian conjugate of the absorption one. Assuming that at a given absorption edge all the intermediate states $|n\rangle$ have the same lifetime, the denominator of Eq. 2.36 can be discarded and the KH formula simplifies to

$$\mathcal{A}^{\epsilon\epsilon'}_{|f,\pm\rangle} \approx \sum_n \langle f,\pm|\mathcal{D}^{\dagger}_{\epsilon'}|n\rangle\,\langle n\,|\mathcal{D}_{\epsilon}|\,0,-\rangle\,. \tag{2.36}$$

2.3.1 Matrix elements in dipole approximation

The calculation of the electric dipole matrix elements are carried out along similar lines of Ref. [56, 57] for $L_{2,3}$ edge RIXS in Cu^{2+} cuprates, i.e. one-hole e_g systems. As we have shown in Section 2.2, the electric dipole operator can be written as $\mathcal{D}_{\boldsymbol{\epsilon}} = \boldsymbol{\epsilon}\cdot\mathbf{r}$. Therefore, in order to calculate the transition probability from an initial state Ψ_i to an intermediate state Ψ_n we have to evaluate integrals of the form

$$\begin{aligned}\langle\Psi_n|\boldsymbol{\epsilon}\cdot\mathbf{r}|\Psi_i\rangle &= \int_0^\infty r^2 R^*_{n_n,l_n} R_{n_i,l_i} dr \int_0^{2\pi}\int_0^{\pi} Y^*_{l_n,m_n}\,\boldsymbol{\epsilon}\cdot\mathbf{r}\,Y_{l_i,m_i}\sin\theta d\theta d\phi \\ &= \int_0^\infty r^3 R^*_{n_n,l_n} R_{n_i,l_i} dr \int_0^{2\pi}\int_0^{\pi} Y^*_{l_n,m_n}\,\boldsymbol{\epsilon}\cdot\hat{\mathbf{r}}\,Y_{l_i,m_i}\sin\theta d\theta d\phi\end{aligned} \tag{2.37}$$

where we have separated radial and angular parts of the wave function according to

$$\Psi_{n,l,m}(r,\theta,\phi) = R_{n,l}(r)\cdot Y_{l,m}(\theta,\phi). \tag{2.38}$$

Since the integral over the radial part $\int_0^\infty r^3 R_{5d}(r)R_{2p}(r)dr$ is in common for all the $2p\to 5d$ transition, it will be neglected in the following and the atomic wave functions will be express only in term of their angular part. We can now expand the dipole operator in spherical harmonics as

$$\begin{aligned}\boldsymbol{\epsilon}\cdot\hat{\mathbf{r}} &= \boldsymbol{\epsilon}_x \sin\theta\cos\phi + \boldsymbol{\epsilon}_y\sin\theta\sin\phi + \boldsymbol{\epsilon}_z\cos\theta && (2.39)\\ &= \sqrt{\frac{4\pi}{3}}\left(\boldsymbol{\epsilon}_z Y_{1,0} + \frac{-\boldsymbol{\epsilon}_x + i\boldsymbol{\epsilon}_y}{\sqrt{2}}Y_{1,1} + \frac{\boldsymbol{\epsilon}_x + i\boldsymbol{\epsilon}_y}{\sqrt{2}}Y_{1,\bar{1}}\right) && (2.40)\\ &= \sqrt{\frac{4\pi}{3}}\sum_q Y_{1,q}P_{\boldsymbol{\epsilon},q} && (2.41)\end{aligned}$$

where

$$P_{\boldsymbol{\epsilon},q} = \begin{cases} \epsilon_z = z_{\boldsymbol{\epsilon}} & \text{for } q = 0 \\ \frac{-\boldsymbol{\epsilon}_x + i\boldsymbol{\epsilon}_y}{\sqrt{2}} = R_{\boldsymbol{\epsilon}} & \text{for } q = 1 \\ \frac{\boldsymbol{\epsilon}_x + i\boldsymbol{\epsilon}_y}{\sqrt{2}} = L_{\boldsymbol{\epsilon}} & \text{for } q = \text{-}1 \end{cases} \tag{2.42}$$

are polarization factors that depend on the polarization state of the light. $q = 0, 1, \text{-}1$ for linear polarization along the quantization axis z, for right

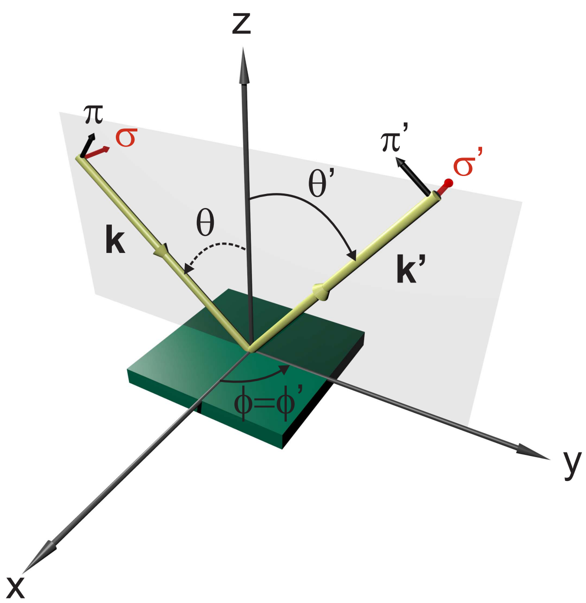

Figure 2.4: Scattering geometry and coordinate system used in the calculation of the X-ray resonant scattering cross-section. The x, y, and z are the octahedral axis in the sample reference.

circular (RC) polarization, and for left circular (LC) polarization respectively. The scattering geometry and the polarization of the radiation enter in the calculation of the cross section by means of these polarization factors.

In order to calculate the dipole transition probabilities for a particular experiment geometry and for a particular light polarization the scattering geometry has to be defined. The incoming and the outgoing unit wavevectors, in spherical coordinates, are defined according to

$$\mathbf{k} = \sin\theta\cos\phi\,\mathbf{x} + \sin\theta\sin\phi\,\mathbf{y} + \cos\theta\,\mathbf{z} \tag{2.43}$$

$$\mathbf{k}' = \sin\theta'\cos\phi'\,\mathbf{x} + \sin\theta'\sin\phi'\,\mathbf{y} + \cos\theta'\,\mathbf{z} \tag{2.44}$$

where $\theta(\theta')$, $\phi(\phi')$ are the polar and azimuthal angles of the incoming (scattered) radiation in the octahedral reference system of the sample. Along similar lines of Section 2.2.1 we can project the incoming (outgoing) polarization $\boldsymbol{\epsilon}^{(\prime)}$ onto the (σ, π) basis

$$\boldsymbol{\epsilon}_{\sigma}^{(\prime)} = \mathbf{k} \times \mathbf{k}' \tag{2.45}$$

$$\boldsymbol{\epsilon}_{\pi}^{(\prime)} = \mathbf{k}^{(\prime)} \times \boldsymbol{\epsilon}_{\sigma}. \tag{2.46}$$

From these, the polarization factors $P_{\boldsymbol{\epsilon},q}$ can be derived as

$$z_{\boldsymbol{\epsilon}^{(\prime)}} = \boldsymbol{\epsilon}^{(\prime)} \cdot \mathbf{z} \tag{2.47}$$

$$R_{\boldsymbol{\epsilon}^{(\prime)}} = -\frac{1}{\sqrt{2}} \left(\boldsymbol{\epsilon}^{(\prime)} \cdot \mathbf{x} - i\boldsymbol{\epsilon}^{(\prime)} \cdot \mathbf{y} \right) \tag{2.48}$$

$$L_{\boldsymbol{\epsilon}^{(\prime)}} = \frac{1}{\sqrt{2}} \left(\boldsymbol{\epsilon}^{(\prime)} \cdot \mathbf{x} + i\boldsymbol{\epsilon}^{(\prime)} \cdot \mathbf{y} \right) \tag{2.49}$$

with $\boldsymbol{\epsilon}^{(\prime)} = \boldsymbol{\epsilon}_{\sigma}^{(\prime)}, \boldsymbol{\epsilon}_{\pi}^{(\prime)}$. The scattering geometry together with the definition of the angles are shown schematically in Fig. 2.4.

We have now all the instruments to calculate the angular part of Eq. 2.37. By making use of the 3j-symbols we can calculate the integral over the three spherical harmonics:

$$\begin{aligned} &\int_0^{2\pi} \int_0^{\pi} Y_{l_1,m_1} Y_{l_2,m_2} Y_{l_3,m_3} \sin\theta d\theta d\phi = \\ &= \sqrt{\frac{(2l_1+1)(2l_2+1)(2l_3+1)}{4\pi}} \begin{pmatrix} l_1 & l_2 & l_3 \\ 0 & 0 & 0 \end{pmatrix} \begin{pmatrix} l_1 & l_2 & l_3 \\ m_1 & m_2 & m_3 \end{pmatrix}, \end{aligned} \tag{2.50}$$

with $m_1 + m_2 = -m_3$.

The matrix element of the electric dipole operator from an initial state $l_i = 2$, m_i=$0, \pm 1, \pm 2$, to an intermediate state $l_n = 1$, m_i=$0, \pm 1$, thus

	$\|Y^+_{2,2}\rangle$	$\|Y^-_{2,2}\rangle$	$\|Y^+_{2,1}\rangle$	$\|Y^-_{2,1}\rangle$	$\|Y^+_{2,0}\rangle$	$\|Y^-_{2,0}\rangle$	$\|Y^+_{2,\overline{1}}\rangle$	$\|Y^-_{2,\overline{1}}\rangle$	$\|Y^+_{2,\overline{2}}\rangle$	$\|Y^-_{2,\overline{2}}\rangle$
$\langle Y^+_{1,1}\|$	$-\sqrt{6}L_\epsilon$	0	$\sqrt{3}z_\epsilon$	0	$-R_\epsilon$	0	0	0	0	0
$\langle Y^-_{1,1}\|$	0	$-\sqrt{6}L_\epsilon$	0	$\sqrt{3}z_\epsilon$	0	$-R_\epsilon$	0	0	0	0
$\langle Y^+_{1,0}\|$	0	0	$-\sqrt{3}L_\epsilon$	0	$2z_\epsilon$	0	$-\sqrt{3}R_\epsilon$	0	0	0
$\langle Y^-_{1,0}\|$	0	0	0	$-\sqrt{3}L_\epsilon$	0	$2z_\epsilon$	0	$-\sqrt{3}R_\epsilon$	0	0
$\langle Y^+_{1,\overline{1}}\|$	0	0	0	0	$-L_\epsilon$	0	$\sqrt{3}z_\epsilon$	0	$-\sqrt{6}R_\epsilon$	0
$\langle Y^-_{1,\overline{1}}\|$	0	0	0	0	0	$-L_\epsilon$	0	$\sqrt{3}z_\epsilon$	0	$-\sqrt{6}R_\epsilon$

Table 2.1: Dipolar matrix elements between the spherical harmonic basis sets $\{|Y^\pm_{1,m}\rangle\}$ and $\{|Y^\pm_{2,m}\rangle\}$ in units of $\sqrt{15}\int_0^\infty r^3 R_{nd}(r)R_{np}(r)dr$

reads

$$\begin{aligned}
&\sum_q \sqrt{\frac{4\pi}{3}} \langle Y_{l_n,m_n}|P_{\boldsymbol{\epsilon},q}Y_{1,q}|Y_{l_i,m_i}\rangle = \\
&= \sum_q \sqrt{\frac{4\pi}{3}} P_{\boldsymbol{\epsilon},q} \int_0^{2\pi}\int_0^{\pi} Y^*_{l_n,m_n} Y_{1,q} Y_{l_i,m_i} \sin\theta d\theta d\phi \\
&= \sum_q (-1)^{m_n} \sqrt{\frac{4\pi}{3}} P_{\boldsymbol{\epsilon},q} \int_0^{2\pi}\int_0^{\pi} Y_{l_n,\overline{m}_n} Y_{1,q} Y_{l_i,m_i} \sin\theta d\theta d\phi \\
&= \sum_q (-1)^{m_n} \sqrt{15} P_{\boldsymbol{\epsilon},q} \begin{pmatrix} 1 & 1 & 2 \\ 0 & 0 & 0 \end{pmatrix} \begin{pmatrix} 1 & 1 & 2 \\ \overline{m}_n & q & m_i \end{pmatrix}.
\end{aligned} \tag{2.51}$$

Dipolar matrix elements between the spherical harmonic basis sets $\{|Y^\pm_{1,m}\rangle\}$ and $\{|Y^\pm_{2,m}\rangle\}$ in units of $\sqrt{15}\int_0^\infty r^3 R_{nd}(r)R_{np}(r)dr$ are shown in Tab. 2.1. The same matrix elements can be more conveniently expressed in the $\{|p_{j,m_j}\rangle\}$ basis and the real harmonic cubic $5d$ basis. In order to do that, we have first to calculate the matrix T_p which transform the $\{|Y_{1,m}\rangle\}$ basis set into the $\{|p_{j,m_j}\rangle\}$ basis. This can be easily done by diagonalizing the spin-orbit Hamiltonian calculated for p states in the spherical harmonics $\{|Y_{1,m}\rangle\}$ basis making use of Eq 1.23. The T_p matrix, which transforms the $\{|Y^+_{1,1}\rangle$, $|Y^-_{1,1}\rangle$,$|Y^+_{1,0}\rangle$, $|Y^-_{1,0}\rangle$, $|Y^+_{1,\overline{1}}\rangle$, $|Y^-_{1,\overline{1}}\rangle\}$ basis into the $\{|p_j, m_j\rangle\}$ basis

$\{|p_{\frac{1}{2},-\frac{1}{2}}\rangle, |p_{\frac{1}{2},\frac{1}{2}}\rangle, |p_{\frac{3}{2},-\frac{3}{2}}\rangle, |p_{\frac{3}{2},-\frac{1}{2}}\rangle, |p_{\frac{3}{2},\frac{1}{2}}\rangle, |p_{\frac{3}{2},\frac{3}{2}}\rangle\}$ finally reads

$$T_p = \begin{pmatrix} 0 & 0 & 0 & 0 & 0 & 1 \\ 0 & \sqrt{\frac{2}{3}} & 0 & 0 & \sqrt{\frac{1}{3}} & 0 \\ 0 & -\sqrt{\frac{1}{3}} & 0 & 0 & \sqrt{\frac{2}{3}} & 0 \\ \sqrt{\frac{1}{3}} & 0 & 0 & \sqrt{\frac{2}{3}} & 0 & 0 \\ -\sqrt{\frac{2}{3}} & 0 & 0 & \sqrt{\frac{1}{3}} & 0 & 0 \\ 0 & 0 & 1 & 0 & 0 & 0 \end{pmatrix}. \tag{2.52}$$

The transformation matrix T from the $\{|Y_{2,m}\rangle\}$ basis set to the $5d$ real cubic basis set has already been calculated in Section 1.4.1 (see Eq. 1.29). The matrix elements from $2p$ $\{|p_{j,m_j}\rangle\}$ to $5d$ real cubic harmonics can finally be derived as

$$\mathcal{D}_{|5d\rangle\to|p_j\rangle} = T_p^\dagger\, \mathcal{D}_{|Y_{2,m}\rangle\to|Y_{1,m}\rangle}\, T. \tag{2.53}$$

Dipolar matrix elements between the $\{|p_j, m_j\rangle\}$and the t_{2g} $\{|xy, \pm\rangle, |xz, \pm\rangle, |yz, \pm\rangle\}$ basis sets, in units of $\sqrt{15}\int_0^\infty r^3 R_{nd}(r) R_{np}(r) dr$, are presented in Tab. 2.2.

2.3.2 Results of the calculations

Having derived the matrix elements for $2p$ to $5d$ transitions we can proceed to evaluate Eq. 2.36. We now focus on the resonant elastic process where the initial and final $|0, -\rangle$ states coincides. We recall that the ground state reads

$$|0,-\rangle_c = \frac{-A|xy,-\rangle + |yz,+\rangle - i|xz,+\rangle}{\sqrt{2+A^2}} \tag{2.54}$$

for magnetic moment $\boldsymbol{\mu} \parallel [0\ 0\ 1]$ as in the bilayer perovskite $Sr_3Ir_2O_7$, and

$$|0,-\rangle_{ab} = \frac{A(-|xy,-\rangle + i|xy,+\rangle)/\sqrt{2} + |yz,+\rangle + i|xz,-\rangle}{\sqrt{2+A^2}} \tag{2.55}$$

for magnetic moment $\boldsymbol{\mu} \parallel [1\ 1\ 0]$ as in the single layer perovskites Sr_2IrO_4 and Ba_2IrO_4. By making use of the matrix elements of Tab. 2.2, and the scattering geometry and the polarization vectors of section 2.3.1 we can

	$\lvert xy,+\rangle$	$\lvert xy,-\rangle$	$\lvert xz,+\rangle$	$\lvert xz,-\rangle$	$\lvert yz,+\rangle$	$\lvert yz,-\rangle$
$\langle p_{\frac{1}{2},-\frac{1}{2}}\rvert$	$i\sqrt{2}\alpha_+R_\epsilon$	$i\sqrt{2}\alpha_-R_\epsilon$	$\frac{\beta_+(L_\epsilon-R_\epsilon)}{\sqrt{2}}-\alpha_+z_\epsilon$	$\frac{\beta_-(L_\epsilon-R_\epsilon)}{\sqrt{2}}-\alpha_-z_\epsilon$	$-\frac{1}{2}i\left(\sqrt{2}\beta_+\left(L_\epsilon+R_\epsilon\right)+2\alpha_+z_\epsilon\right)$	$-\frac{1}{2}i\left(\sqrt{2}\beta_-\left(L_\epsilon+R_\epsilon\right)+2\alpha_-z_\epsilon\right)$
$\langle p_{\frac{1}{2},\frac{1}{2}}\rvert$	$i\sqrt{2}\beta_+L_\epsilon$	$i\sqrt{2}\beta_-L_\epsilon$	$\frac{\alpha_+(-L_\epsilon+R_\epsilon)}{\sqrt{2}}-\beta_+z_\epsilon$	$\frac{\alpha_-(-L_\epsilon+R_\epsilon)}{\sqrt{2}}-\beta_-z_\epsilon$	$\frac{1}{2}i\left(\sqrt{2}\alpha_+\left(L_\epsilon+R_\epsilon\right)+2\beta_+z_\epsilon\right)$	$\frac{1}{2}i\left(\sqrt{2}\alpha_-\left(L_\epsilon+R_\epsilon\right)+2\beta_-z_\epsilon\right)$
$\langle p_{\frac{3}{2},-\frac{3}{2}}\rvert$	$-i\sqrt{3}\beta_+R_\epsilon$	$-i\sqrt{3}\beta_-R_\epsilon$	$\sqrt{\frac{3}{2}}\beta_+z_\epsilon$	$\sqrt{\frac{3}{2}}\beta_-z_\epsilon$	$i\sqrt{\frac{3}{2}}\beta_+z_\epsilon$	$i\sqrt{\frac{3}{2}}\beta_-z_\epsilon$
$\langle p_{\frac{3}{2},-\frac{1}{2}}\rvert$	$-i\alpha_+R_\epsilon$	$-i\alpha_-R_\epsilon$	$\beta_+\left(L_\epsilon-R_\epsilon\right)+\frac{\alpha_+z_\epsilon}{\sqrt{2}}$	$\beta_-\left(L_\epsilon-R_\epsilon\right)+\frac{\alpha_-z_\epsilon}{\sqrt{2}}$	$-\frac{1}{2}i\left(2\beta_+\left(L_\epsilon+R_\epsilon\right)-\sqrt{2}\alpha_+z_\epsilon\right)$	$-\frac{1}{2}i\left(2\beta_-\left(L_\epsilon+R_\epsilon\right)-\sqrt{2}\alpha_-z_\epsilon\right)$
$\langle p_{\frac{3}{2},\frac{1}{2}}\rvert$	$i\beta_+L_\epsilon$	$i\beta_-L_\epsilon$	$\alpha_+\left(L_\epsilon-R_\epsilon\right)-\frac{\beta_+z_\epsilon}{\sqrt{2}}$	$\alpha_-\left(L_\epsilon-R_\epsilon\right)-\frac{\beta_-z_\epsilon}{\sqrt{2}}$	$-\frac{1}{2}i\left(2\alpha_+\left(L_\epsilon+R_\epsilon\right)-\sqrt{2}\beta_+z_\epsilon\right)$	$-\frac{1}{2}i\left(2\alpha_-\left(L_\epsilon+R_\epsilon\right)-\sqrt{2}\beta_-z_\epsilon\right)$
$\langle p_{\frac{3}{2},\frac{3}{2}}\rvert$	$i\sqrt{3}\alpha_+L_\epsilon$	$i\sqrt{3}\alpha_-L_\epsilon$	$-\sqrt{\frac{3}{2}}\alpha_+z_\epsilon$	$-\sqrt{\frac{3}{2}}\alpha_-z_\epsilon$	$i\sqrt{\frac{3}{2}}\alpha_+z_\epsilon$	$i\sqrt{\frac{3}{2}}\alpha_-z_\epsilon$

Table 2.2: Dipolar matrix elements between the $\{\lvert p_j,m_j\rangle\}$ and the t_{2g} $\{\lvert xy,\pm\rangle,\ \lvert xz,\pm\rangle,\ \lvert yz,\pm\rangle\}$ basis sets in units of $\sqrt{15}\int_0^\infty r^3R_{nd}(r)R_{np}(r)dr$

calculate the scattering amplitude as

$$\mathcal{A}^{\boldsymbol{\epsilon}\boldsymbol{\epsilon}'}_{\mathrm{REXS}} = \sum_n \frac{\langle 0,-|\mathcal{D}^{\dagger}_{\boldsymbol{\epsilon}'}|n\rangle\,\langle n\,|\mathcal{D}_{\boldsymbol{\epsilon}}|\,0,-\rangle}{E_0 - E_n + \hbar\omega_{\mathbf{k}} - i\Gamma_n/2}. \tag{2.56}$$

At the Ir L_2 edge the summation runs over the $|p_{\frac{1}{2},-\frac{1}{2}}\rangle$ and $|p_{\frac{1}{2},\frac{1}{2}}\rangle$ intermediate states. The final scattering amplitudes read

$$\mathcal{A}^{\sigma\sigma'}_{\mathrm{REXS}} = \frac{(A-1)^2}{2+A^2} \tag{2.57}$$

$$\mathcal{A}^{\sigma\pi'}_{\mathrm{REXS}} = -\frac{i(A-1)^2\cos\theta'}{2+A^2} \tag{2.58}$$

$$\mathcal{A}^{\pi\sigma'}_{\mathrm{REXS}} = -\frac{i(A-1)^2\cos\theta}{2+A^2} \tag{2.59}$$

$$\mathcal{A}^{\pi\pi'}_{\mathrm{REXS}} = -\frac{(A-1)^2\cos\theta\cos\theta'}{2+A^2} \tag{2.60}$$

for magnetic moments along the [0 0 1] direction and

$$\mathcal{A}^{\sigma\sigma'}_{\mathrm{REXS}} = \frac{(A-1)^2}{2+A^2} \tag{2.61}$$

$$\mathcal{A}^{\sigma\pi'}_{\mathrm{REXS}} = 0 \tag{2.62}$$

$$\mathcal{A}^{\pi\sigma'}_{\mathrm{REXS}} = 0 \tag{2.63}$$

$$\mathcal{A}^{\pi\pi'}_{\mathrm{REXS}} = -\frac{(A-1)^2\cos\theta\cos\theta'}{2+A^2} \tag{2.64}$$

for magnetic moments along the [1 1 0] direction. We recall that the parameter $A = \frac{-1+\delta+\sqrt{9+(-2+\delta)\delta}}{2}$ controls the effect of the tetragonal crystal field Δ via $\delta = 2\Delta/\lambda$, where λ is the Ir SOC constant.

Ignoring the $\sigma\sigma'$ scattering channel for which no magnetic scattering is allowed once the magnetic structure factor is taken into account, we notice that for $\boldsymbol{\mu}\|$ [0 0 1] the scattering amplitude vanishes only when the pure $j_{\mathrm{eff}} = 1/2$ state is realized, i.e. for $\Delta = 0$ ($A = 1$). This is the case, for example, of the bilayer iridate $\mathrm{Sr_3Ir_2O_7}$ in which an analysis of the L_2/L_3 XRMS intensity ratio can be applied in order to determine the deviation from the $j_{\mathrm{eff}} = 1/2$ state due to the tetragonal crystal field. On the contrary, for $\boldsymbol{\mu}\|$ [1 1 0] the scattering amplitude in the cross-polarized $\sigma\pi'$ and $\pi\sigma'$ channels is identically zero irrespective of the tetragonal crystal field. This implies that the $j_{\rm eff}=1/2$ state cannot be inferred from the L_2/L_3 XRMS intensity ratio when the magnetic moment lies in the ab plane as in the single layer iridates $\rm Sr_2IrO_4$ and $\rm Ba_2IrO_4$ [58, 14, 16]. This is an important result since most of XRMS experiments are carried out in the cross-polarized channels in order to minimize the background due to charge scattering. However, in the $\pi\pi$ channel the scattering amplitude vanishes only for $\Delta = 0$, in analogy with the $\boldsymbol{\mu}\|$ [0 0 1] case.

At the Ir L_3 edge the summation runs over the four $|p_{\frac{3}{2},-\frac{3}{2}}\rangle$, $|p_{\frac{3}{2},-\frac{1}{2}}\rangle$, $|p_{\frac{3}{2},\frac{1}{2}}\rangle$, and $|p_{\frac{3}{2},\frac{3}{2}}\rangle$ intermediate states. At this edge the scattering amplitudes read

$$\mathcal{A}^{\sigma\sigma'}_{\rm REXS} = \frac{2\,(1+A+A^2)}{2+A^2} \tag{2.65}$$
$$\mathcal{A}^{\sigma\pi'}_{\rm REXS} = \frac{i[(A-2)A-2]\cos\theta'}{2+A^2} \tag{2.66}$$
$$\mathcal{A}^{\pi\sigma'}_{\rm REXS} = \frac{i[(A-2)A-2]\cos\theta}{2+A^2} \tag{2.67}$$
$$\mathcal{A}^{\pi\pi'}_{\rm REXS} = \frac{6\sin\theta\sin\theta' - 2\,(1+A+A^2)\cos\theta\cos\theta'}{2+A^2} \tag{2.68}$$

for magnetic moments along the [0 0 1] direction and

$$\mathcal{A}^{\sigma\sigma'}_{\rm REXS} = \frac{2\,(1+A+A^2)}{2+A^2} \tag{2.69}$$
$$\mathcal{A}^{\sigma\pi'}_{\rm REXS} = \frac{3iA(\cos\phi-\sin\phi)\sin\theta'}{\sqrt{2}\,(2+A^2)} \tag{2.70}$$
$$\mathcal{A}^{\pi\sigma'}_{\rm REXS} = -\frac{3iA(\cos\phi-\sin\phi)\sin\theta}{\sqrt{2}\,(2+A^2)} \tag{2.71}$$
$$\begin{aligned}\mathcal{A}^{\pi\pi'}_{\rm REXS} = \frac{e^{-i\phi}}{4\,(2+A^2)}\Big[&24e^{i\phi}\sin\theta\sin\theta' \\ &-8\left(1+A+A^2\right)e^{i\phi}\cos\theta\cos\theta' \\ &+(3+3i)\sqrt{2}A\left(i+e^{2i\phi}\right)\sin(\theta+\theta')\Big]\end{aligned} \tag{2.72}$$

for magnetic moments along the [1 1 0] direction. It is interesting to note that for $\boldsymbol{\mu}\|$ [0 0 1] the scattering amplitude in the cross-polarized channels goes to zero when $A = 1+\sqrt{3}$; this corresponds to $\Delta = 3\lambda/2$. The ground state wave function is in fact a linear combination of orbitals of different symmetry and different spin polarization: $|xy,-\rangle$, $|xz,+\rangle$, and

$|yz, +\rangle$. When the system has a perfect cubic symmetry, the SOC mixes exactly in the same proportion the three t_{2g} states and the scattering amplitude at the L_2 edge shows a destructive interference between the different channels. On the other hand, the presence of the tetragonal crystal field changes the mixing between the different t_{2g} orbitals, and when the tetragonal crystal field Δ equalizes the energy separation between $j_{\text{eff}} = 1/2$ state and $j_{\text{eff}} = 3/2$ state ($\Delta = 3\lambda/2$), a destructive interference takes place at the L_3 edge. As a consequence the scattering amplitude for $\boldsymbol{\mu} \| \, [0\,0\,1]$ vanishes.

Having determined the scattering amplitudes at the Ir $L_{2,3}$ edges we have now all the ingredients to calculate the L_2/L_3 XRMS intensity ratio for $\boldsymbol{\mu} \| \, [0\,0\,1]$. The total scattering cross-section is usually calculated as the squared modulus of the amplitude, taking into account the phase factor deriving from the magnetic structure factor, i.e. the relative position of the Ir atoms within the magnetic unit cell. However, this phase factor is equal for the two L edges, and since we are evaluating an intensity ratio it cancels out. The L_2/L_3 XRMS intensity ratio in the cross-polarized channels finally reads

$$\mathcal{I}^{\sigma\pi'}_{L_2/L_3} = \frac{\mathcal{I}^{\sigma\pi'}_{L_2}}{\mathcal{I}^{\sigma\pi'}_{L_3}} = \frac{\left|\mathcal{A}^{\sigma\pi'}_{L_2}\right|^2}{\left|\mathcal{A}^{\sigma\pi'}_{L_3}\right|^2} = \frac{(A-1)^4}{[(A-2)A-2]^2} \frac{\cos^2\theta'_{L_2}}{\cos^2\theta'_{L_3}}, \tag{2.73}$$

$$\mathcal{I}^{\pi\sigma'}_{L_2/L_3} = \frac{\mathcal{I}^{\pi\sigma'}_{L_2}}{\mathcal{I}^{\pi\sigma'}_{L_3}} = \frac{\left|\mathcal{A}^{\pi\sigma'}_{L_2}\right|^2}{\left|\mathcal{A}^{\pi\sigma'}_{L_3}\right|^2} = \frac{(A-1)^4}{[(A-2)A-2]^2} \frac{\cos^2\theta_{L_2}}{\cos^2\theta_{L_3}}. \tag{2.74}$$

The L_2/L_3 intensity ratio in the σ–π' and π–σ' polarization channels as a function of the tetragonal crystal field splitting Δ ranging from -1 to 1 eV, for a given value of the spin-orbit coupling constant ($\lambda = 0.42$ eV), is shown in Fig. 2.5. Here we have neglected the $\cos^2\theta'_{L_2}/\cos^2\theta'_{L_3}$ and $\cos^2\theta_{L_2}/\cos^2\theta_{L_3}$ terms as they are constant factor in the order of unity. The calculated branching ratio drops to zero for $\Delta = 0$, while it diverges for $\Delta = 3\lambda/2$. In the limit for $\Delta \gg \lambda$, the ratio tends to unity, and to 1/4 for $\Delta \ll -\lambda$. The calculated L_2/L_3 intensity ration will be used in Chapter 4 to interpret the XRMS data in the proximity of the $L_{2,3}$ edges in $Sr_3Ir_2O_7$.

When the resonant process involves a transition from the initial $|0, -\rangle$

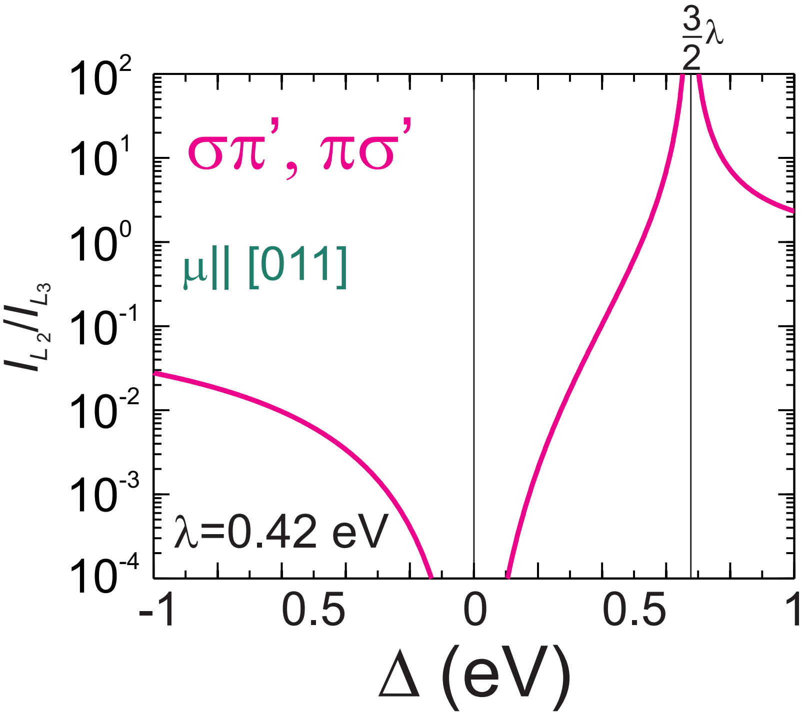

Figure 2.5: L_2/L_3 XRMS intensity ratio for $\boldsymbol{\mu} \| \; [0\,0\,1]$ as a function of the tetragonal crystal field splitting Δ ranging from -1 to 1 eV, for a given value of the spin-orbit coupling constant ($\lambda = 0.42$ eV).

state to the final $|0,+\rangle$ state, the system undergoes a“ spin-flip” process and a magnetic excitation is created. The RIXS cross-section relative to the “spin-flip” channel can be determined in analogy with the REXS cross-section as

$$\mathcal{A}^{\epsilon\epsilon'}_{\text{RIXS}} = \sum_n \frac{\langle 0,+|\mathcal{D}^{\dagger}_{\epsilon'}|n\rangle \, \langle n\,|\mathcal{D}_{\epsilon}|\,0,-\rangle}{E_0 - E_n + \hbar\omega_{\mathbf{k}} - i\Gamma_n/2}. \tag{2.75}$$

Surprisingly the RIXS scattering intensity shows a reciprocal behaviour, vanishing at the L_2 edge in any polarization channels when the magnetic moments point along the $[0\,0\,1]$ direction. While for $\boldsymbol{\mu} \| \; [0\,0\,1]$ it goes to zero only if $\Delta = 0$. This will be discussed more in details in Section 5.2.1.

In a similar way if the final states of the RIXS process are the $|1,\pm\rangle$, $|2,\pm\rangle$ states, a *d*-*d* excitation is created. The scattering amplitudes of this process can be calculated along similar lines of REXS amplitudes and RIXS amplitudes for the “spin-flip” channel. However this goes beyond the scope of this work.

2.4 Experimental set-up

Before presenting two prototypical beamlines, I16 at Diamond Light Source and ID20 at the ESRF, which respectively represent the state-of-the-art for REXS and RIXS instruments, we briefly point out that in both cases a synchrotron source is needed. A charged particle, when accelerated, emits radiation. Synchrotrons are storage rings where particles such as electrons or positrons are accelerated close to the speed of light and are kept in a circular orbit by means of bending magnets. Historically, the radiation coming from the bending magnet— used to maintain the particles in a closed orbit— was the first to be exploited for scientific studies.

Nowadays, in third generation synchrotrons, more powerful sources installed in the straight sections of the storage ring have become the first port of call for “photon-demanding” techniques such as REXS and RIXS. These sources, called undulators, are arrays of permanent magnets that force the electrons to follow an oscillating path rather than moving in a straight way. Since the magnetic field in undulators is rather small, electrons experience small amplitude oscillations and the radiation produced from each oscillation adds up coherently. As a consequence, X-ray radiation from the undulator devices has a very low divergence, very high brilliance and spatial coherence, and it is almost monochromatic. For a detailed treatment of synchrotron radiation source see for instance Attwood [59].

2.4.1 A REXS beamline: I16 at Diamond Light Source

Most of this PhD project work has been carried out at the I16 beamline, Diamond Light Source, Didcot, UK. The beamline is optimized for REXS and X-ray magnetic scattering. These techniques require high photon flux, energy tunability, variable incident polarization, analysis of the scattered beam polarization, high momentum resolution, azimuthal scanning capability and different sample environments.

Optics

At the I16 beamline X-rays are generated by means of a 2m Diamond U27 (27 mm period) in-vacuum undulator insertion device that gives a continuous energy spectrum of X-rays from 3.5 keV to 15 keV. After a fixed gas bremsstrahlung collimator, a liquid-nitrogen-cooled monochromator is used to monochromatize the beam. In this stage three interchangeable crystals are installed: a channel-cut Si (1 1 1), a Si (1 1 1) double crystal and a Si (3 1 1) double crystal. Since the channel-cut Si (1 1 1) has demonstrated to be very stable and easy to use, although a small vertical movement of the beam when the energy is changed has to be taken in account, it is the usual crystal exploited in the beamline. The energy resolution of the incident beam due to the Darwin width of the crystal monochromator ($\Delta E/E = 1.33 \times 10^-4$ for Si 111 [60]) is ~1.49 eV at 11.2 keV plus a small contribution from the undulator.

The X-ray beam is then focused by a pair of 1.2 m mirrors. The first, a 96 mm radius sagittal cylinder, focuses the beam vertically, the second flat mirror with a circular mechanical bender (tangential radius ~5.8 km) gives the horizontal focusing. The result is a beam of gaussian shape with a focus very close to the theoretical value. The beam at the sample position has a $20\mu m \times 200\mu m$ (V×H) size. The coating of the first mirror (Si or Rh selectable) provides the rejection of the higher harmonics coming from the undulator and the monochromator. Additional focusing up to few μm is available via Kirkpatrick-Baez (KB) mirrors.

Between the monochromator and the mirrors a in-vacuum quarter-wave phase retarder permits the manipulation of the photon polarization. This device consists of a diamond crystal that exhibit birefringence close to the Bragg condition. After the mirrors, numerous slits, monitors, attenuators permit to control the intensity, divergence and size of the beam. A schematic view of the optics and experimental hutch layouts is shown in Fig. 2.6.

Diffractometer and sample environment

The core of the beamline is a Newport 6-axis N-6050 Kappa diffractometer. This diffractometer permits to work in both vertical and horizontal scattering geometry. Compared to a classical eulerian diffractometer, the k-circle allows more “exotic” sample environments and gives access to large scattering angles. Several cryostats can be attached to the diffractometer. Most used are a closed cycle Displex cryocooler and, if vibrations must be avoided and the transition temperature is above the nitrogen boiling point, a nitrogen gas jet cooler.

One fundamental property of any modern diffractometer is the possibility to perform *azimuthal scans*. They consist in measuring the scattering intensity as a function of the azimuthal angle Ψ while rotating constantly the sample around the scattering vector $\mathbf{K}$ (see Fig. 2.6, bottom panel). In this way the projection of the magnetic moment with respect to the coordinate system is varied (see Eq 2.33) and the magnetic moment direction can be determined.

Detectors and polarization analyzer

The detector arm supports six permanently mounted X-ray detectors. Five of these, an avalanche photodiode, a Si drift detector, a scintillation detector, a PIN diode and a high resolution imager are mounted on the secondary detector arm of a polarization analyzer (PA) stage. Separate to this, with an angular offset of 9° on the main diffractometer detector arm, a Pilatus 100K area detector is selectable.

The PA stage is composed of a crystal of a specific material at the center of a small two-circle diffractometer. The crystal scattering angle $2\theta_p$ is set in order to satisfy the Bragg condition. In this way only nearly elastic radiation can be transmitted after the analyzer, and the signal is cleaned from all the fluorescence background that is usually emitted several eV below the absorption edges. In addition to this the crystal acts as a polarizer. Recalling the polarization dependence of charge scattering (Eq. 2.31)

$$\boldsymbol{\epsilon}' \cdot \boldsymbol{\epsilon} = \begin{pmatrix} 1 & 0 \\ 0 & \widehat{\mathbf{k}}' \cdot \widehat{\mathbf{k}} \end{pmatrix} = \begin{pmatrix} 1 & 0 \\ 0 & \cos 2\theta_p \end{pmatrix} \tag{2.76}$$

it can be seen that for $\theta_p = 45°$ it is possible to filter only the polarization component perpendicular to the scattering plane of the crystal analyzer. Therefore, by rotating the crystal analyzer around the beam direction by

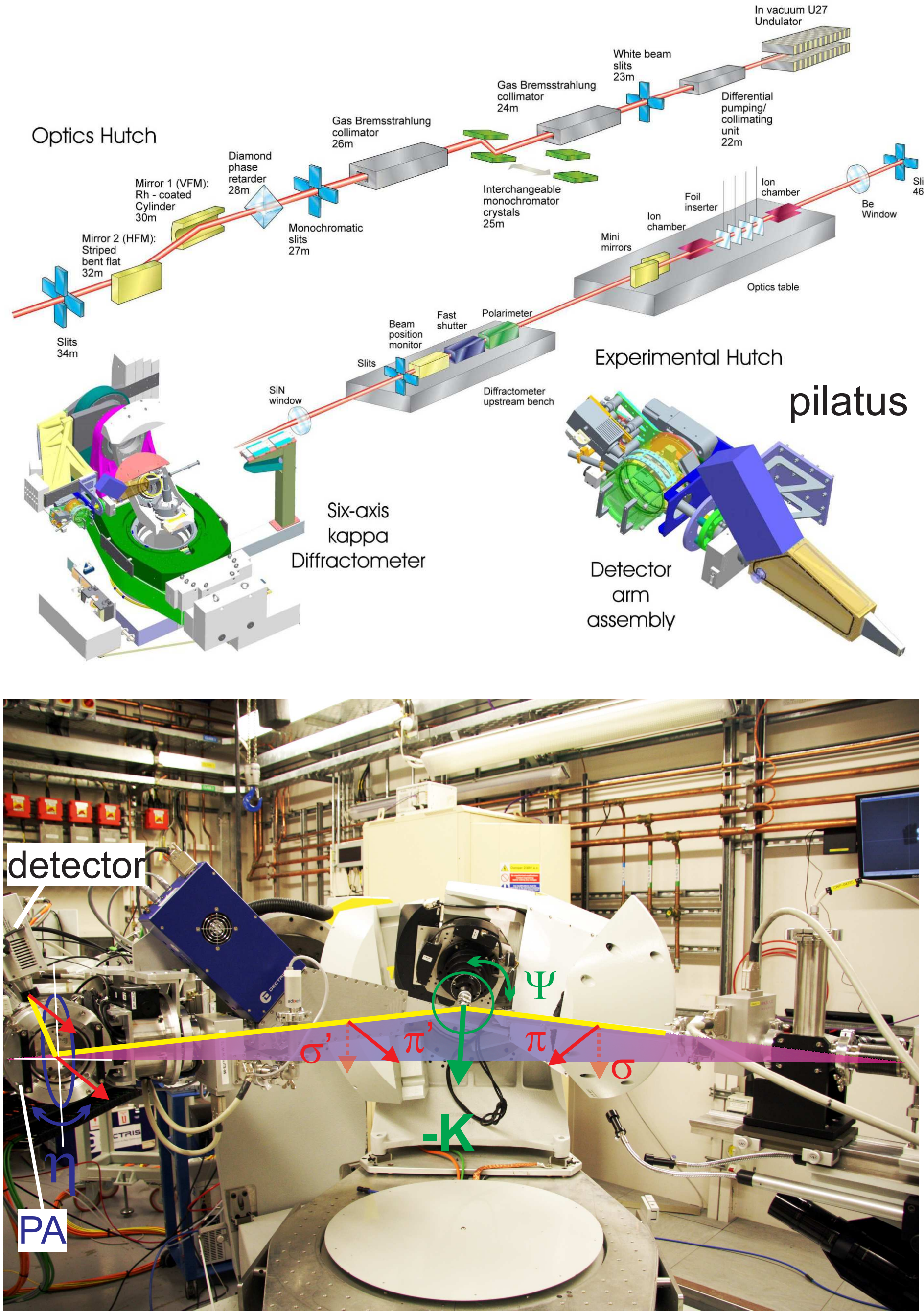

Figure 2.6: Top panel: schematic view of the optics and experimental hutch layouts of I16, Diamond Light Source, UK, showing the diffractometer with the cryostat attached. The detector arm assembly is shown, illustrating the in-vacuum polarization analyzer with five detector systems, the permanent vacuum beam tube, and the Pilatus 100K area detector (blue box), under which is a set of slits. Reproduced from Ref. [61]. Bottom panel: horizontal scattering geometry and polarization analysis.

an angle η different components of the polarization vector can be selected. $\eta = 0°$ corresponds to σ' polarized light whereas $\eta = 90°$ corresponds to π' polarized light.

Since in REXS experiments the energies are fixed by the absorption edges of the material, working in the ideal $\theta_p = 45°$ is impossible. The crystal analyzers close to this condition are Au (3 3 3) ($\theta_p \sim 45°$) and graphite (8 0 0) ($\theta_p \sim 41°$) in the case of Ir L_3 edge. Although Au (3 3 3) offers a better polarization filtering due to a Bragg reflection closer to 45°, a graphite crystal offers higher reflectivity and a bigger angular acceptance. At the Ir L_2 edge the best match is provided by Cu (3 3 3)($\theta_p \sim 44°$). However, in order to compare the scattering intensity with measurements at the L_3, we have used the same Au (3 3 3). At these energies the analyzer scattering angle measures ($\theta_p \sim 38°$). In order to take into account the non ideal nature of the analyzer the measured intensities can be corrected according to [62]:

$$\begin{aligned} I_{\sigma\sigma'} &= \frac{I^m_{\sigma\sigma'} - I^m_{\sigma\pi'} \cos^2\theta_p}{1 - \cos^4 2\theta_p} \\ I_{\sigma\pi'} &= \frac{I^m_{\sigma\pi'} - I^m_{\sigma\sigma'} \cos^2\theta_p}{1 - \cos^4 2\theta_p}, \end{aligned} \tag{2.77}$$

where $I^m_{\sigma\sigma'}$ and $I^m_{\sigma\pi'}$ are the measured scattering intensities. Similar expression can be obtained for incident π polarization.

2.4.2 A RIXS beamline: ID20 at the ESRF

The RIXS measurements of this work have been carried out at the ID20 (previously ID16) beamline at the ESRF, France. A RIXS beamline usually has similar requirements of REXS beamlines: high brilliance, good momentum resolution and energy tunability. In addition, the possibility to analyze the energy of the scattered beam with high resolution is an essential capability.

Optics

Since RIXS is a "photon-hungry" technique, on ID20 the photon flux is maximized by a 6 m long straight section equipped with 4 in-vacuum

U26 undulators and 3 in-vacuum U32 which produce a continuous spectrum from 4 keV to 20 keV. After a collimating mirror (CM) X-rays are monochromatized via a high heat-load liquid-nitrogen-cooled Si(1 1 1) double-crystal monochromator up to a bandwidth of ≈ 1.5 eV at 11.217 keV (this bandwidth is comparable to the usual energy resolution in REXS beamlines). In order to reduce the bandwidth of the incident radiation to the meV range the common set-up exploited in hard X-rays is a second monochromator working in a close-to-backscattering geometry. This means that a suitable Bragg reflection has to be found and that the experimental set-up is appropriate only for a particular energy range. In the following we will present the high resolution set-up for Ir L_3 edge. The choice of the high resolution monochromator is a channel-cut Si (8 4 4) which gives an energy bandwidth, due to the Darwin width of the crystal, $\Delta E_{\mathrm{DW}} \approx 15$ meV. At 11.217 keV, the (8 4 4) Bragg reflection of Si is found at $\theta_{\mathrm{B}} = 85.73°$ The fully monochromatic beam is then focused in two steps, firstly by means of a toroidal focusing mirror (FM) and then via KB mirrors on the sample at the center of the RIXS spectrometer. The beamsize at the sample position measures 8×16 μm^2 (V×H). As we will see in the following section the vertical spot size is a critical parameter in the final resolution of a RIXS spectrometer. The optical layout of ID20 is illustrated in Fig. 2.7.

RIXS spectrometer

The core of a RIXS beamline is the spectrometer. At ID20 it is mounted on a 4 circle Huber diffractometer that permits us to maneuver the sample orientation and to determine the scattering geometry both in the vertical (σ incoming light) and horizontal (π incoming light) scattering plane (See Fig. 2.7(b)). The scattered radiation is collected by a 100 mm-diameter Si (8 4 4) spherical diced analyzer (A) which operates at the same Bragg angle θ_{B} as the back-scattering channel-cut monochromator, and then focused on a 2D pixelated Medipix2 detector (55×55 μm^2 pixel size). The spectrometer works in the Rowland circle geometry, i.e. the sample (S), analyzer and detector (D) position lies on the Rowland circle and the curvature radius of the analyzer ($R = 2$ m) matches the diameter of the

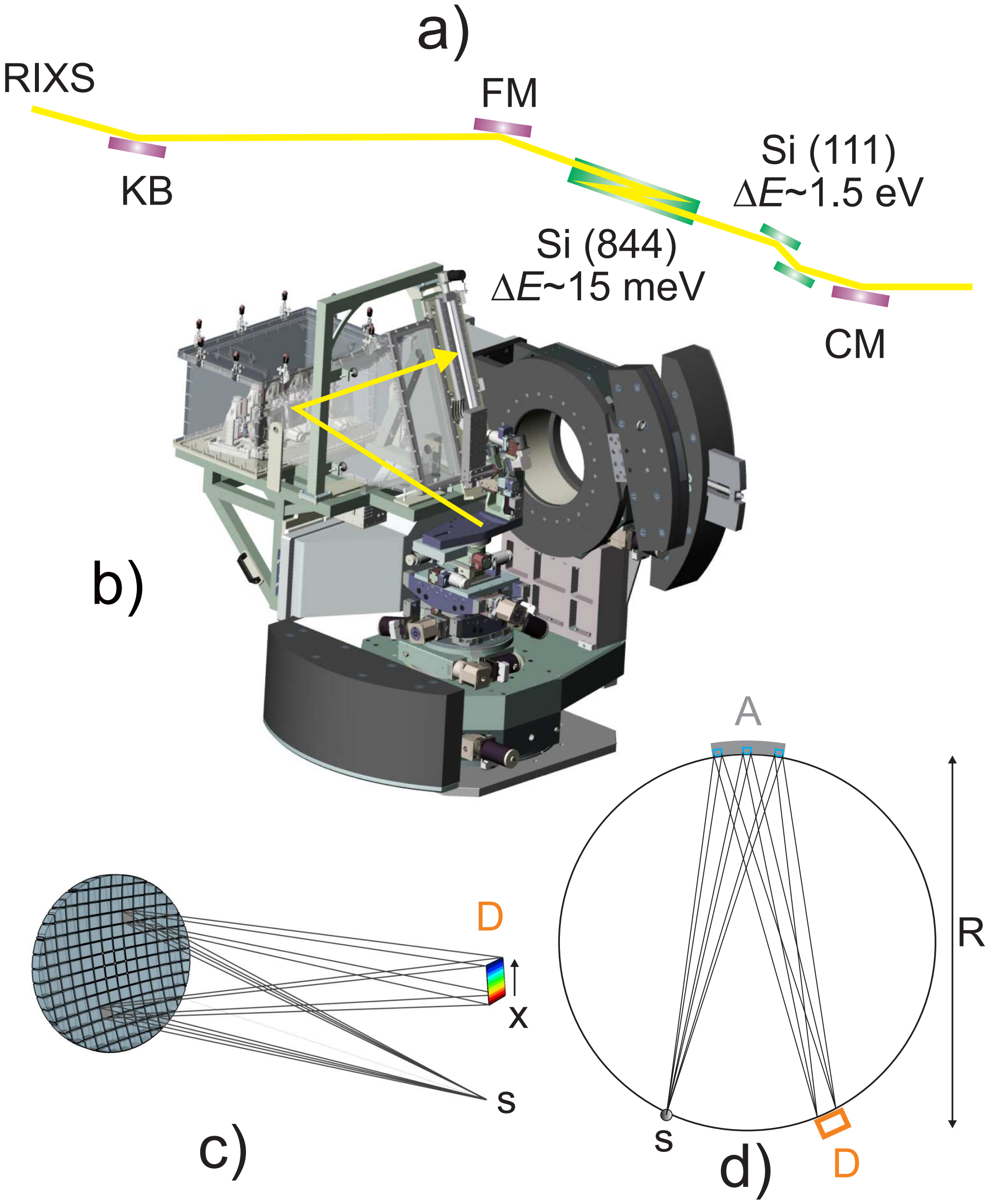

Figure 2.7: (a) Schematic view of the optical layout of the ID20 beamline, ESRF, France. (b) ID20 spectrometer. (c) The diced analyzer and the 2D position-sensitive detector are shown in detail. (d) The position of the source, analyzer, and detector is illustrated in a top view of the Rowland circle.

Rowland circle itself (see Fig. 2.7(d)). The diced analyzers have been introduced to overcome the elastic distortion characteristic of bent analyzers which was degrading the resolution in the former RIXS instruments. They consist of a polygonal approximation to a spherical crystal analyzers made by perfectly cubed dices of edge size $c = 0.72$ mm and spacing between cube centers $r = 0.94$ mm (See Fig. 2.7(c)). However, the finite size of a single dice causes a contribution to the resolution of the form [63]:

$$\frac{\Delta E}{E} = \frac{c}{R} \cot \theta_{\mathrm{B}}. \tag{2.78}$$

The more the analyzer angle moves away from a perfect backscattering geometry ($\theta_{\mathrm{B}} = 90\,^{\circ}$), the bigger is this contribution. In general the broadening due to the size of the dice cannot be decreased below 300 meV [64] for $R = 2$ m, making impossible to use RIXS to study low energy excitations. A way to overcome this limitation has been proposed by Huotari et al. [64, 63] and takes advantage of 2D position-sensitive detector. In fact, every dice crystal disperses in the analyzer vertical scattering plane, since at different Bragg angles correspond different energies of the scattered photons. Since the Rowland condition is satisfied, the image at the detector will be twice the size of a single dice $2c$, and the contribution of different dices almost perfectly superimpose at the detector surface. In the detector plane, in the dispersive direction, there is a well-defined relationship between the energy of the photons and the spatial position x at which photons impinge on the detector surface (see Fig. 2.7(c)):

$$\frac{dE}{dx} = \frac{E}{2R} \cot \theta_{\mathrm{B}}. \tag{2.79}$$

In the case of Ir L_3 edge ($E = 11217$ eV, $R = 2$ m, $\theta_{\mathrm{B}} = 85.73°$) the dispersion is about 210 meV/mm. This means that the resolution is now limited by the pixel size p as

$$\frac{\Delta E}{E} = \frac{p}{2R} \cot \theta_{\mathrm{B}}. \tag{2.80}$$

For the Ir L_3 set-up the pixel size (55 μm) contribution to the resolution will therefore be $\Delta E_{\mathrm{pixel}} \approx 11$ meV. The last contribution to consider to the overall resolution is the finite-size of the source s at the

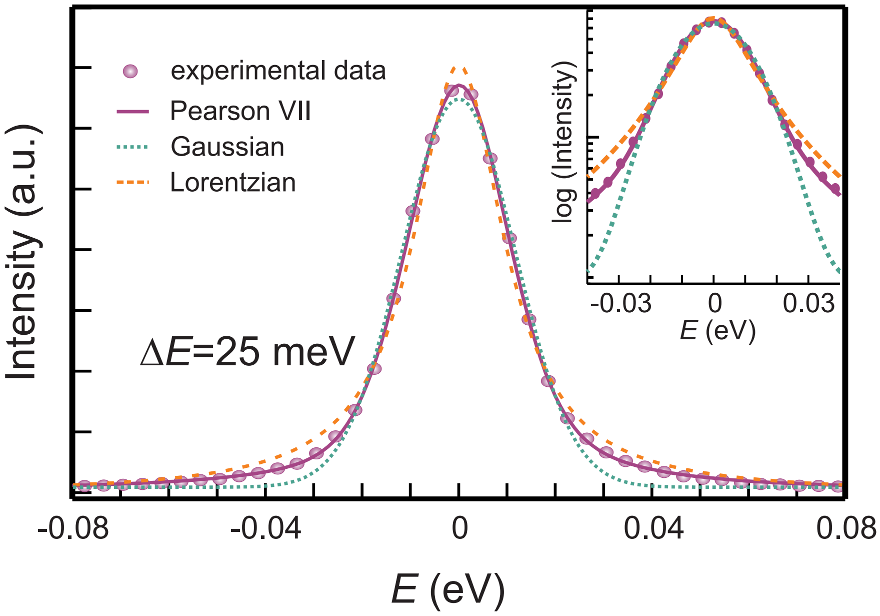

Figure 2.8: Experimental energy resolution at the Ir L_3 edge as determine from an energy scan on a polymer. The purple line is a fit to a Pearson VII function of FWHM = 25 meV. Green dotted (orange dashed) lines are fit to a Gaussian (Lorentzian) line shape. The inset show the same plot on a logarithmic scale to emphasize the effect of the tail of the resolution function.

sample position ($\Delta E_\mathrm{s} \approx 4$ meV for $s = 8$ μm). Adding quadratically all these contribution one gets the resolution of the RIXS spectrometer $\Delta E^\mathrm{calc}_\mathrm{RIXS} = \sqrt{2\Delta^2_\mathrm{DW} + \Delta^2_\mathrm{s} + \Delta^2_\mathrm{pixel}} \approx 24\,\mathrm{meV}$. This value can be compared with the experimental resolution measured on a polymer in order to avoid inelastic contaminations due to the sample. The results together with a fit to a Pearson VII (purple line), Gaussian (dotted green line), and Lorentzian (orange dashed line) functions are presented in Fig. 2.8. The resolution function includes clearly both a Lorentzian and a Gaussian contribution. In virtue of this a Pearson VII line shape that varies from a pure Lorentzian function for $m = 1$ to a pure Gaussian function for $m = \infty$ gives the best fit. The corresponding full-width at half-maximum (FWHM) is $\Delta E_\mathrm{exp} = 25.2(2)$ meV, in excellent agreement with the calculated resolution.

Concerning the momentum resolution of the spectrometer, this is determined by the angular acceptance of the crystal analyzer. For an analyzer diameter of 60 mm[2] and a 2 m spectrometer the angular acceptance is ± 0.85°. The corresponding **K** resolution obtained from Eq.2.2 is therefore ± 0.28 Å^{-1}.

---

[2] the full analyzer of diameter 100 mm is usually masked to reduce background and improve the **K** resolution.

Chapter 3

The magnetic and electronic structure of $(Sr,Ba)_2IrO_4$ studied with XRMS

Sr_2IrO_4 is a prototype of the class of Mott insulators in the strong spin-orbit coupling (SOC) limit described by a $j_{\text{eff}} = 1/2$ ground state. In Sr_2IrO_4, the strong SOC is predicted to manifest itself in the locking of the canting of the magnetic moments to the correlated rotation by 11.8(1)° of the oxygen octahedra that characterizes its distorted layered perovskite structure. Using X-ray resonant scattering at the Ir L_3 edge we have measured accurately the canting of the magnetic moments to be 12.2(8)°. We thus confirm that in Sr_2IrO_4 the magnetic moments rigidly follow the rotation of the oxygen octahedra, indicating that, even in the presence of significant non-cubic structural distortions, it is a close realization of the $j_{\text{eff}} = 1/2$ state.

Ba_2IrO_4 is a close relative of Sr_2IrO_4. In this compound, the lack of octahedral rotation leads to a simple antiferromagnetic structure which is observed with Ir L_3 edge XRMS. A comparative study of these compounds reveals that the dominant, long-range antiferromagnetic order is remarkably similar. The robustness of the magnetic properties to the considerable structural differences between the Ba and Sr analogues is discussed in terms of the enhanced role of the spin-orbit interaction in $5d$ transition metal oxides.

Contents

3.1 Introduction

The discovery of a novel $j_{\text{eff}} = 1/2$ state in Sr_2IrO_4 has triggered intensive theoretical and experimental efforts to understand the validity and limitation of this model [65, 16, 58, 54, 55]. While this model is interesting in its own right, further impetus to the study of these materials is added by the prediction of becoming superconducting upon electron-doping [28, 29]. The search for novel superconductivity represents a flourishing branch of condensed matter physics. In strongly correlated systems, superconductivity is often realized when a long-range order state is destabilized by, for instance, fluctuations. Both cuprate and pnictide superconductors, for example, emerge when doping destabilizes long range antiferromagnetic order, and in each case obtaining a microscopic understanding of the magnetic ground state of the parent compound has played a pivotal role in our knowledge [66, 67]. In particular, Sr_2IrO_4 and Ba_2IrO_4 show striking similarities with the parent compound of high–T_C superconductors La_2CuO_4.

They both crystallize in a layered perovskite structure close to the K_2NiF_4-type, i.e., in a quasi-two-dimensional structure. They have effectively one hole per Cu or Ir ion, and they show $s = 1/2$ or $j_{\text{eff}} = 1/2$ antiferromagnetic (AFM) order. In La_2CuO_4, it is well established that the low-energy magnetic excitations are described by a spin 1/2 AFM Heisenberg model with large superexchange J interactions. As shown in Section 1.5, the dominant low-energy interactions in single layer perovskites are predicted to follow the same model, despite the novel $j_{\text{eff}} = 1/2$ wave function. A detailed study of the magnetic state in Sr_2IrO_4 and Ba_2IrO_4 is therefore required to place a strong constraint on the Hamiltonian and the theoretical model of perovskite iridates.

3.2 Locking of magnetic moment to the octahedral rotation in Sr_2IrO_4

Although first synthesized more than 50 years ago [68], Sr_2IrO_4 has only recently attracted significant interest. The attention of the scientific community was first boosted by the discovery of superconductivity in the close isostructural compound Sr_2RuO_4 [69], and finally exploded after the report of being the first example of "spin-orbit induced" Mott insulator [19]. Since then, several experimental and theoretical studies have investigated the structural, electronic, and magnetic properties of Sr_2IrO_4 [14, 55, 42, 23, 43]. They all agree on the insulating behaviour of Sr_2IrO_4 at all temperatures and on the fact that Sr_2IrO_4 shows a weak ferromagnetic state below 240 K. However, the magnetic structure was not fully established before this work. In particular the relation between the macroscopic weak ferromagnetism and the microscopic magnetic interaction was not unambiguously proved although Crawford et al. [70] proposed that the weak ferromagnetic moment can be originated by a canting of the dominant antiferromagnetic structure.

In Section 3.2.1 we present a general review on the physical properties of Sr_2IrO_4. In Section 3.2.2 we then discuss our comprehensive study of the magnetic structure via XRMS. Finally, in Section 3.2.3, we address the problem of determining the canting angle in Sr_2IrO_4 by a comparison of measured intensities relative to specific magnetic reflections with the scattering intensity calculated for a particular arrangement of Ir moments.

3.2.1 Review on bulk properties of Sr$_2$IrO$_4$

Sr$_2$IrO$_4$ crystallizes in the tetragonal space group I4$_1$/acd ($a = b = 5.48$ Å, and $c = 25.8$ Å) [70]. The symmetry is reduced from the K$_2$NiF$_4$-type structure (space group I4/mmm) by a correlated staggered rotation of the IrO$_6$ octahedra by 11.8° about the c axis. This generates a larger unit cell, $\sqrt{2}a \times \sqrt{2}b \times 2c$, under the rotation of the I4/mmm cell by 45° [70]. The crystal structure of Sr$_2$IrO$_4$ is shown schematically in Fig. 3.1. IrO$_6$ layers where the Ir atoms (grey) are at the center of corner sharing oxygen (red) octahedra are separated by Sr atoms (light green). The significant distance between IrO$_6$ layers (>6 Å) forces the electronic and magnetic interactions to mainly take place in the IrO$_6$ planes. As a consequence, Sr$_2$IrO$_4$ is expected to exhibit all the “physical attributes” of a quasi-2D system.

Another feature of this crystal structure is that the IrO$_6$ octahedra are slightly (4%) elongated along the c axis. This means that it is not a priori obvious that the pure $j_{\mathrm{eff}} = 1/2$ state is realized in a system which deviates from a perfect cubic symmetry. Although the exact space group was recently called into question by two different neutron studies [40, 42], the subtle difference from the commonly used I4$_1$/acd is most likely not relevant in terms of the magnetic structure and therefore the I4$_1$/acd reference will be used in the rest of this work.

As introduced in Chapter 1, Sr$_2$IrO$_4$ was initially expected to be a metallic system. Since then, evidence for its insulating behaviour has been provided [31, 14, 32]. Fig. 3.2 (a) shows the temperature dependence of the in-plane (ρ_{ab}) and out-of-plane (ρ_{ab}) resistivity measured by Kim et al. [14]. The most relevant peculiarities are a significant anisotropic behaviour of the resistivity between the in-plane and out-of-plane directions, which reflects the bi-dimensional nature of this compound, and the lack of anomalies at the magnetic transition $T_M = 240$ K which suggests that the insulating behaviour is not correlated with magnetic degrees of freedom. The temperature dependence of the resistivity can not be fitted to a

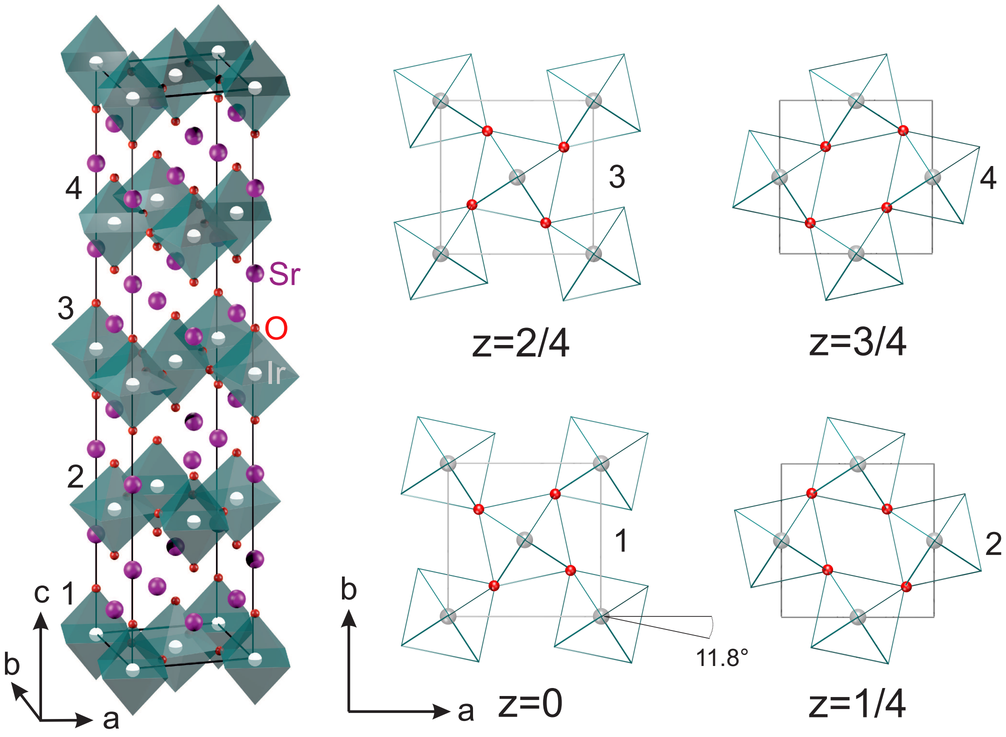

Figure 3.1: Crystal structure of Sr_2IrO_4 (space group $I4_1/acd$). IrO_6 layers where the Ir atoms (grey) are at the center of corner sharing oxygen (red) octahedra are separated by Sr atoms (purple). The IrO_6 octahedra undergo a staggered correlated rotation of $\sim 11.8°$ about the c axis [70].

simple model. However, most authors assume an Arrhenius-type [71, 14], which is characteristic for semiconductor-like behavior.

Further proof of the insulating behaviour in Sr_2IrO_4 and more insights into its electronic properties can be found in optical conductivity measurements. Fig. 3.2 (c) shows the temperature-dependent optical conductivity spectra $\sigma(\omega)$ of Sr_2IrO_4 measured by Moon et al. [31]. A clear optical gap of about 0.25 eV can be observed up to room temperature. Furthermore, two distinct peaks can be observed at all the temperatures at about 0.5 eV (α) and 1 eV (β). As illustrated in the cartoon of Fig. 3.2 (c), top panel, peak α corresponds to the optical transition from the lower Hubbard band to the upper Hubbard band of the $j_{\text{eff}} = 1/2$ states. Peak β corresponds to the optical transition from the $j_{\text{eff}} = 3/2$ band to the upper Hubbard band of the $j_{\text{eff}} = 1/2$ states. The observation of these well defined transitions is a further confirmation of the strong spin-orbit coupling regime

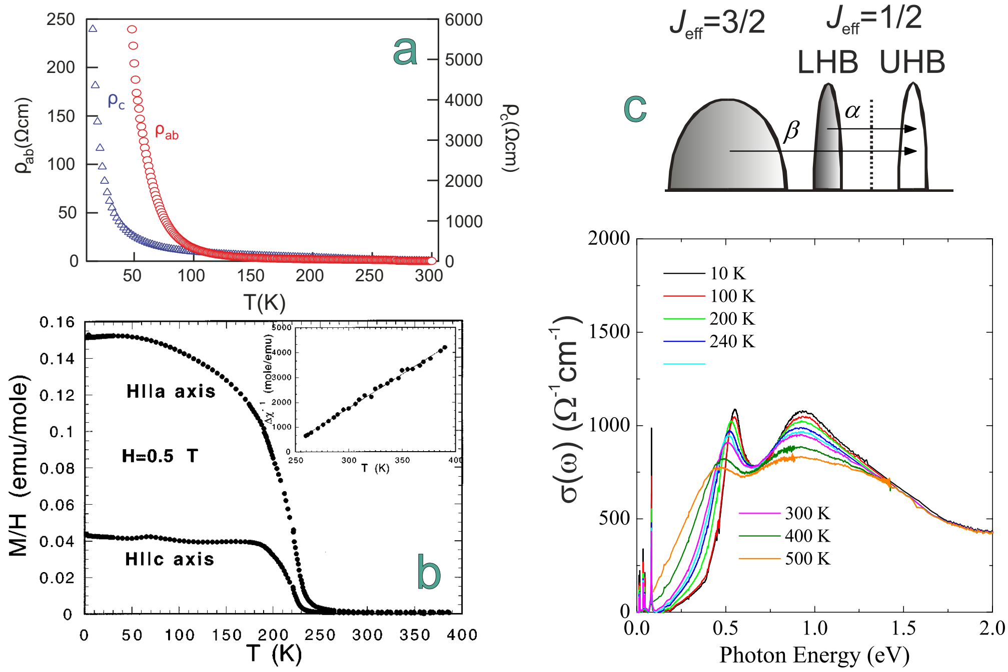

Figure 3.2: (a) Temperature dependence of in-plane resistivity (ρ_{ab}) and out-of-plane resistivity (ρ_{c}). From [14]. (b) Magnetic susceptibility $\chi(T) = M(T)/H$ of Sr_2IrO_4 at $H = 0.5$ T along the two principal crystallographic directions. Inset: $\Delta\chi^{-1}$ in function of the temperature for $T > T_M$, with $\Delta\chi^{-1} = \chi(T) - \chi_0$. From [32]. (c) Top panel: schematic band diagram of the electronic structure of Sr_2IrO_4. Peak α corresponds to the optical transition from the lower Hubbard band to the upper Hubbard band of the $j_{\text{eff}} = 1/2$ states. Peak β corresponds to the optical transition from the $j_{\text{eff}} = 3/2$ band to the upper Hubbard band of the $j_{\text{eff}} = 1/2$ states. Bottom panel: temperature-dependent optical conductivity spectra $\sigma(\omega)$ of Sr_2IrO_4. Taken from [31].

in Sr_2IrO_4.

Fig. 3.2 (b) shows the magnetic susceptibility $\chi(T) = M(T)/H$ of Sr_2IrO_4 at $H = 0.5$ T along the two principal crystallographic directions a and c. There is evidence for weak ferromagnetism below $T_M = 240$ K for both directions above a critical magnetic field $H_C = 0.2$ T. The large anisotropy of the magnetic susceptibility clearly indicates that the easy axis is aligned with the a axis. The magnitude of the weak ferromagnetic moment was estimated to be $\mu_{\text{FM}} \sim 0.03\ \mu_B/\text{Ir}$. Such a small value cannot be assigned to $j_{\text{eff}} = 1/2$ magnetic moments perfectly aligned ferromagnetically. In fact, in Section 1.4.1 we have shown that, in the ionic limit, the expected magnitude of the magnetic moment for the $j_{\text{eff}} = 1/2$ state is 1 μ_B. To justify these findings Crawford et al. [70] suggested that a canted antiferromagnetic (AF) state could be realized in Sr_2IrO_4. In this scenario, the ferromagnetic moment would represent only a small fraction of the total magnetic moment. This is exactly what happens in Sr_2IrO_4 and a definitive proof can be provided via XRMS measurements.

3.2.2 XRMS study of magnetic structure

The work presented in this section has been published as "*Robustness of Basal-Plane Antiferromagnetic Order and the $j_{\text{eff}} = 1/2$ State in Single-Layer Iridate Spin-Orbit Mott Insulators*" by S. Boseggia, R. Springell, H. C. Walker, H. M. Rønnow, Ch. Rüegg, H. Okabe, M. Isobe, R. S. Perry, S. P. Collins, and D. F. McMorrow, Phys. Rev. Lett. **110**, 117207 (2013) [16].

In order to investigate the magnetic structure of Sr_2IrO_4 we performed an XRMS study at the Ir L_3 edge. The XRMS experiments were conducted at the I16 beamline at Diamond Light Source, Didcot, UK and at the P09 beamline of Petra III, Hamburg, Germany. On I16 a monochromatic X-ray beam was provided by means of a U27 undulator insertion device and a channel-cut Si (1 1 1) monochromator, focused to a beam size of 20×200 μm^2 at the sample position. An avalanche photodiode (APD) was used to detect the scattered photons, together with a Au (3 3 3) crystal to analyze the polarization of the scattered beam. The Sr_2IrO_4 sample was mounted in a closed-circle cryostat with the [0 0 1] (perpendicular to the sample surface) and [1 0 0] directions in the vertical scattering plane of a Newport 6-circle Kappa diffractometer at the azimuthal origin. On P09 the X-rays were provided by means of a 2 m long U32 spectroscopy undulator insertion device, and focused to a beam size of 50×50 μm^2 at the sample position, using a set of focusing mirrors and beryllium compound refractive lenses. The scattering geometry was equivalent to the one adopted on the I16 beamline. An APD was used to detect the scattered photons together with a pyrolytic graphite (0 0 8) crystal to analyze the polarization of the

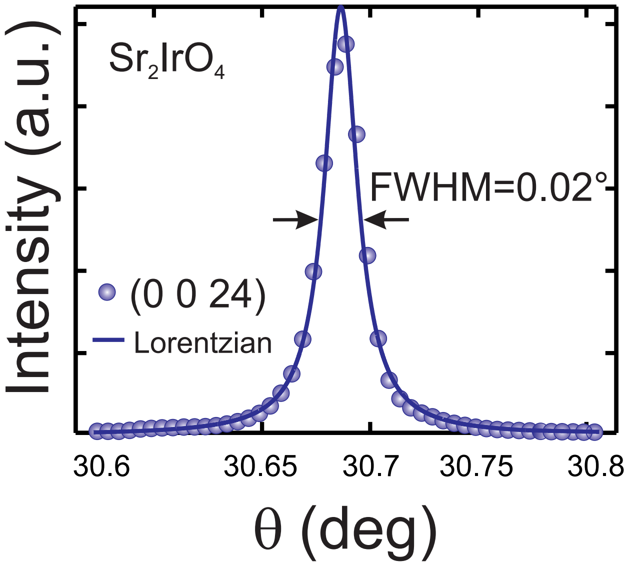

Figure 3.3: θ scan across the (0 0 24) Bragg reflection at room temperature in Sr_2IrO_4.

scattered beam.

Sr_2IrO_4 single crystals have been prepared at the University of Edinburgh following the standard self-flux technique [32]. The crystal mosaic, determined from the full-width at half-maximum (FWHM) of the θ scan across the (0 0 24) specular reflection, was determined to be 0.02° (See Fig. 3.3).

With the incident energy tuned at the Ir L_3 edge (11.217 keV) and well below the expected magnetic transition temperature (T= 10 K), we have explored an extended region of reciprocal space looking for magnetic peaks in the σ-π scattering channel. Magnetic Bragg reflections were observed at $(0\,1\,4n+2)$ and $(1\,0\,4n)$ positions (See Fig. 3.4), which implies that the magnetic moments in the IrO_6 layers are mainly aligned antiferromagnetically[1]. The canting of the moments by an angle ϕ yields a small ferromagnetic (FM) moment within a layer, which orders in a up-down-down-up sequence along the c axis, generating magnetic scattering intensity at the $(0\,0\,2n+1)$ positions (see Fig. 3.4). This can be easily verified by calculating the squared magnetic structure factor for the system. Taking into account the position of the eight magnetic atoms that form the unit cell (see Fig 3.7) this is

---

[1] It should be noted that the charge $(0\,1\,4n+2)$ and $(1\,0\,4n)$ reflections are not allowed in the $I4_1/acd$ space group.

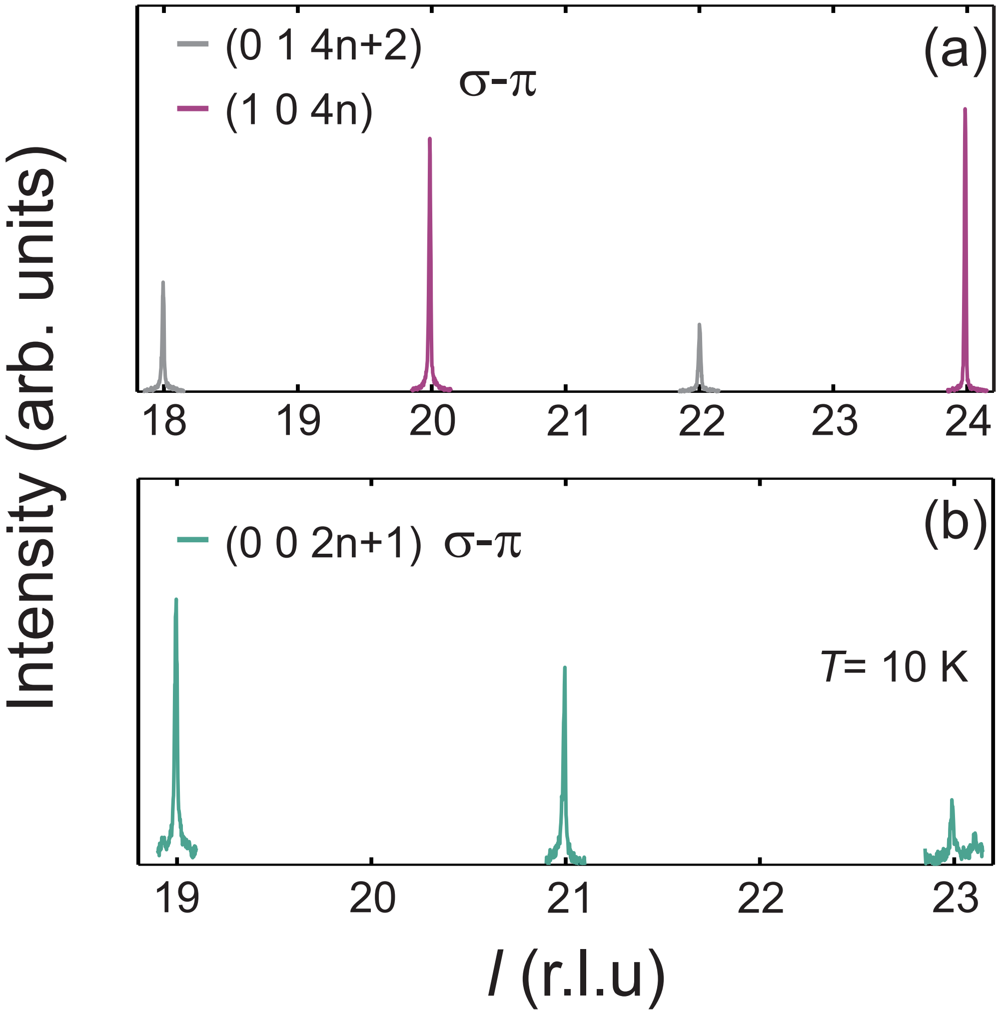

Figure 3.4: l-scan profile of XRMS along the $(0\,1\,l)$ (grey line) and $(1\,0\,l)$ (purple line) directions (a) and the $(0\,0\,l)$ direction (b) at $T = 10$ K, Ir L_3 edge.

$$
\begin{aligned}
|\mathcal{F}_{\mathbf{K}}|^2 = \left|\sum_j e^{2\pi i \mathbf{K}\cdot\mathbf{r}_j}\right|^2 &= \begin{cases} \left|2\left(1+e^{\frac{il\pi}{2}}\right)\left(1+e^{il\pi}\right)\cos\phi\right|^2 & \text{for } \mathbf{K} = (1\,0\,4n), \\ \left|2\left(1-e^{\frac{il\pi}{2}}\right)\left(1+e^{il\pi}\right)\cos\phi\right|^2 & \text{for } \mathbf{K} = (0\,1\,4n+2), \\ \left|-2\left(-1+e^{\frac{il\pi}{2}}\right)^2\left(1+e^{\frac{il\pi}{2}}\right)\sin\phi\right|^2 & \text{for } \mathbf{K} = (0\,0\,2n+1) \end{cases} \\
&= \begin{cases} 64\cos^2\phi & \text{for } \mathbf{K} = (1\,0\,4n), \\ 64\cos^2\phi & \text{for } \mathbf{K} = (0\,1\,4n+2), \\ 32\sin^2\phi & \text{for } \mathbf{K} = (0\,0\,2n+1) \end{cases}
\end{aligned}
\tag{3.1}
$$

in agreement with the observed magnetic reflections. Clearly the intensity of the $(0\,0\,2n+1)$ reflections is much weaker than the $(0\,1\,4n+2)$ and

$(1\,0\,4n)$ basal-plane AF reflections, being the FM component only a fraction of the total moment. In the absence of canting ($\phi \to 0$) the magnetic scattering intensity at the $(0\,0\,2n+1)$ positions will ultimately disappear. The analysis of the FM component will be the main subject of Section 3.2.3.

These results confirm the first XRMS study by Kim et al. [14]. In this study the magnetic structure in an applied magnetic field was also explored. When the applied field in the *ab*-plane is greater than a critical value $H_C = 0.2$ T, the magnetic structure changes. The magnetic peaks at $(0\,1\,4n+2)$ are substituted by peaks at the $(0\,1\,2n+1)$ positions and the canting-derived component aligns in a ferromagnetic way in the planes generating a macroscopic field. As a consequence the $(0\,0\,2n+1)$ magnetic peaks disappear too. This magnetic structure unambiguously explains the weak ferromagnetism observed in bulk measurements (see Fig. 3.2 (b)).

Examples of the basal-plane antiferromagnetic peaks at the $(1\,0\,24)$ position are shown in Fig. 3.5(a) in reciprocal lattice units (r.l.u.). σ-π intensity is shown by solid blue circles and σ-σ by open green diamonds. As expected from magnetic scattering probed through electric dipole transitions (see Section 2.2.1), the signal appears only in the rotated polarization channel σ-π. From a comparison with a nearby charge peak, we conclude that the magnetic peaks are at the resolution limit in the momentum space establishing the long-range nature of the magnetic order.

The magnetic nature of the observed reflections is further confirmed by the energy scan in proximity of the Ir L_3 edge. Fig. 3.5 (b) shows the resonant enhancement of the $(1\,0\,24)$ reflection at the Ir L_3 edge at $T = 90$ K. This data are not corrected for self-absorption since no absorption spectrum was taken during the magnetic scattering measurements. The energy dependence of the magnetic Bragg peak shows a Lorentzian shape (FWHM = 6.26(9) eV), typical of dipole-dipole transitions. It should be noted that the FWHM decreases slightly when absorption corrections are taken into account. The resonant behaviour and the width of the resonance are in agreement with the previous XRMS study [14].

The temperature evolution of the staggered magnetization and the onset of long-range antiferromagnetic order was monitored by means of $\theta - 2\theta$ scans across the $(1\,0\,24)$ magnetic reflection as a function of temperature,

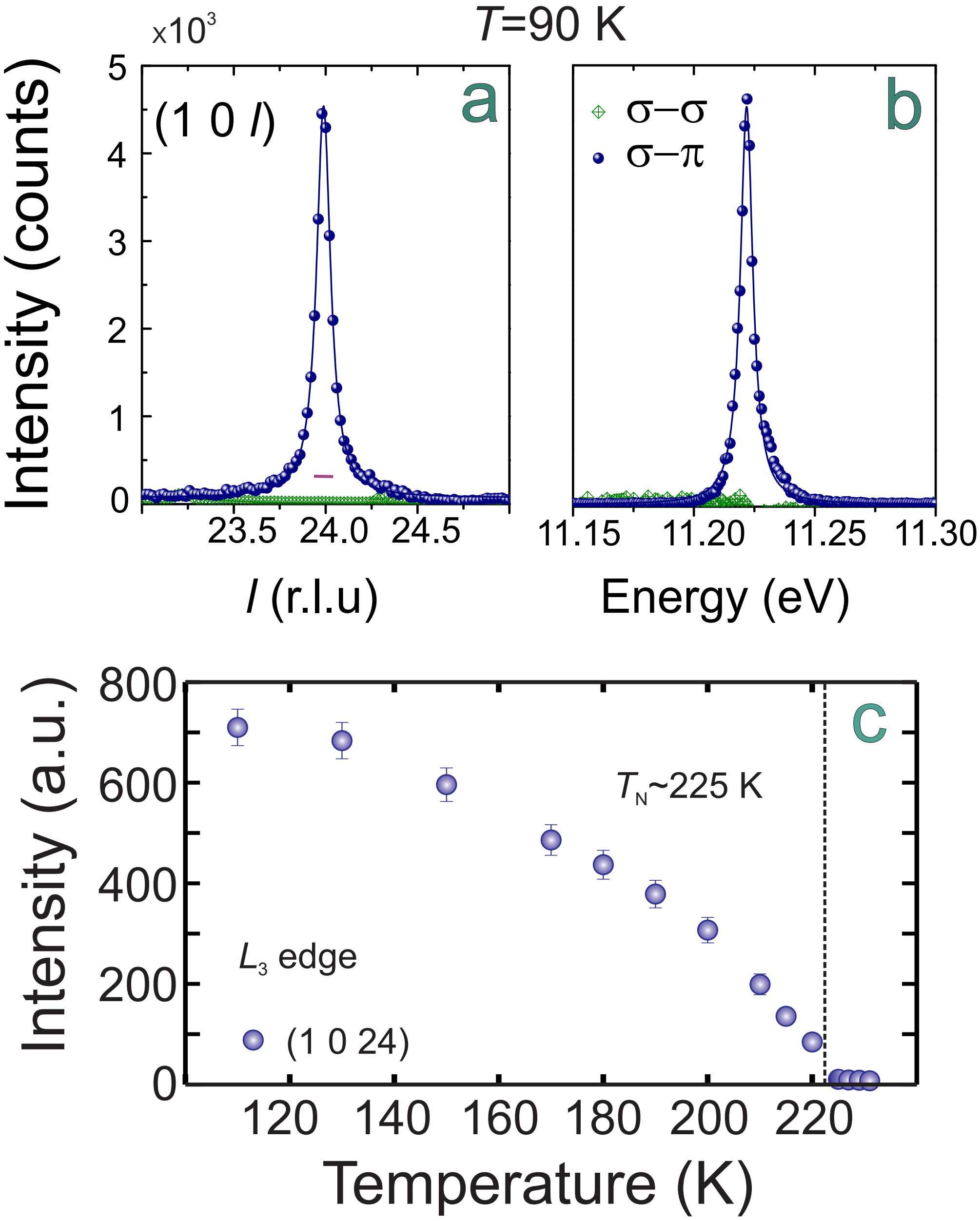

Figure 3.5: Reciprocal space l-scan (a) and energy dependence (b) of the XRMS intensity of the (1 0 24) reflection in Sr_2IrO_4. The blue line is a fit to a Lorentzian function. The purple line is the momentum resolution calculated from a nearby charge reflection. (c) The temperature dependence of the (1 0 24) magnetic reflection in Sr_2IrO_4.

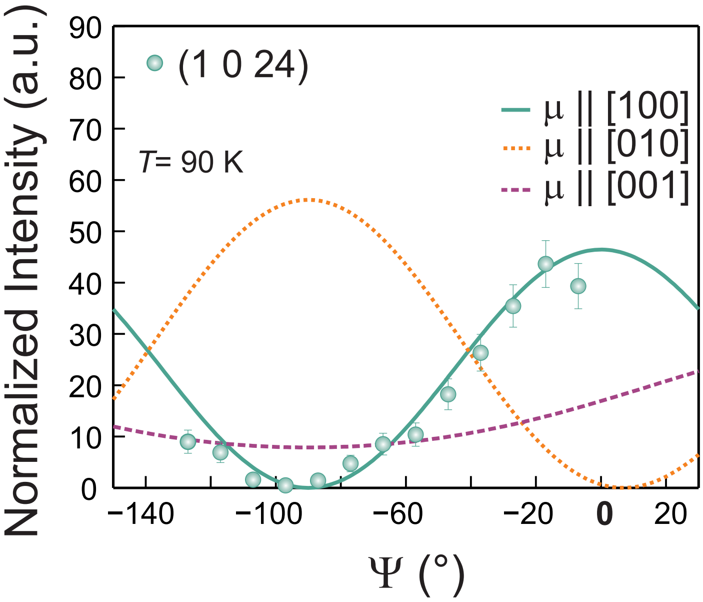

Figure 3.6: The azimuthal dependence of the (1 0 24) magnetic reflection (solid light green spheres) in Sr$_2$IrO$_4$, $T = 90$ K. The lines are the azimuthal dependencies calculated for three different antiferromagnetic structures where the magnetic moments are pointing along the [1 0 0] (light green line), [0 1 0] (dotted orange line), and [0 0 1] (dashed purple line) directions, respectively. The azimuthal angle Ψ is defined with respect to the reference vector [1 0 0].

in the σ-π channel. Fig. 3.5 (c) shows the integrated intensity obtained by fitting a Lorentzian peak shape to the individual scans as a function of temperature. The transition appears to be second order and a long-ranged antiferromagnetic order is realized below the Neel temperature $T_{\mathrm{N}} \sim 225$ K. At this temperature, the onset of the weak ferromagnetism is observed in bulk measurements (See Fig. 3.2(b)), as expected from ferromagnetism derived from the canting of the antiferromagnetic structure.

Having determined the relative phase between the Ir magnetic moments we now focus on the moment direction of the dominant antiferromagnetic structure, i.e. the (1 0 4n+2) and (0 1 4n) type of reflections. This point is particularly relevant since theory makes precise predictions on the moment direction in layered perovskite iridates (see for instance Fig. 1.7). Furthermore, as treated in detail in Section 2.3, the XRMS cross-section is highly dependent on the moment direction. As mentioned in Section 2.2.1, a powerful tool to establish the moment directions are azimuthal scans. This method consists of measuring rocking curves of the sample for different Ψ angles, rotating the sample around the scattering vector. From the azimuthal modulation of the intensity of the XRMS signal it is possible, under favourable circumstances, to determine the orientation of the magnetic moments in an antiferromagnetic material.

Fig. 3.6 shows the azimuthal dependence of the antiferromagnetic reflection (1 0 24) (light green spheres) together with the azimuthal dependence calculated from Eq. 2.33 for three different antiferromagnetic arrangement: $\boldsymbol{\mu}\|[1\,0\,0]$ (light green line), $\boldsymbol{\mu}\|[0\,1\,0]$ (dotted orange line), and $\boldsymbol{\mu}\|[0\,0\,1]$ (dashed purple line), respectively. Experimental data are corrected for self absorption using Eq. 3.2. The azimuthal angle Ψ is defined with respect to the reference vector $[1\,0\,0]$. By close inspection of Fig. 3.6 we conclude that the dominant antiferromagnetic component in Sr_2IrO_4 points along the $[1\,0\,0]$ direction. We note that XRMS does not couple to the canting of the moments since the latter can be seen as a in-plane ferromagnetic component of the magnetic structure. As a consequence, this scattering mechanism occurs in the same position in the reciprocal lattice as the charge scattering and cannot be observed in (1 0 24)-type reflections. In the next Section we will describe a way to utilize XRMS to measure the canted component.

Our finding that the magnetic moments in Sr_2IrO_4 mainly point along the a axis have profound implications on the REXS cross-section for Ir ions in a octahedral cage. In fact, as seen in Section 2.3 (Eq. 2.61), when the magnetic moments are in the ab-plane, the REXS cross-section in the rotated polarization channel is identically zero irrespective of the tetragonal crystal field, implying that the $j_{\text{eff}} = 1/2$ state cannot be deduced from the analysis of the L_2/L_3 XRMS intensity ratio.

The realization of the $j_{\text{eff}} = 1/2$ state in Sr_2IrO_4 has however been confirmed with complementary techniques such as angle resolved photoemission spectroscopy (ARPES), oxygen K-edge XAS and RIXS [19, 72, 73].

3.2.3 Determining the canting angle using XRMS

The work presented in this section has been published as "*Locking of iridium magnetic moments to the correlated rotation of oxygen octahedra* *in Sr_2IrO_4 revealed by X-ray resonant scattering*" by S. Boseggia, H. C. Walker, J. Vale, R. Springell, Z. Feng, R. S. Perry, M. Moretti Sala, H. M. Rønnow, S. P. Collins and D. F McMorrow, J. Phys.: Condens. Matter **25**, 422202 (2013) [39].

As we have shown in Chapter 2, XRMS is a powerful tool to study the orbital state, and in particular the spin-orbit entangled wave function that distinguishes iridates. However, in the case of magnetic moments lying in the basal–plane, the $j_{\text{eff}} = 1/2$ state cannot be inferred from a simple analysis of the L_2/L_3 XRMS intensity ratio. An insight of the true nature of the ground state can instead be achieved by a complete understanding of its magnetic structure. In fact, theory makes accurate predictions on the magnetic ordering in Sr_2IrO_4 which can be tested using XRMS [23]. In our first study we established that in Sr_2IrO_4 the moments lie in the basal plane and form a canted antiferromagnetic (AF) structure. Employing azimuthal scans of magnetic Bragg peaks we have shown that the AF component of the moment is along the a axis in the $I4_1/acd$ reference system [16]. We now address the issue of determining the magnitude of the canting angle ϕ, which has also been discussed in a recent neutron diffraction investigation [40].

From the theoretical point of view, the determination of the canting angle places a strong constraint on the Hamiltonian and the theoretical model of perovskite iridates. As shown in Section 1.5, an effective Hamiltonian including the both tetragonal crystal field (Δ) and octahedral rotation (ρ) has been derived by Jackeli and Khaliullin [23]. According to this model, in the strong SOI limit (for $\Delta \to 0$), the ratio of the magnetic moment canting angle to the IrO_6 octahedral rotation (ϕ/ρ) approaches unity (see Fig. 1.7).

From the theoretical point of view, a strong link between the crystal and magnetic structure is predicted. Due to strong spin-orbit coupling and the tilting of the IrO_6 octahedra, a Dzyaloshinsky-Moriya (DM) interaction arises. However, the anisotropy of the single-layer compound can be gauged away by proper site-dependent spin rotations. The twisted Hubbard model can then be mapped onto a SU(2)-invariant pseudospin-1/2 system, being isostructural with, for instance, the close relative Ba_2IrO_4. In this latter compound, the straight Ir-O-Ir bonds preserve inversion symmetry so that the system shows a simple basal-plane antiferromagnetic structure as we will show in Section 3.3.2 [16]. In the case of Sr_2IrO_4, to obtain the magnetic structure of the twisted system, we have to transform the isotropic system back. As a result, the spins are canted exactly like the IrO_6 octahedra. The proposed magnetic structure of Sr_2IrO_4, illustrated in Figure 3.7, can be decomposed into a basal-plane antiferromagnetic sublattice A, where the moments are pointing along the $[1\,0\,0]$ direction, and a net b-axis ferromagnetic moment due to canting of Ir magnetic moments, that generates a stacked antiferromagnetic structure $(-++-)$ along the c axis (sublattice B). The A sublattice is responsible for the $(1\,0\,4n)$ and $(0\,1\,4n{+}2)$ magnetic peaks, and the B for the $(0\,0\,2n{+}1)$ magnetic peaks. The relative intensity of the magnetic reflections associated with the two magnetic sublattices is ultimately linked to the projection of the magnetic moment on the a and b axes, respectively. In the total absence of the b-axis ferromagnetic component, the intensity of the $(0\,0\,2n{+}1)$ magnetic reflection vanishes, as is the case for Ba_2IrO_4 [16]. It is therefore possible to infer the direction of Ir magnetic moments from the comparison between a theoretical model for the magnetic moments and the measured intensity ratio $\mathcal{I}_\mathrm{A}/\mathcal{I}_\mathrm{B}$ between several magnetic reflections.

With the energy of the incoming photons tuned to the Ir L_3 edge we measured several magnetic peaks along the $(1\,0\,4n)$, $(0\,1\,4n{+}2)$, and $(0\,0\,2n{+}1)$ directions in the σ-π polarization channel at $T = 10$ K. θ-2θ scans of each magnetic peak were numerically integrated and corrected for self-absorption by multiplying the observed intensity by the factor:

$$Abs(\mathbf{K},\psi) = 1 + \frac{\sin\alpha(\mathbf{K},\psi)}{\sin\beta(\mathbf{K},\psi)}, \tag{3.2}$$

where $\alpha(\mathbf{K},\psi)$ and $\beta(\mathbf{K},\psi)$ are respectively the incident and exit angle with respect to the $(0\,0\,1)$ sample surface. The results as a function of the reciprocal lattice direction l are plotted in Fig. 3.8. In order to interpret the experimental data, and to extract the canting angle of Ir magnetic moments, we calculated the resonant scattering cross section for the magnetic moment arrangement of Fig. 3.7. Following the formalism described

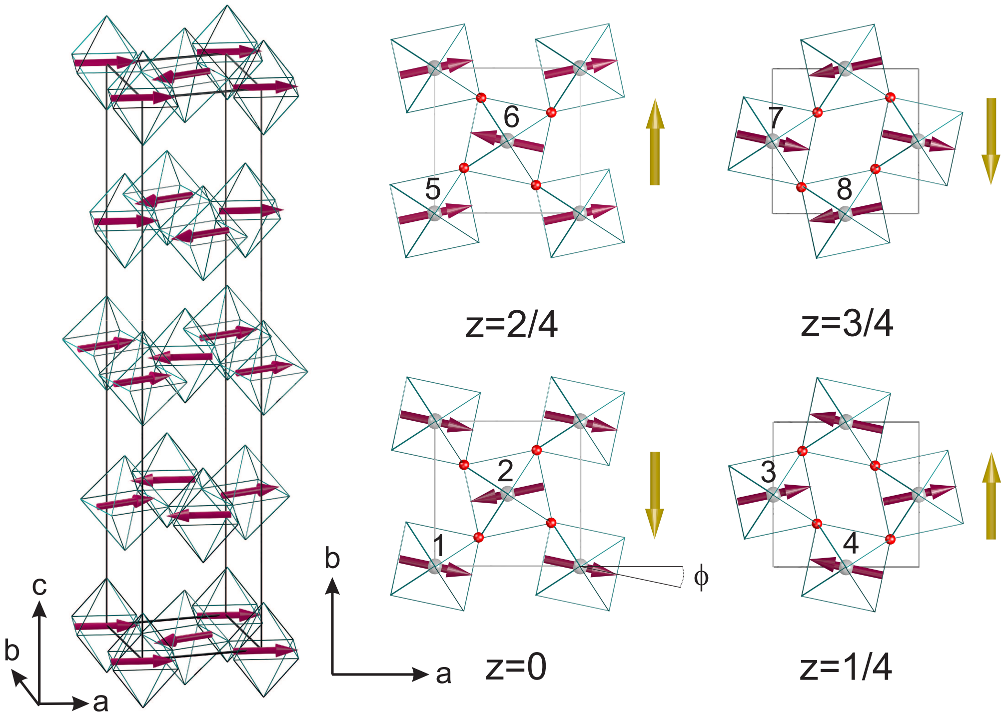

Figure 3.7: Left panel: *ab*-plane canted magnetic structure of $\mathrm{Sr_2IrO_4}$. The magnetic moment canting angle follows the octahedral rotations rigidly. Right panel: Magnetic stacking pattern along the *c* axis. Sites 1-8 in the space group $I4_1/acd$ (#142, origin choice 1) for the Ir ions were used to calculate the XRMS cross section. Ir magnetic moments are canted by an angle ϕ from the *a* axis. The golden arrows represent the canting-derived ferromagnetic component.

in Section 2.2.1 (Eq. 2.25) we can write the E1-E1 resonant magnetic scattering amplitude as:

$$\mathcal{A}^{\mathrm{XRMS}}_{j\mathrm{E1}} = -iF^{(1)}_{\mathrm{E1}}(\boldsymbol{\epsilon}' \times \boldsymbol{\epsilon}) \cdot \hat{\mathbf{z}}_j \tag{3.3}$$

where $\boldsymbol{\epsilon}$ ($\boldsymbol{\epsilon}'$) is the incoming (scattered) X-ray linear polarization orientation, and $\hat{\mathbf{z}}_j$ is a unit vector in the direction of the Ir magnetic moments (see Fig. 2.2). $F^{(1)}_{\mathrm{E1}}$ are coefficients dependent on the electronic transitions that determine the strength of the resonant process [48].

We can then calculate the magnetic scattering amplitude for the Ir magnetic moments pointing along the *a* axis (sublattice A) as:

$$\mathcal{A}^{\mathrm{XRMS}}_{j\mathrm{E1}_{\mathrm{A},(104n)}} \propto i\hat{\mathbf{z}}_j \cos\phi\,(\cos\xi\cos\theta\cos\psi + \sin\theta\sin\xi) \tag{3.4}$$

and

$$\mathcal{A}^{\mathrm{XRMS}}_{j\mathrm{E1}_{\mathrm{A},(014n+2)}} \propto i\hat{\mathbf{z}}_j \cos\phi \cos\psi \cos\theta, \tag{3.5}$$

and the magnetic scattering amplitude for the Ir magnetic moments pointing along the b-axis as

$$\mathcal{A}^{\mathrm{XRMS}}_{j\mathrm{E1}_{\mathrm{B}}} \propto i\hat{\mathbf{z}}_j \sin\phi \sin\psi \cos\theta, \tag{3.6}$$

where ϕ is the canting angle as defined in Fig.3.7, ψ is the azimuthal rotation about the scattering vector $\mathbf{Q}$, θ is the Bragg angle, and ξ is the angle between the scattering vector $\mathbf{Q}$ and the c axis. The total scattering cross section is then calculated as the squared modulus of the amplitude, taking into account the phase factor deriving from the magnetic structure factor as

$$\mathcal{I} \propto \left| \sum_j e^{2\pi i \mathbf{K}\cdot\mathbf{r}_j} \mathcal{A}^{\mathrm{XRMS}}_{j\mathrm{E1}} \right|^2, \tag{3.7}$$

where $\mathbf{K}$ is the scattering vector and $\mathbf{r}_j$ is the crystallographic coordinate of the jth Ir ion. The positions of the eight Ir ions over which the sum runs are illustrated in Fig. 3.7. We can now calculate the resonant cross section for the reflections of the two magnetic sublattices as:

$$\mathcal{I}_{\mathrm{A},(104n)} \propto \left| +2\left(1+e^{\frac{i\pi l}{2}}\right)\left(1+e^{i\pi l}\right) i\hat{\mathbf{z}}_j \cos\phi \left(\cos\xi\cos\theta\cos\psi + \sin\theta\sin\xi\right)\right|^2, \tag{3.8}$$

$$\mathcal{I}_{\mathrm{A},(014n+2)} \propto \left| -2\left(-1+e^{\frac{i\pi l}{2}}\right)\left(1+e^{i\pi l}\right) i\hat{\mathbf{z}}_j \cos\phi\cos\psi\cos\theta\right|^2, \tag{3.9}$$

and

$$\mathcal{I}_{\mathrm{B}} \propto \left| -2\left(-1+e^{\frac{i\pi l}{2}}\right)^2\left(1+e^{\frac{i\pi l}{2}}\right) i\hat{\mathbf{z}}_j \sin\phi\sin\psi\cos\theta\right|^2. \tag{3.10}$$

Fig. 3.8(b) shows the comparison between the calculated intensity ratio $\mathcal{I}_{\mathrm{A}}/\mathcal{I}_{\mathrm{B}}(\phi)$ and the experimental value for five different magnetic reflections: (1 0 24), (0 1 22), (0 1 18) associated with sublattice A, and (0 0 19), (0 0 21), and (0 0 23) associated with the canting-induced magnetic sublattice B. The azimuthal angle was kept fixed at 220° from the a axis. From the intersection between the calculated $\mathcal{I}_{\mathrm{A}}/\mathcal{I}_{\mathrm{B}}(\phi)$ curves and the observed value we can deduce the canting angle of the Ir magnetic moments.

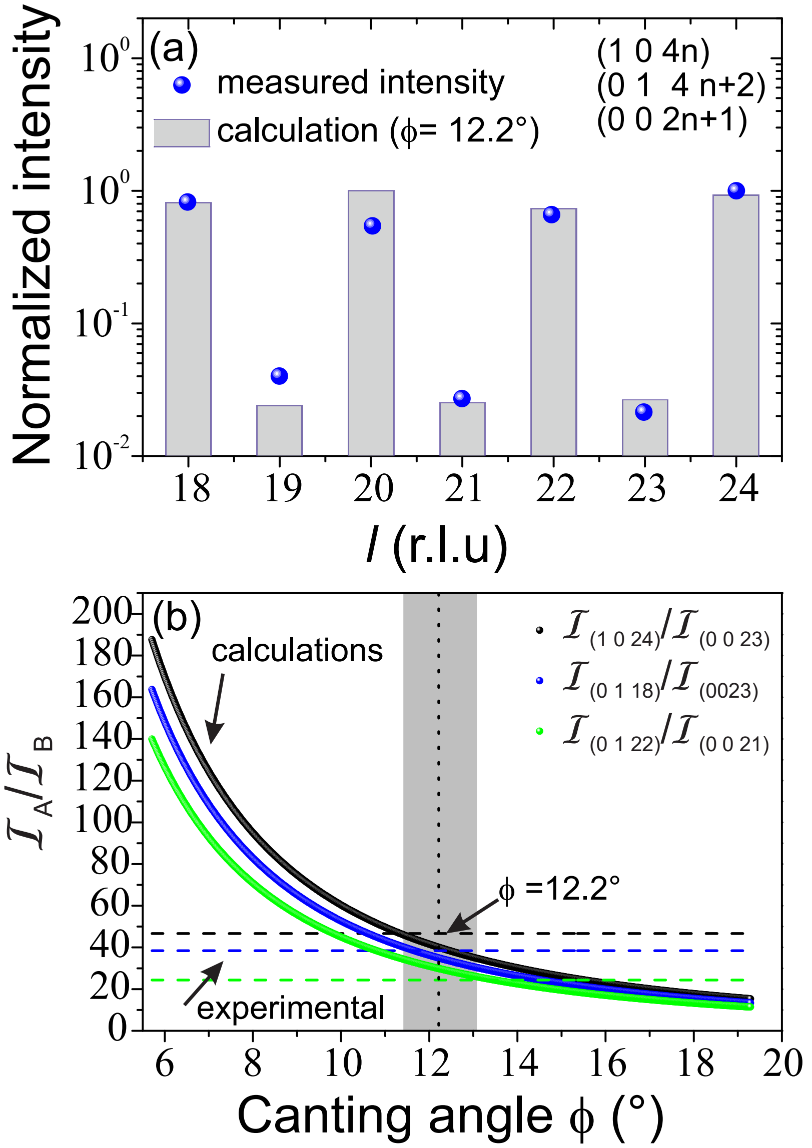

Figure 3.8: (a) l-scan across the $(1\,0\,4n)$, $(0\,1\,4n{+}2)$, and $(0\,0\,2n{+}1)$ reflections at $T = 10\,\mathrm{K}$ at the Ir L_3 edge. The blue spheres represent the integrated intensity of the measured magnetic scattering corrected for absorption as discussed in the text. The heights of the light blue bars represent the calculated intensity for the magnetic moment arrangement of Figure 3.7(c) for a canting angle $\phi = 12.2°$. (b) Intensity ratio ($\mathcal{I}_\mathrm{A}/\mathcal{I}_\mathrm{B}$) between the a-axis in-plane antiferromagnetic reflections (magnetic sublattice A) and the b-axis canting-induced magnetic reflections (magnetic sublattice B) calculated as a function of the canting angle ϕ (solid points). The dashed lines are the experimental intensity ratios at the Ir L_3 edge.

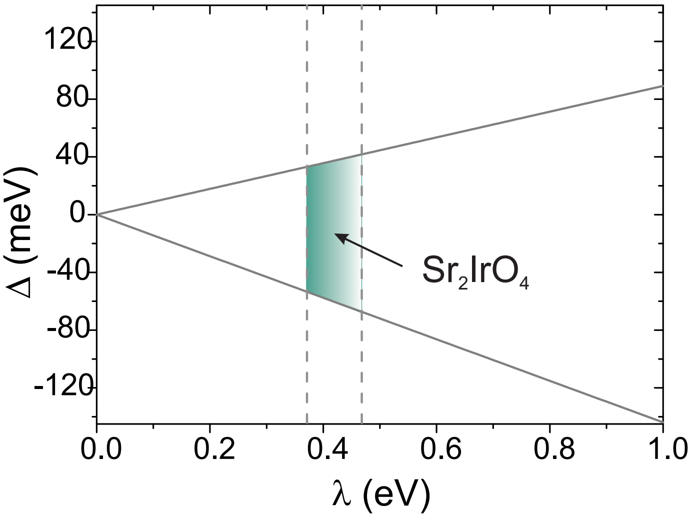

Figure 3.9: Tetragonal crystal field parameter (Δ) as a function of the spin-orbit coupling λ. The boundaries of the tetragonal crystal field were obtained from the Hamiltonian of [23] using, as an input parameter, the error bar in the canting angle ϕ obtained from the present study. The shaded area represents the error in the determination of ϕ as calculated from the standard deviation.

A deviation from the a axis by 12.2(8)° is obtained averaging the canting angle associated with the three intensity ratios $\mathcal{I}_{(1\,0\,24)}/\mathcal{I}_{(0\,0\,23)}$, $\mathcal{I}_{(0\,1\,18)}/\mathcal{I}_{(0\,0\,23)}$, and $\mathcal{I}_{(0\,1\,22)}/\mathcal{I}_{(0\,0\,21)}$ (see Fig. 3.8(b)). We therefore conclude that, within the experimental error, the magnetic moments in Sr_2IrO_4 follow the octahedral rotations rigidly. We note that we cannot determine the sign of the canting angle ϕ from our analysis. Based on the prediction of theoretical models for iridate perovskites, we exclude that the Ir moments could rotate in antiphase with the oxygen octahedra. Our findings therefore support the Hamiltonian derived by Jackeli and Khaliullin [23] for layered iridates in the strong SOC limit. In fact, according to their theoretical model, when the tetragonal crystal field is not strong enough to modify the $j_{\text{eff}} = 1/2$ state, magnetic and crystal structures are intimately related resulting in a perfect equivalence of the magnetic moment and octahedral rotation angles ($\phi = \rho$). This significant coupling between magnetic and structural degrees of freedom suggests the existence of a strong magnetoelastic effect, already observed in Sr_2IrO_4 [74, 75].

Extending further our analysis, the Hamiltonian 1.48 allows us to estimate the magnitude of the DM interaction. If we consider two Ir ions (for instance Ir 1 and Ir 2 of Fig. 3.7), the point bisecting the straight line connecting the two ions lies on a 2-fold axis pointing along the [1 1 0] direction. According to the fourth rule by Moriya [76], the DM vector in Sr_2IrO_4 should point perpendicular to the two-fold axis and therefore along the c axis: $\mathbf{D}_{ij} = (0\,0\,D_z)$. From the exchange Hamiltonian of Eq. 1.48 the canting angle is determined by the ratio D_z/J as $\tan(2\phi) = D_z/J$. Using a superexchange parameter $J = 60$ meV, as extracted from RIXS measurements [72], we obtain $|\mathbf{D}| \approx 27$ meV, a value in excellent agreement with recent calculations [77, 78], and almost ten times larger than that in the single layer cuprate La_2CuO_4 [79]. This enormous value of the DM interaction is certainly a consequence of the strong spin-orbit coupling that characterizes the $j_{\text{eff}} = 1/2$ state. In fact, the DM interaction is remarkably reinforced by the strong SOC and the antiferrommagnetic superexchange via the equation $\mathbf{D} \sim \lambda J/\Delta E$, where ΔE is the first excitation energy for antisymmetric exchange interaction [34].

Furthermore, using the error bar in the determination of the canting angle ϕ as an input parameter, together with the model Hamiltonian 1.48, we can set constraints on the effective tetragonal crystal field affecting the Ir^{4+} ground state. Figure 3.9 shows the tetragonal crystal field parameter Δ as a function of the SOI constant λ. For a typical value of $\lambda = 420(5)$ meV in iridates [16, 65, 80], we find $-60\,\text{meV} \leq \Delta \leq 35\,\text{meV}$, a value too small to induce a significant deviation from the pure $j_{\text{eff}} = 1/2$ picture in Sr_2IrO_4. The measured canting angle $\phi = 12.2°$ corresponds to a tetragonal crystal field $\Delta = -12$ meV. Adopting a pure ligand-field theory approach, this result could appear surprising. In fact, due to an elongation of the IrO_6 octahedra along the c axis (4%), one should expect a positive tetragonal crystal field acting on the t_{2g} manifold. However, this is a local approach which considers only the nearest-neighbours ligands, and long-range crystalline anisotropy is completely neglected. A recent LDA + DMFT calculation, which takes into account also many-body effects, shows that the effective crystal field goes exactly in this direction and that an additional elongation of the c axis is required to recover the SU(2)limit [43]. Our findings suggest that the role of longer-range crystalline anisotropy could be fundamental in generating non-cubic potentials that compete with local distortions of the ligand cage, an aspect not included in ligand-field theory.

Another possible mechanism that could in principle explain the locking of the magnetic moments to the octahedral rotation is the single-ion anisotropy. This effect has found to be negligible in this system by recent *ab initio* calculations [81, 43]. Furthermore, the single-ion anisotropy breaks the rotational symmetry of the in-plane spin components by selecting a local easy axis, whereas DM does not. Sr_2IrO_4 susceptibility data show no detectable in-plane anisotropy[32], thus supporting the DM scenario.

3.3 Magnetic and electronic properties of Ba_2IrO_4

The work presented in this section has been published as “*Robustness of Basal-Plane Antiferromagnetic Order and the* $j_{\text{eff}} = 1/2$ *State in Single-Layer Iridate Spin-Orbit Mott Insulators*” by S. Boseggia, R. Springell, H. C. Walker, H. M. Rønnow, Ch. Rüegg, H. Okabe, M. Isobe, R. S. Perry, S. P. Collins, and D. F. McMorrow, Phys. Rev. Lett. **110**, 117207 (2013) [16].

Ba_2IrO_4 is a close relative of Sr_2IrO_4. Its synthesis involves more difficult procedures in high pressure press. As a consequence is much less common and studied. In this section we will first introduce Ba_2IrO_4 general properties. We then present a detailed XRMS study that unravels for the first time its magnetic structure. Finally, by a comparison between Ba_2IrO_4 and Sr_2IrO_4 we will show how the $j_{\text{eff}} = 1/2$ state evolves as a function of local symmetry and structural distortions.

3.3.1 General overview

Ba_2IrO_4 was first synthesized by Okabe et al. [34] in 2010. It crystallizes in the K_2NiF_4-type structure (space group I4/*mmm*), and it is therefore a closer 5*d* structural analogue of La_2CuO_4 than the Sr compound. A comparison of the crystal structures of Ba$_2$IrO$_4$ and Sr$_2$IrO$_4$ is shown in Fig. 3.10. The crystal structure of Sr$_2$IrO$_4$ (space group I4$_1$/acd) is obtained from the one of Ba$_2$IrO$_4$ by rotating the Ba$_2$IrO$_4$ unit cell cell by 45°. This generates a larger unit cell: $\sqrt{2}a \times \sqrt{2}b \times 2c$. The inset of Fig. 3.10(a) demonstrates the equivalence of the [1 1 0] in the I4/mmm space group with the [1 0 0] direction in I4$_1$/acd by means of a two-dimensional projection onto the basal plane of the unit cell.

The basal-plane crystal structure of the two compounds is rather different. While in Sr$_2$IrO$_4$ the IrO$_6$ octahedra undergo an alternated correlated rotation about the c axis which produces a 156° Ir-O-Ir bonds, Ba$_2$IrO$_4$ has perfectly straight Ir-O-Ir bonds with no octahedral rotation (see Fig. 3.10(b)). Furthermore, in Ba$_2$IrO$_4$, the Ir–O apical distance is 2.155(8) Å, exceeding the in-plane Ir-O length (2.0155(6) Å). This indicates that the tetragonal distortion of the IrO$_6$ cage in Ba$_2$IrO$_4$ ($\sim$7%) almost doubles the relative distortion in Sr$_2$IrO$_4$ ($\sim$4%) (see Fig. 3.10(c)).

These significant structural differences have important implications on the respective magnetic and electronic properties of the two compounds. From the theoretical point of view, in fact, a strong link between the tetragonal distortion, the presence or otherwise of octahedral rotations, and the magnetic structure of single layer iridates is expected. First, as we have shown in Section 1.4.1, it should be noted that the $j_{\text{eff}} = 1/2$ state itself is only strictly realized in a system of cubic symmetry and that a spin flop transition from a basal-plane to a c-axis AF state is predicted when the tetragonal crystal field is greater than a critical value (see Fig. 1.7). Second, the DM interaction, responsible for a canted AF state in Sr$_2$IrO$_4$ is not allowed in Ba$_2$IrO$_4$. Ba$_2$IrO$_4$, in fact, crystallizes in the centrosymmetric space group I4/mmm. In this case, the in-plane ligand oxygen (4c) connecting two adjacent Ir ions has a site symmetry "mmm" and preserves inversion. This is consistent with the necessary and sufficient condition for the absence of the DM interaction: $\mathbf{D} = 0$ [76]. As we have already explored the consequences of these structural features for the electronic and magnetic properties of Sr$_2$IrO$_4$, a natural extension of our work is the study of the magnetic structure of Ba$_2$IrO$_4$. In addition, a comparative study of the magnetic structure of the two compounds can provide significant insights on the evolution of the $j_{\text{eff}} = 1/2$ state as a function of structural distortion.

In analogy with Sr_2IrO_4, Ba_2IrO_4 is a "spin-orbit driven" Mott insulator. Fig. 3.11(a) shows the temperature dependence of the electrical resistivity ρ for polycrystalline Ba_2IrO_4. The increasing of ρ with decreasing temperature indicates that Ba_2IrO_4 behaves like a small band gap insulator in analogy with the Sr counterpart. Recent ARPES measurements on Ba_2IrO_4 confirm the similarity between the electronic structure of the single layer iridates [82].

The magnetic structure of polycrystalline Ba_2IrO_4 has been investigated via bulk measurements and muon spin rotation (μSR) [34]. Ba_2IrO_4 is found to be an antiferromagnet below T_{N} ~240 K. This could be seen in Fig. 3.11(c) where the temperature dependence of the muon spin precession frequencies is shown. From the fit of the experimental data to a $f_1(T) = f(0)[1 - T/T_{\mathrm{N}}]^{\beta}$ function, the Néel temperature $T_{\mathrm{N}} = 243(1)$ K and the critical exponent $\beta = 0.18(1)$ can be extracted. In reality the non-zero muon signal below 240 K indicates only that there exists a coherent internal magnetic field induced by long-range ordered spins. The existence of weak ferromagnetism observed in Sr_2IrO_4 can be excluded on the basis of magnetic susceptibility measurements (Fig. 3.11(b)), in which no signal enhancement due to spontaneous magnetization was observed for the entire measured temperature range. The lack of a cusp typical of antiferomagnetic systems around T_{N} is attributed to the short range order nature of the quasi-2D magnet Ba_2IrO_4, where the spins are thought to be highly correlated but strongly fluctuating within each IrO_2 planes.

3.3.2 Magnetic structure: an XRMS study

In order to ascertain the nature of magnetism and the ground state of Ba_2IrO_4 we performed an XRMS study in proximity of the Ir $L_{2,3}$ edges. The experiment on a Ba_2IrO_4 single crystal was conducted at the I16 beamline of the Diamond Light Source, Didcot, UK. A vertical scattering geometry (σ incoming polarization) was exploited. On I16, X-rays were focussed to a beam size of 20×200 μm^2 (V×H) at the sample position. The sample was mounted in a Displex cryostat with the [1 1 0] and [0 0 1] directions (in the I4/*mmm* system) in the vertical scattering plane.

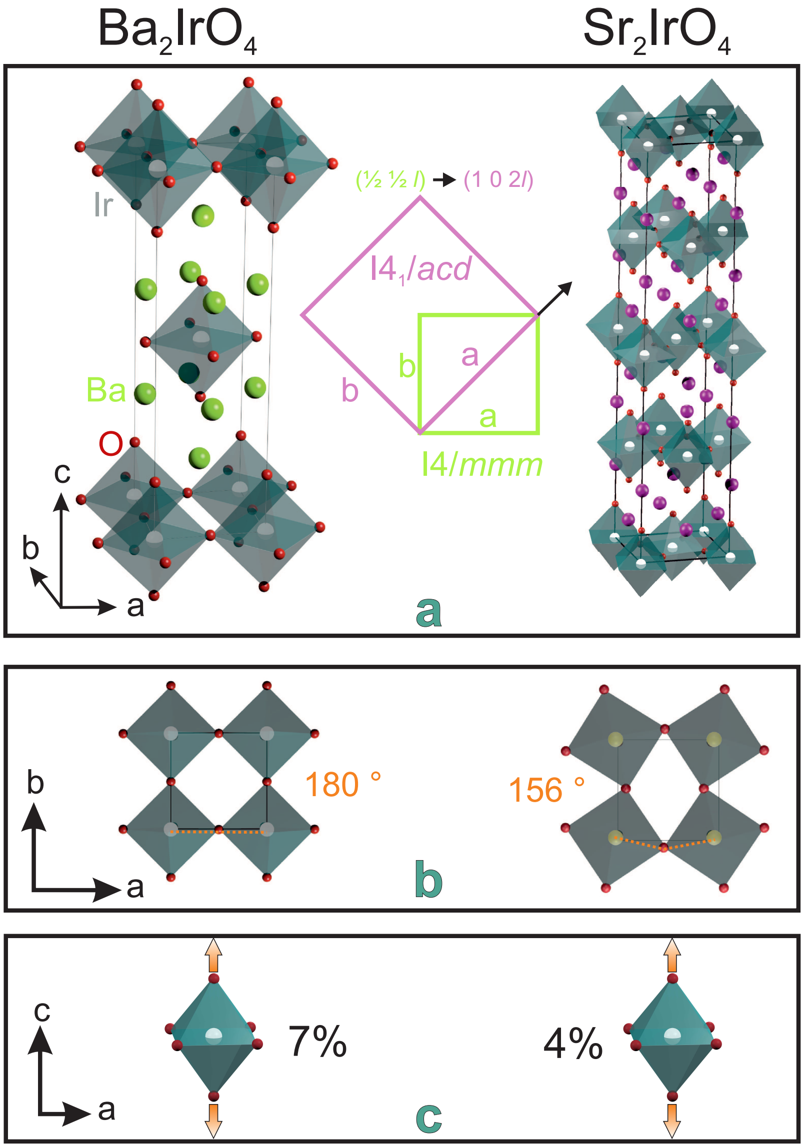

Figure 3.10: The crystal structure of Ba$_2$IrO$_4$ (space group I4/mmm, left panels) is compared to the crystal structure of Sr$_2$IrO$_4$ (space group I4$_1$/acd, right panels). Panel (a) shows the overall crystal structure of Ba$_2$IrO$_4$ and Sr$_2$IrO$_4$. The [1 0 0] direction in I4$_1$/acd corresponds to the [1 1 0] in the I4/mmm space group, as demonstrated in the inset by means of a two-dimensional projection onto the basal plane of the unit cell. Panel (b) shows the basal plane crystal structure. In contrast to Sr$_2$IrO$_4$, Ba$_2$IrO$_4$ possesses perfectly straight Ir-O-Ir bonds. (c) IrO$_6$ octahedra are elongated along the c axis by 7% in Ba$_2$IrO$_4$. This must be compared to a 4% elongation in Sr$_2$IrO$_4$.

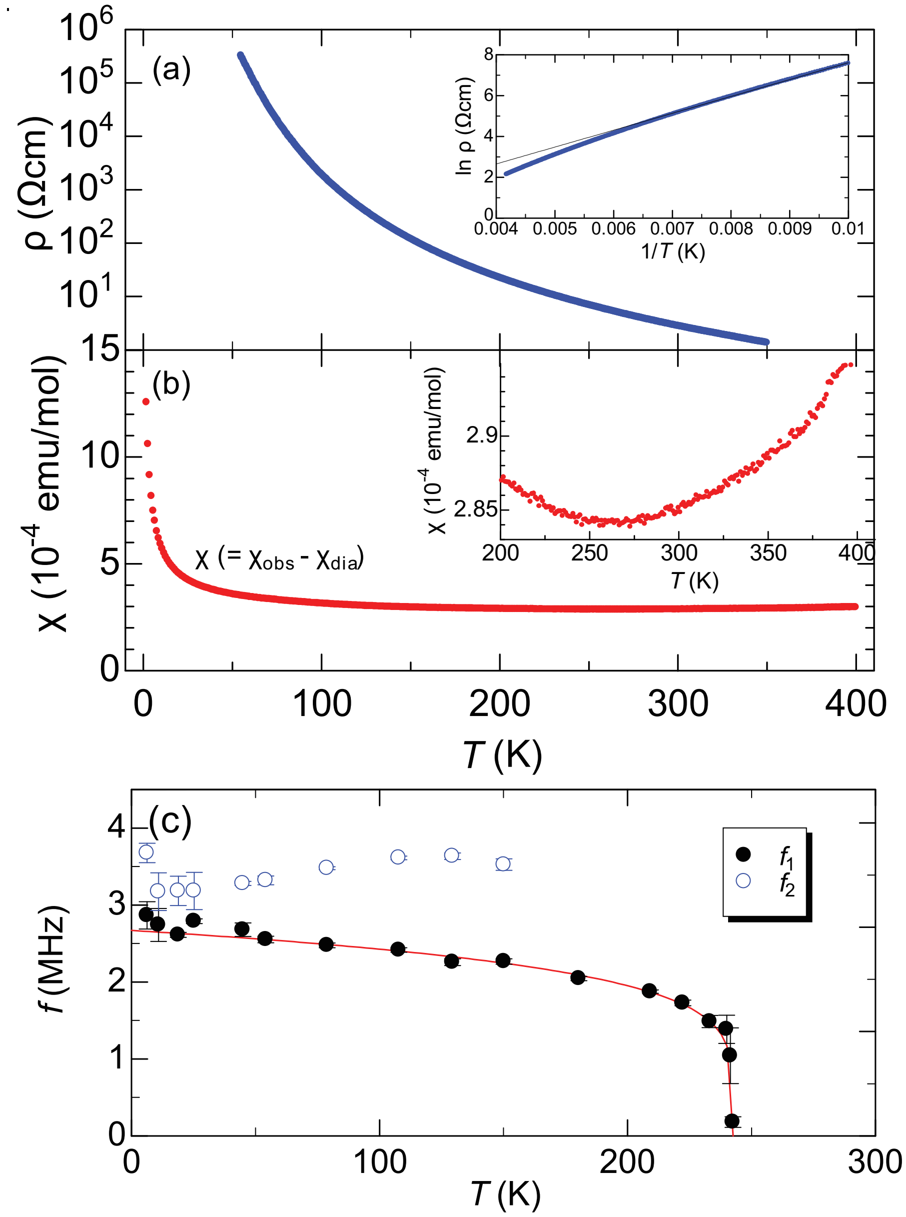

Figure 3.11: (a) Temperature dependence of electrical resistivity ρ for polycrystalline Ba$_2$IrO$_4$. The inset shows a $\ln\rho - 1/T$ plot. (b) Temperature dependence of magnetic susceptibility $\chi(=\chi_{obs} - \chi_{dia})$ for Ba$_2$IrO$_4$, where χ_{obs} is the raw data measured under $H = 1$ T and χ_{dia} ($\sim 1.42 \times 10^{-4}$ emu/mol) is the closed–shell diamagnetic susceptibility. The inset is a magnification of the $\chi - T$ curve around 300 K. (c) Temperature dependence of the muon spin precession frequencies f_i. The red line indicates numerical fit of the f_1 data using the equation $f_1(T) = f(0)[1 - T/T_{\mathrm{N}}]^{\beta}$, where $T_{\mathrm{N}} = 243(1)$ K, and $\beta = 0.18(1)$. Adapted from [34].

The incoming energy was tuned to 11.217 keV (L_3) and 12.831 keV (L_2) probing electric dipole transition from $2p_{3/2}$ and $2p_{1/2}$ to the $5d$ states, respectively. The polarization of the scattered beam was analyzed by means of a Au (3 3 3) crystal at both edges.

Single crystals of $\mathrm{Ba_2IrO_4}$ were prepared at the National Institute for Materials Science (NIMS), Japan, from the solid-state reaction of a stoichiometric mixture of $\mathrm{BaO_2}$ (99.9 %, Furuuchi Chemical Co., Ltd.) and Ir metal powder (99.96 %, Furuya Metal Co., Ltd.), enclosed in platinum capsules. During the crystal growth, the pressure was kept at 3 GPa and the temperature was gradually lowered from 1725 °C to 1625 °C for 6 hours before quenching to room temperature. The samples of size $\sim$ 200 μm $\times$ 200 μm $\times$ 200 μm, were initially checked with a Supernova X-ray diffractometer using a monochromatic Mo source at the Research Complex at Harwell (RCaH), Chilton, UK. The diffraction data are consistent with the I4/mmm space group and cell parameters $a = b = 4.0223(4)$ Å and $c = 13.301(3)$ Å at room temperature. However, a note of caution should be made regarding the sample stability. Single crystals of $\mathrm{Ba_2IrO_4}$ were found to degrade in presence of air, water, oxygen, etc. To prevent sample degradation, $\mathrm{Ba_2IrO_4}$ should be kept in a controlled atmosphere such as argon, nitrogen or in high vacuum.

Ordering wave vector

The crystal mosaic, determined from the full-width at half-maximum (FWHM) of the (0 0 14) specular reflection was 0.08°. With the photon energy tuned close to the L_3 edge (11.217 keV) and the sample cooled to 50 K, sharp peaks were found at the reciprocal lattice points $(\frac{1}{2}\,\frac{1}{2}\,l)$ with l even. These peaks existed in the rotated photon polarization channel σ-π only (see Fig. 3.12) as expected from the selection rules for XRMS arising from electric dipole transitions (see Eq. 2.25). We thus deduce that the Ir^{4+} magnetic moments order in an antiferromagnetic structure, with a doubling of the basal-plane unit cell, described by a magnetic propagation vector of $\mathbf{k} = [\frac{1}{2}\,\frac{1}{2}\,0]$. Examples of these peaks along the h (a), k (b), and l (c) directions at the $(\frac{1}{2}\;\frac{1}{2}\;8)$ position are shown in Fig. 3.12 in reciprocal lattice units (r.l.u.). σ-π intensity is shown by solid green circles and σ-σ by open purple triangle. From a comparison with a nearby charge peak, we conclude that the magnetic peaks are at the resolution limit in all three directions. From the half-width at half-maximum (HWHM) of the magnetic peaks we can determine the lower limit of the respective magnetic correlation length to be $\xi_{\mathrm{MAG}} = latt/(2\pi\ \mathrm{HWHM})$ (where *latt* is the lattice parameter), to be $\xi_{\mathrm{MAG}} \geq 120$, 178 and 155 Å along the a, b, c crystallographic directions, respectively.

It should be noted that since the $(\frac{1}{2}\,\frac{1}{2}\,l)$ reflections in the I4/*mmm* systems correspond to the $(1\,0\,2l)$ reflection in the $\mathrm{I4_1}/acd$ reference systems (see inset of Fig. 3.10(a)), Ba_2IrO_4 shows essentially the same antiferromagnetic structure as Sr_2IrO_4. However, the $(0\,0\,2n+1)$ canting-derived peaks are missing in Ba_2IrO_4 meaning that the system is a simple antiferromagnet.

Order parameter

The thermal evolution of the antiferromagnetic order was determined by performing $\theta - 2\theta$ scans of the $(\frac{1}{2}\,\frac{1}{2}\,10)$ reflection in the $\sigma - \pi$ channel at the energy (11.217 keV) that maximizes the XRMS response. Fig. 3.12(d) shows the integrated intensity obtained by fitting a Lorentzian peak shape to the individual scans as a function of temperature. The transition appears to be second order, and the intensity of the magnetic scattering at the antiferromagnetic Bragg peak is directly proportional to the square of the staggered magnetization M^2. Therefore, from the fit to a $A(1-\frac{T}{T_{\mathrm{N}}})^{2\beta}$ function the Neel temperature $T_{\mathrm{N}} = 241(2)$ K and $\beta = 0.25(4)$ can be obtained. β is the critical exponent relative to magnetization [83]. The factor two is due to the fact that in scattering experiments an intensity is measured, which correspond to a magnetization squared. These values are in good agreement with the ones found by μSR measurements [34].

Although the measurements of the temperature dependence of the magnetic peak were not specifically designed to study in detail the critical behaviour of the system we can discuss a bit further the significance of this value of the critical exponent. Experimental values of the critical exponent β usually range between 0.2–0.4. Ginzberg-Landau theory (mean field approach) predicts $\beta = 0.5$, whilst β is expected to be 0.325 for the

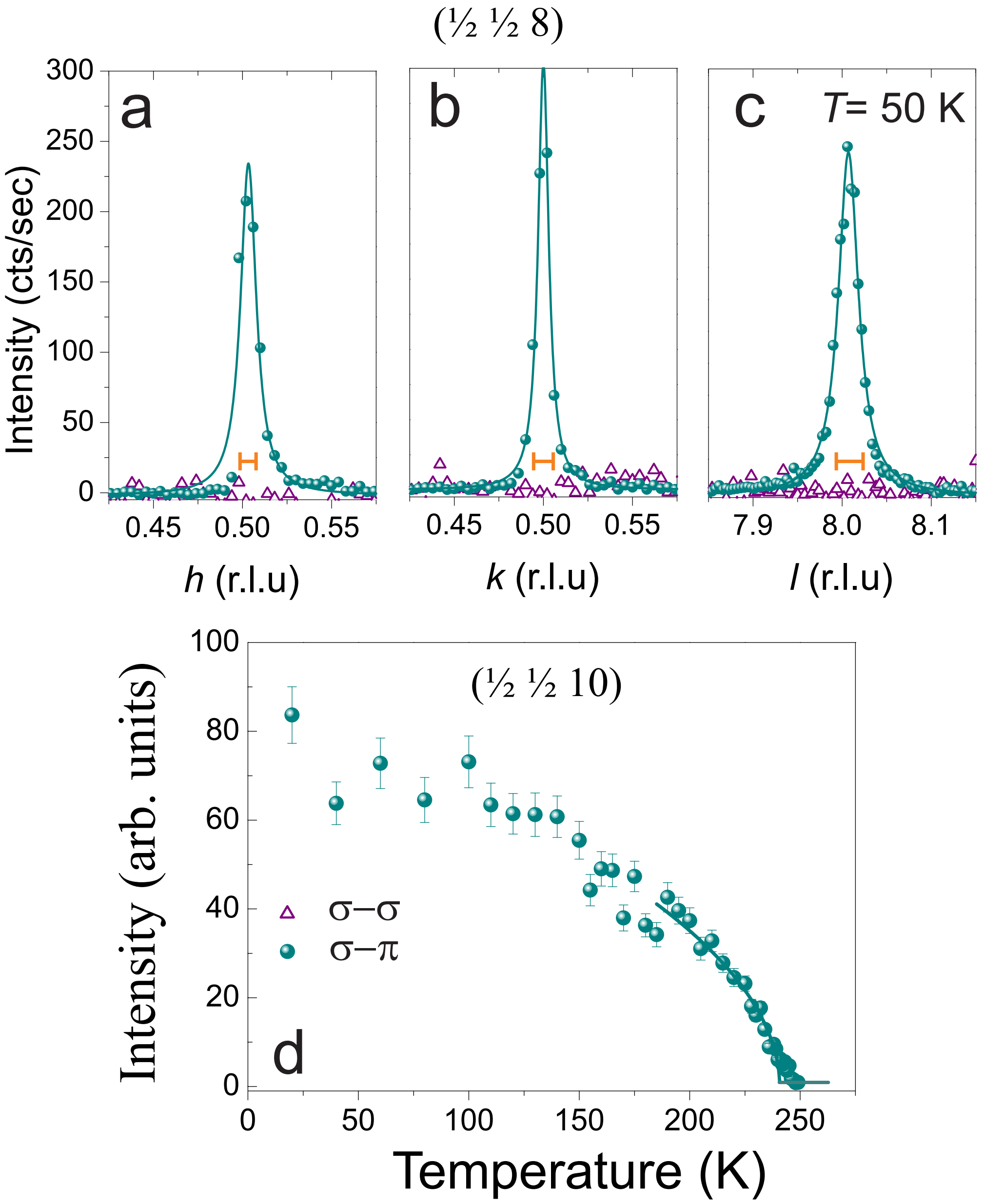

Figure 3.12: h (a), k (b), and l (c) scans of XRMS across the $(\frac{1}{2}\,\frac{1}{2}\,8)$ magnetic reflection at $T = 50$ K at the Ir L_3 edge in Ba_2IrO_4. The green (purple) spheres represent the σ-π (σ-σ) scattering channel. The orange line shows the momentum resolution calculated from a nearby charge reflection. (d) The temperature dependence of the $(\frac{1}{2}\,\frac{1}{2}\,10)$ magnetic reflection in Ba_2IrO_4. The solid green line is a fit to a power law as explained in the text.

three-dimensional (3D) Ising model , 0.346 for the 3D $X-Y$ model , and 0.3647 for the 3D Heisenberg model [83]. Ba_2IrO_4 is considerably far from these values of critical exponent and approaches more closely values for two-dimensional (2D) systems. For 2D systems, an exact solution exists only for the 2D Ising model ($\beta = 0.125$) [84], while no longer range order at finite temperature is expected for 2D X-Y and 2D Heisenberg model, where a vortex state and the suppression of long range order by thermal fluctuation are predicted, respectively. However, a weak interplanar interaction, always presents in any real system can stabilize long range order. Typical example of 2D-like systems are for example compounds isostructural to Ba_2IrO_4 as K_2NiF_4 (2D Heisenberg) or K_2CoF_4 (2D Ising) where the measured value of β are 0.138 [85], and 0.123 [86], respectively. Interestingly, Bramwell and Holdsworth [87] have reported the existence of a class of material, namely 2D $X-Y$ systems with weak perpendicular coupling $J_\perp$ ($J_\parallel/J_\perp \sim 10^3 - 10^4$) with $\beta =$ 0.23. This value is very close to the one we observe in Ba_2IrO_4. This is not surprising, in fact, the spin-orbit entangled wave function typical of the $j_{\text{eff}} = 1/2$ state has a 3D shape that naturally favours 3D-like interactions and it is reasonable to consider Ba_2IrO_4 as a quasi-2D magnet with weak interlayer coupling $J_\perp$.

Energy dependence of XRMS

In Fig. 3.13 we present the energy dependence of the magnetic scattering at $(\frac{1}{2}\,\frac{1}{2}\,8)$ position together with X-ray absorption near edge structure (XANES) measurements (in total fluorescence yield) for energies in the vicinity of the L_3 and L_2 edges. The most notable features of this data are the existence of a well-defined resonance at the L_3 edge, and the complete absence of a response at the L_2 edge within experimental uncertainty. Concerted attempts to find a magnetic response at the L_2 edge by investigating various magnetic reflections all ended in failure. Initially, we interpreted this result along similar lines of the work of Kim et al. [14] in Sr_2IrO_4, i.e. that the absence of any XRMS signal at the L_2 edge serves as a unique fingerprint of the $j_{\text{eff}} = 1/2$ state [16]. However, as we will show in the next section, in Ba_2IrO_4 the magnetic moments lie in the basal-plane in analogy with Sr_2IrO_4. Therefore, according to our

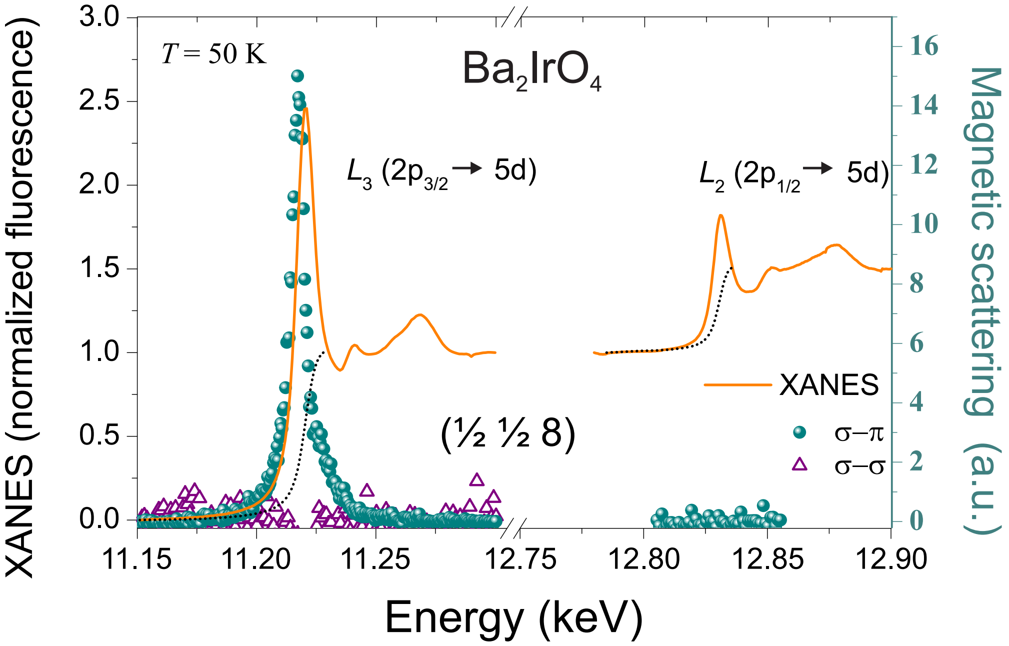

Figure 3.13: Resonant enhancement of the $(\frac{1}{2}\,\frac{1}{2}\,8)$ magnetic reflection across the $L_{2,3}$ edges at $T = 50$ K in Ba_2IrO_4. The solid orange line shows the X-ray absorption near edge structure (XANES) spectra, measured in fluorescence mode, normalized to the number of initial states. The green spheres (σ-π) and purple triangles (σ-σ) show the intensity of the $(\frac{1}{2}\,\frac{1}{2}\,8)$ reflection. The black dashed line demarcates the integrated white line used to calculate the branching ratio.

calculations, the REXS cross-section in the cross-polarized channels (see Eq. 2.61) at the L_2 is identically zero irrespective of the realization of the $j_{\text{eff}} = 1/2$ state. This is consistent with the total absence of XRMS signal at the Ir L_2 edge.

By a close inspection of Fig. 3.13 we can infer some general electronic properties of iridate perovskites. The width of the L_3 resonance is FWHM = 7.6(1) eV, comparable to the values found in Sr_2IrO_4 and in $Sr_3Ir_2O_7$ [14, 15]. The position of the resonance (11.217 keV), similarly to those of Sr_2IrO_4 and $Sr_3Ir_2O_7$, is 3 eV below the maximum of the L_3 white line (11.220 KeV). This shift, as we will show later, represents a good estimation of the cubic crystal field separating the t_{2g} from the e_g states, $10Dq$. In fact, the magnetic peaks at 11.217 keV in the XRMS signal, is only due to the transition from the $2p_{3/2}$ core level to an empty t_{2g}

state, which in our case is the $j_{\text{eff}} = 1/2$ state. Whereas, the strong peaks in the absorption spectrum is a sum of 4 empty e_g states and a single t_{2g} state, which cannot be disentangled for the core-hole broadening typical of XAS measurements. Therefore, the e_g states would lie at slightly higher energies than the maximum in the XAS signal.

However, also the t_{2g} state would reside at higher energies than the maximum of the XRMS signal. This is due to self-absorption effects that influence every scattering process. These effects are not particularly relevant at the Ir L-edge energies but they still have to be taken in account to interpret fine details. The XRMS energy scan of Fig. 3.13 can therefore be corrected for self-absorption using the X-ray attenuation coefficient $\mu(E)$, as explained more in detail in Section 4.4.5. The corrected data (see Fig. 3.14 (b)), show a line shape closer to a perfect Lorentzian, with χ^2 decreasing from 2.2 (raw data) to 1.8, the FWHM becoming 6.3(1) eV and the center shifting to slightly higher energies (11.2177 keV). Considering the XAS white line as an average contribution between one hole in the t_{2g} state and four holes in the e_g state we estimate $10Dq = 2.9$ eV. This large value of the cubic crystal field justifies the initial assumption of neglecting the contribution of e_g intermediate states in the calculation of the REXS/RIXS cross-section in our single-ion model (see Section 2.3).

Branching ratio in XAS

A physical quantity that is is directly related to the expectation value of the spin-orbit operator in the valence states is the branching ratio (BR) of core-valence transitions in X-ray absorption spectroscopy [88, 89, 90]. Significant insights on the spin-orbit coupling in Ba_2IrO_4 can therefore be obtained by analysing the XANES spectra at the L_3 and L_2 edges. The absorption spectrum is formed by three main features: a) a step-like edge which corresponds to transitions from the $2p$ states to a continuum of electronic excitations, b) a sharp white line associated with dipole transitions to bound states $2p \rightarrow 5d$, and c) an oscillating feature at higher energies which is due to the scattering of the ejected photoelectrons by the local environment. Here we focused only on the $L_{2,3}$ white lines which are particularly strong in transition metal oxides due to a substantial

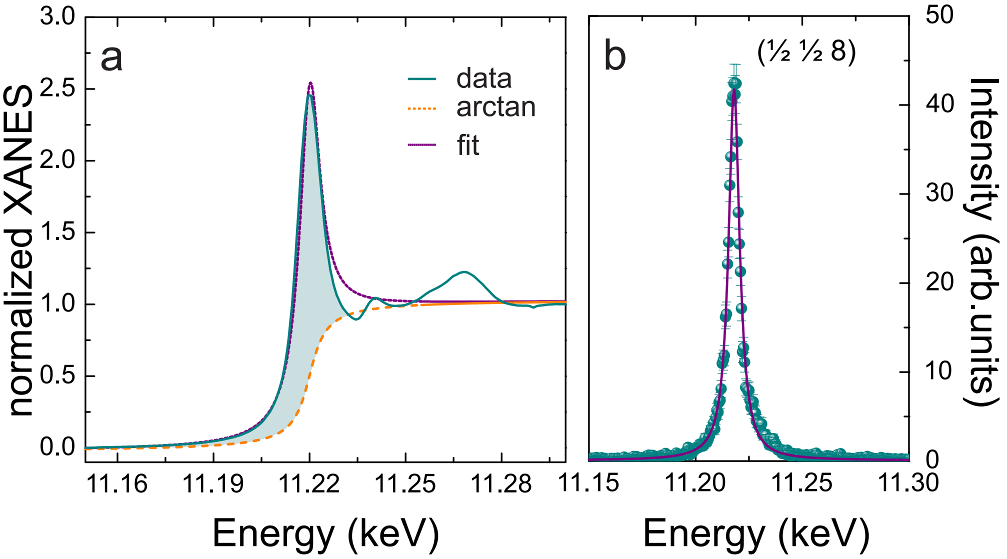

Figure 3.14: (a) Experimental determination of the white line intensity at the Ir L_3 absorption edge in Ba_2IrO_4.The solid green line represents the normalized XANES signal, while the orange dashed line represents the arctangent function used to model the continuum step at the L_3 absorption edge. The dotted purple line represents the fit to the data using a Lorentzian + arctangent fit function. The shaded area has been numerically integrated to calculate the white line intensity. (b) Resonant enhancement, corrected for self-absorption, of the $(\frac{1}{2}\,\frac{1}{2}\,8)$ magnetic reflection across the L_3 edge at $T = 50$ K in Ba_2IrO_4. The fit to a Lorentzian function ($\chi^2 = 1.8$) gives a resonance centered at $E = 11.2177$ keV of FWHM = 6.3 eV.

concentration of well localized states close to the Fermi level. The integrated intensity of these white lines is proportional to the local density of unoccupied final states in the system (in our case the population of 5d holes) [91].

The pioneering work of van der Laan and Thole [88] has demonstrated that the “branching ratio” of the $L_{2,3}$ white line, $BR = I_{L_3}/I_{L_2}$, is directly related to the ground-state expectation value of the angular part of the spin-orbit operator of the d-states via $BR = (2 + r)/(1 - r)$ (in units of $\hbar^2$), where $r = \langle \mathbf{L} \cdot \mathbf{S} \rangle / \langle n_\mathrm{h} \rangle$ and n_h is the number of the holes in the d levels [89]. This result is perhaps not surprising in view of the fact that XAS must obey the selection rules for dipole-allowed electronic transitions

($\Delta J = 0, \pm 1$). This means that, in the atomic limit, the L_2 edge ($2p_{1/2}$) involves transitions only to $5d_{3/2}$ unoccupied states, whereas the L_3 edge ($2p_{3/2}$) involves transitions to both $5d_{3/2}$ and $5d_{5/2}$. In the limit of zero SOC the $5d_{3/2}$ and $5d_{5/2}$ multiplets are degenerate and the branching ratio reflects the number of initial states ($2p^2_{1/2}$, $2p^4_{3/2}$), i.e. $BR = 2$. An interesting exercise is then to calculate the BR for our single-ion model. This can be done by exploiting the matrix elements of Tab. 2.2 and the first step (absorption process) of the Kramers-Heisenberg formula (Eq. 2.56). The BR then reads

$$BR = \frac{\sum\limits_n |\langle n\, |\mathcal{D}_{\boldsymbol{\epsilon}}|\, 0, -\rangle|^2}{\sum\limits_j |\langle j\, |\mathcal{D}_{\boldsymbol{\epsilon}}|\, 0, -\rangle|^2} = \frac{2\,(1 + A + A^2)}{(A-1)^2}, \tag{3.11}$$

where the summations run over the $n = \{|p_{3/2}, m_{3/2}\rangle\}$ and $j = \{|p_{1/2}, m_{1/2}\rangle\}$ states and $A = \frac{-1+\delta+\sqrt{9+(-2+\delta)\delta}}{2}$ controls the effect of the tetragonal crystal field Δ via $\delta = 2\Delta/\lambda$ (see Section 1.4.1), where λ is the Ir SOC constant. The calculated BR as a function of the tetragonal crystal field is shown in Fig. 3.15. The BR tends to the statistical value 2 for $\Delta \gg \lambda$ and $\Delta \ll -\lambda$, i.e. in a regime of weak spin-orbit coupling when a classical $s = 1/2$ state is realized. In the strong SOC limit the $j_{\text{eff}} = 1/2$ state is realized, and $BR \to \infty$ for $\Delta = 0$, which is consistent with the expression $BR = (2 + r)/(1 - r)$ with $\langle \mathbf{L} \cdot \mathbf{S} \rangle_{j_{\text{eff}}} = 1$ (see Section 1.4.1) and $n_{\text{h}} = 1$. The divergence of the BR for $\Delta = 0$ is due to a vanishing XAS signal at the L_2 edge and it is strictly realized only when the effect of the $j_{\text{eff}} = 3/2$ states is neglected. The inclusion of a small contribution of the $j_{\text{eff}} = 3/2$ states gives a finite signal at the L_2 edge and the BR no longer diverges.

Since XAS is a process that involves all the $5d$ levels, Laguna-Marco et al. [92] have shown through configuration interaction calculations that the measured $\langle \mathbf{L} \cdot \mathbf{S} \rangle$ will be the sum of two contributions: a direct term, which involves a single hole in the $j_{\text{eff}} = 1/2$ state ($\langle \mathbf{L} \cdot \mathbf{S} \rangle_{j_{\text{eff}}} = 1$) and an indirect term that derives from the mixing between $j_{\text{eff}} = 3/2$ and e_g states and involves 4 holes in the e_g states ($\langle \mathbf{L} \cdot \mathbf{S} \rangle_{e_g} \cong 4 \times 3\lambda_{5d}/10Dq$) [92]. In the limit $10Dq \to \infty$ this term vanishes and we recover our calculations.

In order to calculate the experimental BR we performed a careful analysis of the white line intensity. First, the absorption spectra were normalized to the number of initial states in such a way that the continuum step at the L_3 is equal to unity and the step at the L_2 is half of that value. Second, we determined the intensity of the white lines by means of two different procedures. In the first method, we subtracted from the experimental data (green line in Fig. 3.14(a)) an arctangent function (dashed orange line) centered at the maximum of the fluorescence spectra. We then integrated numerically only the contribution of the white line, from below the edge up to the intersection with the arctangent function (shaded area). In the second method we fit the experimental data using an arctangent $+n$-Lorentzian fit function which reads

$$\mu(E) = C_1 + \frac{C_2}{\pi} \arctan\left(\frac{E - E_0}{\Gamma_c/2}\right) + \sum_{i=1}^{n} D_i \frac{1}{1 + \left(\frac{E-E_i}{\Gamma_c/2}\right)^2}, \tag{3.12}$$

where the arctangent, as in the first method, derives from the convolution of the edge step function with the core-hole lifetime Γ_c and it is used to model the edge jump at E_0. The n-Lorentzians are exploited to model the possible transitions. In our case a single Lorentzian centered at $E_1 \equiv E_0$ was exploited. C_2, D_i are scaling factors and C_1 describes $\mu(E)$ at low energies. The result of these fits at the L_3 edge is illustrated by the dotted purple line in Fig. 3.14(a). The fit clearly fails to reproduce the high energy fine structure oscillations but captures most of the low energy features. Within the limits of the experimental uncertainties, both the numerical integration and the fitting analysis produced the same results, i.e. BR=5.4(2). A BR significantly greater than the statistical one indicates a strong coupling of the spin and orbital components within the 5d manifold. Using $n_\mathrm{h} = 5$ we obtain $\langle \mathbf{L} \cdot \mathbf{S} \rangle \cong 2.67\hbar^2$, significantly larger that the value of ~ 2 found for BaIrO$_3$ [92] and 2.1 for Sr$_2$IrO$_4$ [55], but comparable to the value found for a large class of iridates [93]. It should be noted that a large value of $\langle \mathbf{L} \cdot \mathbf{S} \rangle$ and the correspondent BR is only a sufficient condition for a strong-spin orbit coupling regime. In fact, in case the spin or orbital moments are quenched the expectation value $\langle \mathbf{L} \cdot \mathbf{S} \rangle$ can vanish even in presence of strong SOC. Taking into account the two contributions to the BR: $\langle \mathbf{L} \cdot \mathbf{S} \rangle_{j_\mathrm{eff}} = 1$ and $\langle \mathbf{L} \cdot \mathbf{S} \rangle_{e_g}$, and the octahedral crystal field splitting ($10Dq = 2.9$ eV) previously determined, we can obtain the SOC parameter $\lambda_{5d} \cong 0.42$ eV, a value in good agreement with the standard estimation of about 0.4 eV for the SOC in iridium [12].

We can now discuss the relevance of these results to the $j_{\text{eff}} = 1/2$ picture in Ba_2IrO_4. In order to do this we adopt an energy diagram (Fig. 3.15(b)) which is complementary to the one illustrated in Fig. 1.4. Here we apply to the $5d$ manifold, in reversed order respect to Fig. 1.4, first the SOC, and second the cubic crystal field. In this picture the $j_{\text{eff}} = 3/2$ states are derived from the lower-lying $j = 3/2$ atomic states, while the $j_{\text{eff}} = 1/2$ state are branched out from the upper $j = 5/2$ atomic states by the action of the cubic crystal field. A branching ratio significantly larger than the statistical one means that the dipole transitions from the L_2 edge ($2p_{1/2} \rightarrow 5d_{3/2}$) are highly unlikely, and the population of the $5d$ holes has mainly a $d_{5/2}$ character, in agreement with the energy diagram of Fig. 3.15(b) and the $j_{\text{eff}} = 1/2$ physics. In a classical $s = 1/2$ system, the ground state is a mixture of $j_{\text{eff}} = 1/2$ and $j_{\text{eff}} = 3/2$ states and transition from the L_2 and L_3 are equally allowed. This is confirmed by our single-ion calculation, which shows that the BR varies between a novel $j_{\text{eff}} = 1/2$ system ($BR \rightarrow \infty$) and a classical $s = 1/2$ system ($BR \rightarrow 2$) with the ratio of SOC to tetragonal crystal field.

An unambiguous method to determine the realization of the $j_{\text{eff}} = 1/2$ state is via oxygen K-edge XAS. This technique is in fact sensitive to the symmetry of the hole in the Ir t_{2g} orbitals which hybridizes with $2p$ oxygen orbitals. Our recent O K-edge XAS measurements confirm the robustness of the $j_{\text{eff}} = 1/2$ state in Ba_2IrO_4 showing an isotropic orbital ratio $xy \div yz \div zx \cong 1 \div 1 \div 1$ among the t_{2g} states [73].

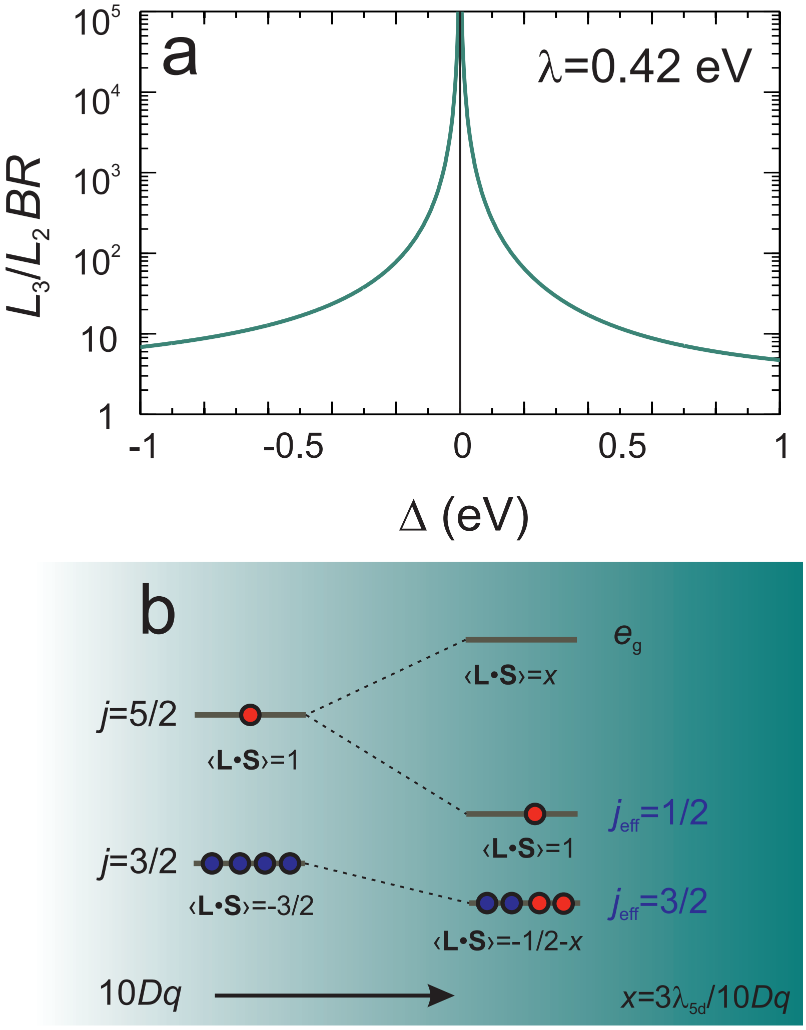

Figure 3.15: (a) The calculated BR (logarithmic scale) as a function of the tetragonal crystal field splitting Δ ranging from -1 to 1 eV, for a given value of the spin-orbit coupling constant ($\lambda = 0.42$ eV) in the ionic limit for a 1 hole t_{2g} system. Panel (b) shows a schematic energy diagram of how the 5d levels split under the influence of the SOC first, and then under the cubic crystal field.

3.3.3 Ba_2IrO_4 vs. Sr_2IrO_4: equivalence of basal-plane antiferromagnetism

Having investigated the electronic properties of Ba_2IrO_4 by means of a detailed analysis of the absorption spectra, we return now to the problem of determining the exact magnetic structure of Ba_2IrO_4.

In order to determine the possible magnetic structures in Ba_2IrO_4, we performed representation analysis by means of the SARA*h* [94] package. Representational analysis allows the determination of the symmetry-allowed magnetic structures that can result from a second-order magnetic phase transition, given the crystal structure before the transition and the propagation vector of the magnetic ordering. The magnetic representation of a crystallographic site can then be decomposed in terms of the irreducible representations (IRs). For a second-order transition a powerful simplification to the number of possible structures arises as a consequence of the Landau theory: the ordering transition can involve only one IR becoming critical. Accordingly, the basis vectors involved in the resulting structure are limited to those associated with a single IR and the number of "symmetry-allowed" magnetic structures possible for a particular crystallographic site is simply the number of nonzero IRs in the decomposition of its magnetic representation [94].

The input parameters of this calculations were the system space group $I4/mmm$, confirmed from X-ray diffraction, the magnetic propagation vector $\mathbf{k} = [\frac{1}{2}\ \frac{1}{2}\ 0]$, resulting from the XRMS measurements, and the atomic coordinates of the Ir atoms. The results of the SARA*h* calculations are presented in Table 3.1. For Ba_2IrO_4 only 3 IRs, with the associated basis vectors, are possible: Γ_3, Γ_5 and Γ_7 (following the numbering scheme of Kovalev [95]). Contrary to Sr_2IrO_4, the symmetry of the system, that preserves the inversion symmetry, rules out any representation that involves a ferromagnetic component, due to the fact that the Dzyaloshinsky-Moriya interaction is not effective [76].

In order to discriminate between the 3 possible structures, we performed azimuthal scans of the $(\frac{1}{2}\ \frac{1}{2}\ 10)$ magnetic reflection at the Ir L_3 edge, $T = 50$ K. This has been achieved by measuring θ-2θ scans for different Ψ angles, rotating the sample around the scattering vector.

IR	BV	Atom	BV components					
			$m_{\|a}$	$m_{\|b}$	$m_{\|c}$	$im_{\|a}$	$im_{\|b}$	$im_{\|c}$
Γ_3	$\boldsymbol{\psi}_1$	1	0	0	1	0	0	0
Γ_5	$\boldsymbol{\psi}_2$	1	1	1	0	0	0	0
Γ_7	$\boldsymbol{\psi}_3$	1	1	-1	0	0	0	0

Table 3.1: Basis vectors for the space group I4/mmm with $\mathbf{k}$=[$\frac{1}{2}\,\frac{1}{2}\,0$]. The decomposition of the magnetic representation for the Ir site (0, 0, 0) is $\Gamma_{Mag} = 0\Gamma_1^1 + 0\Gamma_2^1 + 1\Gamma_3^1 + 0\Gamma_4^1 + 1\Gamma_5^1 + 0\Gamma_6^1 + 1\Gamma_7^1 + 0\Gamma_8^1$. The atom of the primitive basis is defined according to 1: (0, 0, 0).

Fig. 3.16(b) shows the azimuthal dependence of the ($\frac{1}{2}$ $\frac{1}{2}$ 10) reflection (green spheres) corrected for self-absorption using Eq. 3.2. The dashed orange line, solid green line, and dotted purple line are the azimuthal dependence calculated for the Γ_3 ($\mu \| [0\,0\,1]$), Γ_5 ($\mu \| [1\,1\,0]$) and Γ_7 ($\mu \| [1\,\bar{1}\,0]$) IR, respectively. The experimental curve most closely resembles the calculation for the Γ_5 representation. We therefore conclude unambiguously that Ba_2IrO_4 adopts a basal-plane antiferromagnetic structure with the magnetic moments pointing along the [1 1 0] direction. The magnetic structure of Ba_2IrO_4 is shown in Fig. 3.16(a).

We can now compare the azimuthal dependence relative to the ($\frac{1}{2}\,\frac{1}{2}$ 10) reflection of Ba_2IrO_4 (Fig. 3.16(b)) with the analogous azimuthal dependence of the (1 0 24) reflection for Sr_2IrO_4 (Fig. 3.6). We recall that the [1 1 0] direction in Ba_2IrO_4 corresponds to the [1 0 0] direction in Sr_2IrO_4 (see inset of Fig. 3.10(a)), so that the Ψ angles in the two figures are equivalent. It is clear that in Sr_2IrO_4 the antiferromagnetic component is oriented along the [1 1 0] direction of the I4/mmm reference system in analogy with Ba_2IrO_4. We therefore conclude that the two compounds have essentially the same basal-plane antiferromagnetic structure.

We now discuss our results in view of the available theoretical models relative to perovskite iridates. As we have mentioned in Section 3.2.3, the Hamiltonian 1.48 has been used to successfully account for the canted magnetic structure observed in Sr_2IrO_4. For Ba_2IrO_4, it would also seem to offer a natural explanation of our results: with $\rho = 0$, the second and third terms are identically zero, leaving a leading isotropic exchange along with a weaker anisotropy which derives only from Hund's coupling, a Hamil-

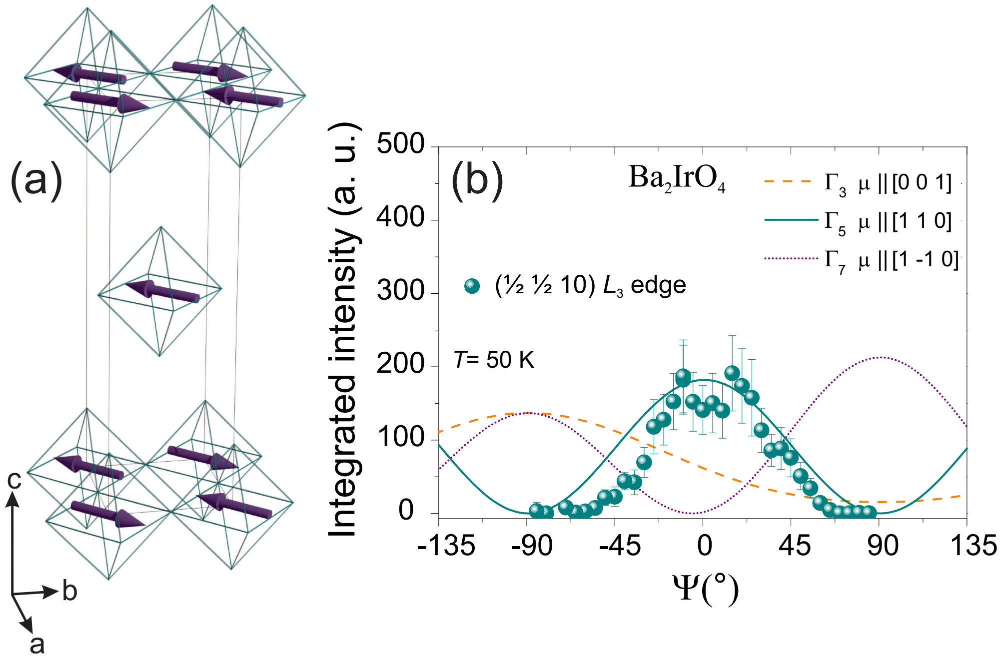

Figure 3.16: Panel (a) shows the basal-plane antiferromagnetic structure of Ba$_2$IrO$_4$, where the magnetic moments are pointing along the [1 1 0] direction. (b) The azimuthal dependence of the ($\frac{1}{2}\,\frac{1}{2}\,10$) magnetic reflection (solid green spheres) at the Ir L_3 edge, T = 50 K in Ba$_2$IrO$_4$. The solid lines are the azimuthal dependencies calculated for the three different IR's. The azimuthal angle Ψ is defined with respect to the reference vector [1 1 0] in the I4/mmm space group.

tonian that readily supports the commensurate antiferromagnetic order observed in our experiments. One important proviso, however, is that the magnetic ground state supported by this Hamiltonian becomes unstable above a critical value of tetragonal distortion leading to a spin reorientation where the moments point along the [0 0 1] direction. Nevertheless it seems, that nearly doubling the tetragonal distortion in moving from Sr to Ba is insufficient to exceed the critical threshold.

Although the above analysis provides a general framework for us to understand the formation of magnetic structures in the layered perovskites, and most especially the canting of the moments in Sr$_2$IrO$_4$, it does not address the key fact revealed in our experiments that the antiferromagnetic components in the two compounds are essentially identical. For this we refer to explicit calculations of the exchange coupling J by Katukuri et al. [96], who have exploited an *ab-initio* many-body approach. Their calculations show that when the SOC is switched off, the ground state and the magnetic interactions are extremely sensitive to the local symmetry and so are very different in the two systems: Ba_2IrO_4 has a hole in the xz/yz states and a strong antiferromagnetic J interaction ($\sim$ 15.4 meV), Sr_2IrO_4 has a hole in the xy state and a ferromagnetic J interaction ($\sim -$19.2 meV). The fact that in Sr_2IrO_4 the nearest-neighbour interactions are ferromagnetic can be easily understood in term of Goodenough-Kanamori rules for superexchange [97]. A hole in the xy state will be in fact highly sensitive to the distorted nature of the Ir-O-Ir bonds in Sr_2IrO_4 making oxygen mediated superexchange not effective. However, upon including the SOC, the hole acquires an equal xy, zx and yz character in both compounds and J in Sr_2IrO_4 becomes antiferromagnetic ($\sim$ 51.3 meV), and almost identical to that in Ba_2IrO_4 ($\sim$ 58 meV).

However, a recent study by the same authors has overturned part of this calculation showing that in the absence of SOC Ba_2IrO_4 has a hole in the xy states while Sr_2IrO_4 has a hole in the xz/yz [98]. This is in agreement with our experimental results that $\Delta = -12$ meV in Sr_2IrO_4 and $\Delta = 50$ meV in Ba_2IrO_4 [73]. Superexchange is always AF in Sr_2IrO_4 while in Ba_2IrO_4 with no SOC the nearest-neighbours J has different signs at different levels of approximation: if just intersite $t_{2g} - t_{2g}$ excitations (Anderson-like) are considered, J is AF (15 meV). If O $2p$ to Ir $5d$ and intersite $t_{2g} - e_g$ excitations are further added, J turns weaker and FM (-2 meV) [98]. Upon the inclusion of the SOC, in analogy with the previous calculation, the t_{2g} hole is equally distributed between the three orbitals and the single layer perovskite show an almost identical AF superexchange, which is the main conclusion of our XRMS investigations. Therefore, the robustness of antiferromagnetic order in the layered perovskites to structural distortions is ultimately linked to the strong SOI, which produces a ground state wave function that is three dimensional and inherently less perturbed by structural distortions.

3.4 Conclusions

In this chapter we presented a detailed analysis of the magnetic structure of the single layered perovskite iridates Sr_2IrO_4 and Ba_2IrO_4 via X-ray resonant magnetic scattering at the Ir $L_{2,3}$ edge. We confirm that Sr_2IrO_4 adopts a canted antiferromagnetic structure, as observed in previous studies [14]. We extend these investigations by solving unambiguously the magnetic structure determining that the dominant antiferromagnetic component of the moment points along the a axis in the $I4_1/acd$ space group, while the total moment is locked to the rotation of the IrO_6 octahedra. These are both consequences of the strong spin-orbit coupling regime and the close realization of the $j_{\text{eff}} = 1/2$ state in Sr_2IrO_4. By means of a comparative XRMS study in the related compound Ba_2IrO_4 we show how the $j_{\text{eff}} = 1/2$ state evolves as a function of structural distortions. Surprisingly, despite the significant structural difference between the compounds, we show that Sr_2IrO_4 and Ba_2IrO_4 share the same basal-plane antiferromagnetic structure. The presence of the strong SOC regime is ascertained by means of XAS measurements which show a very large branching ratio.

Therefore, both the magnetic and electronic structures in the single-layered perovskites are remarkably robust to structural distortions, a fact that can be linked directly to the unique three-dimensional character of the $j_{\text{eff}} = 1/2$ state produced by the strong SOC which renders it insensitive to the perturbations in local symmetry. Furthermore, our findings support the Hamiltonian developed by Jackeli and Khaliullin [23] (Eq.1.48) to describe layer perovskite iridates, which predicts a basal-plane canted antiferromagnetic structure in Sr_2IrO_4 and a simple basal-plane antiferromagnetic structure in Ba_2IrO_4.

Chapter 4

The magnetic and electronic structure of $Sr_3Ir_2O_7$ studied with XRMS

The evolution of the $j_{\text{eff}} = 1/2$ state as a function of dimensionality is studied by a comprehensive investigation of the electronic and magnetic properties of the bilayer $Sr_3Ir_2O_7$ by means of XRMS. Despite the greater metallicity of the bilayer compound, the $j_{\text{eff}} = 1/2$ state survives in $Sr_3Ir_2O_7$, as determined by the vanishing L_2/L_3 XRMS intensity ratio. However, the addition of an extra IrO_6 layer radically modifies the magnetic structure forcing a spin-flop transition from the basal-plane canted antiferromagnetic structure of the single layer Sr_2IrO_4 to the c-axis collinear magnetic structure of $Sr_3Ir_2O_7$.

Contents

4.1 Introduction

The bilayer $Sr_3Ir_2O_7$ is the $n=2$ compound along the Ruddlesden-Popper series $Sr_{n+1}Ir_nO_{3n+1}$ from Sr_2IrO_4. As n is increased, the system is thought to become less insulating up to a strongly correlated metal for $n=\infty$ ($SrIrO_3$). This is due to the fact that the bandwidth W is proportional to the number of neighboring Ir atoms N [99]. N is 4 in the single-layer Sr_2IrO_4, 5 in the bilayer $Sr_3Ir_2O_7$ and 6 in the cubic perovskite $SrIrO_3$.

By means of optical conductivity measurements Moon et al. [99] have investigated the electronic properties of Sr_2IrO_4, $Sr_3Ir_2O_7$, and $SrIrO_3$. As discussed in Chapter 3, Sr_2IrO_4 shows an optical gap of about 0.3 eV and two well defined features: a peak α corresponding to the transition within the $j_{\text{eff}} = 1/2$ manifold from the lower Hubbard band (LHB) to the upper Hubbard band (UHB), and a peak β relative to transitions from the $j_{\text{eff}} = 3/2$ band to the UHB of the $j_{\text{eff}} = 1/2$ band (see Fig. 4.1(a)). As expected, these features become broader and decrease in energy in $Sr_3Ir_2O_7$. Furthermore, the optical gap is almost absent in the bilayer spectra (see Fig. 4.1(b)). In the $n=\infty$ compound, $SrIrO_3$, peak α is no longer present and the system behaves like a metal (Fig. 4.1(c)). The $n=2$ case, the bilayer perovskite $Sr_3Ir_2O_7$, clearly lies in the proximity of a metal-to-insulator transition which should take place between $Sr_3Ir_2O_7$ and $SrIrO_3$, as illustrated in the schematic band diagram of Fig. 4.1(right panel). In this context, it is of considerable importance to understand whether the $j_{\text{eff}} = 1/2$ state is robust enough to overcome the enhancement in the bandwidth. The greater metallicity of the double layer compound could in principle modify the subtle balance between spin-orbit coupling and electronic correlations and lead to a different ground state.

Another important feature of the bilayer structure is that $Sr_3Ir_2O_7$ is no longer a quasi-2D system like Sr_2IrO_4 or Ba_2IrO_4. The addition of an extra IrO_6 layer, in fact, means that the physics at play can be significantly different from the single layer counterpart: the interlayer interactions can in principle play a fundamental role in determining the ground and excited states of $Sr_3Ir_2O_7$. This is strengthened by the fact that the three-dimensional shape of the $j_{\text{eff}} = 1/2$ state favours directionally dependent interactions.

In this chapter we address how the $j_{\text{eff}} = 1/2$ state evolves as a function of dimensionality in the bilayer $Sr_3Ir_2O_7$. In Section 4.2 we present the results of our investigation of the crystal structure of $Sr_3Ir_2O_7$. Understanding the crystal structure in detail is a fundamental requirement to the study of the magnetic structure in this compound. In Section 4.3 we present a general overview of bulk properties in $Sr_3Ir_2O_7$. Finally, in Section 4.4, we present a detailed XRMS study which establishes for the first time the magnetic structure and the ground state properties of $Sr_3Ir_2O_7$.

4.2 Crystal structure

$Sr_3Ir_2O_7$ was first reported to crystallize in the tetragonal I4/*mmm* space group [100]. This picture was refined by recent reports of an orthorhombic *Bbcb* space group [33, 101]. Therefore the exact crystal structure remains debated. It is clear that the structure contains strongly coupled double Ir-O layers, separated by layers of Sr-O and offset along the *c* axis, which results in a double-layered framework of Ir atoms centered inside oxygen octahedra. It is the rotation of these octahedra and the correlation between the rotations that lead to the subtle differences in crystal structure reported thus far.

In order to investigate the crystal structure of $Sr_3Ir_2O_7$, we performed an X-ray diffraction study. Single crystals of $Sr_3Ir_2O_7$ were grown at the Clarendon Laboratory, Oxford University, UK and at the University of Edinburgh, UK. These were synthesized in Pt crucibles using the self-flux technique from off-stoichiometric IrO_2, $SrCO_3$, and $SrCl_2$ compounds. The mixture was heated to 1440°C, fired for 20 h and slowly cooled at 3°C/h.

The resulting samples were plate-like with the c axis along the shortest dimension of $2\times2\times0.1$ mm size crystals. In terms of crystal structure, samples from different growers do not show significant differences.

Crystallographic data were collected with a Supernova X-ray diffractometer equipped with a microfocused monochromatic Mo source at the Research Complex at Harwell (RCaH), Chilton, UK. The $Sr_3Ir_2O_7$ crystal had dimensions of $0.108\times0.134\times0.072$ mm. Using an ω-scan mode within a 2θ range of 7.84° to 64.6° we measured 1369 reflections (204 unique) at room temperature. The data were corrected for Lorentz, polarization and absorption effects. The 1369 reflections were used to obtain the cell parameters: $a=3.987(5)$ and $c=20.892(5)$ Å. For $Z=2$, the calculated density was 7.947 g/cc.

Initially, we modelled the structure with an I4/mmm space group with a full occupancy of the atom sites. As a consequence we obtained a large reliability factor ($R>$0.7) and the thermal parameter of O3 became very large compared to the other atoms, and strongly anisotropic with an ellipse highly elongated along the a axis. The next step was then to remove the O3 atom from its position on the mirror plane and shift it by 0.4 Å from the mirror plane, assigning it an occupancy of 0.5. This model decreased the R-factor up to 4% and lead to a O3 thermal parameter of the same order of magnitude of the other atoms (see Tab. 4.1). Subsequent refinement of several parameters (isotropic extinction, anisotropic thermal parameter for Ir and Sr, isotropic thermal parameters for O) by full-matrix least-squares techniques converged at $R=$ 0.044, $wR=0.09$, and $S=1.089$, where wR is the weighted residual factor and S represents the fit goodness as defined in the International table for Crystallography [102]. This refinement is in close agreement with the initial report on the crystal structure of $Sr_3Ir_2O_7$ by Subramanian et al. [100].

The crystal structure of $Sr_3Ir_2O_7$ is shown in Fig. 4.2(a); the atomic positions and site symmetries are given in Tab. 4.1. Purple spheres and light blue spheres represent Sr and Ir atoms, respectively. The oxygen O1 and O2 are represented by red spheres while grey spheres indicate oxygen atoms with 50% occupancy (O3). The partial occupation of the O3 sites generates the octahedral rotation about the c axis of 11.95° in analogy with the single layer counterpart Sr_2IrO_4. The principal bond angles are

Atom	Site	x	y	z	U_{iso}(Å^2)	Occupancy
Ir	4e	1/2	1/2	0.59741(4)	0.0080(3)	1
Sr1	2b	0	0	1/2	0.0128(6)	1
Sr2	4e	0	0	0.68702(11)	0.0125(4)	1
O1	2a	1/2	1/2	1/2	0.014(4)	1
O2	4e	1/2	1/2	0.6943(8)	0.015(3)	1
O3	16n	0	0.605(4)	0.5964(6)	0.013(3)	0.5

Table 4.1: Atomic coordinates and isotropic displacement parameters of $Sr_3Ir_2O_7$ at 293(2) K, in the I4/mmm space group; $a = 3.897(5)$ Å, $c = 20.892(5)$ Å, and $V = 317.3(6)$ Å^3. Reliability factors: $R = 0.044$, $wR = 0.09$, and $S = 1.089$.

given in Tab. 4.3.

The model with a partial occupation of the O3 sites can be interpreted either as the presence of disorder due to a short-range nature of the correlated octahedral rotations or the average of a two-twin structure with fully correlated rotations. In fact the I4/mmm structure with 50% occupancy of O3 sites can be decomposed in the sum of two pseudo-orthorhombic rotated twins: *Bbcb* and *Acaa*, both belonging to the No. 68 space group of the International Tables for Crystallography. We recall that the unit cell in the *Bbcb* (*Acaa*) reference system is rotated by 45° in respect to the I4/mmm unit cell. The only difference between these twins is in the vertical stacking of the layers for the rotated octahedra. This is illustrated in Fig. 4.2(b-c), while keeping the I4/mmm reference system. Here grey (blue) octahedra represent clockwise (anti-clockwise) rotations about the c axis. For a pair of vertical neighbors, the octahedral rotations are in opposite directions. The coexistence of *Bbcb* and *Acaa* was first suggested by Matsuhata et al. [101] for polycrystalline sample. From the interatomic distances of Tab. 4.2 we can infer that the octahedral oxygen cage is less distorted than in the single layer compounds Ba_2IrO_4 and Sr_2IrO_4, being elongated along the c axis by only 2%. As already discussed in Sections 1.4.1,1.5, this can be relevant for the $j_{\mathrm{eff}} = 1/2$ picture.

In order to investigate in more detail the subtle effects in the position of the oxygen atoms, we recently performed single crystal X-ray diffraction at the ID09 beamline, at the ESRF, Grenoble. These mea-

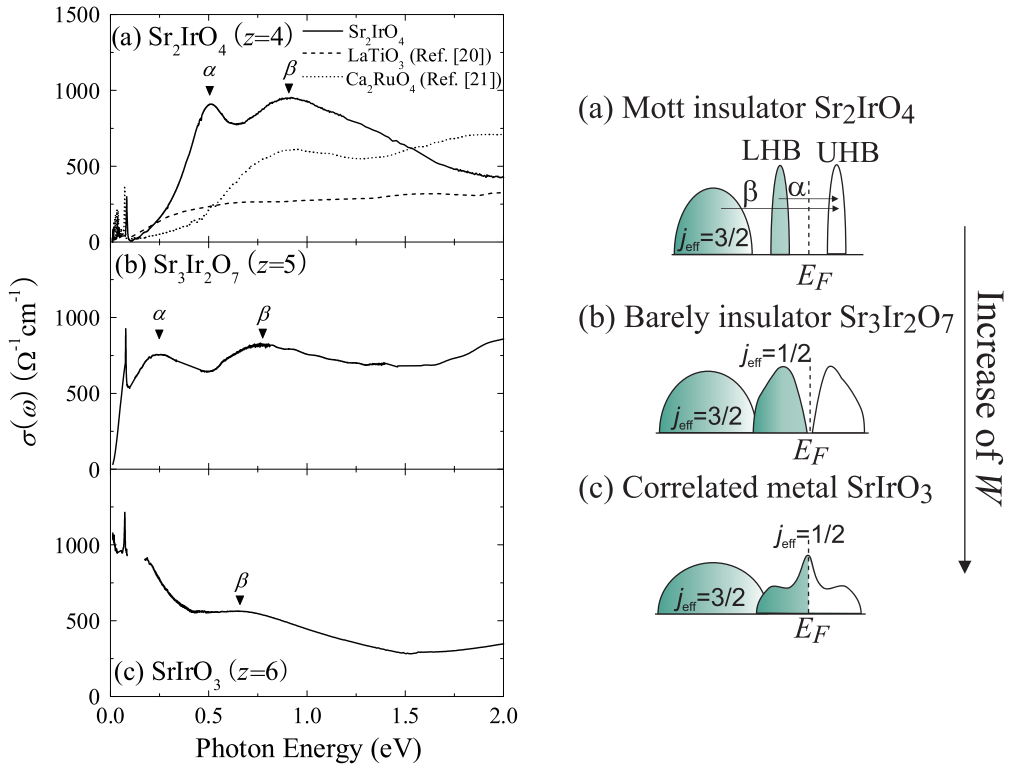

Figure 4.1: Left panel: optical conductivity spectra $\sigma(\omega)$ of (a) Sr_2IrO_4, (b) $Sr_3Ir_2O_7$, and (c) $SrIrO_3$. In (a), $\sigma(\omega)$ of other Mott insulators, such as $3d$ $LaTiO_3$ and 4d Ca_2RuO_4, are shown for comparison. Peak α corresponds to the optical transition from the LHB to the UHB of the $j_{\text{eff}} = 1/2$ states. Peak β corresponds to the transition from the $j_{\text{eff}} = 3/2$ bands to the UHB. Right panel: schematic band diagrams of $5d$ $Sr_{n+1}Ir_nO_{3n+1}$ compounds: (i) Mott insulator Sr_2IrO_4, (ii) barely insulator $Sr_3Ir_2O_7$, and (iii) correlated metal $SrIrO_3$. E_{F} represents the Fermi level and the arrow indicates the increasing direction of the bandwidth W. Figure adapted from Ref. [99].

Ir-O1	2.0351(9)	Sr1-O3	2.534(14)
Ir-O2	2.023(17)	Sr2-O2	2.760(4)
Ir-O3	1.991(4)	Sr2-O3	3.025(14)
Sr1-O1	2.756(4)	O3-O3	0.82(3)

Table 4.2: Interatomic distances (Å) of $Sr_3Ir_2O_7$ at 293(2) K, in the I4/mmm space group.

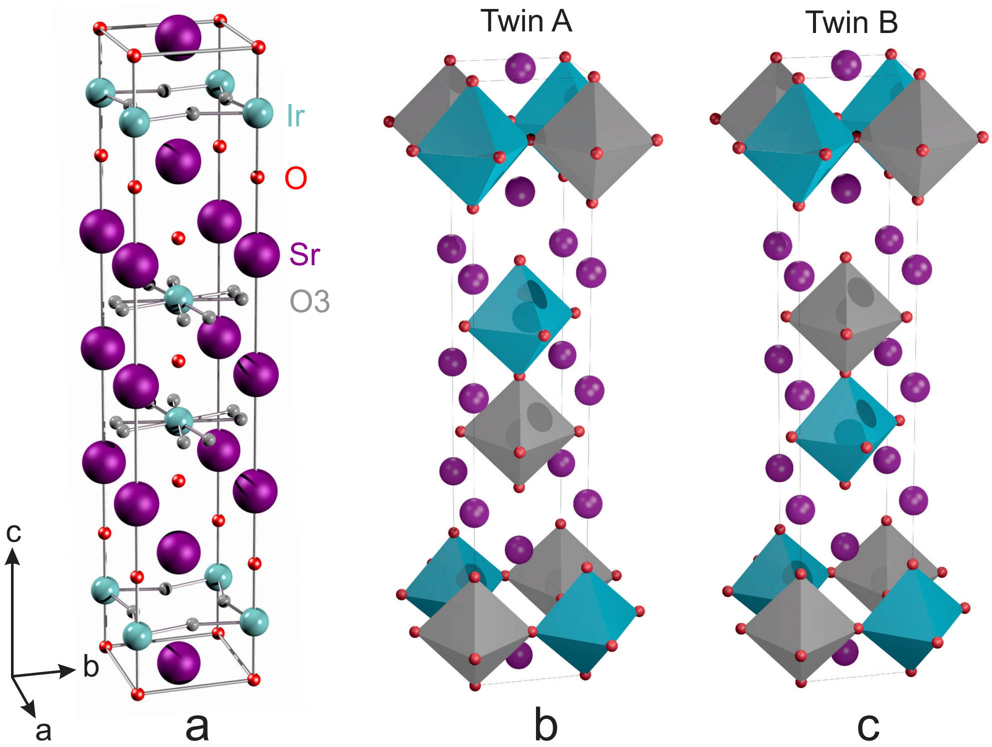

Figure 4.2: (a) The $Sr_3Ir_2O_7$ I4/*mmm* crystal structure with two bilayer molecules per unit cell. A 50% occupancy of the O3 sites (grey atoms) results in an octahedral oxygen environment of the Ir ions rotated from one layer to the next. The I4/*mmm* crystal structure can be decomposed into two symmetry-related twins: A (b) and B (c). The difference between these twins is in the vertical stacking of the octahedral rotations which is opposite in the two cases. Here grey (blue) octahedra represent clockwise (anti-clockwise) rotations about the *c* axis. For a pair of vertical neighbors, the octahedral rotations are in opposite directions.

surements show a 90° twinned structure where a single twin was refined according to the *Bbcb* space group with lattice parameters $a = 5.5342\,(2)$ Å, $b = 20.9864\,(12)$ Å, $c = 5.5350\,(2)$ Å (see Tab. 4.4). This corroborates the existence of two pseudo-orthorhombic twins and the interpretation of the tetragonal I4/*mmm* system as an average of them. The use of the *Bbcb* + *Acaa* system or alternatively the I4/*mmm* is equivalent in terms of describing the magnetic structure of $Sr_3Ir_2O_7$. In fact, as we will show in Section 4.4.1, the irreducible representations generated by the symmetry operations associated with the different space groups are identical. However, having identified the presence of crystallographic domains will

O3-Ir-O3	178.8(7)	Ir-O3-Ir	156.1(8)
O3-Ir-O1	89.4(4)	O3-Ir-O2	90.6(4)

Table 4.3: Bond angles (deg.) of $Sr_3Ir_2O_7$ at 293(2) K, in the I4/*mmm* space group.

Atom	Site	x	y	z	U_{iso}(Å^2)
Ir	$8f$	1/2	0.09741(4)	0	0.0104(3)
Sr1	$4a$	1/2	0	1/2	0.0135(6)
Sr2	$8f$	1/2	0.31251(5)	0	0.0125(4)
O1	$8f$	1/2	0.19471(4)	0	
O2	$4b$	1/2	0	0	
O3	$16i$	0.2118(3)	0.09669(6)	0.2125(5)	

Table 4.4: Atomic coordinates and isotropic displacement parameters of $Sr_3Ir_2O_7$ at 293(3) K, in the *Bbcb* space group; $a = 5.5342(2)$ Å, $b = 20.9864(12)$, $c = 5.5350(2)$ Å, and $V = 642.85(5)$ Å^3. Reliability factors: $R = 0.061$, $wR = 0.077$.

be useful to interpret the magnetic domains observed in $Sr_3Ir_2O_7$ (Section 4.4.3), which appear to be strongly correlated with the crystal structure.

4.3 Overview of bulk properties

$Sr_3Ir_2O_7$ displays bulk properties similar to the single layer compound Sr_2IrO_4. The first report by Cao et al. [33] established, in fact, that $Sr_3Ir_2O_7$ it is barely an insulator which exhibits weak ferromagnetism in the basal plane below $T_C \sim 285$ K. Fig. 4.3(a) shows the resistivity ρ as a function of temperature for the basal plane and the c axis. In analogy with Sr_2IrO_4 (see for example Fig. 3.2(a)), the resistivity shows a semiconductor-like behaviour in both directions. However, in the bilayer compound, the resistivity is significantly reduced, reflecting the more metallic nature of the system. Furthermore, a significant increase of ρ at $T_C \sim 285$ K, concomitant with the onset of the weak ferromagnetism, suggests a coupling of magnetic and transport properties.

Concerning the magnetization data, a weak ferromagnetic component appears in the *ab*-plane at $T_C \sim 285$ K, and a second transition, resulting in a further increase in magnetization, occurs at $T^\star \sim 260$ K, attributed to a spin-reorientation (see Fig. 4.3(b)). The magnetic moment reported at 150 K in an applied field of 7 T is less than 0.003 μ_B/Ir [33], much smaller than the corresponding magnetic moment in Sr_2IrO_4 ($\sim$0.07 μ_B/Ir) [103]. The effective moment, deduced from a high-temperature Curie-Weiss fit to the magnetic susceptibility χ in a field of 7 T, was reported to be 0.67 μ_B/Ir, comparable to the value of 0.5 μ_B/Ir found in Sr_2IrO_4 [32]. These results indicate a similar microscopic magnetism in the Sr-based layered iridates but a different origin of the weak ferromagnetic components in the two compounds.

Fig. 4.3(b) shows the basal plane magnetization M at 0.01 T in a zero field cooled (ZFC) and field cooled (FC) sequence measured by Cao et al. [33]. The inset shows the magnetization behaviour for field cooling at different temperatures. The most notable features of these data are the onset of a weak ferromagnetic component at $T_C \sim 285$ K with a further increase of the magnetization at $T^\star \sim 260$ K. Below $T_D = 50$ K there is a downturn in the magnetization which becomes negative below 20 K. This behaviour is strongly dependent on the field cooling temperature and is absent in the ZFC measurements where no anomalies are observed.

In order to understand the link between the macroscopic physics and the microscopic properties determined by X-ray scattering techniques, we performed magnetization measurements on $Sr_3Ir_2O_7$ samples grown at Clarendon Laboratories (sample A) and at the Edinburgh University (sample B). The bulk magnetization data were collected using a Quantum Design MPMS-7 superconducting quantum interference device (SQUID) magnetometer, at the London Centre for Nanotechnology, UCL, London, UK. Fig. 4.3(c) shows the magnetization M (μ_B/Ir) as a function of temperature T, measured in the basal plane for sample A. Field-cooled (FC) measurements were made on cooling in an applied magnetic field, ranging from 0.05 to 0.5 T. On inspection of the FC data, it is clear that there are two transitions at high temperature, T_C and $T^\star$, with a downturn in the magnetization at low temperature, beginning at $\sim$50 K. This downturn becomes an upturn in M at higher fields and could be interpreted as a canting of magnetic moments in the direction of the applied field. From the second derivative of the 0.005-T FC data, we calculated $T_C = 275$ K and $T^\star = 230$ K.

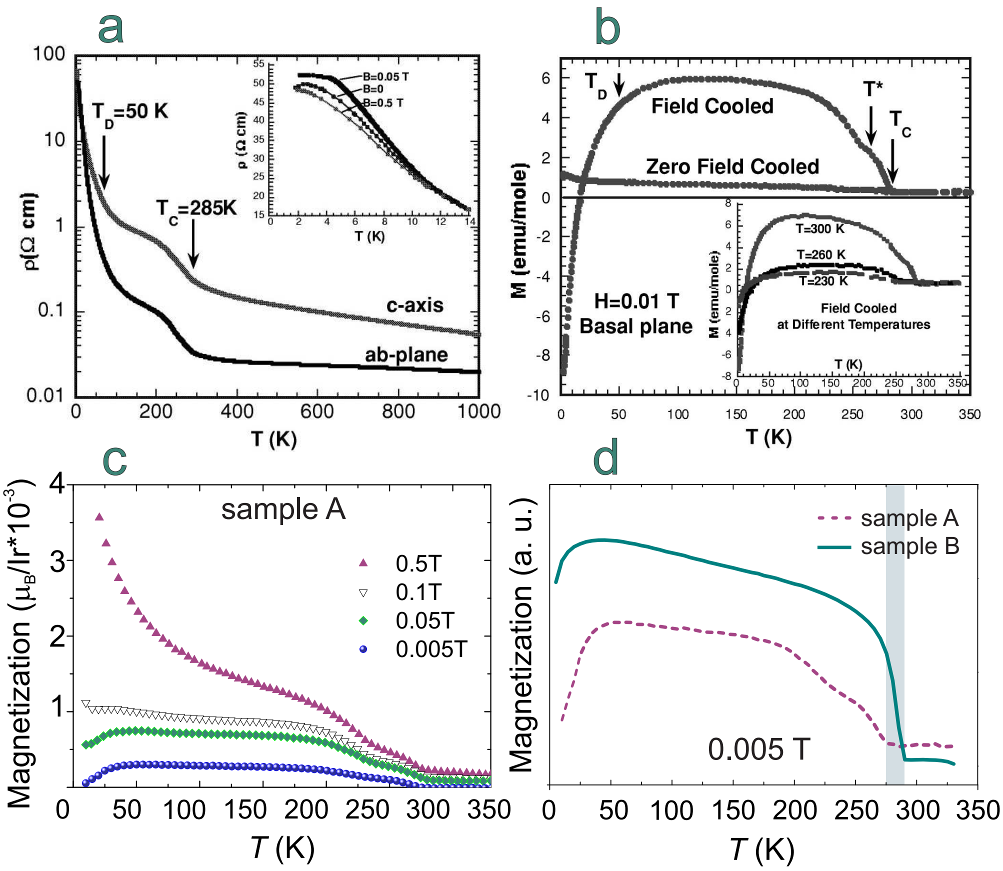

Figure 4.3: (a) Resistivity ρ as a function of temperature for the basal plane and the c axis. Inset: ρ vs T at $B = 0$, 0.05, and 0.5 T. (b) Magnetization M for the basal plane as a function of temperature at 0.01 T. Inset: M vs T measured using the field-cooled (FC) sequence that starts at $T = 300$, 260, and 230 K, respectively. Panel (a) and (b) are reproduced from Ref. [33]. (c) SQUID magnetization data, as a function of temperature for FC measurements in the basal plane, ranging from 0.005 to 0.5 T applied magnetic field for the single crystals grown at the Clarendon Lab, Oxford (sample A). Two transitions can be observed at high temperature along with a downturn in the magnetization at 50 K, which becomes a positive upturn as the field is increased. (d) Comparison between the 0.005 T magnetization data relative to sample A (purple dashed line)and sample B, grown at the University of Edinburgh (green line).

These data are qualitatively similar to those reported previously by Cao et al. [33]. The lower transition temperatures in our case may be due to variations in the sample quality or small differences in oxygen stoichiometry between the two studies. Fig. 4.3(d) shows a comparison of the 0.005-T FC data of sample A and sample B. The data are qualitatively similar although for sample B the $T^{\star}$ transition is absent and the downturn of the magnetization below 50 K is less pronounced. Furthermore, the onset of the ferromagnetic component takes place at slightly higher temperature in sample B ($T_{\mathrm{C}} \sim 290$ K). For both samples the ZFC measurements (not shown here) closely resemble the FC data in contradiction with Ref. [33] but in agreement with later reports [41]. The reversal of magnetization below 20 K was not observed in our data in analogy with Ref. [41].

The peculiar temperature dependence of magnetization in $Sr_3Ir_2O_7$ and the differences among various studies seems to suggest that the weak ferromagnetism could originate from an extrinsic moment produced by defects rather than a canting mechanism as in the single layer counterpart. As we will show in the next sections, the canting picture is in fact inconsistent with the observed magnetic and crystal structure.

4.4 Magnetic and electronic properties

The work presented in this section has been published as "*Antiferromagnetic order and domains in* $Sr_3Ir_2O_7$ *probed by X-ray resonant scattering*" by S. Boseggia, R. Springell, H. C. Walker, A. T. Boothroyd, D. Prabhakaran, D. Wermeille, L. Bouchenoire, S. P. Collins, and D. F. McMorrow, Phys. Rev. B **85**, 184432 (2012) [15].

In order to unravel the electronic and magnetic properties of the ground state in $Sr_3Ir_2O_7$, we performed a detailed XRMS study at the Ir L_2 and L_3 edge. XRMS experiments were conducted at the I16 beamline of the Diamond Light Source, Didcot, UK, and at the BM28 (XMaS) beamline [104] at ESRF, Grenoble, France. The experimental set-up of I16 has already been described in detail in Section 2.4.1. At the BM28 bending magnet beamline the photon energy was selected using a double-bounce Si (111) monochromator, and higher order harmonics were rejected by rhodium-coated mirrors, providing a beam footprint of $\sim 300 \times 800$ μm^2 at the sample position. The diffractometer was a vertical scattering Eulerian cradle type with a Si-drift vortex detector mounted on the 2θ (detector) arm. The degree of linear polarization in the plane of the storage ring (referred to as σ-polarized light) was close to 100%. In both cases the samples were mounted in Displex cryostats with the $[0\,0\,1]$ direction (perpendicular to the sample surface) and the $[1\,1\,0]$ direction in the vertical scattering plane. A Au $(3\,3\,3)$ analyzer was exploited to analyze the outgoing polarization for both edges.

The samples grown at the Clarendon Lab (sample A) and at the Edinburgh University (sample B) do not show any significant variation in the magnetic structure but do exhibit different magnetic transition temperatures. In the following we will therefore refer exclusively to sample A and the difference between the samples will be discussed only in Section 4.4.2. The tetragonal I4/*mmm* reference system will be used and reference to the corresponding orthorhombic *Bbcb* space group will be given if needed.

4.4.1 Ordering wave vector

The crystal mosaic, determined from the full width at half maximum (FWHM) of the specular reflection $(0\,0\,24)$ in the unrotated σ-σ channel, was 0.044°. In the σ-π rotated channel with the energy of the incoming beam tuned in correspondence of the Ir L_3 edge, peaks were found at the $(\frac{1}{2}\,\frac{1}{2}\,l)$ positions of the I4/*mmm* space group. Fig. 4.4(a) shows magnetic Bragg peaks over a wide range of l, with $(h\,k)$ fixed at $(\frac{1}{2}\,\frac{1}{2})$. These positions are crystallographically forbidden and imply that Ir magnetic moments are ordered antiferromagnetically within an IrO_2 plane. The magnetic cell is thus doubled in the basal-plane and described by the magnetic propagation vector $\mathbf{k} = [\frac{1}{2}\,\frac{1}{2}\,0]$. Examples of these peaks at the $(\frac{1}{2}\,\frac{1}{2}\,23)$ and $(\frac{1}{2}\,\frac{1}{2}\,24)$ reflections are shown in Fig. 4.4(b), as measured on I16 at 60 K at the L_3 edge, in reciprocal lattice units (r.l.u). σ-π intensity is shown as the full green circles and σ-σ intensity as the open purple diamonds. As expected from pure magnetic scattering no signal is evident in the σ-σ channel. The solid line is a fit to a Lorentzian peak shape for each reflection in the σ-π channel. FWHM values of 0.031(4) and 0.024(3) r.l.u were found for the $(\frac{1}{2}\,\frac{1}{2}\,23)$ and $(\frac{1}{2}\,\frac{1}{2}\,24)$ reflections, respectively. From a comparison with the nearby charge reflection (0 0 24) (orange line in Fig. 4.4(b)) we conclude that the magnetic peaks are at the resolution limit and that the long range order extends for at least 200 Å along the c direction ($\xi_{\mathrm{MAG}} \geq 215$ Å)[1]. As we shall show, the scattering intensity at both $l = even$ and $l = odd$ positions is due to the presence of magnetic domains. The strong modulation of the scattering intensity as a function of l reflects the bilayer magnetic structure factor that is expected to have a periodicity $1/b = 5.1335$ Å^{-1}, where b represents the interlayer distance within a bilayer.

In order to determine the magnetic structure compatible with the observed magnetic propagation vector $\mathbf{k} = [\frac{1}{2}\,\frac{1}{2}\,0]$ we performed representation analysis using the SARAh package [94], in analogy with Section 3.3. As input parameters we used the space group I4/mmm and the Ir atomic positions obtained from the refinement of the crystal structure (Section 4.2). The results of the calculation are given in Tab. 4.5. The possible irreducible representations (IRs) Γ_i involve either an antiferromagnetic (AF) interlayer coupling (Γ_{2n}) or a ferromagnetic (FM) interlayer coupling (Γ_{2n+1}), where the magnetic moments point along the [0 0 1] direction ($\Gamma_{2,3}$), [1 1 0] direction ($\Gamma_{5,6}$), or [1 $\bar{1}$ 0] direction ($\Gamma_{7,8}$). The scattering intensity observed at the $(\frac{1}{2}\,\frac{1}{2}\,l)$ positions can be explained by these IRs and by decomposing the propagation vector $\mathbf{k} = [\frac{1}{2}\,\frac{1}{2}\,0]$ into the two arms $\mathbf{k}_A = [\frac{1}{2}\,\frac{1}{2}\,0]$ and $\mathbf{k}_B = [\frac{1}{2}\,\text{-}\frac{1}{2}\,0]$ responsible for the magnetic reflections $(\frac{1}{2}\,\frac{1}{2}\,2n)$ and $(\frac{1}{2}\,\frac{1}{2}\,2n + 1)$, respectively. The resulting magnetic structure then consists of two domains, which have intensity for even (domain A) or odd (domain B) l peaks, respectively.

Fig. 4.5 shows the h, k reciprocal space map for $l = 2n$ (a) and $l = 2n+1$ (b). The green circles and the orange squares are the magnetic peaks associated with the magnetic propagating vector $\mathbf{k}_A = [\frac{1}{2}\,\frac{1}{2}\,0]$ and $\mathbf{k}_B = [\frac{1}{2}\,\text{-}\frac{1}{2}\,0]$, respectively. In order to disentangle the contribution of the two domains one can keep fixed the in-plane component of the momentum

---

[1] ξ_{MAG} is estimated as in Section 3.3.2

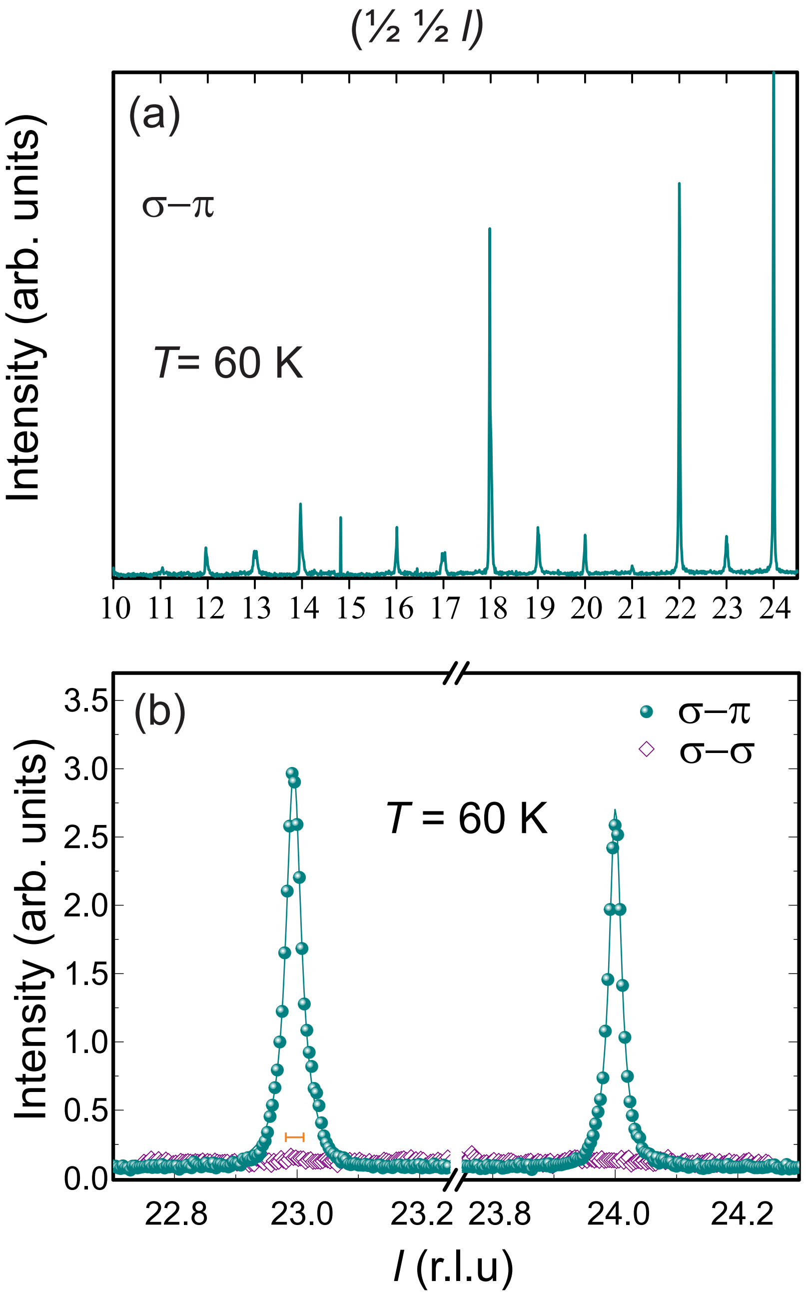

Figure 4.4: (a) l-scan profile along the $(\frac{1}{2}\,\frac{1}{2}\;l)$ direction in the σ-π channel at $T = 60$ K in $Sr_3Ir_2O_7$. (b) l-scan profile of the $(\frac{1}{2}\,\frac{1}{2}\,23)$ and $(\frac{1}{2}\,\frac{1}{2}\,24)$ magnetic reflections in the σ-σ (purple open diamonds) and σ-π (light green spheres) polarization channels. The light green line and the orange line represent a fit to a Lorentzian function and the resolution function, respectively.

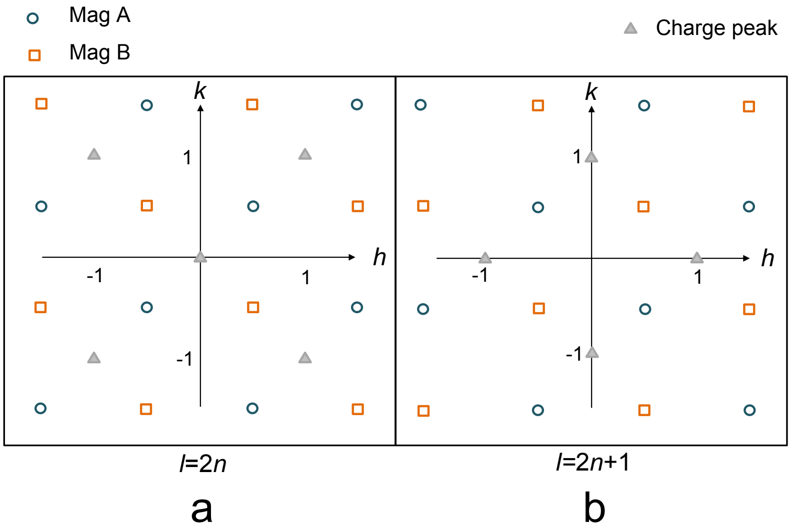

Figure 4.5: Reciprocal space map at constant $l = 2n$ (a) and $l = 2n + 1$ (b). The grey triangles represent charge peak. The green circles (orange squares) are the magnetic peaks associated with the magnetic propagating vector $\mathbf{k}_A = [\frac{1}{2}\,\frac{1}{2}\,0]$ ($\mathbf{k}_B = [\frac{1}{2}\,\text{-}\frac{1}{2}\,0]$).

$\mathbf{k}_{h,k} = [\frac{1}{2}\,\frac{1}{2}]$ and vary the out-of-plane l component.

It should be noted that the choice of the orthorhombic $Bbcb$ space group instead of the high-symmetry tetragonal space group I4/mmm, could in principle lead to different results in terms of IRs due to the different symmetry operations in the space groups. We therefore performed representational analysis using the $Bbcb$ space group and the magnetic propagation vector $\mathbf{k} = [1\,0\,0]$, which is equivalent to $\mathbf{k} = [\frac{1}{2}\,\frac{1}{2}\,0]$ in the I4/mmm reference system. The resulting IRs, shown in Appendix B, are identical to the ones given in Tab. 4.5 for the I4/mmm space group. Remarkably, for both the I4/mmm and $Bbcb$ systems, only collinear magnetic structures are allowed with no evidence of a canted antiferromagnetic state.

We now turn to the l-dependence of the magnetic scattering, in order to extract the relative phase of the interlayer coupling within a bilayer by calculating the magnetic structure factor. The magnetic atoms in the unit cell are located at the positions: $\mathrm{Ir}_1 = (0, 0, -z)$, $\mathrm{Ir}_2 = (0, 0, z)$, $\mathrm{Ir}_3 = (\frac{1}{2}, \frac{1}{2}, \frac{1}{2} - z)$ and $\mathrm{Ir}_4 = (\frac{1}{2}, \frac{1}{2}, \frac{1}{2} + z)$ (see Fig.4.11). The squared mag-

IR	BV	Atom	BV components					
			$m_{\parallel a}$	$m_{\parallel b}$	$m_{\parallel c}$	$im_{\parallel a}$	$im_{\parallel b}$	$im_{\parallel c}$
Γ_2	ψ_1	1	0	0	1	0	0	0
		2	0	0	-1	0	0	0
Γ_3	ψ_2	1	0	0	1	0	0	0
		2	0	0	1	0	0	0
Γ_5	ψ_3	1	1	1	0	0	0	0
		2	1	1	0	0	0	0
Γ_6	ψ_4	1	1	-1	0	0	0	0
		2	-1	1	0	0	0	0
Γ_7	ψ_5	1	1	-1	0	0	0	0
		2	1	-1	0	0	0	0
Γ_8	ψ_6	1	1	1	0	0	0	0
		2	-1	-1	0	0	0	0

Table 4.5: Basis vectors for the space group I4/*mmm* with $\mathbf{k}=[\frac{1}{2}\,\frac{1}{2}\,0]$. The decomposition of the magnetic representation for the Ir site (0, 0, .09743) is $\Gamma_{Mag} = 0\Gamma_1^1{+}1\Gamma_2^1{+}1\Gamma_3^1{+}0\Gamma_4^1{+}1\Gamma_5^1{+}1\Gamma_6^1{+}1\Gamma_7^1{+}1\Gamma_8^1$. The atoms of the nonprimitive basis are defined according to 1: (0, 0, .09743), 2: (0, 0, .90257).

netic structure factor for a generic $(h\,k\,l)$ reflection can be calculated as

$$\left|\mathcal{F}_{(hkl)}\right|^2 \propto \left|\sum_j \frac{e^{i2\pi\mathbf{K}\cdot\mathbf{r}_j}\mathcal{A}_j}{|\mathcal{A}_j|}\right|^2 , \tag{4.1}$$

where r_j is the coordinate of the magnetic atoms in the unit cell, and $\mathcal{A}_j$ is the atomic scattering amplitude. We therefore distinguish four possible cases.

1. For $\mathcal{A}_2 = \mathcal{A}_3 = -\mathcal{A}_1 = -\mathcal{A}_4$, the magnetic structure factor squared reads

$$\begin{aligned}\left|\mathcal{F}^{\mathrm{A,AF}}_{(hkl)}\right|^2 &\propto \left|e^{i2\pi lz} - e^{-i2\pi lz} + e^{i2\pi(\frac{h}{2}+\frac{k}{2}+\frac{l}{2}-lz)} - e^{i2\pi(\frac{h}{2}+\frac{k}{2}+\frac{l}{2}+lz)}\right|^2 \\ &\propto \left|2i\sin(2\pi lz)\left(1-e^{i2\pi(\frac{h}{2}+\frac{k}{2}+\frac{l}{2})}\right)\right|^2 ,\end{aligned} \tag{4.2}$$

which for $h,k = \frac{1}{2}$ becomes

$$\left|\mathcal{F}^{\mathrm{A,AF}}_{(\frac{1}{2}\,\frac{1}{2}\,l)}\right|^2 \propto \left|2i\sin(2\pi lz)\left(1+e^{i\pi l}\right)\right|^2 . \tag{4.3}$$

2. For $\mathcal{A}_1 = \mathcal{A}_2 = -\mathcal{A}_3 = -\mathcal{A}_4$,

$$\left|\mathcal{F}^{\mathrm{A,FM}}_{(\frac{1}{2}\,\frac{1}{2}\,l)}\right|^2 \propto \left|2\cos(2\pi lz)\left(1+e^{i\pi l}\right)\right|^2 . \tag{4.4}$$

3. For $\mathcal{A}_2 = \mathcal{A}_4 = -\mathcal{A}_1 = -\mathcal{A}_3$,

$$\left|\mathcal{F}^{\mathrm{B,AF}}_{(\frac{1}{2}\,\frac{1}{2}\,l)}\right|^2 \propto \left|2i\sin(2\pi lz)\left(1-e^{i\pi l}\right)\right|^2 . \tag{4.5}$$

4. For $\mathcal{A}_1 = \mathcal{A}_2 = \mathcal{A}_3 = \mathcal{A}_4$,

$$\left|\mathcal{F}^{\mathrm{B,FM}}_{(\frac{1}{2}\,\frac{1}{2}\,l)}\right|^2 \propto \left|2\cos(2\pi lz)\left(1-e^{i\pi l}\right)\right|^2 . \tag{4.6}$$

The first term of Eq. 4.3-4.6 is a $\sin^2$ ($\cos^2$) of periodicity $1/2z = 5.1335$, which represents the bilayer modulation due to interlayer AF (FM) coupling. The second term of Eqs. 4.3–4.4 vanishes only for $l = odd$ and therefore explains the magnetic reflections $(\frac{1}{2}\,\frac{1}{2}\,2n)$ observed for the magnetic domain A. The second term of Eqs. 4.5–4.6 is zero only for $l = even$ and thus explains the magnetic reflections $(\frac{1}{2}\,\frac{1}{2}\,2n+1)$ observed for the magnetic domain B. Fig. 4.6(a) shows the calculated magnetic structure factor $|\mathcal{F}^{\mathrm{A}}_{(\frac{1}{2}\frac{1}{2}l)}|^2$ as a function of l relative to the magnetic domain A. The green (purple dashed) line represents AF (FM) ordering between two neighboring IrO_2 planes. Fig. 4.6(b) shows the calculated magnetic structure factor $|\mathcal{F}^{\mathrm{B}}_{(\frac{1}{2}\frac{1}{2}l)}|^2$ as a function of l relative to the magnetic domain B for AF (orange line) and FM (grey dashed line) ordering, respectively. It is clear that the experimental data of Fig. 4.4 closely resemble the behaviour of a two-domain picture with AF interlayer coupling.

In order to make a more precise comparison between theory and experiment we have carefully measured several $(\frac{1}{2}\,\frac{1}{2}\,2n)$ peaks relative to the magnetic domain A. The integrated intensity corrected for absorption according to Eq. 3.2 is plotted in Fig. 4.6(c) and represented by purple spheres. The experimental data can be modelled with great accuracy by the magnetic structure factor of Eq. 4.3 and by calculating explicitly the atomic scattering amplitude $\mathcal{A}$ according to Eq. 2.25 for magnetic moments pointing along the c axis. We therefore conclude that the coupling between neighbour IrO_2 layers is antiferromagnetic and $Sr_3Ir_2O_7$ is a G-type antiferromagnet.

4.4.2 Order parameter

In order to determine the transition temperature of the magnetic ordering and the type of phase transition occurring in $Sr_3Ir_2O_7$, we measured the intensity of the $(\frac{1}{2}\,\frac{1}{2}\,24)$ and $(\frac{1}{2}\,\frac{1}{2}\,23)$ reflections as a function of temperature in proximity of the L_3 edge resonance in the rotated σ-π channel for sample A. Fig. 4.7 (a) shows the integrated intensity of θ-2θ scans at the $l = 23, 24$ peaks along with FC SQUID magnetization data, measured in 0.005 T. The transition appears to be second order with a Néel transition to a commensurate antiferromagnet at $T_\mathrm{N} \approx 230$ K. This is very close to the transition $T^\star$ observed in the bulk magnetization data shown in Fig. 4.7(a) and described in Section 4.3. However, the same measurements on the samples grown at the Edinburgh University (sample B) show that the onset of the long range order magnetic scattering at T_N is closely related to the first temperature transition $T_\mathrm{C} \approx 290$ K observed in the SQUID data (see Fig. 4.7(b). We believe that the lower Néel temperature T_N in sample A could be due to differences in the oxygen stoichiometry. The magnetic signal measured in the SQUID data at $T_\mathrm{C} \approx 285$ K in sample A could be due to some local field, and the system is long-range ordered only below $T_\mathrm{N} \approx 230$ K.

The unusual low-temperature behavior of the magnetization ($T < 50$ K) seen in Fig. 4.3 is dependent on the applied field, and could suggest a canting mechanism away from the direction of the ordered magnetic moments. This would indicate that the zero-field antiferromagnetic ordering does not change at low temperature. In order to verify this, we carried out several measurements from 20 to 70 K, shown as the solid grey triangles in Fig. 4.7 (a), which are approximately constant in intensity.

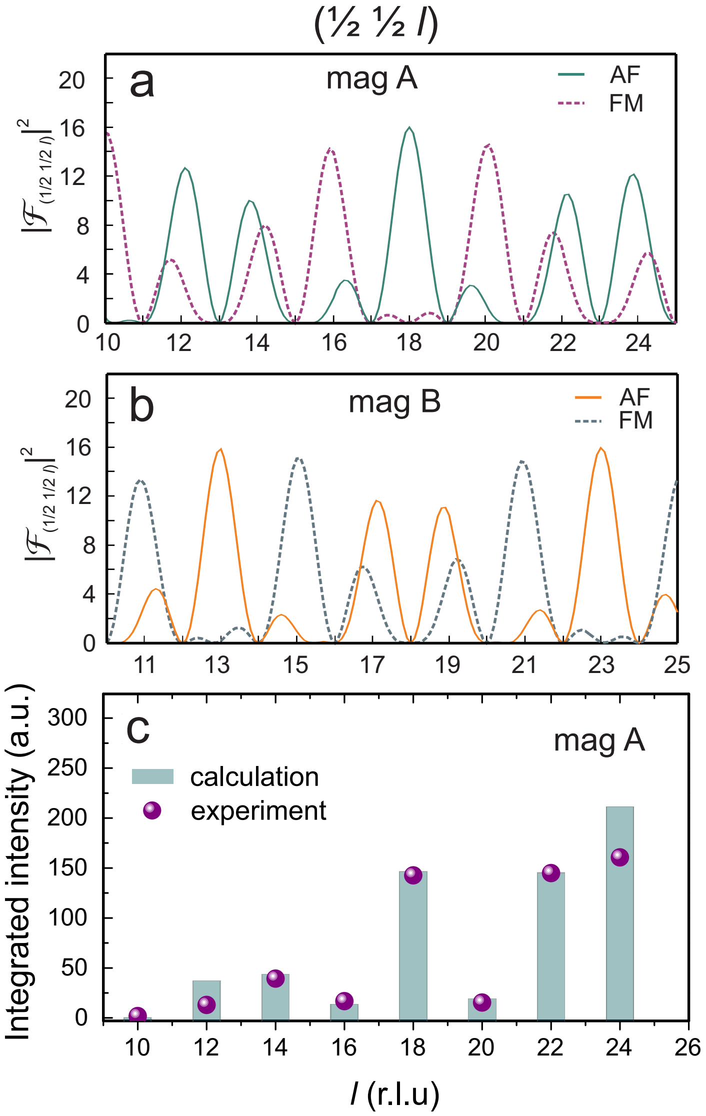

Figure 4.6: (a) Calculated magnetic structure factor $|\mathcal{F}_{(\frac{1}{2}\frac{1}{2}l)}|^2$ as a function of l for the magnetic domain A. The green (purple dashed) line represents AF (FM) ordering between two neighboring IrO_2 planes. (b) Calculated magnetic structure factor $|\mathcal{F}_{(\frac{1}{2}\frac{1}{2}l)}|^2$ as a function of l for the magnetic domain B. The orange (grey dashed) line represents AF (FM) ordering between two neighboring IrO_2 planes. (c) l-scan across the $(\frac{1}{2}\ \frac{1}{2}\ l)$ magnetic reflections at $T = 60$ K for the magnetic domain A. The purple spheres represent the integrated intensity of the measured magnetic scattering, whilst the heights of the light blue bars represent the calculated intensity for the magnetic scattering as discussed in the text.

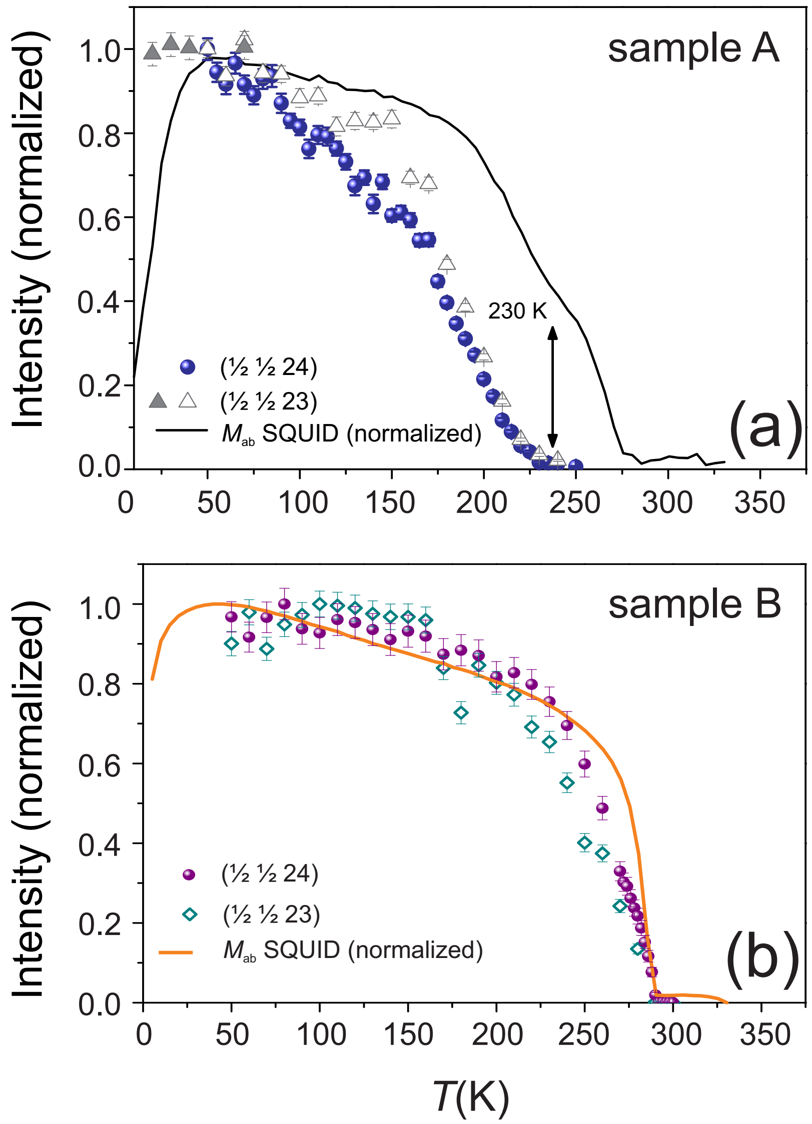

Figure 4.7: (a) The temperature dependence of the $(\frac{1}{2}\,\frac{1}{2}\,24)$ (blue spheres) and $(\frac{1}{2}\,\frac{1}{2}\,23)$ (grey open triangles) peaks , measured on sample A at the L_3 edge on the BM28 beamline, compared to the SQUID magnetization data. The transition temperature of the observed magnetic reflections, determined by XRMS, coincides with the second transition, $T^\star = 230$ K, in the bulk magnetization data. The solid grey triangles show additional low-temperature data down to 20 K. (b) The temperature dependence of the $(\frac{1}{2}\,\frac{1}{2}\,24)$ (purples spheres) and $(\frac{1}{2}\,\frac{1}{2}\,23)$ (green open diamonds) peaks, measured on sample B at the PO9 beamline of Petra III, is compared to the SQUID magnetization data. In this case the onset of antiferromagnetism determined by XRMS coincides with transition at $T_C = 290$ K in the SQUID data.

4.4.3 Imaging magnetic domains

In order to investigate the possibility of domains of odd (even) l in our samples, we compared the intensities of several magnetic reflections. The similar intensities of the $(\frac{1}{2}\,\frac{1}{2}\,24)$ and $(\frac{1}{2}\,\frac{1}{2}\,23)$ peaks measured on the XMaS beamline suggest that if the two-domain picture is correct then the domains are significantly smaller than the 300×800 μm^2 beam size utilized on BM28. An approximately equivalent number of these domains would then be illuminated at each of the peak positions. On the I16 beamline, however, the x rays are much more tightly focused at the sample position. The beam spot is reduced, using a pair of parallel double focusing mirrors and slits, which results in a footprint on the sample surface of 18×100 μm^2. In this case, we observed large differences in the intensities of odd (even) l magnetic reflections as a function of the spatial coordinates.

In order to image the intensity of these magnetic reflections over a selected sample volume we performed a raster in x and y sample position at the $l = 23, 24$ magnetic reflections, at the L_3 edge peak resonance energy at 40 K. Fig. 4.8(a) shows contour plots of the $(\frac{1}{2}\,\frac{1}{2}\,24)$ and $(\frac{1}{2}\,\frac{1}{2}\,23)$ reflections over a 100×300 μm^2 area of the sample. The results are clear; in regions of the sample where there is little to no intensity of the $l = 24$ peak there is a maximum in the intensity of the $l = 23$ peak and vice versa. Domains of odd and even l persist throughout the sample. This is not difficult to imagine, since the only difference between the two ordering wave vectors $\mathbf{k}_{\mathrm{A}}$ and $\mathbf{k}_{\mathrm{B}}$ is the respective orientation of one magnetic bilayer to another and these are of equivalent energy cost. These images indicate a domain size of approximately 100×100 μm^2 and confirm the calculations and results presented in Section 4.4.1, supporting the determination of the magnetic structure.

Furthermore, we investigated the temperature dependence of the magnetic domain population. Figure 4.8(b) shows the domain pattern for the $(\frac{1}{2}\,\frac{1}{2}\,24)$ peak, rastered over an area of approximately 1 mm^2 at 90 K, well below the transition temperature, heated above the Néel transition to 300 K and then cooled back to 90 K, revealing domains that are independent of the thermal history. For these measurements, the X-ray beam size was further reduced to 20×50 μm^2 (V×H) by a set of slits.

The independence of the magnetic domain population on the thermal history suggests that the magnetic domains are locked to the crystal structure and probably associated to the crystallographic twins *Bbcb* and *Acaa*. An unambiguous proof of this could be obtained by mapping the crystallographic twins by looking at Bragg reflections representative only of one specific space group. In fact, the *Bbcb* and *Acaa* structures show l-dependent extinction rules of charge scattering similar to the one observed for magnetic scattering relative to A and B domains. Bragg peaks corresponding to the correlated rotation of the oxygen octahedra can be detected at the $(\frac{3}{2}\,\frac{1}{2}\,l)$ positions (in the tetragonal reference system) with $l = 2n$ $(2n+1)$ for the *Bbcb* (*Acaa*) space group. The $(\frac{3}{2}\,\frac{1}{2}\,l)$ reflections are also allowed for magnetic scattering since the magnetic propagation vector has the form $\mathbf{k}=[\frac{1}{2}\,\frac{1}{2}\,0]$. The contribution of magnetic scattering can be minimized by measuring in the σ-σ scattering channel. We have observed examples of these peaks, which contain both charge and magnetic contributions, but a complete 2D-map as a function of the sample position has not been measured. The intrinsic weakness of these oxygen-related reflections requires the use of synchrotron radiation light.

4.4.4 Spin-flop transition

The work presented in this section has been published as "*On the magnetic structure of* $Sr_3Ir_2O_7$*: an X-ray resonant scattering study*" by S. Boseggia, R. Springell, H. C. Walker, A. T. Boothroyd, D. Prabhakaran, S. P. Collins, and D. F. McMorrow, J. Phys.: Condens. Matter **25**, 422202 (2013) [105].

In the previous sections we have investigated the magnetic structure of $Sr_3Ir_2O_7$. Our study has established some essential features of the electronic and magnetic properties of $Sr_3Ir_2O_7$: $Sr_3Ir_2O_7$ is a G-type antiferromagnet below 290 K. Magnetic domains associated with two different arms of the propagation vector $\mathbf{k} = [\frac{1}{2}\,\frac{1}{2}\,0]$ have been mapped as a function of the sample spatial coordinates.

The following section aims to fully explore the azimuthal and polariza-

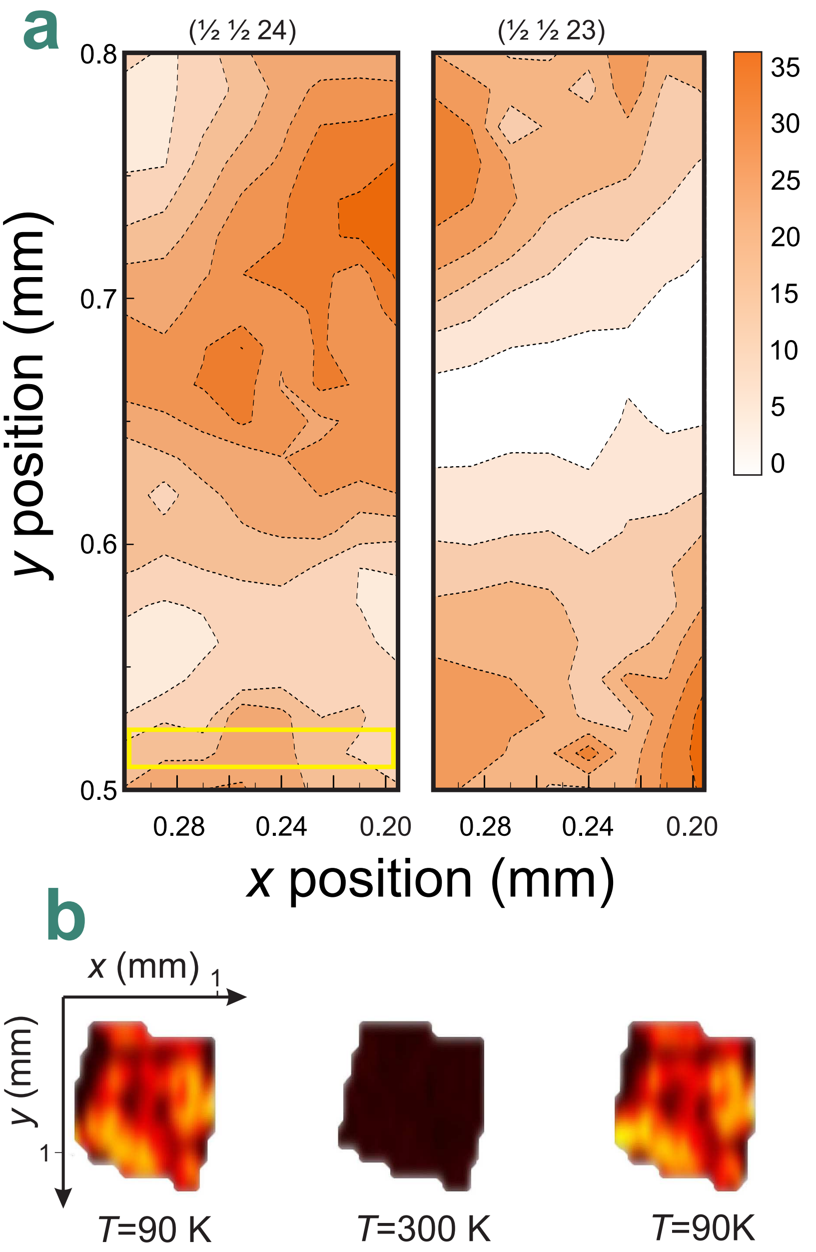

Figure 4.8: (a) Intensity of the $(\frac{1}{2}\,\frac{1}{2}\,24)$ reflection (left panel) and $(\frac{1}{2}\,\frac{1}{2}\,23)$ reflection (right panel), as a function of x and y sample position. These measurements were made at the L_3 edge resonance at a temperature of 40 K, well below the Néel temperature $T_{\mathrm{N}} = 230$ K. The beam size projected on the sample surface is highlighted by the yellow rectangle in the left-hand panel. (b) The intensity of the $(\frac{1}{2}\,\frac{1}{2}\,24)$ reflection, measured as a function of x and y sample position in a temperature sequence 90 K $\rightarrow$ 300 K $\rightarrow$ 90 K. The bright yellow regions are areas of high intensity and the dark areas are close to zero intensity.

tion dependencies of XRMS in order to determine the magnetic moment orientation in $Sr_3Ir_2O_7$. The X-ray magnetic scattering experiment was performed at the I16 beamline, Diamond Light Source, Didcot, UK. A $Sr_3Ir_2O_7$ single crystal was mounted on a boron capillary and a nitrogen gas jet cooler was exploited to avoid mechanical vibrations that might produce uncertainty in the sample position with respect to the incident X-ray beam. The sample was oriented with the [0 0 1] direction perpendicular to the sample surface and the [0 1 0] direction lying in the scattering plane at the azimuthal origin. An horizontal scattering geometry (π polarized incident beam) was used for the polarization analysis whereas a vertical scattering geometry (σ polarized incident beam) was exploited for measuring the azimuthal scans. The experimental geometry is illustrated in Fig. 4.9(d).

The magnetic domains of size $\sim 100\,\mu\text{m} \times 100\,\mu\text{m}$ observed in $Sr_3Ir_2O_7$ makes the use of azimuthal scans very challenging since the rotation about the scattering vector $\mathbf{K}$ changes the relative position between sample and beam. In order to minimize any systematic error deriving from the simultaneous illumination of different domains, we performed polarization analysis at two different azimuthal angles in horizontal scattering geometry, keeping the polarization of the incoming photons (π polarization) fixed and varying continuously the polarization of the scattered beam by rotating the polarization analyzer about the scattering vector by an angle η (see Fig. 4.9(d)). By looking at Eq. 2.25 we notice that using σ polarized incoming light, the cross product $\boldsymbol{\epsilon}' \times \boldsymbol{\epsilon}$ is constant and equal to $-\widehat{\mathbf{k}}'$, leaving unchanged the projection of the magnetic moment $\widehat{\mathbf{z}}_j$ with respect to the reference system. On the contrary, using π polarized incoming light, the cross product $\boldsymbol{\epsilon}' \times \boldsymbol{\epsilon}$ in Eq. 2.25 varies in the plane delimited by the vectors $\widehat{\mathbf{k}}$ and $\widehat{\mathbf{k}} \times \widehat{\mathbf{k}}'$ as a function of the analyzer angle η. For instance at $\eta = 0°$ (σ outgoing polarization) XRMS is sensitive only to the projection of the magnetic moment orthogonal to the scattering plane (along $\widehat{\mathbf{u}_2}$). On the contrary, for $\eta = 90°$ (π outgoing polarization), XRMS probes only the projection of the magnetic moment which lies in the scattering plane (along $\widehat{\mathbf{u}_1}$, $\widehat{\mathbf{u}_3}$). In this way one is able to infer the moment orientation by measuring the polarization dependence for two distinct azimuth separated by 90° and comparing it with the theoretical dependence for a

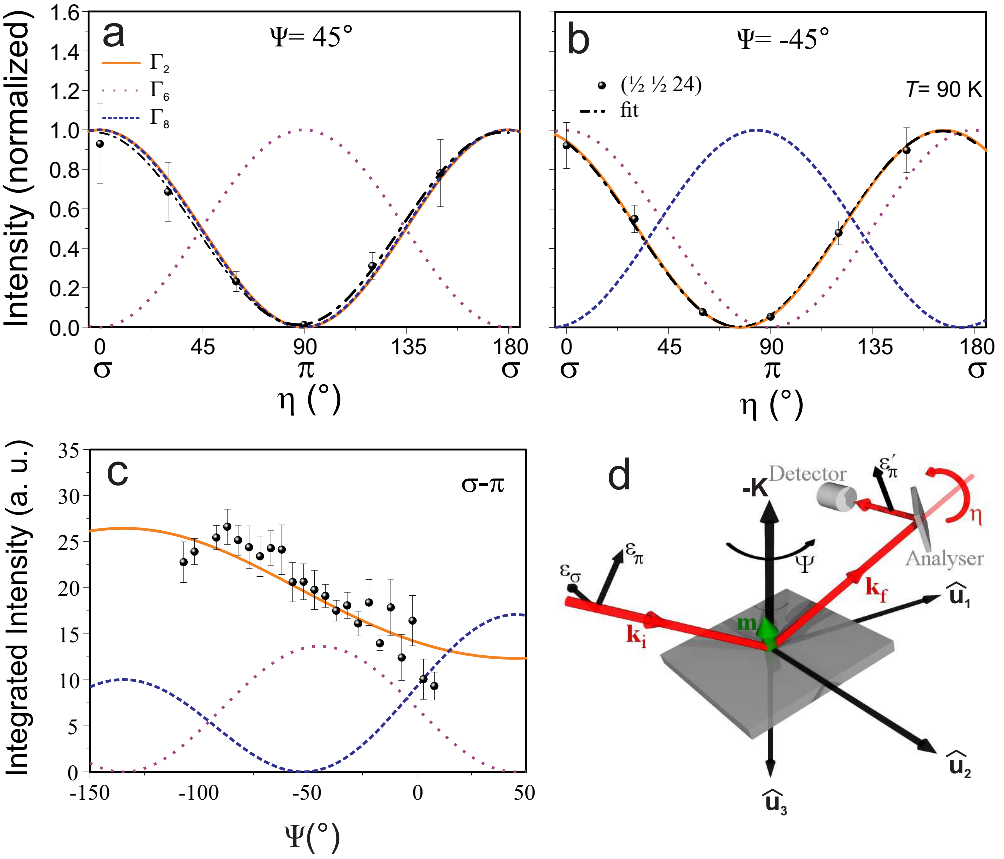

Figure 4.9: Polarization dependence of the $(\frac{1}{2}\,\frac{1}{2}\,24)$ magnetic reflection for two different azimuthal angles Ψ= 45° (a) and Ψ= -45° (b) defined with respect to the reference vector [0 1 0] (π incoming polarization). (c) Azimuthal dependence of the $(\frac{1}{2}\,\frac{1}{2}\,24)$ magnetic reflection at the Ir L_3 edge in the rotated σ-π polarization channel. The solid black spheres represent the integrated intensity of the experimental $(\frac{1}{2}\,\frac{1}{2}\,24)$ magnetic reflection as a function of the analyzser rotation η. The black dashed line is a fit to the equation 4.7. The orange solid line, the purple dotted line and the blue dashed line show the FDMNES calculation relative to the IRs Γ_2, Γ_6 and Γ_8, respectively. (d) The experimental configuration used to perform the azimuthal scans and the polarization analysis measurements. The sample has been oriented with the (0 0 1) and the (0 1 0) reflections lying in the scattering plane, defined by the incoming and outgoing wavevectors. Azimuthal scans were performed in a vertical scattering geometry (σ polarized incident beam) by rotating the sample around the Ψ axis. For domain imaging measurements and the polarization dependence of the X-ray magnetic scattering, a configuration with the [0 0 1] and [0 1 0] directions lying in the horizontal scattering plane was used (π polarized incident beam). The polarization of the scattered beam was scanned between $\eta = 0°$ and 180°, where $\eta = 0°$ corresponds to a σ polarized beam.

precise arrangement of magnetic moments.

Fig. 4.9(a-b) shows calculations for the three IRs $\Gamma_{2,6,8}$ (orange solid, purple dotted and blue dashed lines, respectively) determined in Section 4.4.1 performed by means of the FDMNES software [106] (see Section 4.4.5 for more details), and the integrated intensity of the $(\frac{1}{2}\,\frac{1}{2}\,24)$ magnetic reflection (black solid points) as a function of the analyser rotation, η, for two fixed azimuthal angles, 45° (a) and -45° (b). The dashed black line is a fit to the equation [107, 108]

$$I = \frac{I_0}{2}\left|1 + P_1 \cos 2\eta + P_2 \sin 2\eta)\right|. \tag{4.7}$$

P_1 and P_2 are Poincarè-Stokes parameters, where $P_1 = (I_\sigma - I_\pi)/(I_\sigma + I_\pi)$ and $P_2 = (I_{+45} - I_{-45})/(I_{+45} + I_{-45})$. For a detailed report about the use of the Poincarè-Stokes parameters in magnetic scattering see Ref. [109]. For the 45° (a) azimuth shown in Fig. 4.9(a), only the calculations for the Γ_2 or Γ_8 IRs well replicate the experimental data. In (b) (-45°), it is the Γ_2 and Γ_6 IRs that lie close to the dashed black line, although the Γ_2 representation most precisely follows the data. It is clear that only calculations based on a Γ_2 irreducible representation are able to model the experimental data for both the polarization dependence of the scattered X-rays and the azimuthal dependence. These results indicate that the magnetic moments are aligned along the c axis in the low temperature G-type antiferromagnetic phase, at least for the $(\frac{1}{2}\,\frac{1}{2}\,2n)$ domain probed thus far. In order to determine the orientation of magnetic moments for both domains, we measured the intensity of $(\frac{1}{2}\,\frac{1}{2}\,23)$ and $(\frac{1}{2}\,\frac{1}{2}\,24)$ magnetic reflections as a function of the analyser rotation, η, in a horizontal scattering geometry at $T = 90$ K at the Ir L_3 edge. Data were collected over a wide range of azimuthal angles, Ψ and fitted to Eq. 4.7, these are shown in panels (a) and (c) of Fig. 4.10 for the $l = 23$, 24 reflections, respectively. FDMNES calculations based on the Γ_2 representation were performed in order to model this experimental data and these are shown in panels (b) and (d). The data are well modelled by these calculations, which are based on a two-domain picture of the G-type antiferromagnetic structure with wavevectors $\mathbf{k}_A = [\frac{1}{2}\,\frac{1}{2}\,0]$ and $\mathbf{k}_B = [\frac{1}{2}\,\text{-}\frac{1}{2}\,0]$, with moments aligned collinear along the c axis.

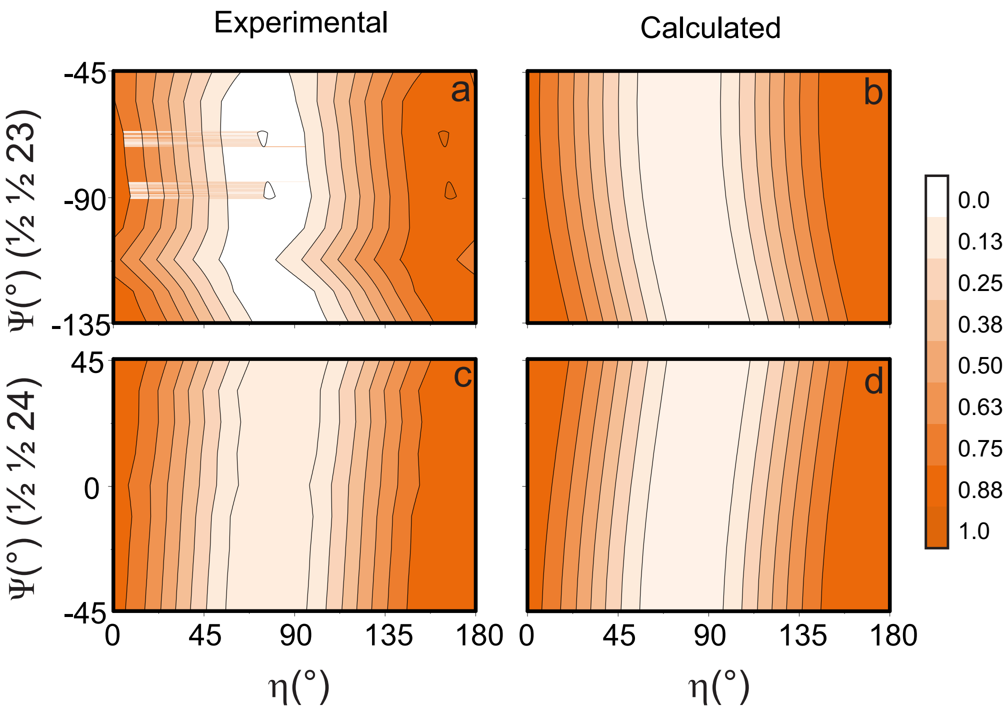

Figure 4.10: The intensity of the $(\frac{1}{2}\,\frac{1}{2}\,23)$ and the $(\frac{1}{2}\,\frac{1}{2}\,24)$ magnetic reflections were fitted to Eq. 4.7 and are shown in panels (a) and (c), respectively. The experimental data were acquired with a π polarized incoming beam at the Ir L_3 edge at 90 K. Panels (b) and (d) show FDMNES calculations for the $(\frac{1}{2}\,\frac{1}{2}\,23)$ magnetic reflection and the $(\frac{1}{2}\,\frac{1}{2}\,24)$ magnetic reflection as a function of the analyser rotation η and the azimuthal angle Ψ.

Similar measurements performed at BM28, ESRF, France, for applied magnetic fields ranging from 0.05 T to 1 T, do not show any variation of the polarization dependence, confirming that the dominant antiferromagnetic order is insensitive to the applied magnetic field.

In order to confirm these observations we investigated the azimuthal dependence of the $(\frac{1}{2}\,\frac{1}{2}\,24)$ magnetic reflection at $T = 90$ K, using the resonant enhancement at the Ir L_3 edge (see Fig. 4.9(c)). The sample was rotated about the scattering vector $\mathbf{K}$ by an angle Ψ and the intensity in the rotated σ-π channel was measured. To avoid to move outside the magnetic domain during the rotation about $\mathbf{K}$, we maximized the XRMS signal by scanning the x, y sample position after each Ψ movement. The integrated intensity of this reflection as a function of azimuthal angle, Ψ, is represented by the solid black points and this has been compared to calculations performed using the FDMNES code for the three possible IRs, $\Gamma_{2,6,8}$ described earlier in the text. It is clear that only the Γ_2 representation, associated with an ordered structure where the magnetic moments point along the [0 0 1]-axis, can adequately model the data. Fig. 4.11 shows representations of the magnetic structures A and B. The magnetic moments are ordered in a G-type antiferromagnetic arrangement with the moments pointing along the c axis. Two of the moments have been highlighted in each case to show the difference between the two magnetic wavevectors $\mathbf{k}_A$ and $\mathbf{k}_B$, responsible for the domain-like nature of the resonant scattering picture.

The spin flop transition taking place when moving from the $n=1$ compound (Sr_2IrO_4) to the $n=2$ compound ($Sr_3Ir_2O_7$) has no analogue in $3d$ transition metal oxides unless accompanied by orbital reconstruction. This is for instance the case in cuprates, where the planar x^2-y^2 ground state cannot support a c-axis magnetic structure once an extra CuO_2 layer is added. By contrast, the "3D" shape of the $j_{\text{eff}}=1/2$ wave function supports naturally directionally-dependent interactions which are strongly sensitive to the number of neighbouring ions. As a consequence, the physics in double-layer iridates is not a simple extension of the physics in the single-layer counterpart. These unique features of magnetism in iridium oxides are strongly related to the spin-orbit entangled wave function that distinguishes this class of materials.

We now discuss our findings in the context of the theoretical models for bilayered systems in the strong spin-orbit coupling regime. As already mentioned in Section 1.5, a good starting point to describe layered iridate is the Hamiltonian 1.48 which we reproduce here for clarity

$$\mathcal{H}_{ij} = J\mathbf{S}_i \cdot \mathbf{S}_j + J_z S_i^z S_j^z + \mathbf{D} \cdot [\mathbf{S}_i \times \mathbf{S}_j] + \mathcal{H}'. \qquad (4.8)$$

The terms on the righthand side are an isotropic Heisenberg superexchange, a pseudo-dipolar (PD) interaction, the antisymmetric Dzyaloshinsky-Moriya (DM) exchange, and finally an anisotropic contribution from the Hund's coupling. $\mathbf{S}_{i,j}$ is a pseudospin operator acting on the $j_{\text{eff}}=1/2$ manifold. This Hamiltonian supports the basal-plane canted (collinear) antiferromagnetic structure observed in Sr_2IrO_4 (Ba_2IrO_4) and predicts a spin-flop transition in Sr_2IrO_4 as a function of the tetragonal crystal field θ. However, in Sr_2IrO_4 the anisotropies due to the PD interaction and DM interaction can be gauged away by a proper site-dependent spin rotation, and the system can be mapped onto a dominant isotropic Heisenberg model with weak anisotropies induced only by the Hunds's coupling term. This is not the case of $Sr_3Ir_2O_7$ where, due to the presence of the interlayer coupling, a full elimination of the twist cannot be carried out, resulting in an intrinsic anisotropy of $Sr_3Ir_2O_7$. Extending the Hamiltonian 4.8 to interlayer interactions strongly enhances the PD interaction which is responsible for the magnetic moment reorientation along the c axis.

By solving Hamiltonian 4.8 Kim et al. [110] have obtained a phase diagram as a function of η and θ (see Fig. 4.14(b)), where η is the ratio between Hund's coupling and on-site Coulomb repulsion and θ parameterizes the tetragonal crystal field. Whereas for Sr_2IrO_4 a distinct spin flop transition from a basal-plane canted to a c-axis collinear AF state takes place at $\theta = \pi/4$ $(\Delta = \lambda/2)$, in $Sr_3Ir_2O_7$ the c-axis collinear AF structure is stable in a wider window of the parameter space and the PD interaction drives the spin-flop transition which is almost insensitive to the tetragonal distortion θ. Fig. 4.14(b) shows the phase diagram of Sr_2IrO_4 (dashed line) and $Sr_3Ir_2O_7$ (solid line). The shaded area shows the values of θ inferred from the L_2/L_3 XRMS intensity ratio as measured in our experiment (see Section 4.4.5).

A different approach to interpret the c-axis collinear magnetic structure would be to consider the interlayer superexchange $J_\perp$ as comparable or even greater than the intralayer superexchange $J_\parallel$. This can be justified by the fact that the in-plane Ir-O-Ir bons are twisted by about 11.95° while the out-of-plane bonds are perfectly straight. In virtue of the Goodenough-Kanamori-Anderson rules [97], the interlayer superexchange interaction should be greater than the in-plane one . In order to avoid the competition between interlayer superexchange $J_\perp$ and DM interaction which favours basal-plane canting, the system will adopt a c-axis magnetic structure with the moments parallel to the DM vector, which minimizes the DM interaction. An alternative model for magnetism in $Sr_3Ir_2O_7$ based on a dominant interlayer superexchange $J_\perp$ will be presented in Section 5.3 in order to interpret the magnetic excitation spectra of $Sr_3Ir_2O_7$.

Finally we briefly discuss the relation between the microscopic magnetic structure addressed in our study and the bulk susceptibility data. The c-axis collinear AF state explains the lack of zero-field magnetic susceptibility, measured along the [0 0 1] direction, reported previously [33]. However, the origins of the unusual low temperature, ab-plane behaviour, and the small inconsistencies found in different reports are a more complex problem [33, 15, 41, 103]. Although XRMS cannot detect a pure canting-derived ferromagnetic component, as we have discussed in Section 4.4.1 and in Appendix B the IRs associated with the crystallographic space group I4/mmm and $Bbcb$ do not support a canted ground state. This is in agreement with the study of Lovesey et al. [111] in which the authors suggested that the magnetic structure observed in $Sr_3Ir_2O_7$ has to be associated with either the $Cmcm$ or $Cmma$ space group in order to allow an in-plane weak ferromagnetic component. However, our high-resolution X-ray analysis confirms that the crystal structure can be decomposed into two symmetry related twins: $Bbcb$ and $Acaa$ (see Section 4.2) in correspondence to a study on policrystalline material [101]. Our XRMS experiment suggests that the magnetic domains are pinned to the crystallographic twins. We thus believe that the weak ferromagnetic component observed in bulk measurements is not an intrinsic property of the system but could reasonably originate in the domain walls which separate different crystallographic twins/magnetic domains. This could explain the peculiar temperature dependence of the magnetic susceptibility (see Fig. 4.3) and the differences between reported studies [33, 15, 41, 103].

4.4.5 Energy dependence and branching ratio

We now turn to the energy dependence of the magnetic scattering in $Sr_3Ir_2O_7$, which can be used to determine the Ir wave function by measuring the L_2/L_3 XRMS for magnetic moments pointing perpendicularly to the perovskite planes. Before proceeding with the analysis of the energy dependence of XRMS we briefly discuss how magnetic scattering data are corrected for absorption effects.

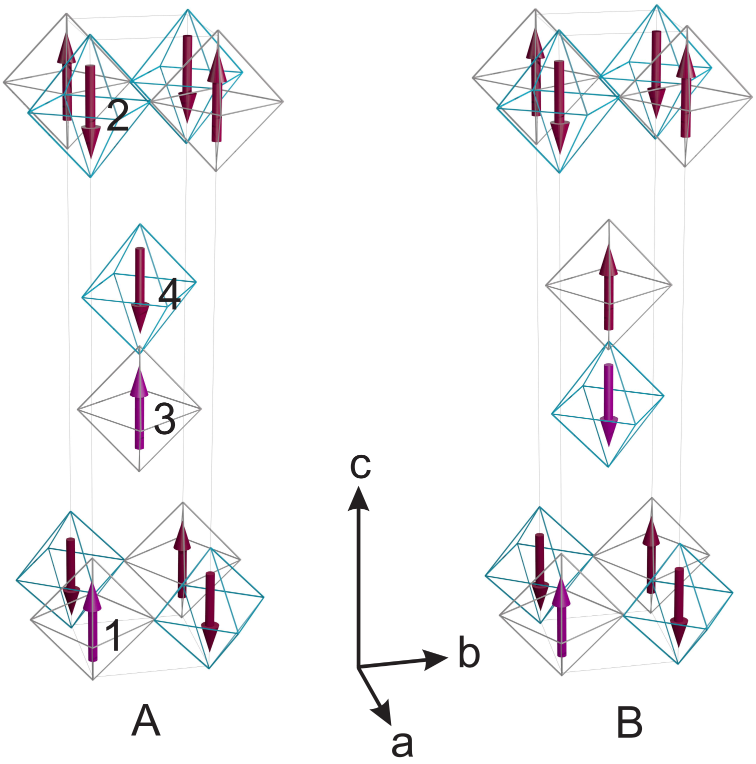

Figure 4.11: The c-axis G-type magnetic structure of $Sr_3Ir_2O_7$ for the magnetic domains A and B. The arrows on light purple highlight the different phase between the magnetic domains. The numbers indicate the Ir atomic positions used to calculate the magnetic structure factor.

Absorption corrections

The first step in the correction of resonant magnetic scattering data consists in obtaining the linear absorption coefficient $\mu(E)$. A detailed treatment of this is given for instance in Ref. [112, 113]. The absorption coefficient far from any absorption edge is roughly proportional to λ^3, where λ is the incident photon wavelength. Values of μ far from the absorption edge are tabulated [114]. However, in proximity of the absorption edges, the absorption coefficient changes rapidly and the values from the tables have to be integrated by a direct estimate of μ obtained via fluorescence or transmission measurements $I(E)$. Here we assume the absorption coefficient μ to be isotropic. This is not a priori true, but measurements of μ in different experimental geometries have not shown significant anisotropy. The energy dependent absorption coefficient near the absorption edge for a thick crystal can be calculated as [112]:

$$\mu(E) = \mu_L + \mu_a(E) = \mu_L + \frac{(I(E) - I_L)\left(1 + \frac{\sin\alpha}{\sin\beta}\right)\mu_L(\mu_H - \mu_L)}{(I_H - I_L)\left(\mu_H + \mu_L\frac{\sin\alpha}{\sin\beta}\right) - (I(E) - I_L)(\mu_H - \mu_L)}, \tag{4.9}$$

where μ_L is the absorption coefficient far below the absorption edge which can be found in tables [114], and $\mu_a(E)$ is the energy dependent part of the absorption coefficient. The latter can be calculated from the tabulated values of μ far below (above) the edge μ_L (μ_H), the fluorescence spectrum $I(E)$, the value of the fluorescence spectrum well below (above) the edge I_L (I_H), and the angle α (β) between the incoming (outgoing) wavevector $\mathbf{k}$ ($\mathbf{k}'$) and the sample surface. The absorption coefficient $\mu(E)$ in proximity of the L_3 edge is shown in Fig. 4.12 (purple line) together with tabulated values from Ref. [114] (green line). Finally for a thick crystal the measured intensity has to be multiplied by the factor

$$Abs(\mathbf{K}, \psi) = \mu\left(1 + \frac{\sin\alpha(\mathbf{K}, \psi)}{\sin\beta(\mathbf{K}, \psi)}\right), \tag{4.10}$$

where $\mathbf{K}$ and ψ are the scattering vector and the azimuthal angle, respectively.

L_2/L_3 XRMS intensity ratio and BR

We can now discuss the energy dependence of the magnetic scattering and the absorption branching ratio in $Sr_3Ir_2O_7$. Fig. 4.13(a) shows the resonant enhancement of the $(\frac{1}{2}\,\frac{1}{2}\,24)$ magnetic reflection across the Ir L_3 and L_2 edges in the σ-π (green spheres) and σ-σ (purple diamonds) polarization channels along with the XANES spectra (orange line). Magnetic scattering data have been corrected for self-absorption according to Eq. 4.10 and for the non ideality of the polarization analyzer according to Eq. 2.77.

As already reported in the single layer Ba_2IrO_4 and Sr_2IrO_4 a strong resonant enhancement is observed at the L_3 edge, whilst at the L_2 edge

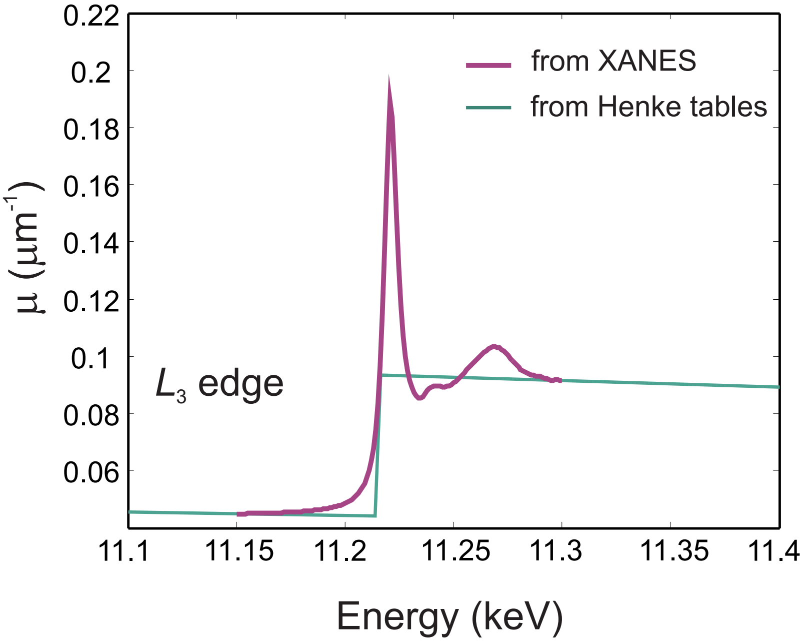

Figure 4.12: Linear absorption coefficient μ as a function of the incoming photon energy (purple line) as calculated from Eq. 4.9. The light green line are tabulated values for normal incidence and sample density of 7.47 g/cc [114].

magnetic scattering is significantly weaker. The L_3 resonance shows a nice Lorentzian shape (FWHM = 6.83 eV) which peaks at 11.2186(3) eV. The maximum in the XANES spectra is instead 3 eV above the magnetic resonance in analogy with Ba_2IrO_4 (see Section 3.3.2). Along similar lines we can thus estimate the cubic crystal field to be $10Dq = 2.7$ eV in $Sr_3Ir_2O_7$, which is in good agreement with Ba_2IrO_4 and other iridates [65, 73, 16, 80], validating the approximation of considering only the t_{2g} subspace in the calculation of the REXS cross section (see Section 2.3). At the L_2 edge, the much weaker magnetic scattering signal peaks at 12.831 eV (FWHM = 5.03 eV) in correspondence of the maximum in the XANES spectrum. This is in analogy with the single layer counterpart Sr_2IrO_4 (see Fig. 2.3). This could suggest that the signal measured at the L_2 edge is due to a weak mixing of the e_g and t_{2g} states, and the magnetic signal owing to the t_{2g} orbitals only is actually less.

To analyze the L_2/L_3 XRMS intensity ratio quantitatively, we have integrated the XRMS signal at both edges. From the area of the Lorentzian function (blue dashed line in Fig. 4.13(a)) that has been fit to the XRMS signal we calculate that the L_2/L_3 XRMS intensity ratio is less than 0.3 %. Since the magnetic moments point along the c axis in $Sr_3Ir_2O_7$ (see Section 4.4.4), the XRMS cross section at the L_2 edge vanishes only in perfect cubic symmetry (see Eq.2.57) and it is possible to investigate the realization of the $j_{\mathrm{eff}} = 1/2$ state from the L_2/L_3 XRMS intensity ratio. In Fig. 4.13(b) we therefore compare the measured L_2/L_3 XRMS intensity ratio with the calculated one according to Eq. 2.73. The experimental ratio of at most 0.3% provides the lower and upper bounds for a nearly pure $j_{\mathrm{eff}} = 1/2$ ground state. We note, however, that these bounds correspond to a relatively large energy window in Δ (0.37 eV$\leq \Delta \leq$0.21 eV), for which the ground state may deviate slightly from the pure $j_{\mathrm{eff}} = 1/2$ state, as seen for instance in the change of the shape of the ground state wave function (see top panel of Fig. 4.13(b)).

In order to better understand the origin of the very small L_2/L_3 XRMS intensity ratio, calculations were performed with the FDMNES code [106]. FDMNES is an *ab initio* cluster-based, monoelectronic code that calculates XAS and REXS spectra. We used the fully relativistic monoelectronic calculation (DFT-LSDA) with spin-orbit coupling on the basis of the Green formalism (multiple scattering) for a muffin-tin potential. In order to take into account the effect of the on-site Coulomb repulsion U, not negligible in many theories of 5d Mott-insulators, we included the Hubbard correction (LSDA+U). The value of $U = 0.25$ eV was chosen according to the optical conductivity measurements reported by Moon et al. [99] which identify at this energy the transition between lower and upper Hubbard band (see Fig. 4.1). The simulated spectrum derives entirely from the dipole-dipole interaction (we previously checked there were no effects due to higher order terms). For the calculation we used a magnetic unit cell of size $2a \times 2b \times c$ containing 128 atoms with a cluster radius 3.8 Å with an average of 19 atoms per cluster.

Fig. 4.14 shows a comparison of several different calculation in order to quantify the potential effect of the SO coupling and the Hubbard U term on the relative intensities of the $L_{2,3}$ edge resonances for the $(\frac{1}{2}\,\frac{1}{2}\,24)$ magnetic reflection. It is clear that the spin-orbit coupling term plays the greater role in the relative strengths of the L_3 and L_2 edge resonances. Including the Hubbard U term dampens the L_2 edge signal still further,

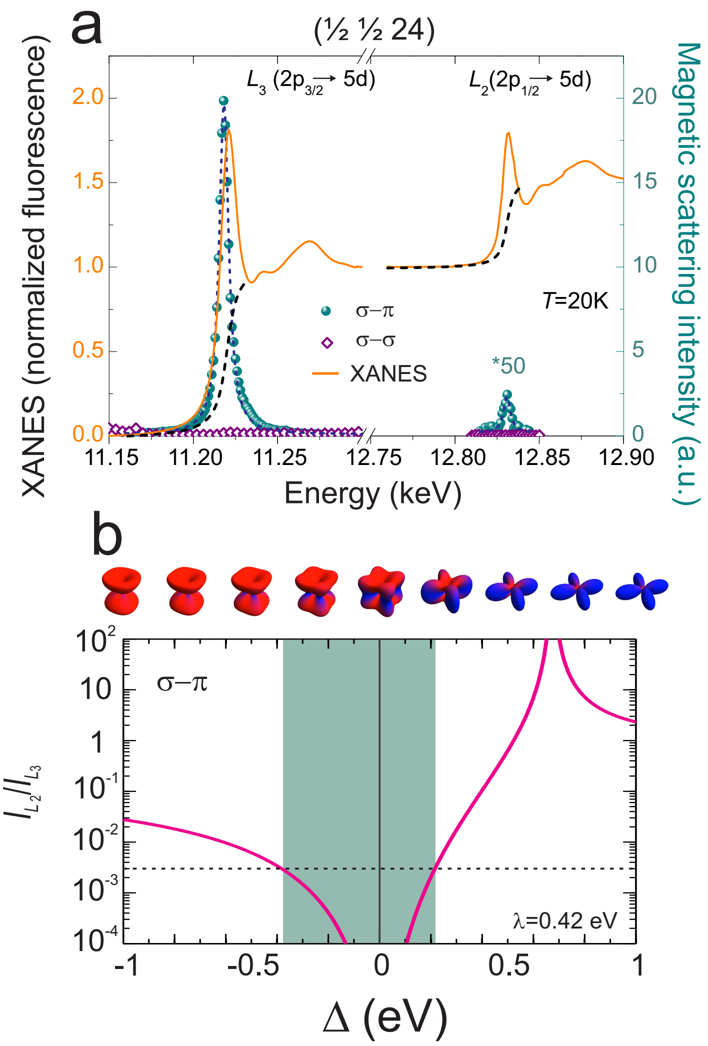

Figure 4.13: (a)Resonant enhancement of the $(\frac{1}{2}\,\frac{1}{2}\,24)$ magnetic reflection across the $L_{2,3}$ edges at $T = 20$ K in the σ-π (green spheres) and σ-σ (purple diamonds) scattering channel. The solid orange line shows XANES spectra, measured in fluorescence mode, normalized to the number of initial states. The black dashed line demarcates the integrated white line used to calculate the absorption branching ratio, while the dashed blue line represents a fit to a Lorentzian shape function. Panel (b) shows the L_2/L_3 XRMS intensity ratio for $\boldsymbol{\mu}\|$ [0 0 1] as a function of the tetragonal crystal field splitting Δ ranging from -1 to 1 eV, for a given value of the spin-orbit coupling constant ($\lambda = 0.42$ eV) as calculated from Eq. 2.73. The shaded area demarcates values of the tetragonal crystal field for which the measured L_2/L_3 XRMS intensity ratio is less than 0.3%. The top panel shows the evolution of the angular part of the ground state wave function varying Δ.

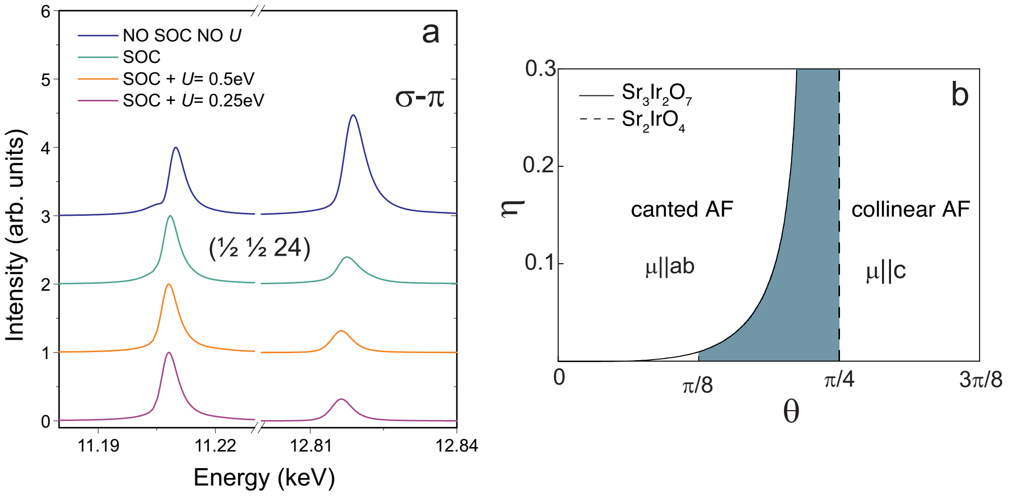

Figure 4.14: (a) FDMNES calculations of the XRMS at the $(\frac{1}{2}\,\frac{1}{2}\,24)$ position performed at the Ir $L_{2,3}$ edges for the $Sr_3Ir_2O_7$ compound for various initial parameters: assuming negligible SOC and U (blue line), including SOC but with no U (green line), including SOC and $U = 0.25$ eV [99] (orange line), and SOC + $U = 0.5$ eV (purple line). (b) The ground state phase diagram of the Hamiltonian 1.48 in terms of $\eta = J_H/U$ and the tetragonal distortion parameter θ. The solid (dashed) line marks the spin-flop transition in bilayer (single-layer) system. The shaded area indicates the parameter space for $Sr_3Ir_2O_7$ constrained by the current study. Adapted from Ref. [110]

but there is relatively little difference between 0.25 eV and 0.5 eV; the values calculated for the $Sr_3Ir_2O_7$ and Sr_2IrO_4, respectively [99]. However, the L_2/L_3 XRMS intensity ratio ($\sim$20%) is largely overestimated by the FDMNES calculation. We believe this is due to the fact that this calculation fails to reproduce the cubic symmetry of the novel $j_{\text{eff}} = 1/2$ ground state that is ultimately responsible of the destructive interference in the matrix elements at the L_2 edge.

In analogy with the Ba_2IrO_4 compound we can calculate the XAS branching ratio (BR). The procedures to extract the BR from the XAS spectra have already been discussed in detail in Section 3.3.2. Fig. 4.13(a) shows the XANES spectra together with the black dashed line which demarcates the integrated white line used to calculate the absorption branching ratio, $BR = 4.84(3)$. This value is slightly smaller than in the Ba single-layer, but much greater than the statistical one ($BR = 2$) and in good agreement with other iridium oxides [93]. The large BR is a further confirmation of the strong SOC regime in $Sr_3Ir_2O_7$.

4.5 Conclusions

In this chapter we have presented a detailed study of the electronic and magnetic properties of $Sr_3Ir_2O_7$ using XRMS at the Ir $L_{2,3}$ edge. $Sr_3Ir_2O_7$ is found to be a G-type antiferromagnet. From the l dependence of magnetic scattering we deduce that magnetic moments show an antiferromagnetic coupling both in-plane and out-of-plane. The observation of scattering intensity for $(\frac{1}{2}\,\frac{1}{2}\,2n)$ and $(\frac{1}{2}\,\frac{1}{2}\,2n+1)$ magnetic reflections suggest the presence of two magnetic domains A and B, associated with two arms of the magnetic propagation vector $\mathbf{k}=[\frac{1}{2}\,\frac{1}{2}\,0]$: $\mathbf{k}_A=[\frac{1}{2}\,\frac{1}{2}\,0]$ and $\mathbf{k}_B=[\frac{1}{2}\,\text{-}\frac{1}{2}\,0]$, respectively.

From the comparison of the experimental L_2/L_3 XRMS intensity ratio with single-ion calculations, we deduce that the $j_{\text{eff}}=1/2$ state survives even in the bilayer compound despite $Sr_3Ir_2O_7$ being a more metallic system in proximity of a metal-to-insulator transition.

Contrary to the single layer counterpart which is found to be a basal-plane canted antiferromagnet, in $Sr_3Ir_2O_7$ the addition of an extra IrO_6 layer strongly enhances the interlayer interactions and favours a c-axis collinear magnetic ground state. This unusual behaviour can be ascribed to the “3D” nature of the $j_{\text{eff}}=1/2$ wave function.

Chapter 5

Magnetic excitations in $Sr_3Ir_2O_7$ investigated with RIXS

In copper oxides, Cu $L_{2,3}$ edge RIXS direct “spin-flip” scattering is allowed and widely used to study collective magnetic excitations. In a similar way we show that Ir L_3 edge spin-flip direct RIXS is allowed in iridium oxides. L_3 edge RIXS is then performed on the $Sr_3Ir_2O_7$ system where single magnons, multi magnons and a spin-orbit exciton are observed. Notably the low-energy magnetic spectrum shows unusual features: a dispersive 90 meV-gap mode and a more weakly dispersive 155 meV-gap mode which suggest that strong anisotropies dominate in the bilayer iridates and the physics at play is not a simple continuation of the one of the single layer Sr_2IrO_4.

With the help of a theoretical model developed by our collaborators at the EPFL, we are able to assign these modes to excitations from a dimerised singlet ground state to a transverse and longitudinal triplet states, respectively.

Contents

5.1 Introduction

Although resonant inelastic X-ray scattering (RIXS) was discovered more than 30 years ago [115], its renaissance is rather recent. This has been driven by the substantial increase of the energy resolution up to a resolving power ($E/\Delta E$) of 10^5, which has made RIXS a valuable tool to study low-energy magnetic and electronic excitations.

The systems that have been mostly studied with RIXS are the high-T_C cuprate superconductors and their parent compounds. This is mainly due to the fact that spin waves may provide the "glue" which binds the electrons in Cooper pairs in copper oxides. A comprehensive understanding of magnetic excitations of these compounds could therefore lead to significant insights into the superconducting mechanism. Due to the strong exchange coupling between spins in cuprates ($J \sim 100$ meV), it is nowadays possible to study magnetic excitations with soft RIXS at the Cu $L_{2,3}$ edge. Direct RIXS in the soft X-ray regime, like in cuprates and nickelates, involves very strong $2p \rightarrow 3d$ resonances which can be used to increase the measured signal although the access to reciprocal space is limited to a small portion of the Brillouin zone ($\lambda_{\text{photon}} \sim 13$ Å).

A theoretical description of how the dispersion of magnetic excitations in copper oxides can be determined using RIXS has been given by Ament et al. [116]. One of the pioneering RIXS experiments in the copper oxide La_2CuO_4 performed by Braicovich et al. [117] shows that the momentum dependence of the spin waves can be measured by RIXS in analogy with

INS (see Fig. 5.1(e)). The microscopic mechanism involves the creation of a local spin-flip by transferring the angular momenta of the photons to the system. Contrary to neutron scattering where spin 1/2 particles can transfer only $\Delta S_z = 0{,}1$, photons of angular momentum $L = 1$ can transfer $\Delta S_z = 0{,}1{,}2$, potentially creating not only single-magnon excitations with $\Delta S_z = 1$ but also $\Delta S_z = 2$ two-magnons excitations. The transfer of the photon angular momentum to the spin of the electrons is due to the SOC of the core hole, as explained in Section 2.2.

The spin-flip process is described by the Kramers-Heisenberg formula (Eq. 2.36), and strongly depends on the polarization of the electromagnetic radiation and the symmetry of the atomic wave functions. If spin-flip scattering is allowed, the full magnetic dispersion can be measured. Spin waves can be seen as the superposition of spin-flips at different sites which carry a non-local magnetic excitation with momentum $\hbar\mathbf{K}$. In order to obtain the total RIXS cross section, one has to multiply the spin-flip cross section by the appropriate spin-susceptibility in analogy with neutron scattering. In this way one obtains the momentum dependence of the magnetic excitations that can be measured with RIXS [116]. For a comprehensive theoretical and experimental review of RIXS in transition metal oxides see Ref. [118].

As we will show in the next sections RIXS gives also access to high-energy excitations like *d*-*d* and charge transfer (CT) excitations, which are more difficult to study with INS.

5.2 L_3 edge RIXS studies in iridates, background

As mentioned in Chapter 2, resonant scattering at the Ir $L_{2,3}$ edges involves very strong dipolar transitions from the $2p$ core level to the $5d$ valence band. In analogy with soft RIXS at the L edges in $3d$ TMOs we can exploit hard RIXS at the Ir L edges to study collective electronic and magnetic excitations in iridium oxides. The possibility of using Ir L_3 RIXS to study dynamical properties of iridates was first proposed by Ament et al. [120] for the case of magnetic moments aligned along the octahedral z axis.

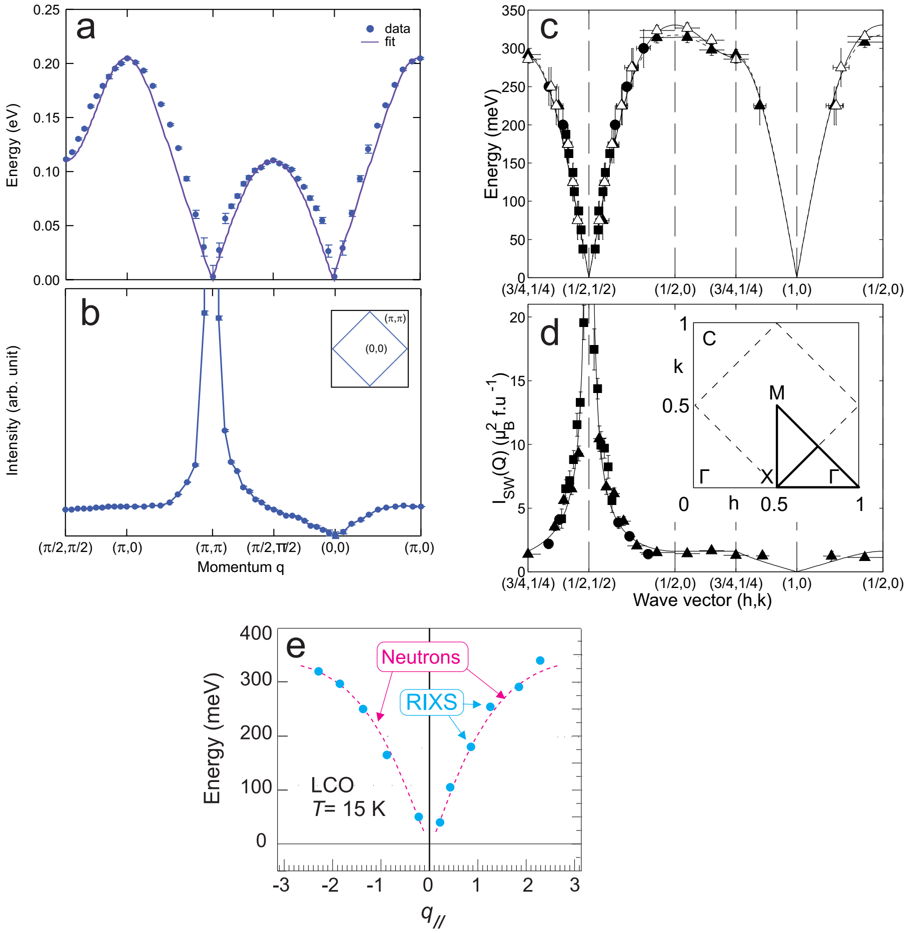

Figure 5.1: (a) Single magnon dispersion along high-symmetry directions determined by RIXS (blue dots) in Sr_2IrO_4. The blue line is a fit to a J-J'-J'' model. (b) Momentum dependence of the spin wave intensity determined by RIXS in Sr_2IrO_4. Panels (a-b) are taken from Ref. [72].(c) Single magnon dispersion along high-symmetry directions determined by INS in La_2CuO_4. (d) Momentum dependence of the spin wave intensity determined by INS in La_2CuO_4. Solid lines are a fit to a J-J'-J''-J_c model. Panels (c-d) are taken from Ref. [119] (e) Single magnon dispersion determined by RIXS (blue dots) is compared with inelastic neutron scattering (purple dashed line)(Ref. [119]). Taken from Ref. [117]

In the following we will complete this picture by presenting the RIXS scattering amplitude for out-of-plane and in-plane magnetic moments as a function of the tetragonal crystal field Δ.

5.2.1 Spin-flip cross-section in iridium oxides

This calculation is an extension of the REXS cross-section calculation presented in Section 2.3. In order to calculate the RIXS scattering amplitude in the spin-flip channel we need to evaluate the Kramers-Heisenberg formula which we rewrite as

$$\mathcal{A}_{\text{RIXS}}^{\boldsymbol{\epsilon}\boldsymbol{\epsilon}'} = \sum_n \frac{\langle 0, +|\mathcal{D}_{\boldsymbol{\epsilon}'}^{\dagger}|n\rangle \, \langle n\,|\mathcal{D}_{\boldsymbol{\epsilon}}|\, 0, -\rangle}{E_0 - E_n + \hbar\omega_{\mathbf{k}} - i\Gamma_n/2}, \tag{5.1}$$

where initial and final states are defined in Eqs.1.34,1.40 for moments pointing along the [0 0 1] and [1 1 0] direction, respectively. Having derived in Section 2.3.1 the matrix elements for dipolar transitions from $2p$ to $5d$ states, we can proceed to evaluate Eq. 5.1. By making use of the matrix elements of Tab. 2.2, the scattering geometry and the polarization vectors of Section 2.3.1 we can calculate the RIXS scattering amplitude in the spin-flip channel.

At the Ir L_2 edge the summation runs over the $|p_{\frac{1}{2},-\frac{1}{2}}\rangle$ and $|p_{\frac{1}{2},\frac{1}{2}}\rangle$ intermediate states. The final scattering amplitudes read

$$\mathcal{A}_{\text{RIXS}}^{\sigma\sigma'} = 0 \tag{5.2}$$

$$\mathcal{A}_{\text{RIXS}}^{\sigma\pi'} = 0 \tag{5.3}$$

$$\mathcal{A}_{\text{RIXS}}^{\pi\sigma'} = 0 \tag{5.4}$$

$$\mathcal{A}_{\text{RIXS}}^{\pi\pi'} = 0 \tag{5.5}$$

for magnetic moments along the [0 0 1] direction and

$$\mathcal{A}^{\sigma\sigma'}_{\text{RIXS}} = 0 \tag{5.6}$$

$$\mathcal{A}^{\sigma\pi'}_{\text{RIXS}} = \frac{i(A-1)^2\cos\theta'}{2+A^2} \tag{5.7}$$

$$\mathcal{A}^{\pi\sigma'}_{\text{RIXS}} = \frac{i(A-1)^2\cos\theta}{2+A^2} \tag{5.8}$$

$$\mathcal{A}^{\pi\pi'}_{\text{RIXS}} = 0 \tag{5.9}$$

for magnetic moments along the [1 1 0] direction. We recall that the parameter $A = \frac{-1+\delta+\sqrt{9+(-2+\delta)\delta}}{2}$ controls the effect of the tetragonal crystal field Δ via $\delta = 2\Delta/\lambda$, where λ is the Ir SOC constant. The scattering geometry together with the definition of the angles are shown schematically in Fig. 2.4.

At the Ir L_3 edge the summation runs over the four $|p_{\frac{3}{2},-\frac{3}{2}}\rangle$, $|p_{\frac{3}{2},-\frac{1}{2}}\rangle$, $|p_{\frac{3}{2},\frac{1}{2}}\rangle$, and $|p_{\frac{3}{2},\frac{3}{2}}\rangle$ intermediate states. At this edge the scattering amplitudes read

$$\mathcal{A}^{\sigma\sigma'}_{\text{RIXS}} = 0 \tag{5.10}$$

$$\mathcal{A}^{\sigma\pi'}_{\text{RIXS}} = \frac{3A(i\cos\phi+\sin\phi)\sin\theta'}{2+A^2} \tag{5.11}$$

$$\mathcal{A}^{\pi\sigma'}_{\text{RIXS}} = -\frac{3iAe^{-i\phi}\sin\theta}{2+A^2} \tag{5.12}$$

$$\mathcal{A}^{\pi\pi'}_{\text{RIXS}} = -\frac{3Ae^{-i\phi}\sin(\theta+\theta')}{2+A^2} \tag{5.13}$$

for magnetic moments along the [0 0 1] direction and

$$\mathcal{A}^{\sigma\sigma'}_{\text{RIXS}} = 0 \tag{5.14}$$

$$\mathcal{A}^{\sigma\pi'}_{\text{RIXS}} = \frac{-2i[(A-2)A-2]\cos\theta' + 3\sqrt{2}A(\cos\phi+\sin\phi)\sin\theta'}{2\,(2+A^2)} \tag{5.15}$$

$$\mathcal{A}^{\pi\sigma'}_{\text{RIXS}} = \frac{e^{-i\phi}\left\{-4i[(A-2)A-2]e^{i\phi}\cos\theta + 6(-1)^{3/4}A\left(i+e^{2i\phi}\right)\sin\theta\right\}}{4\,(2+A^2)} \tag{5.16}$$

$$\mathcal{A}^{\pi\pi'}_{\text{RIXS}} = \frac{3A(\sin\phi-\cos\phi)\sin(\theta+\theta')}{\sqrt{2}\,(2+A^2)} \tag{5.17}$$

for magnetic moments along the [1 1 0] direction.

By inspecting Eqs. 5.2–5.17 we notice that, in contrast to the elastic channel, σ-σ' scattering cannot reverse the electron spin and it is therefore not allowed in the spin-flip channel. At the L_2 edge the RIXS cross-section in the spin-flip channel shows a reciprocal behaviour as a function of the moment direction compared to the REXS cross-section. For magnetic moments pointing along the [0 0 1] direction it is identically zero in every polarization channel irrespective of the tetragonal crystal field Δ. For magnetic moments along the [1 1 0] direction the RIXS cross-section vanishes in the cross-polarized channel only for $\Delta = 0$. i.e. when the pure $j_{\text{eff}} = 1/2$ state is realized.

At the Ir L_3 RIXS is fully allowed in agreement with Ament et al. [120], and can be used to study magnetic excitations. In a similar way, if the final states of the RIXS process are the $|1, \pm\rangle$, $|2, \pm\rangle$ states (for a definition see Eqs. 1.35–1.36,1.41–1.42), an intra-t_{2g} excitation is created with an additional magnon if the spin of the electron is reversed ($|1, +\rangle$, $|2, +\rangle$ states). The scattering amplitudes of these transitions can be calculated along similar lines, however this goes beyond the scope of this work.

The total RIXS spectra as a function of transferred energy can be calculated as

$$\mathcal{I}^{\boldsymbol{\epsilon}}_{\text{RIXS}}(\omega_{\mathbf{k}}, \omega_{\mathbf{k}'}) = \sum_{\boldsymbol{\epsilon}'} \sum_{f} \left| \mathcal{A}^{\boldsymbol{\epsilon}\boldsymbol{\epsilon}'}_{|f,\pm\rangle} \right|^2 \frac{\Gamma_f/\pi}{(E_f + \hbar\omega_{\mathbf{k}'} - E_0 - \hbar\omega_{\mathbf{k}})^2 + \Gamma_f^2/4}, \tag{5.18}$$

where the energy-conservation δ-function is broadened into a Lorentzian of FWHM Γ_f in order to account for the finite lifetime of the final states f. The sum over the outgoing polarization is necessary because in RIXS experiments the outgoing polarization is not currently analyzed. Notably, the lifetime broadening of the final state $\Gamma_f \equiv \Gamma_{5d}$ in RIXS is strongly reduced compared to the lifetime broadening of the intermediate state $\Gamma_n \equiv \Gamma_{2p}$, which corresponds to the final state in absorption spectroscopies. In this way RIXS can easily overcome the core-hole broadening which limits the resolution in absorption experiments.

5.2.2 Magnetic excitations in Sr_2IrO_4

The first L_3 edge RIXS experiment in Sr_2IrO_4 was performed by Ishii et al. [121]. This study reports a strong resonant inelastic signal, however, due to the low-energy resolution of the experimental set-up (∼1 eV), the low-energy magnetic and electronic excitations were not investigated. Following this preliminary experiment, a comprehensive study of the magnetic and electronic excitations in Sr_2IrO_4 was conducted by Kim et al. [72]. In this pioneering study, taking advantage of the improved energy resolution of ∼130 meV, the full dispersion of the single magnon spectrum was mapped over the entire Brillouin zone.

The magnon dispersion (Fig. 5.1(a)) and the momentum dependent spectral weight (Fig. 5.1(b)) show striking similarities to those observed in cuprates, for instance in La_2CuO_4 (Fig. 5.1(c-d)) [119]. The magnon dispersion of Sr_2IrO_4 closely resembles the one of La_2CuO_4. In Sr_2IrO_4 magnons disperse up to ∼ 205 meV at the zone boundary (BZ) as compared to ∼ 300 meV in La_2CuO_4 [119]. The intensity of the magnetic excitations diverges at (π,π) where the magnons collapses into the magnetic Bragg peak and vanishes at (0,0). The high-symmetry points are shown in the inset of Fig. 5.1(b). The dispersion at $(\pi/2,\pi/2)$ is reduced by a ferromagnetic next nearest neighbour interaction J'. From the fit of a linear spin wave theory based on the Hamiltonian 1.48 to the experimental data, the superexchange parameters $J=60$, $J'=$-20, and $J''=15$ meV are extracted. The first nearest neighbour parameter J is in good agreement with *abinitio* many-body calculations [96]. The reduction of J compared to cuprates is consistent with a smaller on-site Coulomb repulsion U and hopping parameter t in iridates.

Although in Sr_2IrO_4 the $j_{\text{eff}} = 1/2$ spin-orbit entangled wave function is significantly different from the $s=1/2$ pure spin state in La_2CuO_4, the measured magnon dispersion supports a low-energy Hamiltonian which maintains a dominant 2D Heisenberg-like character in agreement with the theoretical arguments presented in Section 1.5.

In addition to the low-energy magnon spectrum, high-energy excitations in the range 0.4–0.8 eV are observed in Sr_2IrO_4. These features will be discussed in Section 5.3.3 for the $Sr_3Ir_2O_7$ compound.

5.3 Spin waves and spin-orbit excitations in $Sr_3Ir_2O_7$

In Chapter 4 we used REXS to investigate the evolution of the $j_{\mathrm{eff}} = 1/2$ ground state in the bilayer compound $Sr_3Ir_2O_7$. We now address the investigation of the excited states of the bilayer $Sr_3Ir_2O_7$ by RIXS and compare it to the single layer counterpart. We recall that passing from Sr_2IrO_4 to $Sr_3Ir_2O_7$, the system shows a weaker insulating state and the addition of an extra IrO_6 layer changes dramatically the magnetic structure from a basal-plane canted antiferromagnetic (AF) state to a c-axis collinear AF (see Section 4.4.4). In this context, the excitation spectra can thus deviate significantly from the Heisenberg-like behaviour exhibited by the single layer counterpart.

Before proceeding to present our high-resolution RIXS study of magnons in $Sr_3Ir_2O_7$, we briefly mention which excitations can be measured with L_3 edge RIXS in iridium oxides. Fig. 5.2 shows a RIXS map at low-energy-resolution ($\sim$ 130 meV) in $Sr_3Ir_2O_7$ acquired at the ID20 beamline, where the energy loss is measured as a function of the incoming energy of the photons. Four main features are observable. Close to zero energy loss an elastic line and magnetic excitations are found. At increasing energy loss, features can be assigned to intra-t_{2g} ($t_{2g}^5 \rightarrow t_{2g}^5$) at $\sim$0.5 eV, t_{2g} to e_g ($t_{2g}^5 \rightarrow t_{2g}^4 e_g^1$) at $\sim$3 eV, and charge transfer (CT) excitations ($5d^5 \rightarrow 5d^6 \underline{L}$) at $\sim$8 eV, where $\underline{L}$ represents a hole in the ligand oxygens. This assignment is consistent with quantum chemistry calculations for layered iridates [96]. The fact that the energy loss is independent of the incident energy is a direct signature of the Raman character of the excitations, which correspond to specific atomic transitions and cannot be ascribed to a fluorescence signal. Whereas t_{2g} to e_g and CT excitations resonate at the maximum of the XAS signal (11.2188 keV, dashed line), magnetic and intra-t_{2g} excitations are more enhanced about 3 eV below the maximum in the absorption spectrum (11.2158 keV, solid line). This can be explained using the same argument of Section 3.3.2. While the former transitions promote an electron into an intermediate e_g state, the latter remain only within the t_{2g} manifold, resonating $10Dq$ before the absorption edge. For

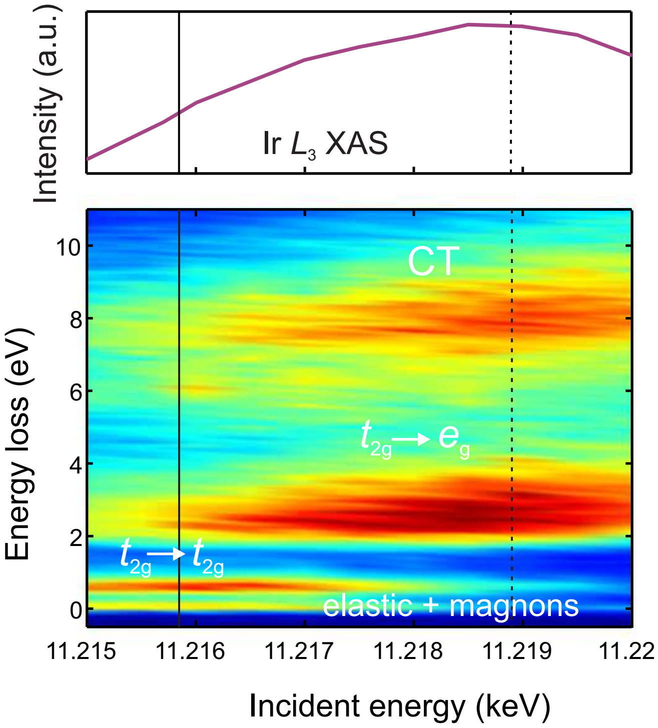

Figure 5.2: (a) X-ray absorption spectrum (XAS) of $Sr_3Ir_2O_7$ in proximity of the Ir L_3 edge. (b) RIXS color map of energy loss vs. incident photon energy at $\mathbf{K}=(\frac{1}{2}\,\frac{1}{2}\,25.5)$. The dashed line corresponds to the maximum in the XAS spectrum at which $t_{2g} \rightarrow e_g$ and charge transfer (CT) excitations (11.2188 keV) resonate. The solid line corresponds to the energy that maximizes intra-t_{2g} and magnetic excitations (11.2158 keV).

the high-energy resolution RIXS measurements we have fixed the incident energy of the photons at 11.2158 keV in order to maximize intra-t_{2g} and magnetic excitations.

5.3.1 Experimental results

Resonant inelastic X-ray scattering (RIXS) measurements were performed at the new ID20 beam line of the European Synchrotron Radiation Facility (ESRF), Grenoble. The experimental set-up for Ir L_3 measurement is given in Section 2.4.2 . The overall energy-resolution achieved was 25 meV, implying a resolving power better than 4×10^5. The scattering plane was horizontal in the laboratory frame, as was the polarization of the incoming radiation (π incident polarization). The $Sr_3Ir_2O_7$ sample was an oriented single crystal, used for the XRMS study presented in Chapter 4. The sample temperature was kept at 15 K during the whole experiment by means of a He-flow cryostat.

Fig. 5.3(a) shows a color map of the RIXS data measured along the in-plane high symmetry directions and out-plane scattering vector fixed at $\mathbf{K}_c = 28.5$ r.l.u. in $Sr_3Ir_2O_7$. Fig. 5.4 shows the same data by means of stack plots. A strong elastic feature with some phonon contribution (A) dominates the spectra at energies close to zero. At higher energy a magnetic band dispersing from 90 to 180 meV is found (B). The gap of this feature is comparable with the overall bandwidth. The fact that feature B is highly sensitive to the magnetic transition and its spectral weight peaks at (π,π) (see Fig. 5.7(b)), i.e. in correspondence of the antiferromagnetic wavevector, suggest its magnetic nature. Feature C copies the dispersion of B at higher energies.

Features A, B, C were already reported in a previous RIXS study performed by Kim et al. [122]. Our data shows two additional features: a weakly dispersive feature around 155 meV (D) and a highly dispersive feature (E) between 400 and 600 meV. Feature E, not present in the data of Ref. [122] because they extend only up to 400 meV energy loss, corresponds to a spin-orbit exciton, as reported in Sr_2IrO_4 [72]. Feature D, reported for the first time in our investigations, is more visible around the (0,0) point where it displays a small, but finite dispersion versus momentum transfer around 155 meV. Conversely, away from the Γ point, it practically merges into feature B and contributes to its lineshape and spectral weight. Noteably, its intensity is strongly dependent on the out-of-plane component of the momentum transfer: feature D almost completely vanishes when changing the out-of-plane component of the momentum transfer from $l = 28.5$ to $l = 25$ r.l.u. (see Fig. 5.3(b)). Raw spectra for in-plane transferred momentum close to the Γ point are reported in Fig. 5.6. Feature D (purple line) is clearly distinguished as a separate peak for $l = 28.5$, while it is barely visible for $l = 25$ r.l.u..

Features B and C have been identified and discussed by Kim et al. [122]. In particular, feature B has been interpreted as the superposition of almost degenerate acoustic and optical magnons and their dispersion was modeled on the basis of Hamiltonian 1.48, as used in Sr_2IrO_4, and in

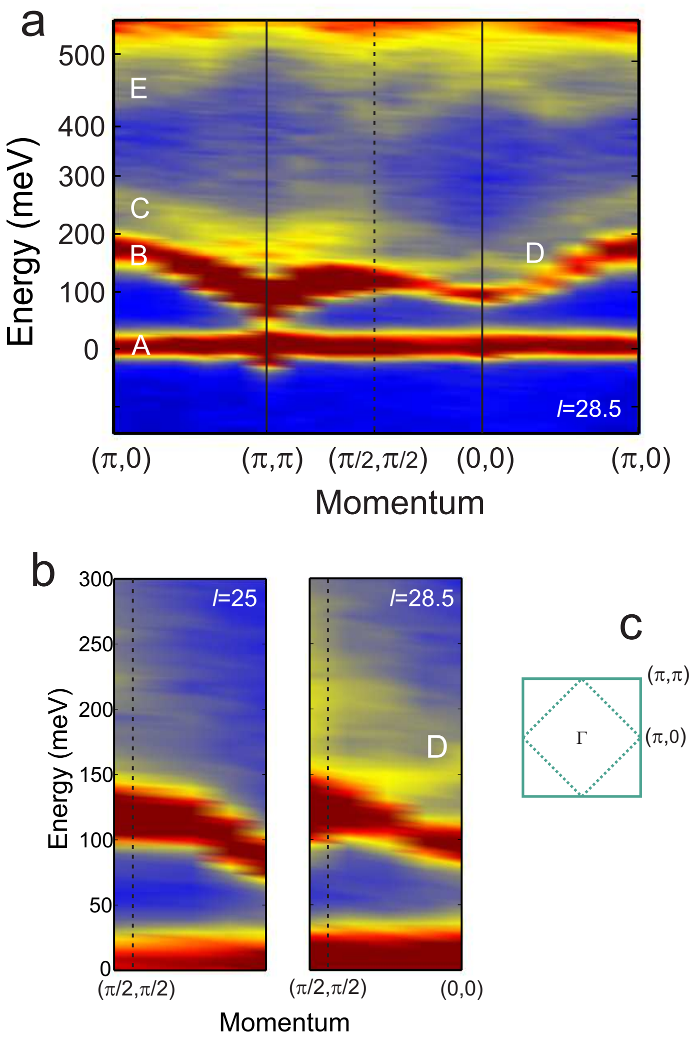

Figure 5.3: (a) Colour map of the RIXS data measured at $T = 15$ K with in-plane scattering vector $\mathbf{K}_{ab}$ along the high symmetry directions and out-plane scattering vector $\mathbf{K}_c = 28.5$ r.l.u.. (b) Color map of the RIXS data close to the Γ point for $\mathbf{K}_c = 25$ (left panel) and $\mathbf{K}_c = 28.5$ r.l.u. (right panel). (c) The Brillouin zone of the undistorted tetragonal unit cell (solid square) and the magnetic cell (dashed square) is shown with the notation following the convention for the tetragonal unit cell, as, for instance, in La_2CuO_4 [119].

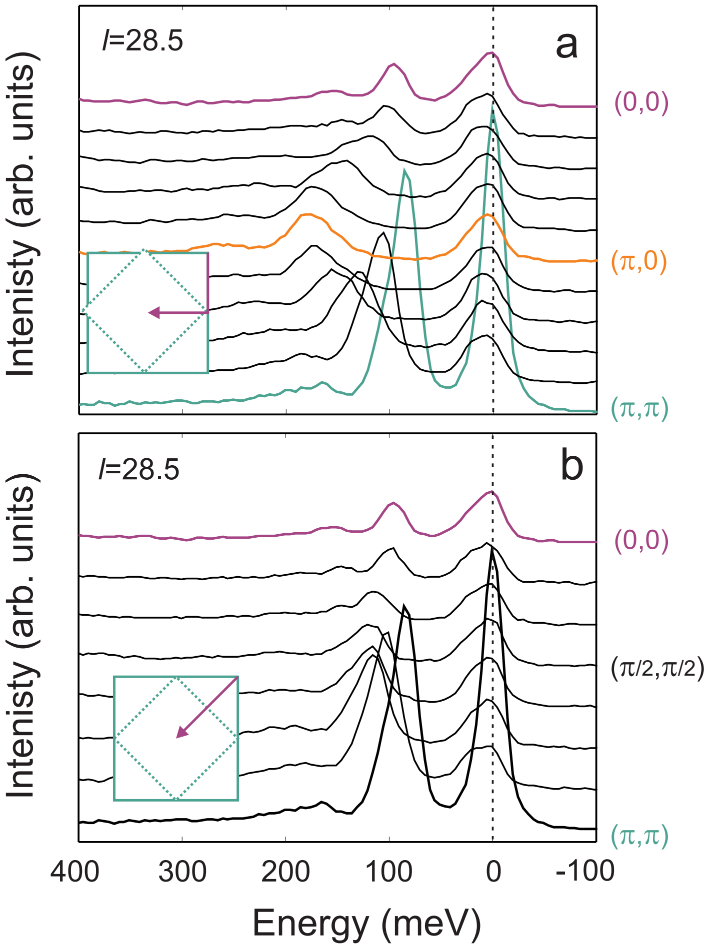

Figure 5.4: Stack plot of the RIXS data measured at $T=$ 15 K with in-plane scattering vector $\mathbf{K}_{ab}$ along the high symmetry directions and out-plane scattering vector $\mathbf{K}_c = 28.5$ r.l.u..

$Sr_3Ir_2O_7$ once that interlayer coupling terms are included.

It is common knowledge that bilayered systems present a magnetic excitation spectrum formed by parity-even and parity-odd excitations which are named optical and acoustic magnons in analogy with the terminology used for lattice vibrations. Indeed optical and acoustical magnetic modes have been revealed by means of INS in bilayer manganites [123] and cuprates [124]. The following Hamiltonian has been successfully used to interpret the experimental results in these studies

$$\mathcal{H} = J^{\parallel} \sum_{n=1,2} \sum_{\langle i,j \rangle} \mathbf{S}_i^n \cdot \mathbf{S}_j^n + J^{\perp} \sum_i \mathbf{S}_i^1 \cdot \mathbf{S}_i^2, \tag{5.19}$$

where $J^\perp$ is the superexchange coupling between adjacent planes, $J^\parallel$ is the in-plane nearest neighbour superexchange constant, $\langle i, j\rangle$ is a in-plane nearest-neighbor pair, and n is the layer index. The interaction in these $3d$ TMOs are well described by a dominant Heisenberg model with different in-plane and out-of-plane isotropic interactions. Diagonalization of Hamiltonian 5.19 according to spin wave theory of the Holstein-Primakoff type [125] results in the magnon dispersion

$$E(\mathbf{K}_{ab})^2 = \left(2J^\parallel + \frac{1}{2}J^\perp\right)^2 - \left(J^\parallel\left(\cos K_x + \cos K_y\right) \pm \frac{1}{2}J^\perp\right)^2, \quad (5.20)$$

where K_x and K_y are the in-plane component of $\mathbf{K}$. The sign $+(-)$ applies to acoustic (optical) magnons.

Fig. 5.5 shows the dispersion calculated according to Eq. 5.20 with $J^\parallel = 85$ meV and $J^\perp = 25$ meV, together with the in-plane dispersion of the main magnetic mode B in $Sr_3Ir_2O_7$. It is clear that the magnetic excitations in $Sr_3Ir_2O_7$ cannot be described by a simple Heisenberg model for bilayered systems but additional anisotropies must be included. It should be noted that usually acoustic and optical magnetic excitations can be distinguished by different dependencies of their intensity on the out-of plane momentum $\mathbf{K}_c$ [124]

$$\left(\frac{d^2\sigma}{d\Omega dE}\right)_{\text{acoustic}} \sim \frac{f^2(\mathbf{K})\sin^2(\pi l d)}{E(\mathbf{K}_{ab})}, \quad (5.21)$$

$$\left(\frac{d^2\sigma}{d\Omega dE}\right)_{\text{optical}} \sim \frac{f^2(\mathbf{K})\cos^2(\pi l d)}{E(\mathbf{K}_{ab})}, \quad (5.22)$$

where d is the interlayer distance and $f(\mathbf{K})$ is the magnetic form factor. We therefore measured the intensity of feature B for several l but did not observe any substantial variation. This can be seen for instance in Fig. 5.3(b) where feature B has similar intensity for l=25, 28.5 r.l.u. corresponding to $\mathbf{K}_c \sim 0, \pi$, respectively.

In the study by Kim et al. [122] the magnetic feature B has been interpreted as the superposition of quasi-degenerate optical and acoustic mode. This is supported by the fact that the energy position of feature

B shifts by 5 meV upon scanning the out-of-plane momentum $\mathbf{K}_c$ from 0 to π. This energy shift is due to the spectral weight of feature B that according to Eq. 5.21 moves from the acoustic branch at $\mathbf{K}_c = \pi$ to the optical one at $\mathbf{K}_c = 0$, producing a dispersive behaviour as a function of $\mathbf{K}_c$. Feature C, instead, has been assigned to multi-magnon excitations and we support this hypothesis on the basis of the energy scale of this feature and on the fact that it mimics the dispersion of the single magnon process.

Feature D, on the contrary, has not been previously detected, likely because of the nontrivial dependence of its intensity on momentum transfer. The dispersion and the integrated intensity of features B, C, D, and E as a function of the in-plane momentum transfer, for $l = 28.5$ r.l.u., is summarized in Fig.5.7(a,b), respectively. The dispersion curves of features B and C are similar and agree well with published results [122] , while feature D behaves somewhat differently: in particular, features B and D almost coincide at ($\pi/2$,$\pi/2$) and are well separated around (0,0), with intersecting points around (0,$\pi/4$) and ($\pi/4$,0). It should be noted that the dispersion curves of features B and D are not compatible with those corresponding to an acoustical and optical magnetic excitations.

The data in Fig. 5.7(a,b) have been obtained by fitting the RIXS raw spectra. Examples of the fitting procedure for different momentum transfer $\mathbf{K} = (\pi/7\ \pi/7\ 28.5)$ (a), $\mathbf{K} = (2\pi/7\ 2\pi/7\ 28.5)$(b), $\mathbf{K} = (\pi/7\ \pi/7\ 25)$(c), and $\mathbf{K} = (2\pi/7\ 2\pi/7\ 25)$(d) are given in Fig. 5.6. Feature A has been fit to a sum of an elastic and quasi-elastic Pearson VII functions to include the phonon contribution. Features B-E were fit to four Pearson VII functions with an additional Pearson VII to include higher-energy inelastic signal. We recall that the Pearson VII function is found to represent well the experimental resolution (see Section 2.4.2). The elastic and single magnon peaks were constrained to have a FWHM of 25 meV, which is the instrumental resolution determined in Section 2.4.2.

5.3.2 Theory, the strong coupling limit

In order to elucidate the nature of these excitations, our collaborators from École polytechnique fédérale de Lausanne (EPFL) have developed

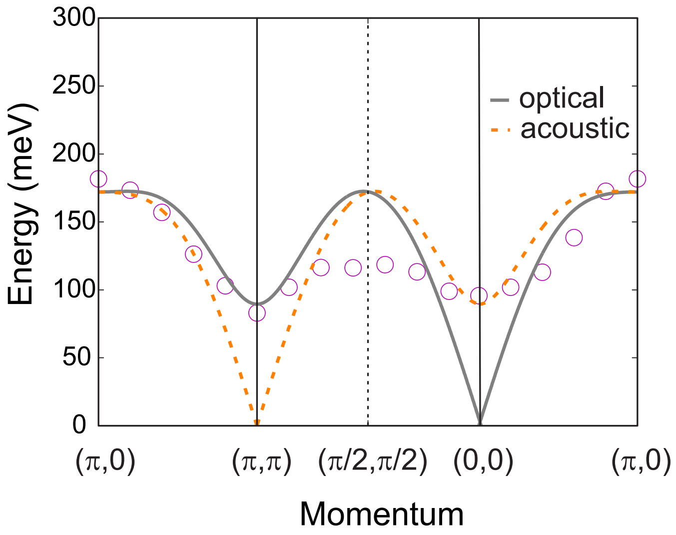

Figure 5.5: Schematic diagram of the in-plane spin wave dispersions in an antiferromagnetic bilayer from Eq. 5.20. The superexchange parameters used are $J^{\|} = 85$ meV and $J^{\perp} = 25$ meV. Coupling between different bilayers and in-plane anisotropies are not included. Open dots are the experimental energy position of the main magnetic mode as extracted from the fit to the RIXS data.

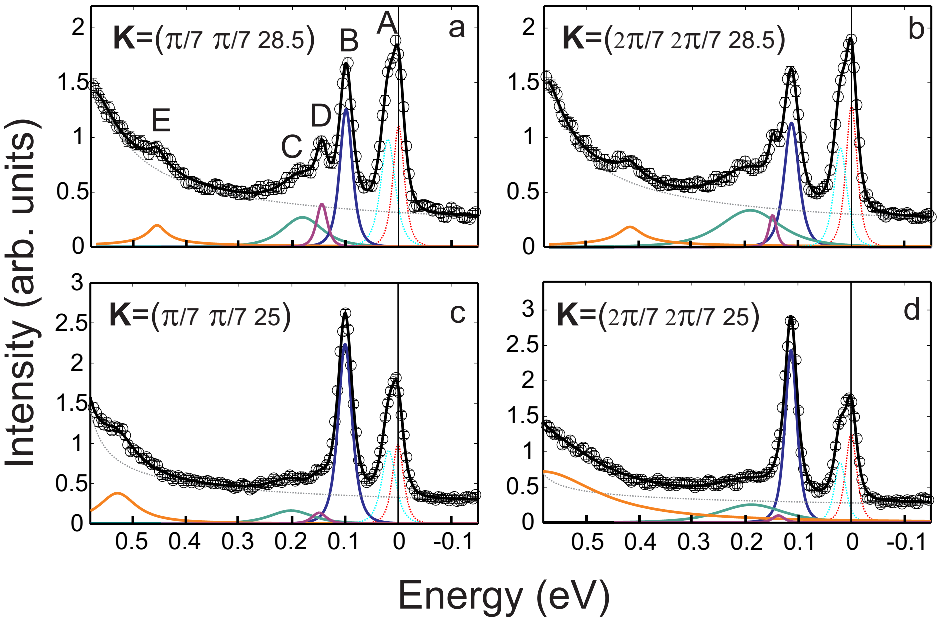

Figure 5.6: RIXS spectra taken at $\mathbf{K} = (\pi/7\ \pi/7\ 28.5)$ (a), $\mathbf{K} = (2\pi/7\ 2\pi/7\ 28.5)$ (b), $\mathbf{K} = (\pi/7\ \pi/7\ 25)$ (c), and $\mathbf{K} = (2\pi/7\ 2\pi/7\ 25)$(d). Colored lines are the result of the fit as described in the text.

a model Hamiltonian based on a pseudospin-1/2 frustrated Heisenberg model which simultaneously takes into account intrinsic anisotropy and spin-orbit coupling effects. For a detailed review of the theoretical model see Ref. [126]. The starting point is to introduce an anisotropic Hamiltonian with frustration and longer range interactions

$$\begin{aligned}\mathcal{H} =& J_1^{||} \sum_{<i,j>,\ l} \Big[\cos(2\theta)\mathbf{S}_{li}\cdot\mathbf{S}_{lj} + 2\sin^2(\theta) S^z_{li} S^z_{lj} \\ & \qquad\qquad - \epsilon_i\epsilon_l \sin(2\theta)(\mathbf{S}_{li}\times\mathbf{S}_{lj})\cdot\hat{e}_z \Big] \\ & + J^{\perp}\sum_i \mathbf{S}_{1i}\cdot\mathbf{S}_{2i} + J_d^{\perp}\sum_{<i,j>}\mathbf{S}_{1i}\cdot\mathbf{S}_{2j} \\ & + J_2^{||}\sum_{\ll i,j\gg,l}\mathbf{S}_{li}\cdot\mathbf{S}_{lj} + J_3^{||}\sum_{\lll i,j\ggg,l}\mathbf{S}_{li}\cdot\mathbf{S}_{lj}. \end{aligned} \tag{5.23}$$

The indices $<i,j>$, $\ll i,j\gg$ and $\lll i,j\ggg$ denote nearest, next-nearest and next-next-nearest neighbours within each layer $l = 1, 2$. θ is the twisting angle of the Ir_6 octahedra in each layer. The second term $2\sin^2(\theta)S^z_{li}S^z_{lj}$ accounts for pseudodipolar interactions driven by Hund's coupling and the staggered rotation of the IrO_6 octahedra. Dzyaloshinskii-Moriya interaction is included with the third term $\propto (\mathbf{S}_{li}\times\mathbf{S}_{lj})\cdot\hat{e}_z$. The magnetic interactions of Hamiltonian 5.23 are illustrated in Fig. 5.8(a). As the interlayer coupling can in principle be the dominant magnetic interaction in $Sr_3Ir_2O_7$, it is reasonable to try to describe the system in terms of singlet and triplet bonds between pairs of spins. The so-called bond-operator mean-field method, introduced by Sachdev and Bhatt [127], has proved to be an accurate method for many bilayer spin systems and was successfully applied to describe magnetic interactions of spin ladder systems [128, 129, 130].

The four states $|\uparrow\downarrow\rangle$, $|\downarrow\uparrow\rangle$, $|\uparrow\uparrow\rangle$ and $|\downarrow\downarrow\rangle$ on each rung can be combined to form one singlet state $|s\rangle$ and three triplet states $|t_\alpha\rangle$, $\alpha{=}x, y, z$. Singlet and triplet creation operators, that create the states out of the vacuum

$|0\rangle$, are introduced:

$$\begin{aligned}
|s\rangle \equiv & s^{\dagger}\,|0\rangle = \frac{1}{\sqrt{2}}(|\uparrow\downarrow\rangle - |\downarrow\uparrow\rangle),\\
|t^x\rangle \equiv & t^{x,\dagger}\,|0\rangle = -\frac{1}{\sqrt{2}}(|\uparrow\uparrow\rangle - |\downarrow\downarrow\rangle),\\
|t^y\rangle \equiv & t^{y,\dagger}\,|0\rangle = \frac{\mathrm{i}}{\sqrt{2}}(|\uparrow\uparrow\rangle + |\downarrow\downarrow\rangle),\\
|t^z\rangle \equiv & t^{z,\dagger}\,|0\rangle = \frac{1}{\sqrt{2}}(|\uparrow\downarrow\rangle + |\downarrow\uparrow\rangle).
\end{aligned} \tag{5.24}$$

The bond operators create and annihilate singlet and triplet bonds between a pair of spins. The representation is useful in describing the transition between dimerised and magnetically ordered phases of quantum antiferromagnets. Inserting this representation into the Hamiltonian 5.23 one can try to describe the ground state by a condensation of singlet and triplet t_z operators. With this assumption, the Hamiltonian can be easily diagonalized via Bogoliubov transformation to obtain two dispersive modes, one longitudinal and one two-fold degenerate transverse mode. This approach is an alternative to the theory developed in Ref. [122] which applies spin wave theory to an ordered Néel state where $J^{\parallel} \gg J^{\perp}$. Here we come from the other side of the phase diagram where $J^{\parallel} \ll J^{\perp}$. As a consequence we obtain a dimerised singlet ground state that shows excitations into gapped triplet states (see Fig. 5.8(b)).

The comparison between theoretical and experimental results is presented in Fig. 5.7(a). The in-plane momentum transfer dependence of features B and D is remarkably well reproduced by the dispersion curves associated to the transverse (blue line) and the longitudinal (purple line) triplet modes, respectively. The best agreement is obtained for $J_1^{\parallel}=26$, $J_2^{\parallel}=$-21, $J_3^{\parallel}=8$, $J^{\perp}=125$, $J_d^{\perp}=38$, and $\theta=15°$ which indicates a strong interlayer coupling of $J^{\perp}/J_1^{\parallel}=4.8$ in combination with a small ferromagnetic next-nearest in-plane coupling.

Using this model the intensity of the transverse and and longitudinal modes can be calculated from the spin-spin correlation function. Unfortunately the detailed analysis is still ongoing and will not be presented here. However, it is important to mention that the intensity measured with RIXS is a superposition of the symmetric and antisymmetric intensities depending on the out-of-plane component of the momentum transfer in analogy with Eqs. 5.21–5.22. In the case of the longitudinal mode this simplifies to $\mathcal{I}^L \propto \cos^2(\pi l d)$ and the intensity is simply a periodic function of the out-of-plane component of the momentum transfer. It is now clear that the point $l = 28.5$ ($l = 25$) r.l.u. is close to a maximum (minimum) of the scattering intensity, therefore explaining the behaviour observed in Figs. 5.3,5.6 and the fact that feature D has not been observed in the data set of Kim et al. [122].

The excitation spectrum of $Sr_3Ir_2O_7$ strongly deviates from the 2D Heisenberg model which has been used to describe the single layer Sr_2IrO_4. The addition of an extra IrO_6 layer seems to strongly enhance interlayer interactions which produce a dimerized system with the magnetic moment pointing along the c axis. The low-energy magnetic excitations are therefore composed of a dispersive 90 meV-gap transverse triplet and a more weakly dispersive 155 meV-gap longitudinal triplet. While our model is able to explain the existence of feature D in the RIXS data, which is reported here for the first time and is not compatible with theoretical arguments of Ref. [122], it falls short in calculating the magnitude of the ordered moment, which appear to be one order of magnitude smaller that the value measured with neutron scattering [41].

5.3.3 Spin-orbit exciton

We now briefly discuss the feature E observed in the 400–600 meV energy range. This energy range belongs to d-d excitations, and in particular to the intra-t_{2g} excitations. These excitations have been widely investigated in 3d TMOs. In cuprates very strong d-d excitations are found, which show a negligible momentum dispersion due to their local character [57, 117]. In iridates, intra-t_{2g} excitations are observed due to electronic transitions from the $|0, \pm\rangle$ ground state to the $|1, \pm\rangle$ and $|2, \pm\rangle$ multiplets. The RIXS amplitude can be calculated with Eq. 5.1 where the final state is substituted by the $|1, \pm\rangle$ and $|2, \pm\rangle$ states, whose definition we have already reported in Section 1.4.1 (Eqs. 1.34–1.42). In the case of perfect cubic symmetry the $|1, \pm\rangle$ and $|2, \pm\rangle$ multiplets degenerate into the $j_{\text{eff}} = 3/2$

band, and RIXS measures transitions from the $j_{\text{eff}} = 1/2$ to the $j_{\text{eff}} = 3/2$ bands. It is therefore not surprising that the energy scale of these excitations coincides with the energy scale of the SOC, since the separation between $j_{\text{eff}} = 1/2$ and $j_{\text{eff}} = 3/2$ states is about $3\lambda/2$ (see Eqs. 1.37–1.39). In several iridates like the honeycomb $(Na/Li)_2IrO_3$ [80], Sr_3CuIrO_6 [65] or the pyrochlore $RE_2Ir_2O_7$ [131] these excitations maintain a local character. On the contrary in the single layer Sr_2IrO_4 [72] and in $Sr_3Ir_2O_7$ the intra-t_{2g} excitations show a strong momentum dependence. This is due to the fact that the spin-orbit excitations between $j_{\text{eff}} = 1/2$ and $j_{\text{eff}} = 3/2$ band propagate through the system. A detailed treatment of this process is given in Ref. [72].

The RIXS process, schematically illustrated in Fig. 5.8(c), creates a hole on the site e in the $|1, \pm\rangle$, $|2, \pm\rangle$ quadruplet that is almost degenerate in the strong SOC limit ($\Delta \to 0$). The hole can then hop to the neighboring site f with an intermediate energy U. The hole in the $j_{\text{eff}} = 1/2$ manifold on the site f hops back to the e site completing the hopping process and producing a magnetic excitations.

Our RIXS data set does not extend to energies higher that 600 meV showing the dispersion of only one of the “spin-orbit exciton” modes (either $|1, \pm\rangle$ or $|2, \pm\rangle$) in the $j_{\text{eff}} = 3/2$ manifold. Feature E shows the same momentum dependence as the lower-energy mode of the spin-orbit exciton observed in Sr_2IrO_4 [72], a large bandwidth of about 200 meV and a minimum in the dispersion at $(\pi/2,\pi/2)$. Analogies with cuprate superconductors can be found by noticing that a hole propagating in the background of AF order in copper oxides shows a minimum in the dispersion at $(\pi/2,\pi/2)$, i.e. at the boundary of the AF Brillouin zone [132]. In layered iridates, instead, we have chargeless particles that propagate through the lattice in a very similar way, therefore strengthening the prediction that doped carriers in layered iridate will show similar dynamics to the motion of the doped carriers in cuprates [29, 28].

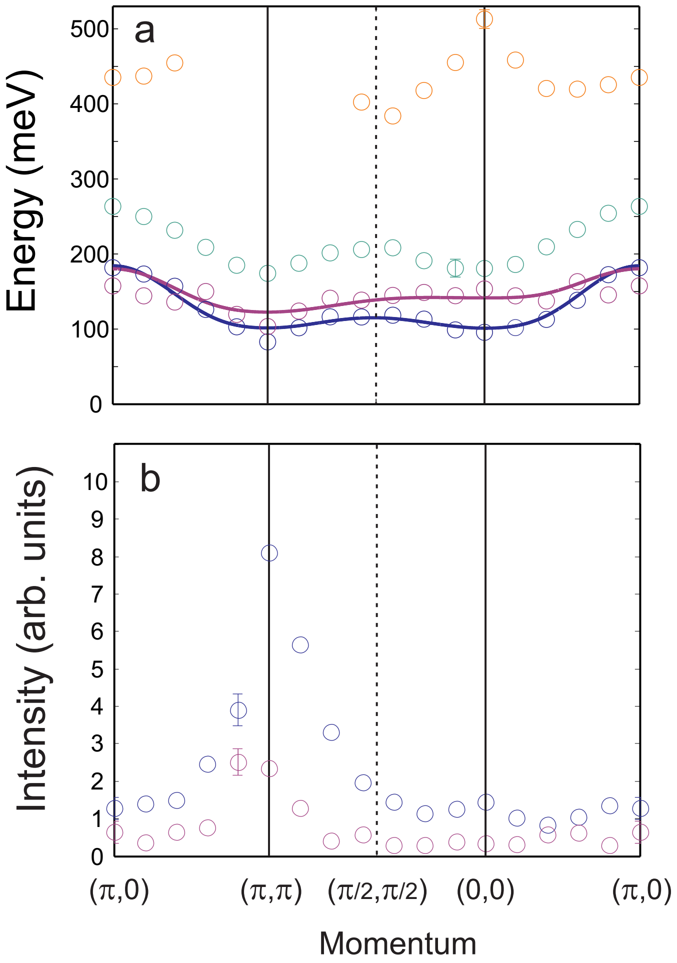

Figure 5.7: (a) Momentum dependence of the energy position of the transverse magnetic mode (blue dots), longitudinal magnetic mode (purple dots), multiple magnetic excitations (green dots) and spin-orbit exciton (orange dots) as extracted from the fit to the RIXS data. The solid line superimposed to the transverse and longitudinal magnons are fit from the theory model.(b) The integrated intensity of features B and D is reported as a function of the in-plane momentum for $\mathbf{K}_c = 28.5$ r.l.u..

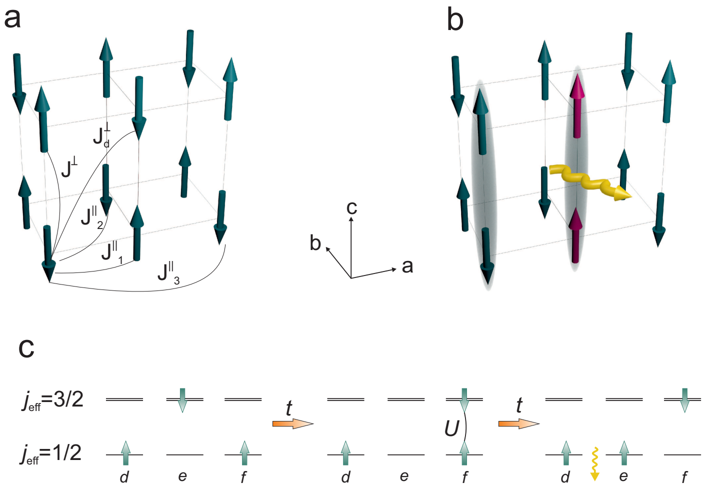

Figure 5.8: (a) Schematic of the dominant magnetic interaction in $Sr_3Ir_2O_7$. (b) Schematic of the creation of magnetic excitations in $Sr_3Ir_2O_7$. A dimerised spin singlet is excited into a triplet state and a magnon is created. (c) Schematic representation of the spin-orbit exciton hopping process. The RIXS process creates a hole on the site e in the $|1, \pm\rangle$, $|2, \pm\rangle$ quadruplet that is almost degenerate in the strong SOC limit ($\Delta \to 0$). The hole can then hop to the neighboring site f with an intermediate energy U. The hole in the $j_{\text{eff}} = 1/2$ manifold on the site f hops back to the e site completing the hopping process and producing a magnetic excitations.

5.4 Conclusions

In this chapter we have presented a detailed L_3 edge RIXS study of the low-energy magnetic excitation in $\mathrm{Sr_3Ir_2O_7}$. RIXS is demonstrated to be a powerful tool to study momentum dependent excitations in $5d$ transition metal oxides due to the strong enhancement of the inelastic signal at the $5d$ L edges and the large access to the reciprocal space that this energy range allows.

Our RIXS experiment establishes the existence of two main magnetic modes: a dispersive 90 meV-gap mode already reported in Ref. [122] and a more weakly dispersive 155 meV-gap mode never reported previously. Using a bond-operator mean-field method on a pseudospin-1/2 frustrated Heisenberg model developed by our collaborators at the EPFL, we are able to assign these modes to excitations from a dimerised singlet ground state to a transverse and longitudinal triplet states, respectively.

From the fit of the theoretical model to the experimental data the leading superexchange parameters are extracted. Surprisingly the nearest-neighbour interlayer superexchange $J^{\perp}$ is found to be five times larger that the in-plane superexchange $J^{\parallel}$, marking a significant departure from the 2D Heisenberg model used to described the properties of the single layer cousin $\mathrm{Sr_2IrO_4}$.

Chapter 6

Conclusions and perspective

In this thesis I have investigated the magnetic order and excitations in layered perovskite iridates with resonant X-ray scattering techniques. Layered perovskite iridates belong to a recently rediscovered class of $5d$ transition metal oxides, where it is now realized that a novel $j_{\text{eff}} = 1/2$ ground state emerges from the combined effect of cubic crystal field and the spin-orbit interaction which act jointly on the Ir ion.

X-ray resonant scattering techniques have played a leading role in driving the field forward mainly due to the fact that iridate samples are extremely small, and Ir is a strong neutron absorber, making the use of more popular techniques like neutron scattering extremely challenging for these materials. Furthermore, by exploiting atomic resonances in correspondence of the Ir $L_{2,3}$ edges the scattering signal is greatly enhanced and the access to a large portion of the reciprocal space is allowed. In this scenario, XRMS and RIXS techniques have been used to investigate the ground and the excited states of perovskite iridates, respectively.

It has been established earlier that XRMS can be used to determine the atomic wave function in iridium oxides due to the inherent quantum interference between different scattering paths which distinguishes XRMS. In this work I have developed a single ion model that treats on an equal footing the spin-orbit interaction (SOI) and the tetragonal crystal field which typically affects the Ir ion in perovskite iridates. By calculating the XRMS cross-section as a function of the magnetic moment direction I have shown that XRMS exhibits a non-trivial dependence on the moment direction. While XRMS allows the observation of the orbital state when the magnetic moments point perpendicular to the perovskite planes like in the bilayer $Sr_3Ir_2O_7$, on the contrary, when the moments lie in the basal-plane like in the single layer perovskites Sr_2IrO_4 and Ba_2IrO_4, XRMS prevents to unambiguously determine the atomic wave function.

XRMS at the Ir L_3 edge has been used to study the magnetic and electronic structures of the single layered iridates Ba_2IrO_4 and Sr_2IrO_4. Ba_2IrO_4 is found to be a basal-plane commensurate antiferromagnet below $T_N = 241$ K. Azimuthal scans combined with group theory calculations have been employed to prove that the moments order along the $[1\,1\,0]$ direction. From a comparison with XRMS data on the related compound Sr_2IrO_4, I have established that both compounds have essentially the same basal-plane antiferromagnetic structure, in spite of their structural differences. Thus the magnetic structures in the layered perovskites are remarkably robust to structural distortions, a fact that can be linked directly to the unique three-dimensional character of the $j_{\text{eff}} = 1/2$ state produced by the strong SOI, which renders it insensitive to the perturbations in local symmetry.

In Sr_2IrO_4 a correlated alternated rotation of the IrO_6 removes the inversion symmetry on the Ir sites activating a finite Dzyaloshinskii-Moriya interaction. As a consequence, in Sr_2IrO_4 the total moment is slightly canted from the simple basal-plane structure of Ba_2IrO_4. From a comparison between the observed intensity of several magnetic Bragg peaks and the calculated resonant magnetic cross-section for a model arrangement of Ir moments, I have found that the Ir magnetic moments rigidly follow the IrO_6 octahedra deviating by 12.2° from the a axis. My results thus add to the growing weight of evidence that, in spite of the fact that the local environment of the Ir^{4+} ions is distorted from perfect cubic symmetry, the ground state in Sr_2IrO_4 has many of the attributes of the proposed $j_{\text{eff}} = 1/2$ state. More generally, the fact that the magnetic moment canting is locked to the oxygen rotation lends strong support to the theoretical model which has been developed to understand the properties of this and other iridate perovskites.

The effect of dimensionality on the magnetic and electronic properties of perovskite iridates has been investigated in the bilayer system $Sr_3Ir_2O_7$. Here, the addition of an extra IrO_6 layer pushes the system closer to a metal-to-insulator transition and introduces additional interlayer interacions. From the analysis of the L_2/L_3 XRMS intensity ratio we show that $Sr_3Ir_2O_7$ lies in proximity of a pure $j_{\text{eff}} = 1/2$ state. Despite this, the addition of an extra IrO_6 layer significantly modifies the magnetic structure of $Sr_3Ir_2O_7$ which, compared to the single layer counterpart Sr_2IrO_4, shows a *c*-axis collinear antiferromagnetic structure.

The fact that the physics at play in the bilayer iridate greatly departs from the 2D Heisenberg-like one which distinguishes the single layer Sr_2IrO_4 is further confirmed by our high-energy-resolution L_3 edge RIXS study of the low energy magnetic excitations. In the RIXS spectra we identify two main magnetic modes: a dispersive 90 meV-gap mode observed also in previous studies, and a more weakly dispersive 155 meV-gap mode never reported previously. Using a bond-operator mean-field method on a pseudospin-1/2 frustrated Heisenberg model developed by our collaborators at the EPFL, I am able to assign these modes to excitations from an essentially dimerised singlet ground state to a transverse and longitudinal triplet states, respectively. Surprisingly the nearest-neighbour interlayer interaction results five time bigger that the in-plane one, marking a significant departure from the 2D-like physics of the single layer compound.

Tuning electronic states in layered perovskite iridates via pressure, epitaxial strain, and doping is the natural continuation of the work described in this thesis. Since the orbital state, due to the SOI is no longer quenched like in 3*d* metals, interactions are thought to depend strongly on the lattice geometry and give rise to new exotic phases. A change in the local symmetry can be induced in several ways. The first port of call is the application of hydrostatic pressure. Another possibility is the growth of epitaxially strained film on top of various substrates. Both this two methods will permit to study the entanglement between lattice and electronic/magnetic degrees of freedom that is predicted to dominate in iridates.

Doping an AFM system could have unexpected consequences. For examples, in the case of layered cuprates doping studies led to the discovery of high-T_C superconductivity. Interestingly, superconductivity has been predicted in electron-doped layered iridates too [28, 29]. RIXS at the Cu L_3 has developed into a very powerful tool to study magnetic excitations in high-T_C cuprates as a function of doping. Along similar lines, the study of the magnetic excitations in doped iridates by exploiting the very high energy resolution of Ir L_3 RIXS could become a new flourishing field.

In addition to the studies on the iridates, new exotic properties are emerging in other $5d$ TMOs. In particular, osmium oxides are attracting growing attention. The ground state in the osmates does not show the same symmetry properties as in the iridates, namely the realization of the $j_{\text{eff}} = 1/2$ state. Nonetheless, the SOI is strong in osmates too, and unusual metal-insulator transitions, correlated with the magnetic degrees of freedom occur [133, 134]. It is therefore of significant interest to elucidate the correlated physics of osmates in comparison with the iridium oxides.

With the development of X-ray free electron lasers (XFELs), time-resolved RIXS studies of excited electronic states have become possible. Such studies can be carried out in a pump-probe mode where an optical or THz pump pulse is used to induce an out-of-equilibrium state, and the X-ray probe pulses reveal the time evolution of low-energy excited states. Contrary to synchrotron radiation sources where within a femtosecond time interval no more than a single photon is typically present in the sample, the XFEL pulses contain up to 10^9 equivalent photons within the same time interval. In this context, iridium oxides represent an interesting playground for the full development of time-resolved RIXS.

Appendix A

Atomic d orbitals in cubic ligand field

In an isolated atom the potential experienced by a single electron is spherical. In a molecule or a crystal it has in general a lower symmetry. Therefore electronic states that are degenerate in the isolated atom can be separated in the crystal. This is due to the crystal field, that is in general a sum of two contributions, the Coulomb potential generated by all the surrounding atoms, and the ligand field with the nearest neighbors. In the following we will assume that the crystal is ionic and the ions can be regarded as point charges, neglecting thus the ligand field.

We consider an hydrogen-like atom surrounded by 6 point charges, $-Ze$, with $Z > 0$ for the negative charges and $Z < 0$ for the positive ones at a distance a from the central atom M(see Fig. A.1). The potential energy of an electron at a position $\mathbf{r}$ generated by the 6 charges at a position $\mathbf{R_i}$ is given by

$$V_c(\mathbf{r}) = \sum_{i=1}^{6} \frac{Ze^2}{|\mathbf{R_i} - \mathbf{r}|} = Ze^2 \left[\frac{1}{\sqrt{(x-a)^2 + y^2 + z^2}} + \frac{1}{\sqrt{(x+a)^2 + y^2 + z^2}} \right. + \frac{1}{\sqrt{x^2 + (y-a)^2 + z^2}} + \frac{1}{\sqrt{x^2 + (y+a)^2 + z^2}} + \frac{1}{\sqrt{x^2 + y^2 + (z-a)^2}} \left. + \frac{1}{\sqrt{x^2 + y^2 + (z+a)^2}} \right]. \tag{A.1}$$

Expanding $V_c(\mathbf{r})$ around the origin the first non vanishing term is:

$$V_c(\mathbf{r}) = V_0 + D\left(x^4 + y^4 + z^4 - \frac{3}{5}r^4\right) \tag{A.2}$$

where $V_0 = \frac{6Ze^2}{a}$ shifts all the atomic energy by the same amount, on the contrary $D = \frac{35Ze^2}{4a^5}$ is the term responsible of removing the degeneracy between the atomic states as we will show later. In order to calculate the matrix elements of the cubic potential in the atomic d-state basis is convenient to expand $V_c(\mathbf{r})$ in terms of spherical harmonics as:

$$V_c(\mathbf{r}) = \frac{6Ze^2}{a} + \frac{7Ze^2}{2a^5}\sqrt{\frac{4\pi}{9}}r^4 \left[Y_0^4(\theta,\phi) + \sqrt{\frac{5}{14}}\left(Y_4^4(\theta,\phi) + Y_{-4}^4(\theta,\phi)\right)\right] \tag{A.3}$$

where

$$Y_0^4(\theta,\phi) = \frac{3\left(3 - 30\cos(\theta)^2 + 35\cos(\theta)^4\right)}{16\sqrt{\pi}},$$

$$Y_{\pm 4}^4(\theta,\phi)\frac{3}{16}e^{\pm 4i\phi}\sqrt{\frac{35}{2\pi}}\sin(\theta)^4.$$

Bearing in mind that the atomic d-wave functions can be written as

$$\Psi_{nlm}(\mathbf{r}) = R_{nd}(r) \cdot Y_m^l(\theta,\phi) \tag{A.4}$$

where $R_{nd}(r)$ is the radial wave function of the d-states that depends on the principal quantum number n. Y_m^l are spherical harmonics representing the angular component of the wave functions, where l=2 and m=2, 1, 0, -1, -2.

We are now interested in calculating the matrix element of the cubic potential in the d-state basis

$$\langle\Psi_{nlm}|V_c(\mathbf{r})-V_0|\Psi_{nlm'}\rangle=\int\Psi_{nlm}(\mathbf{r})^*(V_c(\mathbf{r})-V_0)\Psi_{nlm'(\mathbf{r})}d\mathbf{r} \tag{A.5}$$

where the cubic potential has been rigidly shifted by the quantity V_0 which is independent on the spatial coordinates. We can now proceed in evaluating the matrix elements of the crystal field potential calculating integrals of the form:

$$\int_0^\pi\int_0^{2\pi}Y_m^2(\theta,\phi)^*Y_k^4(\theta,\phi)Y_{m'}^2(\theta,\phi)\sin(\theta)d\phi d\theta \tag{A.6}$$

The calculation is straightforward and the non vanishing matrix elements are the following:

$$\begin{aligned}\langle\Psi_{n20}|V_c(\mathbf{r})-V_0|\Psi_{n20}\rangle&=6Dq\\ \langle\Psi_{n2\pm1}|V_c(\mathbf{r})-V_0|\Psi_{n2\pm1}\rangle&=-4Dq\\ \langle\Psi_{n2\pm2}|V_c(\mathbf{r})-V_0|\Psi_{n2\pm2}\rangle&=Dq\\ \langle\Psi_{n2\pm2}|V_c(\mathbf{r})-V_0|\Psi_{n2\mp2}\rangle&=5Dq\end{aligned} \tag{A.7}$$

where $q=\frac{2}{105}\langle r^4\rangle_{nd}$ and $\langle r^4\rangle_{nd}=\int r^4r^2|R_{nd}(r)|^2dr$. The crystal field splitting can be obtained by diagonalizing the crystal field Hamiltonian

$$H_{\mathrm{CF}}=\begin{pmatrix}Dq&0&0&0&5Dq\\0&-4Dq&0&0&0\\0&0&6Dq&0&0\\0&0&0&-4Dq&0\\5Dq&0&0&0&Dq\end{pmatrix}. \tag{A.8}$$

We find that the eigenvectors are composed by double degenerate states

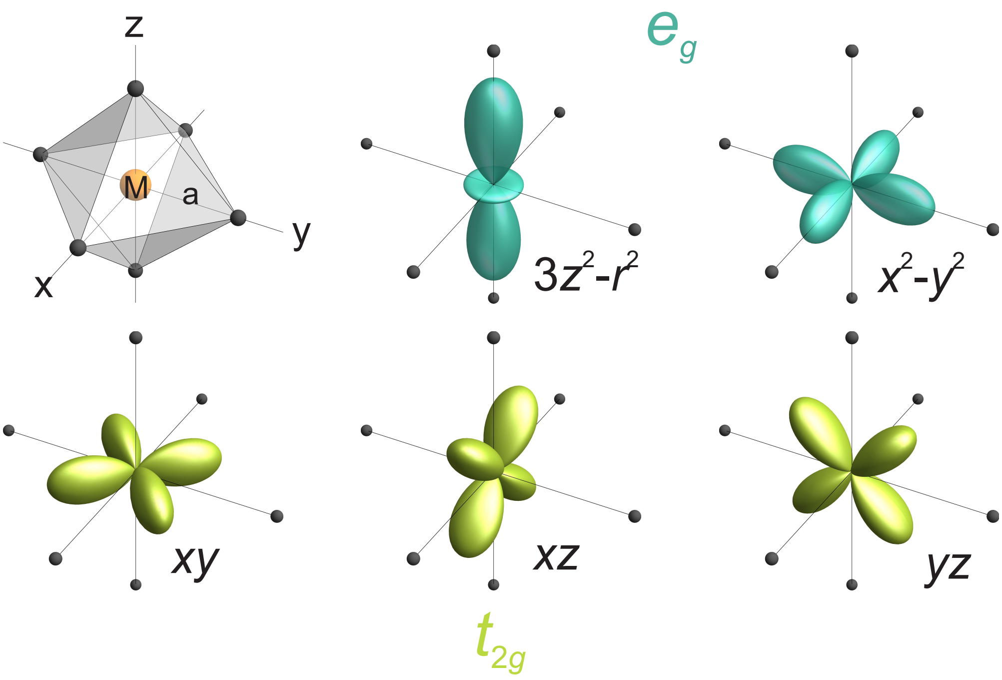

Figure A.1: Angular behaviour of the atomic d states in a cubic crystal field. The orbitals pointing toward the ligands form the higher e_g doublet ($3z^2-r^2$, x^2-y^2), whilst the others form the lower t_{2g} triplet (xy, xz, yz).

of energy 6 Dq

$$\left.\begin{aligned} |\Psi_{n20}\rangle &= |3z^2-r^2\rangle \\ \frac{1}{\sqrt{2}}\left[|\Psi_{n2\bar{2}}\rangle + |\Psi_{n22}\rangle\right] &= |x^2-y^2\rangle \end{aligned}\right\} \quad e_g, \tag{A.9}$$

which are commonly referred as e_g states, and 3-fold degenerate eigenstates of energy -4Dq

$$\left.\begin{aligned} \frac{1}{\sqrt{2}}\left[|\Psi_{n2\bar{2}}\rangle - |\Psi_{n22}\rangle\right] &= |\phi_1\rangle \\ |\Psi_{n2\bar{1}}\rangle &= |\phi_2\rangle \\ |\Psi_{n21}\rangle &= |\phi_3\rangle \end{aligned}\right\} \quad \phi_i. \tag{A.10}$$

The latter eigenvectors are not real in the ϕ_i basis, but by choosing a suitable unitary transformation

$$U = \begin{pmatrix} 0 & 0 & i \\ \frac{i}{\sqrt{2}} & \frac{1}{\sqrt{2}} & 0 \\ \frac{i}{\sqrt{2}} & \frac{-1}{\sqrt{2}} & 0 \end{pmatrix}, \tag{A.11}$$

we can obtain the well known t_{2g} states as $|t_{2g}\rangle = \sum_i U|\phi_i\rangle$,

$$\left.\begin{aligned} \frac{i}{\sqrt{2}}\left[|\Psi_{n2\bar{2}}\rangle - |\Psi_{n22}\rangle\right] &= |xy\rangle \\ \frac{1}{\sqrt{2}}\left[|\Psi_{n2\bar{1}-} - |\Psi_{n21}\rangle\right] &= |xz\rangle \\ \frac{i}{\sqrt{2}}\left[|\Psi_{n2\bar{1}-} + |\Psi_{n21}\rangle\right] &= |yz\rangle \end{aligned}\right\} \quad t_{2g}. \tag{A.12}$$

Finally the crystal field splitting is given by

$$E(e_g) - E(t_{2g}) = 10Dq \tag{A.13}$$

Therefore considering negative point charges (Z >0) the energy of the e_g states will be higher than that of the t_{2g} states. This result can be easily interpreted by looking at the real space angular dependence of the d-state wave functions (Fig. A.1). The electrons belonging to an e_g orbital, which points directly to the negative ligand, will experienced a stronger Coulomb repulsion than the t_{2g} electrons.

We note that in order to calculate precisely the crystal field splitting in real materials this model is not sufficient. In fact, the adoption of a pure ionic model lead us to neglect any covalent effect, potentially significant, between nearest neighbors. Corrections to the point charge approximation and the inclusion of the ligan field by means of density functional theory calculation are often necessary to estimate the crystal field splitting.

Appendix B

Irreducible representations for the *Bbcb* space group in $Sr_3Ir_2O_7$

We report group theory calculations with the SARAh package [94] for the irreducible representations (IRs) relative to space group *Bbcb* in $Sr_3Ir_2O_7$. The input parameters were the magnetic propagation vector $\mathbf{k} = [1\,0\,0]$ which corresponds to $\mathbf{k} = [\frac{1}{2}\,\frac{1}{2}\,0]$ in the $I4/mmm$ reference system, as obtained from the XRMS experiment presented in Section 4.4.1, and the Ir atomic positions of Tab. 4.4.

The results of the calculations are shown in Tab. B.1. The obtained IRs are equivalent to the one in Tab. 4.5 calculated for the $I4/mmm$ space group. In particular the IRs Γ_1 and Γ_2 of Tab. B.1 correspond to Γ_2 of Tab. 4.5 for the different magnetic domains A and B, respectively, i.e. to the *G*-type *c*-axis collinear magnetic structure observed in $Sr_3Ir_2O_7$. On the contrary, the Γ_7 and Γ_8 IRs of Tab. B.1 correspond to Γ_3 of Tab. 4.5 where the bilayer are coupled ferromagnetically. Notably, even for the *Bbcb* space group, there is no IRs which involve any in-plane ferromagnetic component that explains the *ab*-plane weak ferromagnetism observed in $Sr_3Ir_2O_7$.

IR	BV	Atom	BV components					
			$m_{\parallel a}$	$m_{\parallel b}$	$m_{\parallel c}$	$im_{\parallel a}$	$im_{\parallel b}$	$im_{\parallel c}$
Γ_1	$\boldsymbol{\psi}_1$	1	0	0	1	0	0	0
		2	0	0	-1	0	0	0
		3	0	0	-1	0	0	0
		4	0	0	1	0	0	0
Γ_2	$\boldsymbol{\psi}_2$	1	0	0	1	0	0	0
		2	0	0	-1	0	0	0
		3	0	0	1	0	0	0
		4	0	0	-1	0	0	0
Γ_3	$\boldsymbol{\psi}_3$	1	1	0	0	0	0	0
		2	1	0	0	0	0	0
		3	-1	0	0	0	0	0
		4	-1	0	0	0	0	0
	$\boldsymbol{\psi}_4$	1	0	1	0	0	0	0
		2	0	-1	0	0	0	0
		3	0	-1	0	0	0	0
		4	0	1	0	0	0	0
Γ_4	$\boldsymbol{\psi}_5$	1	1	0	0	0	0	0
		2	1	0	0	0	0	0
		3	1	0	0	0	0	0
		4	1	0	0	0	0	0
	$\boldsymbol{\psi}_6$	1	0	1	0	0	0	0
		2	0	-1	0	0	0	0
		3	0	1	0	0	0	0
		4	0	-1	0	0	0	0
Γ_5	$\boldsymbol{\psi}_7$	1	1	0	0	0	0	0
		2	-1	0	0	0	0	0
		3	-1	0	0	0	0	0
		4	1	0	0	0	0	0
	$\boldsymbol{\psi}_8$	1	0	1	0	0	0	0
		2	0	1	0	0	0	0
		3	0	-1	0	0	0	0
		4	0	-1	0	0	0	0
Γ_6	$\boldsymbol{\psi}_9$	1	1	0	0	0	0	0
		2	-1	0	0	0	0	0
		3	1	0	0	0	0	0
		4	-1	0	0	0	0	0
	$\boldsymbol{\psi}_{10}$	1	0	1	0	0	0	0
		2	0	1	0	0	0	0
		3	0	1	0	0	0	0
		4	0	1	0	0	0	0

IR	BV	Atom	BV components					
			m_a	m_b	m_c	im_a	im_b	im_c
Γ_7	$\boldsymbol{\psi}_{11}$	1	0	0	1	0	0	0
		2	0	0	1	0	0	0
		3	0	0	-1	0	0	0
		4	0	0	-1	0	0	0
Γ_8	$\boldsymbol{\psi}_{12}$	1	0	0	1	0	0	0
		2	0	0	1	0	0	0
		3	0	0	1	0	0	0
		4	0	0	1	0	0	0

Table B.1: Basis vectors for the space group $Ccca$: origin 1 with $\mathbf{k}$=[1 0 0].The decomposition of the magnetic representation for the Ir site (0, 0, .0974) is $\Gamma_{Mag} = 1\Gamma_1^1{+}1\Gamma_2^1{+}2\Gamma_3^1{+}2\Gamma_4^1{+}2\Gamma_5^1{+}2\Gamma_6^1{+}1\Gamma_7^1{+}1\Gamma_8^1$. The atoms of the nonprimitive basis are defined according to 1: (0, 0, .0974), 2: (0, 0, .9026), 3: (0, .5, .4026), 4: (0, .5, .5974).

Bibliography

[1] William Witczak-Krempa, Gang Chen, Yong Baek Kim, and Leon Balents. Correlated Quantum Phenomena in the Strong Spin-Orbit Regime. *Annual Review of Condensed Matter Physics*, 5(1):57–82, 2014. URL `http://dx.doi.org/10.1146/annurev-conmatphys-020911-125138`. 24, 36, 38

[2] J.G. Bednorz and K.A. Müller. Possible high-T_c superconductivity in the BaLaCuO system. *Zeitschrift fr Physik B Condensed Matter*, 64(2):189–193, 1986. ISSN 0722-3277. URL `http://dx.doi.org/10.1007/BF01303701`. 28

[3] A P Ramirez. Colossal magnetoresistance. *Journal of Physics: Condensed Matter*, 9(39):8171, 1997. URL `http://stacks.iop.org/0953-8984/9/i=39/a=005`. 28

[4] Sang-Wook Cheong and Maxim Mostovoy. Multiferroics: a magnetic twist for ferroelectricity. *Nat Mater*, 6:13–20, 2007. URL `http://dx.doi.org/10.1038/nmat1804`. 28

[5] J. Hubbard. Electron correlations in narrow energy bands. *Proceedings of the Royal Society of London. Series A. Mathematical and Physical Sciences*, 276(1365):238–257, 1963. URL `http://rspa.royalsocietypublishing.org/content/276/1365/238.abstract`. 28

[6] J. Hubbard. Electron correlations in narrow energy bands. iii. an improved solution. *Proceedings of the Royal Society of London. Series A. Mathematical and Physical Sciences*, 281(1386):401–419, 1964. URL `http://rspa.royalsocietypublishing.org/content/281/1386/401.abstract`. 28

[7] G. Kotliar and D. Vollhardt. Strongly Correlated Materials: Insights From Dynamical Mean-Field Theory. *Physics Today*, 3(53), 2004. URL `http://dx.doi.org/10.1063/1.1712502`. 29

[8] Masatoshi Imada, Atsushi Fujimori, and Yoshinori Tokura. Metal-insulator transitions. *Rev. Mod. Phys.*, 70:1039–1263, Oct 1998. URL `http://link.aps.org/doi/10.1103/RevModPhys.70.1039`. 30

[9] A. D. Jackson. *Classical electrodynamics*. John Wiley & Sons, Inc., 1962. 32

[10] P. A. M Dirac. *The Principles of Quantum Mechanics*. The International Series of Monographs on Physics. Oxford University Press, 1958. 32

[11] E. Francisco and L. Pueyo. Theoretical spin-orbit coupling constants for 3 d ions in crystals. *Phys. Rev. B*, 37:5278–5288, Apr 1988. URL `http://link.aps.org/doi/10.1103/PhysRevB.37.5278`. 32

[12] L. F. Mattheiss. Electronic structure of RuO_2, OsO_2, and IrO_2. *Phys. Rev. B*, 13:2433–2450, Mar 1976. URL `http://link.aps.org/doi/10.1103/PhysRevB.13.2433`. 32, 127

[13] E. Clementi, D. L. Raimondi, and W. P. Reinhardt. Atomic Screening Constants from SCF Functions. II. Atoms with 37 to 86 Electrons. *The Journal of Chemical Physics*, 47(4):1300–1307, 1967. URL `http://scitation.aip.org/content/aip/journal/jcp/47/4/10.1063/1.1712084`. 33

[14] B. J. Kim, H. Ohsumi, T. Komesu, S. Sakai, T. Morita, H. Takagi, and T. Arima. Phase-Sensitive Observation of a Spin-Orbital Mott

State in Sr_2IrO_4. *Science*, 323(5919):1329–1332, 2009. URL http://www.sciencemag.org/content/323/5919/1329.abstract. 35, 38, 45, 70, 71, 79, 95, 96, 97, 98, 102, 121, 122, 133

[15] S. Boseggia, R. Springell, H. C. Walker, A. T. Boothroyd, D. Prabhakaran, D. Wermeille, L. Bouchenoire, S. P. Collins, and D. F. McMorrow. Antiferromagnetic order and domains in $Sr_3Ir_2O_7$ probed by x-ray resonant scattering. *Phys. Rev. B*, 85:184432, May 2012. URL http://link.aps.org/doi/10.1103/PhysRevB.85.184432. 35, 45, 122, 145, 164

[16] S. Boseggia, R. Springell, H. C. Walker, H. M. Rønnow, Ch. Rüegg, H. Okabe, M. Isobe, R. S. Perry, S. P. Collins, and D. F. McMorrow. Robustness of Basal-Plane Antiferromagnetic Order and the $J_{\rm eff}$=1/2 State in Single-Layer Iridate Spin-Orbit Mott Insulators. *Phys. Rev. Lett.*, 110:117207, Mar 2013. URL http://link.aps.org/doi/10.1103/PhysRevLett.110.117207. 35, 45, 48, 79, 94, 99, 106, 107, 112, 113, 121, 167

[17] S. J. Moon, M. W. Kim, K. W. Kim, Y. S. Lee, J.-Y. Kim, J.-H. Park, B. J. Kim, S.-J. Oh, S. Nakatsuji, Y. Maeno, I. Nagai, S. I. Ikeda, G. Cao, and T. W. Noh. Electronic structures of layered perovskite Sr_2MO_4 (M = Ru, Rh, and Ir). *Phys. Rev. B*, 74:113104, Sep 2006. URL http://link.aps.org/doi/10.1103/PhysRevB.74.113104. 35, 45

[18] Dmytro Pesin and Leon Balents. Mott physics and band topology in materials with strong spin-orbit interaction. *Nat Phys*, 6:376–381, 2010. URL http://dx.doi.org/10.1038/nphys1606. 36, 38

[19] B Kim, Hosub Jin, S Moon, J-Y Kim, B-G Park, C Leem, Jaejun Yu, T Noh, C Kim, S-J Oh, J-H Park, V Durairaj, G Cao, and E Rotenberg. Novel jeff=1/2 mott state induced by relativistic spin-orbit coupling in Sr2IrO4. *Physical review letters*, 101(7), 2008. URL http://dx.doi.org/10.1103/PhysRevLett.101.076402. 37, 38, 40, 95, 105

[20] Kazuyuki Matsuhira, Makoto Wakeshima, Yukio Hinatsu, and Seishi Takagi. Metal–Insulator Transitions in Pyrochlore Oxides $Ln_2Ir_2O_7$. *Journal of the Physical Society of Japan*, 80(9):094701, 2011. URL `http://jpsj.ipap.jp/link?JPSJ/80/094701/`. 38, 40

[21] William Witczak-Krempa and Yong Baek Kim. Topological and magnetic phases of interacting electrons in the pyrochlore iridates. *Phys. Rev. B*, 85:045124, Jan 2012. URL `http://link.aps.org/doi/10.1103/PhysRevB.85.045124`. 38

[22] Xiangang Wan, Ari M. Turner, Ashvin Vishwanath, and Sergey Y. Savrasov. Topological semimetal and fermi-arc surface states in the electronic structure of pyrochlore iridates. *Phys. Rev. B*, 83:205101, May 2011. URL `http://link.aps.org/doi/10.1103/PhysRevB.83.205101`. 38

[23] G. Jackeli and G. Khaliullin. Mott Insulators in the Strong Spin-Orbit Coupling Limit: From Heisenberg to a Quantum Compass and Kitaev Models. *Phys. Rev. Lett.*, 102:017205, Jan 2009. URL `http://link.aps.org/doi/10.1103/PhysRevLett.102.017205`. 38, 51, 54, 95, 106, 111, 133

[24] Jiří Chaloupka, George Jackeli, and Giniyat Khaliullin. Kitaev-heisenberg model on a honeycomb lattice: Possible exotic phases in iridium oxides A_2IrO_3. *Phys. Rev. Lett.*, 105:027204, Jul 2010. URL `http://link.aps.org/doi/10.1103/PhysRevLett.105.027204`. 38

[25] S. K. Choi, R. Coldea, A. N. Kolmogorov, T. Lancaster, I. I. Mazin, S. J. Blundell, P. G. Radaelli, Yogesh Singh, P. Gegenwart, K. R. Choi, S.-W. Cheong, P. J. Baker, C. Stock, and J. Taylor. Spin waves and revised crystal structure of honeycomb iridate Na_2IrO_3. *Phys. Rev. Lett.*, 108:127204, Mar 2012. URL `http://link.aps.org/doi/10.1103/PhysRevLett.108.127204`. 38

[26] Yogesh Singh, S. Manni, J. Reuther, T. Berlijn, R. Thomale, W. Ku, S. Trebst, and P. Gegenwart. Relevance of the Heisenberg-Kitaev

Model for the Honeycomb Lattice Iridates A_2IrO_3. *Phys. Rev. Lett.*, 108:127203, Mar 2012. URL `http://link.aps.org/doi/10.1103/PhysRevLett.108.127203`. 38

[27] X. Liu, T. Berlijn, W.-G. Yin, W. Ku, A. Tsvelik, Young-June Kim, H. Gretarsson, Yogesh Singh, P. Gegenwart, and J. P. Hill. Long-range magnetic ordering in Na_2IrO_3. *Phys. Rev. B*, 83:220403, Jun 2011. URL `http://link.aps.org/doi/10.1103/PhysRevB.83.220403`. 38

[28] Fa Wang and T. Senthil. Twisted Hubbard Model for Sr_2IrO_4: Magnetism and Possible High Temperature Superconductivity. *Phys. Rev. Lett.*, 106:136402, Mar 2011. URL `http://link.aps.org/doi/10.1103/PhysRevLett.106.136402`. 38, 94, 192, 200

[29] Hiroshi Watanabe, Tomonori Shirakawa, and Seiji Yunoki. Monte Carlo Study of an Unconventional Superconducting Phase in Iridium Oxide J_{eff}=1/2 Mott Insulators Induced by Carrier Doping. *Phys. Rev. Lett.*, 110:027002, Jan 2013. URL `http://link.aps.org/doi/10.1103/PhysRevLett.110.027002`. 38, 94, 192, 200

[30] A. Abragam and B. Bleaney. *Electron paramagnetic resonance of transition ions*. International series of monographs on physics. Clarendon P., 1970. 39

[31] S. J. Moon, Hosub Jin, W. S. Choi, J. S. Lee, S. S. A. Seo, J. Yu, G. Cao, T. W. Noh, and Y. S. Lee. Temperature dependence of the electronic structure of the $j_{\mathrm{eff}} = 1/2$ Mott insulator Sr_2IrO_4 studied by optical spectroscopy. *Phys. Rev. B*, 80:195110, Nov 2009. doi: 10.1103/PhysRevB.80.195110. URL `http://link.aps.org/doi/10.1103/PhysRevB.80.195110`. 40, 96, 97, 98

[32] G. Cao, J. Bolivar, S. McCall, J. E. Crow, and R. P. Guertin. Weak ferromagnetism, metal-to-nonmetal transition, and negative differential resistivity in single-crystal Sr_2IrO_4. *Phys. Rev. B*, 57: R11039–R11042, May 1998. URL `http://link.aps.org/doi/10.1103/PhysRevB.57.R11039`. 40, 96, 98, 100, 113, 143

[33] G. Cao, Y. Xin, C. S. Alexander, J. E. Crow, P. Schlottmann, M. K. Crawford, R. L. Harlow, and W. Marshall. Anomalous magnetic and transport behavior in the magnetic insulator $Sr_3Ir_2O_7$. *Phys. Rev. B*, 66:214412, Dec 2002. URL `http://link.aps.org/doi/10.1103/PhysRevB.66.214412`. 40, 137, 142, 143, 144, 145, 164

[34] H. Okabe, M. Isobe, E. Takayama-Muromachi, A. Koda, S. Takeshita, M. Hiraishi, M. Miyazaki, R. Kadono, Y. Miyake, and J. Akimitsu. Ba_2IrO_4: A spin-orbit Mott insulating quasi-two-dimensional antiferromagnet. *Phys. Rev. B*, 83:155118, Apr 2011. URL `http://link.aps.org/doi/10.1103/PhysRevB.83.155118`. 40, 112, 113, 115, 117, 119

[35] J.-G. Cheng, J.-S. Zhou, J. B. Goodenough, Y. Sui, Y. Ren, and M. R. Suchomel. High-pressure synthesis and physical properties of perovskite and post-perovskite $Ca_{1-x}Sr_xIrO_3$. *Phys. Rev. B*, 83:064401, Feb 2011. URL `http://link.aps.org/doi/10.1103/PhysRevB.83.064401`. 40

[36] R. Comin, G. Levy, B. Ludbrook, Z.-H. Zhu, C. N. Veenstra, J. A. Rosen, Yogesh Singh, P. Gegenwart, D. Stricker, J. N. Hancock, D. van der Marel, I. S. Elfimov, and A. Damascelli. Na_2IrO_3 as a Novel Relativistic Mott Insulator with a 340-meV Gap. *Phys. Rev. Lett.*, 109:266406, Dec 2012. URL `http://link.aps.org/doi/10.1103/PhysRevLett.109.266406`. 40

[37] M. Moretti Sala, S. Boseggia, D. F. McMorrow, and G. Monaco. Resonant x-ray scattering and the $j_{\text{eff}} = 1/2$ electronic ground state in iridate perovskites. *Phys. Rev. Lett.*, 112(2):026403–, January 2014. URL `http://link.aps.org/doi/10.1103/PhysRevLett.112.026403`. 41, 70

[38] H. Gretarsson, J. P. Clancy, Yogesh Singh, P. Gegenwart, J. P. Hill, Jungho Kim, M. H. Upton, A. H. Said, D. Casa, T. Gog, and Young-June Kim. Magnetic excitation spectrum of Na_2IrO_3 probed with resonant inelastic x-ray scattering. *Phys. Rev. B*, 87:220407,

Jun 2013. URL http://link.aps.org/doi/10.1103/PhysRevB.87.220407. 45

[39] S Boseggia, H C Walker, J Vale, R Springell, Z Feng, R S Perry, M Moretti Sala, H M Rønnow, S P Collins, and D F McMorrow. Locking of iridium magnetic moments to the correlated rotation of oxygen octahedra in Sr_2IrO_4 revealed by x-ray resonant scattering. *Journal of Physics: Condensed Matter*, 25(42):422202, 2013. URL http://stacks.iop.org/0953-8984/25/i=42/a=422202. 47, 106

[40] Feng Ye, Songxue Chi, Bryan C. Chakoumakos, Jaime A. Fernandez-Baca, Tongfei Qi, and G. Cao. Magnetic and crystal structures of Sr_2IrO_4: A neutron diffraction study. *Phys. Rev. B*, 87:140406, Apr 2013. URL http://link.aps.org/doi/10.1103/PhysRevB.87.140406. 49, 96, 106

[41] Chetan Dhital, Sovit Khadka, Z. Yamani, Clarina de la Cruz, T. C. Hogan, S. M. Disseler, Mani Pokharel, K. C. Lukas, Wei Tian, C. P. Opeil, Ziqiang Wang, and Stephen D. Wilson. Spin ordering and electronic texture in the bilayer iridate $Sr_3Ir_2O_7$. *Phys. Rev. B*, 86:100401, Sep 2012. URL http://link.aps.org/doi/10.1103/PhysRevB.86.100401. 49, 145, 164, 191

[42] Chetan Dhital, Tom Hogan, Z. Yamani, Clarina de la Cruz, Xiang Chen, Sovit Khadka, Zhensong Ren, and Stephen D. Wilson. Neutron scattering study of correlated phase behavior in Sr_2IrO_4. *Phys. Rev. B*, 87:144405, Apr 2013. URL http://link.aps.org/doi/10.1103/PhysRevB.87.144405. 49, 95, 96

[43] Hongbin Zhang, Kristjan Haule, and David Vanderbilt. Effective J=1/2 Insulating State in Ruddlesden-Popper Iridates: An LDA+DMFT Study. *Phys. Rev. Lett.*, 111:246402, Dec 2013. URL http://link.aps.org/doi/10.1103/PhysRevLett.111.246402. 50, 95, 112, 113

[44] S. W. Lovesey. *Theory of neutron scattering from condensed matter*, volume 1 of *International series of monographs on physics*. Clarendon Press, 1984. 56

[45] F. de Bergevin and M. Brunel. Observation of magnetic superlattice peaks by x-ray diffraction on an antiferromagnetic nio crystal. *Physics Letters A*, 39(2):141 – 142, 1972. ISSN 0375-9601. URL `http://www.sciencedirect.com/science/article/pii/0375960172910547`. 57

[46] F. de Bergevin and M. Brunel. Diffraction of X-rays by magnetic materials. I. General formulae and measurements on ferro- and ferrimagnetic compounds. *Acta Crystallographica Section A*, 37(3):314–324, 1981. URL `http://dx.doi.org/10.1107/S0567739481000739`. 57

[47] J. Als-Nielsen and D. McMorrow. *Elements of Modern X-ray Physics*. John Wiley & Sons, 2011. ISBN 9780470973950. URL `http://books.google.co.uk/books?id=rlqlboWlTRMC`. 57

[48] J. P. Hannon, G. T. Trammell, M. Blume, and Doon Gibbs. X-ray resonance exchange scattering. *Phys. Rev. Lett.*, 61:1245–1248, Sep 1988. doi: 10.1103/PhysRevLett.61.1245. URL `http://link.aps.org/doi/10.1103/PhysRevLett.61.1245`. 57, 67, 108

[49] M. Moretti Sala, C. Henriquet, L. Simonelli, R. Verbeni, and G. Monaco. High energy-resolution set-up for Ir L_3 edge RIXS experiments . *Journal of Electron Spectroscopy and Related Phenomena*, 188(0):150 – 154, 2013. ISSN 0368-2048. URL `http://www.sciencedirect.com/science/article/pii/S0368204812001077`. 60

[50] M. Blume. Magnetic scattering of x rays (invited). *Journal of Applied Physics*, 57(8):3615–3618, 1985. URL `http://scitation.aip.org/content/aip/journal/jap/57/8/10.1063/1.335023`. 60

[51] Luuk Ament. *Resonant Inelastic X-ray Scattering Studies of Elementary Excitations*. PhD thesis, University Delft-Leiden, November 2010. 65

[52] Massimo Altarelli. Resonant x-ray scattering: A theoretical introduction. In Eric Beaurepaire, Herv Bulou, Fabrice Scheurer, and

Jean-Paul Kappler, editors, *Magnetism: A Synchrotron Radiation Approach*, volume 697 of *Lecture Notes in Physics*, pages 201–242. Springer Berlin Heidelberg, 2006. URL `http://dx.doi.org/10.1007/3-540-33242-1_8`. 65

[53] J. P. Hill and D. F. McMorrow. Resonant Exchange Scattering: Polarization Dependence and Correlation Function. *Acta Crystallographica Section A*, 52(2):236–244, Mar 1996. URL `http://dx.doi.org/10.1107/S0108767395012670`. 67

[54] L C Chapon and S W Lovesey. The magnetic motif and the wavefunction of Kramers ions in strontium iridate (Sr_2IrO_4). *Journal of Physics: Condensed Matter*, 23(25):252201, Jun 2011. URL `http://dx.doi.org/10.1088/0953-8984/23/25/252201`. 71, 94

[55] D. Haskel, G. Fabbris, Mikhail Zhernenkov, P. P. Kong, C. Q. Jin, G. Cao, and M. van Veenendaal. Pressure Tuning of the Spin-Orbit Coupled Ground State in Sr_2IrO_4. *Phys. Rev. Lett.*, 109:027204, Jul 2012. URL `http://link.aps.org/doi/10.1103/PhysRevLett.109.027204`. 71, 94, 95, 126

[56] Marco Moretti. *Magnetic and orbital resonant inelastic soft x-ray scattering*. PhD thesis, Politecnico di Milano, 2011. 72

[57] M Moretti Sala, V Bisogni, C Aruta, G Balestrino, H Berger, N B Brookes, G M de Luca, D Di Castro, M Grioni, M Guarise, and et al. Energy and symmetry of dd excitations in undoped layered cuprates measured by Cu L_3 resonant inelastic x-ray scattering. *New Journal of Physics*, 13(4):043026, Apr 2011. doi: 10.1088/1367-2630/13/4/043026. URL `http://dx.doi.org/10.1088/1367-2630/13/4/043026`. 72, 191

[58] S. Fujiyama, H. Ohsumi, T. Komesu, J. Matsuno, B. J. Kim, M. Takata, T. Arima, and H. Takagi. Two-Dimensional Heisenberg Behavior of J_{eff}=1/2 Isospins in the Paramagnetic State of the Spin-Orbital Mott Insulator Sr_2IrO_4. *Physical Review Letters*, 108 (24), Jun 2012. URL `http://dx.doi.org/10.1103/PhysRevLett.108.247212`. 79, 94

[59] D. Attwood. *Soft X-Rays and Extreme Ultraviolet Radiation: Principles and Applications*. Cambridge University Press, 2007. ISBN 9780521029971. URL `http://books.google.co.uk/books?id=clAANTKBStcC`. 82

[60] J H Beaumont and M Hart. Multiple bragg reflection monochromators for synchrotron x radiation. *Journal of Physics E: Scientific Instruments*, 7(10):823, 1974. URL `http://stacks.iop.org/0022-3735/7/i=10/a=014`. 83

[61] S. P. Collins, A. Bombardi, A. R. Marshall, J. H. Williams, G. Barlow, A. G. Day, M. R. Pearson, R. J. Woolliscroft, R. D. Walton, G. Beutier, and G. Nisbet. Diamond Beamline I16 (Materials & Magnetism). *AIP Conference Proceedings*, 1234(1):303–306, 2010. URL `http://scitation.aip.org/content/aip/proceeding/aipcp/10.1063/1.3463196`. 85

[62] F. Vaillant. Utilisation des paramètres de Stokes dans le calcul de l'état de polarisation d'un faisceau de rayons X après diffraction par un cristal mosaïque. *Acta Crystallographica Section A*, 33(6):967–970, Nov 1977. URL `http://dx.doi.org/10.1107/S0567739477002307`. 86

[63] S. Huotari, F. Albergamo, Gy. Vank, R. Verbeni, and G. Monaco. Resonant inelastic hard x-ray scattering with diced analyzer crystals and position-sensitive detectors. *Review of Scientific Instruments*, 77(5):053102, 2006. URL `http://scitation.aip.org/content/aip/journal/rsi/77/5/10.1063/1.2198805`. 89

[64] S. Huotari, Gy. Vankó, F. Albergamo, C. Ponchut, H. Graafsma, C. Henriquet, R. Verbeni, and G. Monaco. Improving the performance of high-resolution X-ray spectrometers with position-sensitive pixel detectors. *Journal of Synchrotron Radiation*, 12(4):467–472, Jul 2005. URL `http://dx.doi.org/10.1107/S0909049505010630`. 89

[65] X. Liu, Vamshi M. Katukuri, L. Hozoi, Wei-Guo Yin, M. P. M. Dean, M. H. Upton, Jungho Kim, D. Casa, A. Said, T. Gog, T. F.

Qi, G. Cao, A. M. Tsvelik, Jeroen van den Brink, and J. P. Hill. Testing the Validity of the Strong Spin-Orbit-Coupling Limit for Octahedrally Coordinated Iridate Compounds in a Model System Sr_3CuIrO_6. *Phys. Rev. Lett.*, 109:157401, Oct 2012. URL `http://link.aps.org/doi/10.1103/PhysRevLett.109.157401`. 94, 112, 167, 192

[66] Patrick A. Lee, Naoto Nagaosa, and Xiao-Gang Wen. Doping a mott insulator: Physics of high-temperature superconductivity. *Rev. Mod. Phys.*, 78:17–85, Jan 2006. URL `http://link.aps.org/doi/10.1103/RevModPhys.78.17`. 94

[67] Jun Zhao, Q Huang, Clarina de la Cruz, Shiliang Li, J W Lynn, Y Chen, M a Green, G F Chen, G Li, Z Li, J L Luo, N L Wang, and Pengcheng Dai. Structural and magnetic phase diagram of CeFeAsO(1- x)F(x) and its relation to high-temperature superconductivity. *Nature materials*, 7(12):953–9, December 2008. ISSN 1476-1122. URL `http://www.ncbi.nlm.nih.gov/pubmed/18953342`. 94

[68] J. J. Randall, Jr. L. Katz, and R Ward. The Preparation of a Strontium-Iridium Oxides Sr_2IrO_4. *J. Am. Chem. Soc.*, 79:266, 1957. 95

[69] Y. Maeno, H. Hashimoto, K. Yoshida, S. Nishizaki, T. Fujita, J. G. Bednorz, and F. Lichtenberg. Superconductivity in a layered perovskite without copper. *Nature*, 372:532–534, December 1994. URL `http://dx.doi.org/10.1038/372532a0`. 95

[70] M. K. Crawford, M. A. Subramanian, R. L. Harlow, J. A. Fernandez-Baca, Z. R. Wang, and D. C. Johnston. Structural and magnetic studies of Sr_2IrO_4. *Phys. Rev. B*, 49:9198–9201, Apr 1994. URL `http://link.aps.org/doi/10.1103/PhysRevB.49.9198`. 95, 96, 97, 99

[71] N S Kini, A M Strydom, H S Jeevan, C Geibel, and S Ramakrishnan. Transport and thermal properties of weakly ferromagnetic Sr_2IrO_4.

Journal of Physics: Condensed Matter, 18(35):8205, 2006. URL http://stacks.iop.org/0953-8984/18/i=35/a=008. 97

[72] Jungho Kim, D. Casa, M. H. Upton, T. Gog, Young-June Kim, J. F. Mitchell, M. van Veenendaal, M. Daghofer, J. van den Brink, G. Khaliullin, and B. J. Kim. Magnetic Excitation Spectra of Sr_2IrO_4 Probed by Resonant Inelastic X-Ray Scattering: Establishing Links to Cuprate Superconductors. *Phys. Rev. Lett.*, 108: 177003, Apr 2012. URL http://link.aps.org/doi/10.1103/PhysRevLett.108.177003. 105, 112, 176, 180, 183, 192

[73] M. Moretti Sala, M. Rossi, S. Boseggia, J. Akimitsu, N. B. Brookes, M. Isobe, M. Minola, H. Okabe, H. M. Rønnow, L. Simonelli, D. F. McMorrow, and G. Monaco. Orbital occupancies and the putative $j_{\mathrm{eff}} = 1/2$ ground state in Ba_2IrO_4: A combined oxygen K-edge XAS and RIXS study. *Phys. Rev. B*, 89:121101, Mar 2014. URL http://link.aps.org/doi/10.1103/PhysRevB.89.121101. 105, 127, 132, 167

[74] M. Ge, T. F. Qi, O. B. Korneta, D. E. De Long, P. Schlottmann, W. P. Crummett, and G. Cao. Lattice-driven magnetoresistivity and metal-insulator transition in single-layered iridates. *Phys. Rev. B*, 84:100402, Sep 2011. URL http://link.aps.org/doi/10.1103/PhysRevB.84.100402. 111

[75] S. Chikara, O. Korneta, W. P. Crummett, L. E. DeLong, P. Schlottmann, and G. Cao. Giant magnetoelectric effect in the j_{eff}=1/2 Mott insulator Sr_2IrO_4. *Phys. Rev. B*, 80:140407, Oct 2009. doi: 10.1103/PhysRevB.80.140407. URL http://link.aps.org/doi/10.1103/PhysRevB.80.140407. 111

[76] Tôru Moriya. Anisotropic superexchange interaction and weak ferromagnetism. *Phys. Rev.*, 120:91–98, Oct 1960. URL http://link.aps.org/doi/10.1103/PhysRev.120.91. 112, 114, 129

[77] Beom Hyun Kim, G. Khaliullin, and B. I. Min. Magnetic Couplings, Optical Spectra, and Spin-Orbit Exciton in Sr_2IrO_4. *Phys. Rev.*

Lett., 109:167205, Oct 2012. URL `http://link.aps.org/doi/10.1103/PhysRevLett.109.167205`. 112

[78] Natalia B. Perkins, Yuriy Sizyuk, and Peter Wölfle. Interplay of many-body and single-particle interactions in iridates and rhodates. *Phys. Rev. B*, 89:035143, Jan 2014. URL `http://link.aps.org/doi/10.1103/PhysRevB.89.035143`. 112

[79] S-W. Cheong, J. D. Thompson, and Z. Fisk. Metamagnetism in La_2CuO_4. *Phys. Rev. B*, 39:4395–4398, Mar 1989. URL `http://link.aps.org/doi/10.1103/PhysRevB.39.4395`. 112

[80] H. Gretarsson, J. P. Clancy, X. Liu, J. P. Hill, Emil Bozin, Yogesh Singh, S. Manni, P. Gegenwart, Jungho Kim, A. H. Said, D. Casa, T. Gog, M. H. Upton, Heung-Sik Kim, J. Yu, Vamshi M. Katukuri, L. Hozoi, Jeroen van den Brink, and Young-June Kim. Crystal-Field Splitting and Correlation Effect on the Electronic Structure of A_2IrO_3. *Phys. Rev. Lett.*, 110:076402, Feb 2013. URL `http://link.aps.org/doi/10.1103/PhysRevLett.110.076402`. 112, 167, 192

[81] Hosub Jin, Hogyun Jeong, Taisuke Ozaki, and Jaejun Yu. Anisotropic exchange interactions of spin-orbit-integrated states in Sr_2IrO_4. *Phys. Rev. B*, 80:075112, Aug 2009. URL `http://link.aps.org/doi/10.1103/PhysRevB.80.075112`. 113

[82] S Moser, L Moreschini, A Ebrahimi, B Dalla Piazza, M Isobe, H Okabe, J Akimitsu, V V Mazurenko, K S Kim, A Bostwick, E Rotenberg, J Chang, H M Rnnow, and M Grioni. The electronic structure of the high-symmetry perovskite iridate Ba_2IrO_4. *New Journal of Physics*, 16(1):013008, 2014. URL `http://stacks.iop.org/1367-2630/16/i=1/a=013008`. 115

[83] Malcom F. Collins. *Magnetic Critical Scattering*. Oxford University Press, 1989. 119, 121

[84] Lars Onsager. Crystal Statistics. I. A Two-Dimensional Model with an Order-Disorder Transition. *Phys. Rev.*, 65:117–149, Feb 1944.

doi: 10.1103/PhysRev.65.117. URL http://link.aps.org/doi/10.1103/PhysRev.65.117. 121

[85] R. J. Birgeneau, J. Skalyo, and G. Shirane. Critical Magnetic Scattering in K_2NiF_4. *Phys. Rev. B*, 3:1736–1749, Mar 1971. doi: 10.1103/PhysRevB.3.1736. URL http://link.aps.org/doi/10.1103/PhysRevB.3.1736. 121

[86] Hironobu Ikeda and Kinshiro Hirakawa. Neutron scattering study of two-dimensional Ising nature of K_2CoF_4 . *Solid State Communications*, 14(7):529 – 532, 1974. URL http://www.sciencedirect.com/science/article/pii/0038109874910047. 121

[87] S T Bramwell and P C W Holdsworth. Magnetization and universal sub-critical behaviour in two-dimensional XY magnets. *Journal of Physics: Condensed Matter*, 5(4):L53, 1993. URL http://stacks.iop.org/0953-8984/5/i=4/a=004. 121

[88] G. van der Laan and B. T. Thole. Local Probe for Spin-Orbit Interaction. *Phys. Rev. Lett.*, 60:1977–1980, May 1988. URL http://link.aps.org/doi/10.1103/PhysRevLett.60.1977. 123, 124

[89] B. T. Thole and G. van der Laan. Linear relation between x-ray absorption branching ratio and valence-band spin-orbit expectation value. *Phys. Rev. A*, 38:1943–1947, Aug 1988. URL http://link.aps.org/doi/10.1103/PhysRevA.38.1943. 123, 124

[90] B. T. Thole and G. van der Laan. Branching ratio in x-ray absorption spectroscopy. *Phys. Rev. B*, 38:3158–3171, Aug 1988. URL http://link.aps.org/doi/10.1103/PhysRevB.38.3158. 123

[91] M. Brown, R. E. Peierls, and E. A. Stern. White lines in x-ray absorption. *Phys. Rev. B*, 15:738–744, Jan 1977. URL http://link.aps.org/doi/10.1103/PhysRevB.15.738. 124

[92] M. A. Laguna-Marco, D. Haskel, N. Souza-Neto, J. C. Lang, V. V. Krishnamurthy, S. Chikara, G. Cao, and M. van Veenendaal. Orbital magnetism and spin-orbit effects in the electronic structure of $bairo_3$.

Phys. Rev. Lett., 105:216407, Nov 2010. URL `http://link.aps.org/doi/10.1103/PhysRevLett.105.216407`. 125, 126

[93] J. P. Clancy, N. Chen, C. Y. Kim, W. F. Chen, K. W. Plumb, B. C. Jeon, T. W. Noh, and Young-June Kim. Spin-orbit coupling in iridium-based $5d$ compounds probed by x-ray absorption spectroscopy. *Phys. Rev. B*, 86:195131, Nov 2012. URL `http://link.aps.org/doi/10.1103/PhysRevB.86.195131`. 126, 171

[94] A.S Wills. A new protocol for the determination of magnetic structures using simulated annealing and representational analysis (SARAh). *Physica B: Condensed Matter*, 276278(0):680–681, 2000. URL `http://www.sciencedirect.com/science/article/pii/S0921452699017226`. 129, 147, 207

[95] O. V. Kovalev. *Representations of the Crystallographic Space*. Gordon and Breach Science Publishers, 1993. 129

[96] Vamshi M. Katukuri, Hermann Stoll, Jeroen van den Brink, and Liviu Hozoi. *Ab initio* determination of excitation energies and magnetic couplings in correlated quasi-two-dimensional iridates. *Phys. Rev. B*, 85:220402, Jun 2012. URL `http://link.aps.org/doi/10.1103/PhysRevB.85.220402`. 132, 180, 181

[97] J. B. Goodenough. *Magnetism and the Chemical Bond*. John Wiley & Sons, New York-London, 1963. 132, 163

[98] Vamshi M. Katukuri, Hermann Stoll, Jeroen van den Brink, and Liviu Hozoi. Electronic structure of low-dimensional $4d^5$ oxides: interplay of ligand distortions, overall lattice anisotropy, and spin-obit interactions. Private communication submitted to Inorg. Chemistry, 2014. 132

[99] S. J. Moon, H. Jin, K. W. Kim, W. S. Choi, Y. S. Lee, J. Yu, G. Cao, A. Sumi, H. Funakubo, C. Bernhard, and T. W. Noh. Dimensionality-Controlled Insulator-Metal Transition and Correlated Metallic State in $5d$ Transition Metal Oxides $Sr_{n+1}Ir_nO_{3n+1}$ ($n=$1, 2, and ∞). *Phys. Rev. Lett.*, 101:226402, Nov

2008. URL `http://link.aps.org/doi/10.1103/PhysRevLett.101.226402`. 136, 140, 168, 170

[100] M.A. Subramanian, M.K. Crawford, and R.L. Harlow. Single crystal structure determination of double layered strontium iridium oxide [$Sr_3Ir_2O_7$]. *Materials Research Bulletin*, 29(6):645 – 650, 1994. URL `http://www.sciencedirect.com/science/article/pii/0025540894901201`. 137, 138

[101] Hirofumi Matsuhata, Ichiro Nagai, Yoshiyuki Yoshida, Sigeo Hara, Shin ichi Ikeda, and Naoki Shirakawa. Crystal structure of $Sr_3Ir_2O_7$ investigated by transmission electron microscopy. *Journal of Solid State Chemistry*, 177(10):3776 – 3783, 2004. URL `http://www.sciencedirect.com/science/article/pii/S0022459604003615`. 137, 139, 164

[102] E. Prince, editor. *International Tables for Crystallography Volume C: Mathematical, Physical and Chemical Tables*. Springer, 1992. 138

[103] S. Fujiyama, K. Ohashi, H. Ohsumi, K. Sugimoto, T. Takayama, T. Komesu, M. Takata, T. Arima, and H. Takagi. Weak antiferromagnetism of $J_{\text{eff}} = 1/2$ band in bilayer iridate $Sr_3Ir_2O_7$. *Phys. Rev. B*, 86:174414, Nov 2012. URL `http://link.aps.org/doi/10.1103/PhysRevB.86.174414`. 143, 164

[104] S. D. Brown, L. Bouchenoire, D. Bowyer, J. Kervin, D. Laundy, M. J. Longfield, D. Mannix, D. F. Paul, A. Stunault, P. Thompson, M. J. Cooper, C. A. Lucas, and W. G. Stirling. The XMaS beamline at ESRF: instrumental developments and high-resolution diffraction studies. *Journal of Synchrotron Radiation*, 8(6):1172–1181, Nov 2001. URL `http://dx.doi.org/10.1107/S0909049501015394`. 145

[105] S Boseggia, R Springell, H C Walker, A T Boothroyd, D Prabhakaran, S P Collins, and D F McMorrow. On the magnetic structure of $Sr_3Ir_2O_7$: an x-ray resonant scattering study. *Journal of Physics: Condensed Matter*, 24(31):312202, 2012. URL `http://stacks.iop.org/0953-8984/24/i=31/a=312202`. 156

[106] Y. Joly. X-ray absorption near-edge structure calculations beyond the muffin-tin approximation. *Phys. Rev. B*, 63:125120, Mar 2001. URL `http://link.aps.org/doi/10.1103/PhysRevB.63.125120`. 160, 168

[107] P.D. Hatton, R.D. Johnson, S.R. Bland, C. Mazzoli, T.A.W. Beale, C.-H. Du, and S.B. Wilkins. Magnetic structure determination using polarised resonant x-ray scattering. *Journal of Magnetism and Magnetic Materials*, 321(7):810 – 813, 2009. URL `http://www.sciencedirect.com/science/article/pii/S0304885308012134`. 160

[108] C. Mazzoli, S. B. Wilkins, S. Di Matteo, B. Detlefs, C. Detlefs, V. Scagnoli, L. Paolasini, and P. Ghigna. Disentangling multipole resonances through a full x-ray polarization analysis. *Phys. Rev. B*, 76:195118, Nov 2007. URL `http://link.aps.org/doi/10.1103/PhysRevB.76.195118`. 160

[109] C. Detlefs, M. Sanchez del Rio, and C. Mazzoli. X-ray polarization: General formalism and polarization analysis. *The European Physical Journal Special Topics*, 208(1):359–371, 2012. URL `http://dx.doi.org/10.1140/epjst/e2012-01630-3`. 160

[110] J. W. Kim, Y. Choi, Jungho Kim, J. F. Mitchell, G. Jackeli, M. Daghofer, J. van den Brink, G. Khaliullin, and B. J. Kim. Dimensionality Driven Spin-Flop Transition in Layered Iridates. *Phys. Rev. Lett.*, 109:037204, Jul 2012. URL `http://link.aps.org/doi/10.1103/PhysRevLett.109.037204`. 163, 170

[111] S W Lovesey, D D Khalyavin, P Manuel, L C Chapon, G Cao, and T F Qi. Magnetic symmetries in neutron and resonant x-ray Bragg diffraction patterns of four iridium oxides. *Journal of Physics: Condensed Matter*, 24(49):496003, 2012. URL `http://stacks.iop.org/0953-8984/24/i=49/a=496003`. 164

[112] K. Dumesnil, A. Stunault, Ph. Mangin, C. Vettier, D. Wermeille, N. Bernhoeft, S. Langridge, C. Dufour, and G. Marchal. Resonant

magnetic x-ray studies of magnetic ordering in dysprosium layers. *Phys. Rev. B*, 58:3172–3179, Aug 1998. URL `http://link.aps.org/doi/10.1103/PhysRevB.58.3172`. 165, 166

[113] Th. Brückel, D. Hupfeld, J. Strempfer, W. Caliebe, K. Mattenberger, A. Stunault, N. Bernhoeft, and G.J. McIntyre. Antiferromagnetic order and phase transitions in GdS as studied with X-ray resonance-exchange scattering. *The European Physical Journal B - Condensed Matter and Complex Systems*, 19(4):475–490, 2001. URL `http://dx.doi.org/10.1007/s100510170293`. 165

[114] B.L. Henke, E.M. Gullikson, and J.C. Davis. X-ray interactions: Photoabsorption, scattering, transmission, and reflection at e = 50-30,000 ev, z = 1-92. *Atomic Data and Nuclear Data Tables*, 54(2): 181 – 342, 1993. URL `http://www.sciencedirect.com/science/article/pii/S0092640X83710132`. 165, 166, 167

[115] Cullie J. Sparks. Inelastic Resonance Emission of X Rays: Anomalous Scattering Associated with Anomalous Dispersion. *Phys. Rev. Lett.*, 33:262–265, Jul 1974. URL `http://link.aps.org/doi/10.1103/PhysRevLett.33.262`. 174

[116] Luuk J. P. Ament, Giacomo Ghiringhelli, Marco Moretti Sala, Lucio Braicovich, and Jeroen van den Brink. Theoretical Demonstration of How the Dispersion of Magnetic Excitations in Cuprate Compounds can be Determined Using Resonant Inelastic X-Ray Scattering. *Phys. Rev. Lett.*, 103:117003, Sep 2009. URL `http://link.aps.org/doi/10.1103/PhysRevLett.103.117003`. 174, 175

[117] L. Braicovich, J. van den Brink, V. Bisogni, M. Moretti Sala, L. J. P. Ament, N. B. Brookes, G. M. De Luca, M. Salluzzo, T. Schmitt, V. N. Strocov, and G. Ghiringhelli. Magnetic Excitations and Phase Separation in the Underdoped $La_{2-x}Sr_xCuO_4$ Superconductor Measured by Resonant Inelastic X-Ray Scattering. *Phys. Rev. Lett.*, 104:077002, Feb 2010. URL `http://link.aps.org/doi/10.1103/PhysRevLett.104.077002`. 174, 176, 191

[118] Luuk J. P. Ament, Michel van Veenendaal, Thomas P. Devereaux, John P. Hill, and Jeroen van den Brink. Resonant inelastic x-ray scattering studies of elementary excitations. *Rev. Mod. Phys.*, 83:705–767, Jun 2011. URL `http://link.aps.org/doi/10.1103/RevModPhys.83.705`. 175

[119] R. Coldea, S. M. Hayden, G. Aeppli, T. G. Perring, C. D. Frost, T. E. Mason, S.-W. Cheong, and Z. Fisk. Spin Waves and Electronic Interactions in La_2CuO_4. *Phys. Rev. Lett.*, 86:5377–5380, Jun 2001. URL `http://link.aps.org/doi/10.1103/PhysRevLett.86.5377`. 176, 180, 184

[120] Luuk J. P. Ament, Giniyat Khaliullin, and Jeroen van den Brink. Theory of resonant inelastic x-ray scattering in iridium oxide compounds: Probing spin-orbit-entangled ground states and excitations. *Phys. Rev. B*, 84:020403, Jul 2011. URL `http://link.aps.org/doi/10.1103/PhysRevB.84.020403`. 175, 179

[121] K. Ishii, I. Jarrige, M. Yoshida, K. Ikeuchi, J. Mizuki, K. Ohashi, T. Takayama, J. Matsuno, and H. Takagi. Momentum-resolved electronic excitations in the Mott insulator Sr_2IrO_4 studied by resonant inelastic x-ray scattering. *Phys. Rev. B*, 83:115121, Mar 2011. URL `http://link.aps.org/doi/10.1103/PhysRevB.83.115121`. 180

[122] Jungho Kim, A. H. Said, D. Casa, M. H. Upton, T. Gog, M. Daghofer, G. Jackeli, J. van den Brink, G. Khaliullin, and B. J. Kim. Large Spin-Wave Energy Gap in the Bilayer Iridate $Sr_3Ir_2O_7$: Evidence for Enhanced Dipolar Interactions Near the Mott Metal-Insulator Transition. *Phys. Rev. Lett.*, 109:157402, Oct 2012. URL `http://link.aps.org/doi/10.1103/PhysRevLett.109.157402`. 183, 186, 187, 190, 191, 195

[123] T. G. Perring, D. T. Adroja, G. Chaboussant, G. Aeppli, T. Kimura, and Y. Tokura. Spectacular Doping Dependence of Interlayer Exchange and Other Results on Spin Waves in Bilayer Manganites. *Phys. Rev. Lett.*, 87:217201, Oct 2001. URL `http://link.aps.org/doi/10.1103/PhysRevLett.87.217201`. 185

[124] D. Reznik, P. Bourges, H. F. Fong, L. P. Regnault, J. Bossy, C. Vettier, D. L. Milius, I. A. Aksay, and B. Keimer. Direct observation of optical magnons in $YBa_2Cu_3O_{6.2}$. *Phys. Rev. B*, 53:R14741–R14744, Jun 1996. URL `http://link.aps.org/doi/10.1103/PhysRevB.53.R14741`. 185, 186

[125] D.D. Stancil and A. Prabhakar. *Spin Waves: Theory and Applications*. Springer, 2009. URL `http://books.google.co.uk/books?id=ehN6-ubvKwoC`. 186

[126] Vera Irina Schnells. Theory of the magnetic properties of the bilayer iridate $Sr_3Ir_2O_7$. Master's thesis, Philipps Universitat Märburg, 2013. 189

[127] Subir Sachdev and R. N. Bhatt. Bond-operator representation of quantum spins: Mean-field theory of frustrated quantum Heisenberg antiferromagnets. *Phys. Rev. B*, 41:9323–9329, May 1990. URL `http://link.aps.org/doi/10.1103/PhysRevB.41.9323`. 189

[128] B. Normand and Ch. Rüegg. Complete bond-operator theory of the two-chain spin ladder. *Phys. Rev. B*, 83:054415, Feb 2011. URL `http://link.aps.org/doi/10.1103/PhysRevB.83.054415`. 189

[129] O. P. Sushkov and V. N. Kotov. Bound States of Magnons in the $S = 1/2$ Quantum Spin Ladder. *Phys. Rev. Lett.*, 81:1941–1944, Aug 1998. URL `http://link.aps.org/doi/10.1103/PhysRevLett.81.1941`. 189

[130] Sudha Gopalan, T. M. Rice, and M. Sigrist. Spin ladders with spin gaps: A description of a class of cuprates. *Phys. Rev. B*, 49:8901–8910, Apr 1994. URL `http://link.aps.org/doi/10.1103/PhysRevB.49.8901`. 189

[131] L. Hozoi, H. Gretarsson, J. P. Clancy, B.-G. Jeon, B. Lee, K. H. Kim, V. Yushankhai, Peter Fulde, D. Casa, T. Gog, Jungho Kim, A. H. Said, M. H. Upton, Young-June Kim, and Jeroen van den Brink. Longer-range lattice anisotropy strongly competing with spin-orbit interactions in pyrochlore iridates. *Phys. Rev. B*, 89:

115111, Mar 2014. URL `http://link.aps.org/doi/10.1103/PhysRevB.89.115111`. 192

[132] B. O. Wells, Z. X. Shen, A. Matsuura, D. M. King, M. A. Kastner, M. Greven, and R. J. Birgeneau. E versus k Relations and Many Body Effects in the Model Insulating Copper Oxide $Sr_2CuO_2Cl_2$. *Phys. Rev. Lett.*, 74:964–967, Feb 1995. URL `http://link.aps.org/doi/10.1103/PhysRevLett.74.964`. 192

[133] P. Zheng, Y. G. Shi, Q. S. Wu, G. Xu, T. Dong, Z. G. Chen, R. H. Yuan, B. Cheng, K. Yamaura, J. L. Luo, and N. L. Wang. Continuous magnetic phase transition in half-frustrated $Ca_2Os_2O_7$. *Phys. Rev. B*, 86:195108, Nov 2012. URL `http://link.aps.org/doi/10.1103/PhysRevB.86.195108`. 200

[134] J. Yamaura, K. Ohgushi, H. Ohsumi, T. Hasegawa, I. Yamauchi, K. Sugimoto, S. Takeshita, A. Tokuda, M. Takata, M. Udagawa, M. Takigawa, H. Harima, T. Arima, and Z. Hiroi. Tetrahedral Magnetic Order and the Metal-Insulator Transition in the Pyrochlore Lattice of $Cd_2Os_2O_7$. *Phys. Rev. Lett.*, 108:247205, Jun 2012. URL `http://link.aps.org/doi/10.1103/PhysRevLett.108.247205`. 200

Acknowledgments

First, I would like to express my gratitude to my supervisors, Des McMorrow and Steve Collins, whose expertise, understanding, and patience, added considerably to my research experience. I appreciate their vast knowledge and skills in many areas, in particular I was impressed by the ability of writing captivating articles and stories (Des), and the meticulous art of running an amazing beamline (Steve). I wish I can make some of these skills mine in the near future.

I would like to thank all the I16 team that welcomed me. During the last three years I have felt at home. A special thanks goes to Carlo, Alessandro, Ben, and Gareth for their help in several occasions. Gareth deserves a special mention for representing a constant challenge for improving my understanding of the Irish inflection. A very special thanks goes to Nicola for endless coffees, sports discussions, and great support with crystallographic measurements.

I must also acknowledge Helen and Ross for the infinite hours spent side by side during beamtimes. I really appreciate your support along the way.

A special thanks goes to Marco Moretti (Sala) for many reasons. First, I believe our discussions about physics in iridates helped greatly our understanding of this field. Second, I am indebted to you for introducing me to the wonderful world of resonant inelastic scattering and spherical harmonics. Finally, every dinner we had downtown was a dinner not spent at the ESRF canteen. For this I will be forever grateful.

A thanks goes to Luigi Paolasini (Gigi) for the running (quitting smoking has been remarkably beneficial), and the amazing pizza, the best in Grenoble.

Thanks to Christian for the careful reading of this manuscript and to Robin Perry, Dharmalingam Prabhakaran, and Andrew Boothroyd for providing me great samples.

I would also like to thank my family for the support they provided me through my entire life, and in particular I must acknowledge my girlfriend Maya for her unconditional love.

Finally, I recognize that this research would not have been possible without the financial assistance of the Impact Studentship awarded jointly by UCL and Diamond Light Source.